IntechOpen

Green Nanotechnology

Overview and Further Prospects

Edited by Marcelo L. Larramendy and Sonia Soloneski

GREEN NANOTECHNOLOGY - OVERVIEW AND FURTHER PROSPECTS

Edited by **Marcelo L. Larramendy** and **Sonia Soloneski**

Green Nanotechnology - Overview and Further Prospects
http://dx.doi.org/10.5772/61432
Edited by Marcelo L. Larramendy and Sonia Soloneski

Contributors

Seyed Mohsen Sadeghzadeh, Mehdi Mogharabi, Francesco Ruffino, Giuseppe Cacciato, Massimo Zimbone, Maria Grazia Grimaldi, Fahmina Zafar, Eram Sharmin, Nahid Nishat, Sharif Ahmad, André Decroly, Marc Debliquy, Arnaud Krumpmann, Driss Lahem, Man Singh, Xianfeng Chen, Jia Lin, Xiaolin Liu, Shu Zhu, Vladimir V. V. Kouznetsov, Carlos A. Andrés Martínez Bonilla, Ahmad Alshammari, V. Narayana Kalevaru, Andreas Martin, Guilin Chen, Shuiyuan Chen, Zhigao Huang, Jorge A.R. Salvador, Samuel Silvestre, Maria Manuel Silva

Notice

First published in Croatia, 2016 by INTECH d.o.o.
eBook (PDF) Published by IN TECH d.o.o.
Place and year of publication of eBook (PDF): Rijeka, 2019.
IntechOpen is the global imprint of IN TECH d.o.o.
Printed in Croatia

Legal deposit, Croatia: National and University Library in Zagreb

Additional hard and PDF copies can be obtained from orders@intechopen.com

Green Nanotechnology - Overview and Further Prospects
Edited by Marcelo L. Larramendy and Sonia Soloneski

p. cm.

Print ISBN 978-953-51-2409-2

Online ISBN 978-953-51-2410-8

eBook (PDF) ISBN 978-953-51-4199-0

Meet the editors

Marcelo L. Larramendy, Ph.D., serves as Professor of Molecular Cell Biology at the School of Natural Sciences and Museum (National University of La Plata, Argentina). He has been appointed as Senior Researcher of the National Scientific and Technological Research Council of Argentina. He is also Former Member of the Executive Committee of the Latin American Association of Environmental Mutagenesis, Teratogenesis and Carcinogenesis. He is author of more than 470 contributions, including scientific publications, research communications and conferences worldwide. He is recipient of several national and international awards. Prof. Larramendy is a regular Lecturer at the international A. Hollaender Courses organized by the IAEMS and is former guest scientist at the NIH, USA, and University of Helsinki, Finland. He is expert in Genetic Toxicology and is, or has been, referee for more than 30 international scientific journals. He is also member of the International Panel of Experts at the International Agency for Research on Cancer (IARC, WHO, Lyon, France) in 2015 for the evaluation of DDT, 2,4-D, and Lindane. Presently, Prof. Dr. Larramendy is Head of the Laboratory of Molecular Cytogenetics and Genotoxicology at the UNLP.

Sonia Soloneski is PhD in Natural Sciences and Professor Assistant of Molecular Cell Biology at the Faculty of Natural Sciences and Museum of La Plata, National University of La Plata, Argentina. She became a member of the National Scientific and Technological Research Council (CONICET) of Argentina in Genetic Toxicology field. Presently, she is member of the Latin American Association of Environmental Mutagenesis, Teratogenesis and Carcinogenesis (ALAMCTA), the Argentinean Society of Toxicology (ATA), and the Argentinean Society of Genetics (SAG). She is author of more than 290 scientific publications on the field, including scientific publications in research papers, reviewed journals, and conferences worldwide. She is a referent for issues related to Genetic Toxicology, Mutagenesis, and Ecotoxicology field.

Contents

Preface

In the 1990s, a new emerging scientific field arose with the potential to radically generate new products and processes: nanoscience, the study of structures and materials on the scale of nanometers. Nanoparticles have dimensions ranging from 1 up to 100 nanometers, and they possess physicochemical characteristics and coatings that impart upon them unique electrical, thermal, mechanical, and imaging properties that make them highly attractive for applications within the commercial, pharmaceutical, medical, food packaging, cosmetics, household appliance, and environmental sectors, among others. It has been estimated that the production of nanomaterials will continue to increase, and that by 2020, it will increase to more than 25 times the current rate. Nanoscience and nanotechnology can be used across all other scientific fields, such as chemistry, biology, physics, materials science, and engineering.

During recent years, proactive multidisciplinary research initiatives have been launched by regulatory institutions such as the U.S. Environmental Protection Agency (U.S. EPA), the National Institute of Environmental Health Sciences (NIEHS, USA), the European Food Safety Authority (EFSA, Italy), and the International Agency of Research on Cancer (IARC, France), who are charged with the protection of human health and the environment and warranting that the employment of engineered nanotechnological products can occur without hazardous consequences. Occupational health risks associated with manufacturing and using nanomaterials are not yet clearly understood. Minimal information is currently available on dominant exposure routes, potential exposure levels, and material toxicity of nanoscale materials. Although the potential health effects of such exposures are not entirely understood at this time, research investigations indicate that at least some of these nanoparticles are biologically active. Nowadays, there is general and accepted recognition worldwide that the *in vitro, in vivo*, and *in silico* testing strategies and safety assessments currently in place can also be used for nanomaterials to obtain relevant data to help in the development of guidelines for regulating human and environmental exposure to nanoparticles.

Studies in the field of emerging nanomaterials and nanotechnologies are of increasing importance; most scientific databases reveal increasing numbers of publications such as books, papers, reviews, and even patents, and there is an increasing market share of nanotechnology products, currently in the thousands of billons of US dollars worldwide. Furthermore, the number of publications on the topic of nanoparticles has increased at an almost exponential rate since the early 1990s. In agreement, in the beginning of 2016, a search on the two major databases Scopus and PubMed indicated the existence of nearly 310,000 and 120,000 documents reported so far, respectively.

Actually, researchers are studying and analyzing different approaches and ways that nanotechnology can be made beneficial to the environment and its compartments. This scientific aspect has been branded or labeled "green nanotechnology," since it focuses on challenges at the nanoscale level that have to be overcome to ensure eco-friendly processes and products. In other words, the purposes of green nanotechnology are to create eco-friendly designs within nanotechnology and use them to diminish health and environmental hazards by creating new methodologies to replace existing applications using green nanotechnology products. In this sense, nanotechnology will not merely initiate the next industrial scientific revolution; it will surely facilitate technological solutions. In this regard, it is clearly expected and accepted that green nanotechnology will assist, for example, in helping to provide clean water worldwide through novel filtration methodologies and the proficiency to decontaminate dirty water; in solving a large number of efficiency issues stopping the extensive use of renewable energy generation; in helping waste management and environmental remediation, by reducing waste dramatically or by developing new industrial and chemical procedures; and in developing materials that will act as alternative replacements for hazardous processes and constituents, causing reductions in material, energy, and waste generation, among other practical solutions.

This book, *Green Nanotechnology – Overview and Further Prospects*, is intended to provide an overview and practical examples of the use of nanomaterials in the new scientific challenges of the green nanotechnology world. We aimed to compile information from a diversity of sources into a single volume to give some real-time examples, extending the concept that green nanotechnology is far from being a scientific conundrum, and instead a real answer to some of the actual problems the whole planet is dealing with.

This book comprises, first, three chapters describing metal and magnetic nanoparticles and their application as green catalysts. The first chapter is aimed at providing a comprehensive overview about metal nanoparticles and their application as emerging green catalysts. The second chapter clearly describes a selection of the most recent and relevant applications of pharmaceutical green chemistry in oxidative steroid synthesis using chemical methods, stressing the catalytic processes, especially those involving the use of heterogeneous nanocatalysts, whose application in this context has increased over the last years. Finally, the third chapter describes both the use of magnetic nanoparticles in organic reaction as a scaffold for the immobilization of metal complexes and the improvement of the methods of production and applying catalysts with magnetic properties in organic reaction. Then, four chapters are incorporated describing the synthesis, characterization, and photocatalytic and antibacterial activity of TiO_2 and other metal nanoparticles for their application in sustainable photocatalytic water purification and for photovoltaic and gas sensing applications. Furthermore, the use of these nanostructures in solar cells to enhance light harvesting and charge collection and the advanced applications of quantum dot-based nanomaterials are addressed, with special emphasis on the pursuit of sustainable development in clean energy resources. The next two chapters discuss, respectively, alkyd coatings and their classification and preparation methods, and nanocomposite coatings, their "green" synthesis routes, their use in the preparation of $Cu_2ZnSnSe_4$ and Cu_2ZnSnS_4 thin films from oxide precursors, and the rationality of applying the oxide method in thin films, including the reactive thermodynamics and annealing process. Last, this book includes a final chapter on friccohesity and fentropy as new models for nanoscale molecular science.

Many researchers have contributed to the publication of this book. Given the fast pace of new scientific publications shedding light on the matter, this book will probably be outdated very soon. We regard this as a positive and healthy fact. The editors hope that this book will continue to meet the expectations and needs of all interested in the green nanotechnology scientific world.

Marcelo L. Larramendy Ph.D. and Sonia Soloneski Ph.D.
School of Natural Sciences and Museum
National University of La Plata
La Plata, Argentina

Chapter 1

Metal Nanoparticles as Emerging Green Catalysts

Ahmad Alshammari, V. Narayana Kalevaru and Andreas Martin

Additional information is available at the end of the chapter

http://dx.doi.org/10.5772/63314

Abstract

Green nanotechnology is defined as the technology applied for building clean technology by which one can reduce the potential risks of environment and also improve human health conditions. It is linked with the implementation of products of nanotechnology and its process of manufacturing. Green nanotechnology synthesizes new nanoproducts with improved properties in such a way that they can substitute some of the existing low-quality products. The main motive of developing new nanoproducts is to enhance sustainability and also to make them more environment friendly. In particular, nanoscale materials (e.g., nanoparticles) can be defined as those having characteristic length scale lying within the nanometric range, that is, in the range between one and several hundreds of nanometers. Within this length scale, the properties of matter are sufficiently different from individual atoms/molecules or from bulk materials. The primary objective of this chapter is to provide comprehensive overview about metal nanoparticles (MNPs) and its application as emerging green catalysts. This chapter contains six sections in total. Section 1 starts with a general introduction, recent progress, and brief summary of the application of MNPs as green catalyst. Section 2 reviews the preparation and characterization of supported metal nanoparticles for a wide range of catalytic applications. Section 3 presents the catalytic properties of supported metal nanoparticles. Section 4 describes briefly some of the most commonly reported supported MNPs in different green catalytic applications. Section 5 concentrates on our own results that related to the application of supported MNPs in catalysis. In this section, the oxidation of benzyl alcohol to benzaldehyde, the production of adipic acid from cyclohexane, the photodegradation of dyes using green route will be discussed. Finally, Section 6 describes the summary of main points and also presents an outlook of the application of MNPs in green chemistry.

Keywords: metal nanoparticles (MNPs), MNPs for environmental application, green catalyst, photocatalysis, MNPs characterization, oxidation reaction

1. Introduction to metal nanoparticles

Materials whose length lies within the nanometric range of one to several hundred nanometers are known as nanoscale materials or nanoparticles [1]. Matter at this scale is characterized by significantly different material properties than molecules, atoms, or bulk items [2]. Because of this, the field of *Nanoscience* was coined to address this relatively novel scientific field. Although the concept of this scientific area is not new, contemporary science is constantly discovering new and favorable applications for both the manufacture sector and academia, which has cast *Nanoscience* as a burgeoning and exciting field. The applications referred to are diverse, and range from environmental development to consumer products, and even therapeutic use (**Figure 1**).

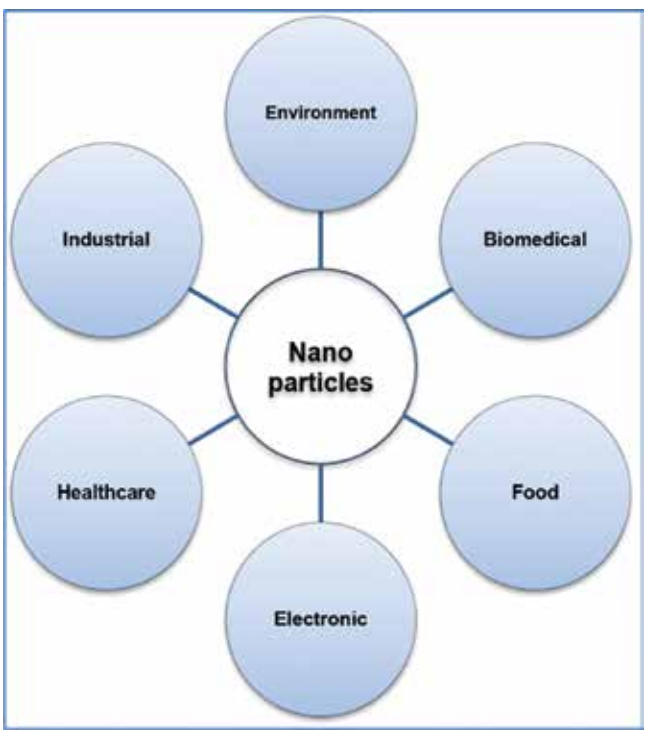

Figure 1. Potential application of nanoparticles in various fields.

Nanoparticles can take many forms, including powder, crystal, and cluster formulae. Nanopowder is used to describe mixtures of fine powder, whereas ultrafine particle mixtures are described as nanocrystals [2]. Clusters can be further classified as nanoclusters if they have a narrow size distribution in the range of 1–10 nm and a minimum of one dimension. Prior to the 1700s, nanoparticle use was limited to high-quality glass, pottery, and tile production. In the mid-nineteenth century, Michael Faraday began to explore nanoparticle stability. At the beginning of the twentieth century, Mie conducted research into nanoparticle color properties.

http://dx.doi.org/10.5772/63314

Shortly thereafter, Richard Zsigmondy received the 1925 Nobel Prize in Chemistry for his work on colloidal suspension of gold nanoparticles using ultramicroscopic techniques.

Metal nanoparticles (MNPs) are deemed to be likely candidates for catalysis due to their relatively large surface area per volume or weight unit as compared with bulk metal, meaning heterogeneous MNPs catalysts typically function on metal surfaces [3]. A variety of techniques are used to develop supports for industrial metal catalysts, which are frequently inorganic and characterized by highly dispersed metals and voluminous surface area. Metal particles tend to be ensemble affairs, consisting of more than one particle in a range of forms and dimensions. Polyhedral particles are formed from the interaction of MNPs with the inorganic supports. Silica gel, activated charcoal, and alumina, among others, are examples of transition metals that are formed from metal particles distributed onto inorganic supports. These are superior to metal powders for numerous reasons, including their stable thermic capacity, diminished cost, greater surface area, and efficacious use of MNPs in the form of wide dispersion.

The electrochemical makeup of particularly dimensioned MNPs allows them to be used as catalysts. As compared with bulk metallic catalysts, greater surface area and measured edge step ratio result in higher outputs. MNPs also are well suited to stereoselective synthesis. MNPs have been increasingly examined in recent years due to their catalytic properties in a range of contexts, for example, as a surfactant for water-soluble polymer, resins, vesicles, and so on. Other examples are the reactions including Fischer-Tropsch, isomerization, and hydroformylation, etc., which also use nanoparticles such as Rh, Pt, Ir, Au, and Pd as catalysts [4]. The size of the metal particles holds great influence over the catalytic abilities of the metal. Additionally, if one looks to the use of gold nanoparticles in catalysis, the size of the gold particle is directly linked to catalytic activity and/or selectivity. Gold particles with diameters less than 10 nm are deemed to be very active catalysts, while such activity considerably diminishes as the Au diameter increases, and also virtually disappears when the diameter is measured in micrometers range [5, 6].

MNPs are functionalized in many situations as they typically have greater stability in solutions as compared to nonfunctionalized metallic nanoparticles. This is because the nonfunctionalized particles present with a reduced surface area and thus lower catalytic ability due to their tendency to aggregate while in solution. Although ligands can be used to avoid aggregation, they have the consequence of altering catalyst functionality. Nanocatalysts can also be functionalized using polymers and oligomers. Typically, catalytic nanoparticles have been implemented in tandem with polymer matrices; otherwise, they were detained on solid supports [7]. The petrochemical industry has a long history of utilizing supported metal catalysts, particularly Pt, which is used for naphtha reforming. However, new techniques that employ electrostatic interaction forces are now being created that will enable stable catalytic aggregate of a preferred form [8]. Multilayer polyelectrolyte film is formed through the adsorption of metal ions (Ag^{+}, Pt^{2+}) [9].

MNPs are primarily defined by their size; so, it follows that size is the real driving force of their catalytic capabilities. Because metal particle surface area is inversely proportional to squared nanoparticle diameter, as particles decrease in size, the surface area increases. This decreasing size results in greater catalytic activity, as all chemical reactions occur on the

catalyst surface [10, 11]. The rate of reaction is also influenced by particle size in case of some chemical reactions. In these instances, slower reactions are caused by reduced nanocatalyst size. For example, when using Pt nanocatalysts for the generation of photochemical hydrogen, it is ideal to use catalysts with 3 nm particle diameters. Any other size, greater or less, will slow down the chemical reaction [12]. Catalyst selectivity is also affected by size. For example, when creating monoene in cyclopentadiene partial hydrogenation, a size of <2 nm is considered ideal. However, the particles having larger size will alter the reaction's selectivity due to the Pt nanoparticles' steric effects [13].

In addition, material arrangement of nanocatalysts also plays a key role in catalytic activity, wherein the addition of other metals can result in added value. The ligand and ensemble effects are most often cited as the cause of this effect. Because of the redox potential of metals, the reaction is also impacted by nanocatalysts' core-shell construction [14]. As an example, the ratio of Pd/Pt = 4 is considered to be the ideal nanoparticle ratio for high performance during the process of selective partial hydrogenation of 1,3-cyclooctadiene to cyclooctene. However, these bimetallic nanoparticles will experience diminished catalytic activity if such ratio is altered. The ligands effect resulting from the incidence of Pt at the particle cores means the bimetallic catalysts have greater activity levels as compared with monometallic Pd catalysts [15].

The catalytic performances of supported MNPs are dependent on catalyst stability, which can be proven when considering the relationship between MNP size and catalytic activity. However, agglomeration means naked colloidal nanoparticles, which are already thermodynamically unstable, are further unstable in the long run. In order to prevent such agglomeration, these particles must be stabilized for the long term, which can be achieved in a number of ways. Two methods would be supporting them on a solid surface or coordination with ligands/anionic species [16]. Metallic nanocatalysts can be stabilized in either aqueous or nonaqueous solutions using polymers, as is the case with the use of polystyrene-b-poly-4-vinylpyridine being used to ensure Pd is stable during a Heck reaction in which a styrene and 4-bromoacetophenone coupling takes place [17].

2. Synthesis and characterization of metal nanoparticles

2.1. Synthesis methods [1, 2]

Metal particle synthesis typically takes place in one of two ways: top-down or bottom-up, as shown in **Figure 2**. The top-down approach uses an external force to pressure bulk materials, eventually causing these materials to break down into smaller components by means of mechanical, chemical, or some other energy sources. A bottom-up approach takes place in a reverse tactic, growing precursor particle size by using chemical reactions to combine atomic or molecular species. It should be noted that the top-down approach is considered to be a physical method while the bottom-up approach is chemical, although both approaches can be applied in a range of states, including liquid, solid, gas, supercritical fluids, or vacuum. The final desired outcome and manufacturer must play into the choice between the two methods.

http://dx.doi.org/10.5772/63314

Because size and shape of the metal particles is the most vital aspect to be altered for improved application performance, it is a vital aspect to take into account for catalysis as an example. This section will address some selected methods for fabricating metal nanoparticles, including physical and chemical methods.

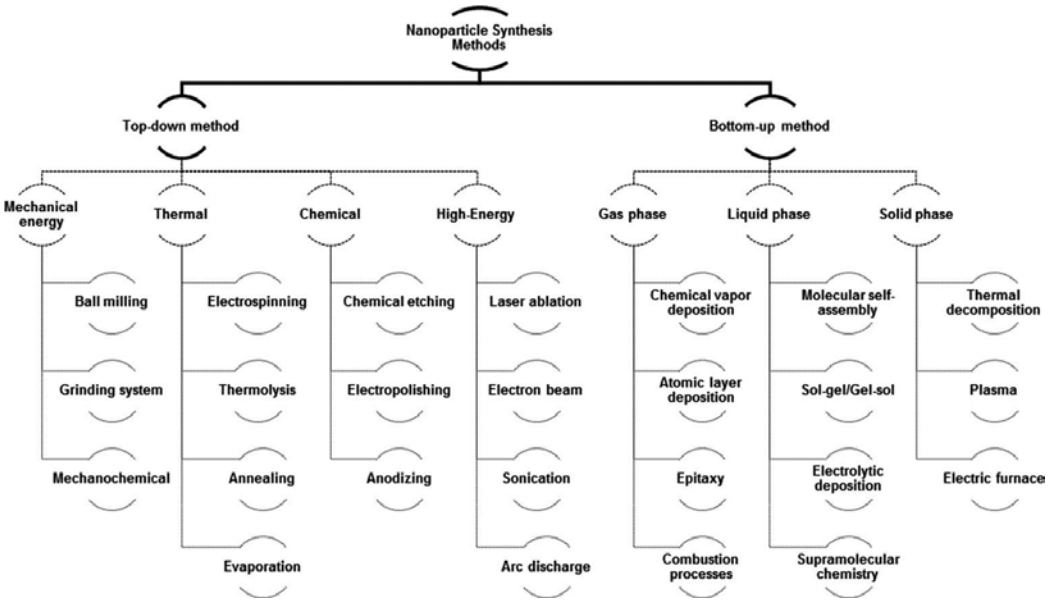

Figure 2. Main synthetic approaches for fabricating metal nanoparticles.

2.1.1. Chemical methods

When it comes to synthesizing metal nanoparticles from a range of source materials, chemical methods have become a reliable technique. They are relatively simple and are implemented under mild conditions. The following section will examine the production process for isolated nanocrystals dispersible in solvents (sols).

2.1.1.1. Chemical reduction

The most ancient and widely used chemical method for synthesis of nanoparticles is the reduction of metallic ions in solution. In ion reduction method, metal ions are reduced by providing some extra energy and using the different types of chemical reductants. The provided energy is used to decompose the material, and usually, photo energy, electricity, or thermal energy is used. It is the most frequent chemical method used for the production of stable metallic nanoparticles. Turkevich used this method to produce spherical nanoparticles of gold by reducing the gold hydrochlorate solution with sodium tricitrate [18]. Nanoparticles of gold can also be produced by reducing the solution of chloroauric acid; this reaction reduces Au^{+3} ions to Au^{+} and further into Au^{0}. Brust method and Perrault method were also used to

produce metallic nanoparticles; the main theme of both these methods is the same as in Turkevich method with different reducing and anticoagulant agents.

2.1.1.2. Coreduction of mixed ions

Coreduction of mixed ions is similar to chemical reduction in many ways. However, this method is mainly used for preparing bimetallic nanoparticles. The preparation of the colloidal dispersions of bimetallic nanoparticles containing gold can be prepared using chemical methods [2]. Coreduction is the simplest preparative method of bimetallic nanoparticles. In this method, metal ions of two or more metals are usually reduced by suitable reductants (e.g., citrate) [18]. The average diameter of bimetallic nanoparticles depends on the metal composition.

2.1.2. Physical methods

Physical methods require solid material to be evaporated into supersaturated vapor, which supports the homogenous nucleation of nanoparticles in order to prepare MNPs [1]. This also allows particle size to be temporarily controlled either by introducing gas molecules that collide with the particles, or by momentarily halting the evaporation source. Because growth occurs over a matter of milliseconds or seconds, experimental parameters must be securely controlled. Recent years have seen the development of several particular methods that can be categorized according to their use of solid or liquid (vapor) precursors, as well as the energy source employed.

2.1.3. Other methods

In this section, some additional methods for preparing nanoparticles are reviewed. These methods include both chemical and physical methods.

2.1.3.1. Vapor synthesis

In order to create conditions that support particle nucleation, a hot wall reactor is used on material, and other variable factors (pressure and temperature) are adjusted during the vapor phase. The vapor synthesis model is favored for multicomponent or bimetallic nanoparticles. This process has been recently used by Schmechel to translate organometallic yttrium and europium to europium-doped yttria nanoparticles [19].

2.1.3.2. Sputtering

Inert gas in the form of high-velocity ion is applied in this technique to vaporize material from a solid surface. The application results in the solid surface ejecting atoms, and is typically done in a vacuum state. It is also possible to deploy electrons in the place of atoms [20]. This technique is preferred for its ability to create nanoparticles with a composition matching that of the targeted material [21].

2.1.3.3. Laser reactors

This technique uses laser beams to heat a substrate in the presence of an inert gas. Laser beam energy is absorbed by the substrate during the vapor phase, resulting in direct warming. As a result, temperature increases due to collision, and despite the fact that inert or carrier are not directly heated. The dropping temperature of inert gas causes supersaturation and prompts the formation of nanoparticles on the reactor wall [22]. Laser pyrolysis is typically carried out with ruby laser and CO_2-type lasers. The fact that there is no need to use a heat wall is a major benefit of this method. This avoids contamination, which can otherwise be introduced by the heat wall, making this method more efficient than sputtering methods. However, the technique has drawbacks as well—the use of laser increases costs [23].

2.1.3.4. Flame reactors

Nanoparticles can also be produced using flame, whose heat initiates a reaction resulting in condensable monomers that are frequently in agglomerate form. The flame reactor method is considered cost-effective [24]. For instance, $TiCl_4$ can be heated and oxidized in the presence of flame, resulting in the nanoparticles of TiO_2. This is just one example on the use of this method. Small modifications allow flame reactors to be used for complex and free agglomerate outputs as well [25].

2.1.3.5. Plasma reactors

Nanoparticle production can be initiated using plasma as an energy source. This is because plasma temperature is high enough to isolate atoms and radicals from the substrate, which results in nanoparticles establishing themselves on the cooling gases. Dc arc plasma, dc plasma jet, and radio-frequency (rf) induction plasma are the most frequently used plasmas in this method, which can be used to generate multicomponent nanoparticles [26, 27]. It is possible to speed up production by introducing cold gas to plasma-formed vapors, but this can cause destruction of nanoparticle homogeneity [27].

2.1.3.6. Wire electrical explosion

Heat and vapors are produced in this method by passing a high current through a metallic wire. It is useful when dealing with metals that are difficult to vaporize in a furnace due to their high boiling point (Si, C) [28]. The method has previously been used to create 2–4 nm Si nanoparticles using Ar inert gas as a carrier. Reaction and carrier duties are carried out by reactive gases to form binary metallic and multicomponent nanoparticles [29].

2.1.3.7. Expansion–cooling

Abrupt expansion and cooling are used to stimulate homogenous nucleation by passing condensed gas through a nozzle, resulting in gas expansion and temperature reduction. Particle size is then able to be altered using pressure change: bigger sizes are achieved using higher pressure. For example, N_2 gas in a subsonic nozzle will result in 100 nm particles if 2

bar pressure is applied. However, using 0.75 bar pressure under the same conditions produces 5 nm particles [20].

2.1.3.8. Electrospray systems

This is the simplest means of creating nanoparticles and requires a small droplet of dilute solution to be evaporated. The intended matter is made into diluted solution and dried in small droplets of 1 μm, producing nanoparticles. However, it is difficult to create this very small size of droplet required, and hence there is an added challenge that the solvent can introduce some impurities [30].

2.2. Characterization methods

Nanoscale materials have a unique set of properties, making them suitable for a variety of applications and resulting in them being a focal point for a range of researches. Deep understanding of the properties of metal particles at nanoscale level is necessary to understand the nature of active sites, which in turn can help to find and tune the key performance signs. Several techniques exist that are designed to characterize nanoparticles, although none of these are able to supply full information regarding investigated materials. For this reason, several techniques must be used to categorize each sample in order to understand the size, structure, and catalytic properties. **Figure 3** depicts various methods of analyses for MNPs.

Characterization Method	• Information obtained
Dynamic light scattering (DLS)	• Size and size distribution of MNPs in solution
UV-Vis spectrum	• Formation of colloidal MNPs (Plasmon band)
X-ray diffraction (XRD)	• Crystal structure and size, chemical composition
Nuclear magnetic resonance (NMR)	• Molecular physics, crystals and non-crystalline materials
X-ray photoelectron spectroscopy (XPS)	• Surface composition of supported MNPs
Transmission electron microscopy (TEM) Scanning electron microscopy (SEM)	• Size and Morphology of MNPs
Energy Dispersive X-Ray (EDX)	• Element and distribution of MNPs
Scanning tunneling microscope	• Size and structure of MNPs

Figure 3. Summary of some selected characterization techniques of MNPs.

Common means of characterizing MNPs include transmission electron microscopy (TEM) and scanning electron microscopy (SEM). Other common techniques include X-ray photoelectron spectroscopy (XPS), UV spectroscopy, atomic force microscopy, powder X-ray diffractometry (XRD), and dynamic light scattering (DLS). UV spectroscopy and Fourier transformed infrared spectroscopy (FTIR) methods would be combined to examine gold and palladium nanoparti-

cles, as described elsewhere [31, 32]. Conversely, silver nanoparticles would be examined using TEM, high-resolution TEM, and selected area diffraction pattern (SAED) [33]. Finally, X-ray diffraction, SEM, and FTIR would be combined to examine magnetite, Ag, zinc, and Au nanoparticles [33–35].

3. Catalytic properties of supported metal nanoparticles

Supported metal nanoparticles (SMNPs) are used today in several application fields such as sensors, nanoelectronics, medical-technical applications, and in heterogeneous catalysis [36, 37]. In general, SMNPs consist of metal nanoparticles (MNPs) from transition metal or noble metal pools that are deposited on high surface area supports (150–1200 m^2/g). In general, the metal load of supported metal catalysts is generally in the range of 0.5 up to 10 wt.% (even higher in rare cases). MNPs are often in a size range of roughly 1–30 nm. Such particles reveal chemical and physical properties that are intermediate between those of a single metal atom and a bulky metal particle of a size much larger than 100 nm. However, careful handling is important, that is, once activated, most of these SMNP solids are pyrophoric by contact with oxygen.

The activity of supported metal catalysts in heterogeneously catalyzed reactions is mainly determined by the shape and size of the metal species (i.e., MNPs) deposited onto the support, because only surface metal atoms might take part in a chemical reaction [37–39]. Heterogeneous catalyst performance is very sensitive to particle size, because the structure of the solid surface and the electronic properties may significantly change depending on the size of the MNPs [37, 38]. For example, the activation energy for CO dissociation and the heat of adsorption for CO alter with changing size of MNPs. These changing properties affect its performance in several CO-converting reactions like Fischer-Tropsch (FT) synthesis for the manufacture of hydrocarbons from gas synthesis. Supported Au-containing catalysts show similar size effects with respect to applied supports [40, 41]. Au nanoparticles on alumina smaller than 4 nm show complete conversion in ethylene glycol oxidation, but increasing nanoparticle diameter above 5 nm leads to significant drop to roughly 40% conversion only [40].

Therefore, one crucial property of supported heterogeneous MNP catalysts is that they contain the metals as finely dispersed particles on the support surface, in general [38, 42, 43]. Incidentally, the term dispersion describes the degree of metal distribution (**Figure 4**); a dispersion degree of close to 1 means that all offered metal atoms exist in an atomic dispersed monolayer at the surface, whereas a dispersion degree of almost 0 says that only one large particle is present [44, 45]. Thus, the dispersion degree is inversely proportional to the MNP size. The dispersion degree might be determined by chemical methods such as hydrogen or CO chemisorption; a nice overview on CO chemisorption on metal particles is given by Hammer et al. [46]. However, one has to know adsorption chemistry well to draw the right conclusions from experimental data; for example, CO can be adsorbed on Pt surfaces linearly, bridged or multibound, as proven by different bands obtained from FTIR spectra [47]. Thus, the number of CO atoms adsorbed on a nanoparticle surface does not necessarily mirror the number of

surface atoms and the dispersion degree. Nowadays, DFT calculations and several adsorption models help to refine experimental data [48]. Small-angle X-ray scattering (SAXS), X-ray diffraction, and TEM can also be applied; in addition, several in situ studies can be included for characterizations [37, 49]. The latter needs some more intense sample preparation and examination efforts to get statistically reliable conclusions.

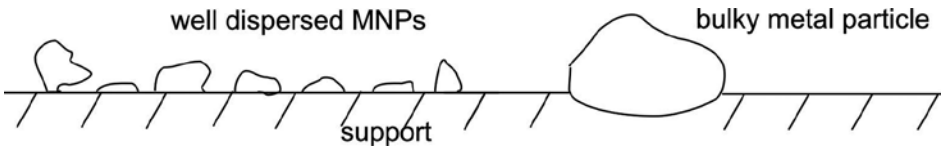

Figure 4. Well-dispersed metal nanoparticles (MNPs) versus a large metal particle on a support surface.

Besides MNPs' size and shape, the catalytic properties of such particles might be influenced by a second metal, the so-called bimetallic catalysts. The addition of a second metal often leads to alloys showing quite different electronic and also structural properties. Some examples are the formation of PtNi or Pt-bimetal SMNPs for electrocatalytic applications [50, 51] or AuNi SMNPs for steam reforming of hydrocarbons [52]. Moreover, support properties strongly influence the catalytic performance of SMNPs. Matsumura and Nakamori describe in detail the effect of various supports on catalytic properties of such nickel catalysts in the steam reforming of methane (SRM) reaction [53]. Au nanoparticles (<4 nm) on alumina reveal full conversion in glycol conversion, whereas Au nanoparticles on carbon need a size of 7–8 nm to reach complete conversion [40]. Support-metal interaction is studied in detail for several catalyst systems and also reviewed in Ref. [54].

Mainly hydrogenation (dehydrogenation), oxidation, automotive off-gas cleaning, and C-C coupling reactions run on such SMNP catalysts [42, 43, 55]. Most of these reactions proceed in the gas phase, and various examples of liquid phase or trickle bed reactions are also known. In particular, in the latter cases, loss of active MNPs by leaching might be a catalyst deactivation reason. Further deactivation reasons are due to MNPs sintering by high reaction temperatures or easy movability on a support surface. Furthermore, MNPs might deactivate by accumulation of products or oligomers and coke-like products on their surface. In general, the latter can be easily regenerated by hydrogen or air (oxygen) treatment in case of oxidic carriers with subsequent reduction. Au, Pd, Rh, Ru, Ni, or Ag are the mostly widely used MNPs for the above-mentioned transformations [55]. In general, various oxidic supports, such as diverse aluminas, silicas, titanias, etc., and several carbon materials, are usually used as supports for the MNPs. White et al. recently summarized various synthesis protocols in a concise review [55]. Impregnation, coprecipitation, and deposition-precipitation are some of the classical chemical synthesis routes. Precursor compounds have to be first calcined under air and second reduced by hydrogen or hydrides to receive MNPs. Physical synthesis routes include the application of microwaves, sonic waves, or supercritical fluids. Moreover, there are several protocols to deposit pre-prepared colloidal MNPs onto the surface of various supports [56]. This is a very interesting approach, because colloidal particles can be synthesized very uniformly with respect to size and shape [37, 56].

Supported metal catalysts are applied in large scale in several industries such as refining of petroleum, hydrogenation of carbon monoxide, hydrogenation of fats, and many other processes [43, 55, 56]. They are also the heart of automotive catalysts to clean automobile exhaust gases [57]. Such catalysts and the significance of a high dispersion are known for over hundred years, in particular, from various hydrogenation reactions. The hydrogenation of carbon monoxide to methane over supported nickel catalysts was discovered in the beginning of the last century by Sabatier and Senderens [58, 59]. This reaction is known today as "Sabatier reaction" or methanization, in general. It is applied in large scale in industry to remove traces of CO from ammonia synthesis gas, but it also gains importance in energy-storage efforts by converting solar energy via hydrogen to storable methane [60]. In this process chain, CO_2 reacts nearly quantitatively with hydrogen to methane over Ni or NiRu containing catalysts at about 300–350°C, with H_2:CO_2 feed ratio of 4 and slightly increased pressure up to 10 bar [60, 61]. Paul Sabatier received together with Victor Grignard the Noble Prize in Chemistry in 1912 for his method of hydrogenating organic compounds in the presence of finely disintegrated metals, whereby the progress of organic chemistry has been greatly advanced in recent years [62]. The explanatory statement explicitly points to the necessity of the "finely disintegrated metals" that we know today as metal nanoparticles.

One of the most common hydrogenation catalyst formulation is nickel on oxidic (e.g., alumina, zirconia, ceria, titania, or silica) [55, 63, 64] or carbon [65, 66] supports. As mentioned above, such catalysts are normally used as methanization catalysts, and other applications are also in common use such as catalysts, for example, for hardening of oils and fats in food industry, dry reforming of methane to manufacture syngas by using CO_2 [67, 68], or in petrochemical industries and refinery. In the latter case, they are of interest in the hydrogenation of various aromatic compounds to reduce their content in fuels. Nickel-containing catalysts are also in large-scale operation with respect to SRM reaction to generate hydrogen and/or syngas (CO, H_2) [53, 69]. The SRM reaction is carried out in general over Ni/alumina catalysts at around 800°C. Additional hydrogen can be manufactured by the water gas shift (WGS) reaction converting CO and water to CO_2 and H_2. The WGS reaction is industrially carried out using supported high-temperature shift FeCr (350–500°C) and low-temperature shift CuZn catalysts (180–250°C), respectively [70, 71]. Nowadays, this reaction gains much importance for ion fuel cell applications too [72]; mainly nonnoble metals such as Cu or Ni on ceria are under development [71].

Nickel-containing catalysts play an increasing role in chemical transformation of biomass-derived feedstock. Song et al. studied Ni on various carbons or MgO supports for depolymerization of lignosulfonate and identified three Ni functions being (i) the active sites for hydrogenolysis of C–O–C bonds; (ii) as active sites for hydrogenolysis of C–OH bonds at side chains to alkane chains, and (iii) as convertors for sulfonate to H_2S [73]. In a detailed study on hydrodeoxygenation of phenol as model compound and pyrolysis oil as a real feed, we recently could show the potential of bimetallic NiCo NPs supported on zeolite supports [74].

Further examples of the industrial application of SMNP catalysts are FT synthesis of hydrocarbons over Co, Fe, Ni, Ru catalysts [75, 76] or the synthesis of ethylene oxide from ethylene and oxygen over Ag/alumina [77, 78]. Another good example is the use of sulfided CoMo and

NiMo catalysts in refinery industry for the removal of sulfur from different distillation cuts by special hydrodesulfurization (HDS) units [79]. Mainly alumina is used as support; however, improvements in deeper HDS are reached by a variation of supports (silicas, zeolites, amorphous aluminosilicates, etc.) or the addition of further (noble) metals to the conventional catalyst composition [80, 81].

Besides these applications in well-studied industrial fields, novel SMNP materials are manufactured in recent years that might lead to new catalyst developments with respect to synthesis procedures, catalyst performance, and possible applications. Novel support materials like carbon nanotubes [82], graphene oxide [83], or carbon nitrides [84] might lead to novel interactions with MNPs resulting in novel catalysts. Jin et al. recently reported on the use of mesoporous metal oxide microspheres as support for Pd NPs and their use in reduction of nitro compounds [85]. Increasingly, noble metals are replaced by transition metals, or their alloys lead to cheaper catalysts, improved performance, NP stability, and/or new applications [37, 60, 86].

4. Green catalytic application of metal nanoparticles

Even though most of the catalysts are made by mixing and shaking some components, their surface structures are not yet well controlled. For any catalyst, it is desired to achieve long life cycle, 100% selectivity, and low energy consumptions, and these properties can only be gained by controlling their size, shape, electronic structure, and chemical and thermal stabilities of catalyst particles [87]. In the case of dealing with catalysts in the nanoscale level, selectivity ratio can be adjusted by precisely controlling the size of nanoparticles. Hence, precious metallic catalysts are usually used in the form of nanoparticles to improve their selectivity.

Nanocatalysts are used in chemical processing industries due to their lower energy consumption, environment-friendly behavior, with an improved economy. For instance, nanocatalysts of NiO with novel aluminum oxide support are used in the production of syngas and bio-oil from pyrolysis of biomass. Nanocatalysts improved the quality of syngas by decreasing the fraction of carbon monoxide in the syngas; it also reduced the proportion of tar in the product [88, 89].

Biomass energy is fulfilling about 15% of total energy requirement of the world; the broad range of organic materials included wood, crops, organic wastes (animal dung, municipal wastes, etc.), which are used for the production of biomass energy. And mostly, these materials are produced from the process of photosynthesis; according to the study of Luo and Demirbas, approximately 720 tons of biomass are produced per year [90, 91]. There are three main types of reactions for the conversion of biomass into fuel energy, such as combustion, pyrolysis, and gasification. Pyrolysis technique is preferred on other techniques due to its product named as pyrolytic oil or bio-oil. High moisture content, long-chain hydrocarbon, and low hydrogen-carbon ratio make it difficult to burn. Therefore, mainly biofuel is not directly used as fuel. Aravind [92] and Malik [93] studied the effect of nanocatalysts on the processing of bio-oil into syngas and concluded that nanoparticles with high surface area are the best alternatives of

conventional catalysts to improve the yield of syngas. Tar is an undesirable by-product in syngas production due to its high boiling point, and hence it blocks the filter and pipes. Tar is also a poison to the catalyst [94]. There are two methods to control the production of tar: one is treatment within gasifier and the second one is hot gases treatment after the gasifier. The second method is most economical, and hence it is only used in industries. Nanocatalysts of sodium, potassium, and calcium are used for hot gases treatment of effluent to reduce the amount of tar [95]. Catalytic reforming of tar by using metallic nanocatalysts is preferred because there is no need for any additional energy, and that is the reason why nanocatalysts are called green catalysts. This catalytic reaction also includes steam reforming, hydrocracking, and hydroreforming [96, 97].

In the Fischer-Tropsch synthesis of green diesel, nanocatalysts of iron and Co of size 10–15 nm are used in slurry reactors to improve the production of high molecular waxes. These waxes then hydrocracked to generate green diesel [98, 99]. Fischer-Tropsch's is an important method to convert nanopetroleum feedstock such as coal and biomass into clean diesel, which can be used as a fuel. Uses of nanocatalysts dramatically decrease the cost of this process as reported elsewhere [100].

FT syntheses technology produced high-quality ultraclean fuel with low aromatic content and zero sulfur. The product mostly consists of the mixture of linear and branched hydrocarbons [101]. Two types of techniques are adopted for FT synthesis, but the slurry bubble column techniques gain more interest due to its low pressure and stable temperature [102]. Generally, the Fischer-Tropsch synthesis follows the ASF distribution mechanism, but this distribution is unselective in this case. Later on, the novel Fischer-Tropsch catalysts are developed; the novel FT nanocatalyst containing Co with porous silica support is more selective toward hydrocarbons of C_{10}–C_{20} (diesel) [103]. Study of Kang et al. [99] showed that the nanocatalyst of Ru is more favorable in the high moisture content, but the only issue they have is low activity. This issue was solved by using carbon nanotube supported ruthenium catalyst, which gives excellent selectivity for diesel hydrocarbons and also high activity of the catalyst [99, 104].

Solid catalysts of Aluminum dodecatungstophosphate ($Al_{0.9}H_{0.3}PW_{12}O_{40}$) or nanotubes of $Zn_{1.2}H_{0.6}PW_{12}O_{40}$ are used for esterification of waste cooking oil to produce biodiesel; these catalysts improved yield from 42.6 to 96%. It is due to improved surface area of the nanocatalysts from the bulk conventional catalyst [99]. Animal and used cooking oil are alternative sources of diesel fuel to run the vehicles [105]. However, high water content and the high ratio of free fatty acid make them unfavorable for the production of diesel fuel. Sulfuric acid with a large quantity of methanol at high temperature and pressure reduces the quantity of free fatty acids. High pressure and high temperature increase the diesel fuel production cost [106]. According to the study of Li et al., ZnPW nanotubes can be used to reduce free fatty acid at lower temperature and pressure [107].

MNPs are also used in fossil fuel sector to improve the reaction; selective hydrogenation, paraffin hydrogenation, naphtha reforming, and hydrodesulfurization are some of the major units where nanocatalysts are used in oil refineries. Nanoparticles hexanethiol monolayer-protected palladium of size 1.5 nm are used to improve energy consumption of catalytic

combustion of JP-10 activation fuel. These nanoparticles decrease the ignition temperature to 240°C [108, 109].

Meurig et al. [110] studied the bimetallic nanocatalysts of size range 3–30 nm with nanoporous silica support in single-step hydrogenation and found that this catalyst greatly facilitates the separation of product from reactant, with easy recycling at low temperature and pressure conditions.

Hydrogen gas can be used in fuel cell to generate green energy; now, almost 95% of hydrogen is produced by using partial oxidation and steam reforming of hydrocarbons. Both oxidation and steam reforming produce carbon dioxide, which is a major constituent of global warming [111]. Catalytic reforming of green biofuel such as ethanol can be a green way for the production of hydrogen gas; ethanol is usually available with high water content; the water present in ethanol and other impurities deactivate the conventional catalysts. Nicolas et al. [112] worked on the designing of nanocatalysts for the production of hydrogen gas by using ethanol and concluded that nanocatalyst rhodium metal with alumina support gives the highest yield of hydrogen gas with a better protection from water. Rhodium catalyst produces cleavage between carbon and hydrogen, and this is the main reason of C–C bond rupture. Hydrogen in fuel cell gives 50–60% efficiency, while in diesel engine only 20–25% fuel is converted into useful energy [113, 114].

In brief, MNPs are used to increase the selectivity and activity of catalyst, which resulted in less energy consumption and high yield. In general, the majority of the chemical reactions obtain on the surface of the catalyst and hence with decreasing size of particles there is an increase in catalytic activity. Slower reactions are caused by continuously decreasing the size of the metal nanoparticle catalysts whereas increasing the size of the catalyst will decrease the rate of reaction. Nanocatalysts are energy-efficient; they reduce global warming by reducing the required energy for any catalytic process with less poisoning ratio. They also decrease the chemical wastes; all these factors resulted into an improved economy and safer environment.

5. Own results

The nature of the support has great influence over MNPs' catalytic performance. This is because the support allows for efficient pathways to the target outcome, which compounds the impact of particle size stabilization when it comes to small MNPs' growth. Supports must have a strong metal-support interaction (SMSI), a high surface area, and incidence of active sites that can contribute to the reaction process [115]. This section investigates the catalytic application of MNPs, particularly for the oxidation of cyclohexane to adipic acid, the oxidation of benzyl alcohol to benzaldehyde, and the photodegradation of dyes. These reactions can be evaluated through the technique of placing MNPs on various kinds of metal oxide supports. The supports are used to afford high metal surface areas as well as stabilize the small MNPs characterized by high dispersion degrees [116]. Catalytic performance of heterogeneous reactions can also be affected by the support material characteristics, type of catalyst preparation method, degree of metal loading, and particle size. Specifically, supported noble metals

(e.g., gold) will have catalytic properties highly dependent on the type of support material at hand [116]. One example notes that acidic supports typically augment electron deficiencies on noble metals, when compared to basic supports. Strong metal-support interaction (SMSI) is demonstrated by metals supported on reducible oxides (e.g., TiO_2 and CeO_2) [117]. Robust interaction between the metallic components results in considerably higher catalytic activity compared to the catalysts having only one metal. This is in opposition to relatively inert irreducible oxides (e.g., Al_2O_3, SiO_2). This section will examine five kinds of supports, taking into consideration the benefits derived from metal oxide supports. These different kinds have different impacts in terms of particle size, dispersion, and performance. The oxidation of benzyl alcohol and cyclohexane were both tested with these five supports described below, and the reactions were performed in the liquid phase. In addition, evaluation of gold nanoparticles supported on TiO_2 and ZnO will also be evaluated photocatalytically. The outcomes of these examinations are detailed below.

5.1. Oxidation of benzyl alcohol to benzaldehyde

Green chemistry emphasizes the importance of using oxidation to formulate chemical intermediates and fine chemicals with high selectivity [118], as is the case with forming benzaldehyde (BAl) from benzyl alcohol (BA) oxidation (**Scheme 1**). The resulting solution is frequently used in pharmaceutical, agrochemical, and perfume industries. Reaction of benzyl alcohol with excessive ammonium permanganate or potassium is possible in aqueous acidic medium to form benzaldehyde (BAI). However, this method has significant toxic by-products formation, and hence it is not really environment-friendly. Efforts have been made to amend this process by oxidizing benzyl alcohol using a green oxidant in the presence of organic solvent, such as H_2O_2 or O_2, and applying various catalysts such as Pd/C, Pd(II) hydrotalcite, Pd-Ag/pumice, Ru-Co-Al hydrotalcite, Ni-containing hydrotalcite [119], but these techniques are still not considered to be environmentally acceptable due to the solvent use. Solvent-free oxidation is possible, using tert-Butyl hydroperoxide (TBHP) over MnO_4^{2-}-exchanged hydrotalcite and a transition metal containing layered double hydroxides and/or mixed hydroxides. However, this is not a clean process as the TBHP produces tert-butanol. To be considered clean and environmentally friendly, there must be no solvent used, and the oxidant ought to be molecular oxygen (i.e., clean and inexpensive). Prati et al. successfully demonstrated such a process using Au/C catalysts to selectively oxidize alcohols and polyols [120]. According to Rossi et al., gas-phase oxidation of volatile alcohols into aldehydes and ketones is possible using Au catalysts [121]. A similar process oxidizing glycerol to glyceric acid using Au/graphite catalysts was carried out by Carretin et al. [122], and was deemed to be fully selective of the target output. This high selectivity of Au/CeO_2 was further proven by Abad et al. [123]. In case of benzyl alcohol oxidation to benzaldehyde, Enache et al. used supported Au on TiO_2 catalyst [124]. The same researchers also investigated the selective oxidation using Au-Pd alloy particles supported on TiO_2 [125]. In the end, the most efficient and environment-friendly means of oxidizing benzyl alcohol to benzaldehyde uses molecular oxygen. The technique also uses separable and recyclable supported gold nanoparticles over various metal oxide supports to provide high selectivity of the desired product, benzaldehyde.

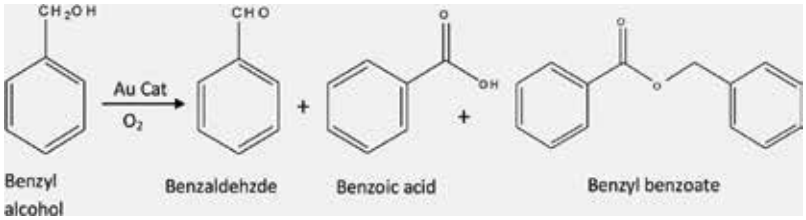

Scheme 1. Oxidation of benzyl alcohol with O_2 using Au catalyst.

For the past several years, the oxidation of benzyl alcohol is being investigated specifically looking at the impact of different supported MNPs (such as Au nanoparticles) on various metal oxide carriers [120, 125]. In the present study, we have used different oxide supports (CaO, MgO, ZrO_2, Al_2O_3, TiO_2) for AuNPs that were prepared with impregnation techniques [126]. A range of spectroscopic and microscopic techniques was deployed to characterize these catalysts and gather data regarding their individual properties. Catalytic performance of the AuNPs was tested on solvent-free oxidation of benzyl alcohol with oxygen (5 bar) as an oxidant in a Parr autoclave reactor at a reaction temperature of 140°C. **Figure 5** demonstrates that Au catalyst performance is strongly dependent on the kind of applied support. Although BAI is the primary output, some by-products were also produced, including small amounts of benzyl benzoate, benzoic acid, and acetal. Benzyl benzoate occurs because of the additional esterification reactions due to benzoic acid and benzyl alcohol. Benzoic acid is a natural occurrence when benzaldehyde over-oxidizes. Finally, acetal is produced when benzyl alcohol does not react and instead forms hemiacetal, which eventually forms acetal through protonation and deprotonation reactions. Acetal occurred in this instance only to a smaller extent, which is however negligible in this case. The most active catalyst found is TiO_2-supported AuNPs (at

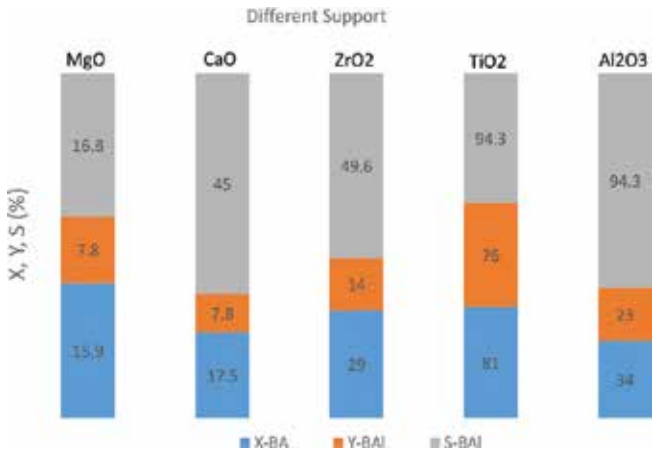

Figure 5. Influence of support on oxidation of benzyl alcohol to benzaldehyde over 1% Au/M catalysts (*M* = MgO, CaO, ZrO_2, TiO_2, Al_2O_3). Reaction conditions: 30 ml BA, 0.15 g catalyst, 140°C, 5 bar O_2, 4 h (*X*, conversion; *Y*, yield; *S*, selectivity).

X-BA = 81%), while the least active is MgO supported (at X-BA = 16% and S-BAI = 17%) (**Figure 5**). The enhanced performance of the former is due to several factors, including high dispersion of Au, smaller Au size, and comparatively greater surface enrichment of Au. These are completely opposite in the case of poor performing catalyst. TEM and XPS have been used to validate these claims.

5.2. Oxidation of cyclohexane to adipic acid

There are important industrial implications for selective oxidation of dicarboxylic acids from cycloaliphatic hydrocarbons, such as forming adipic acid (AA) from cyclohexane (CH) (**Scheme 2**). AA is a vital component when producing polyamides (such as nylon), polyesters, plasticizers (such as PVS), polyurethanes, and carpets. It is also used in the pharmaceutical and insecticides manufacturing processes [127], and has extensive applications for food products and medicines.

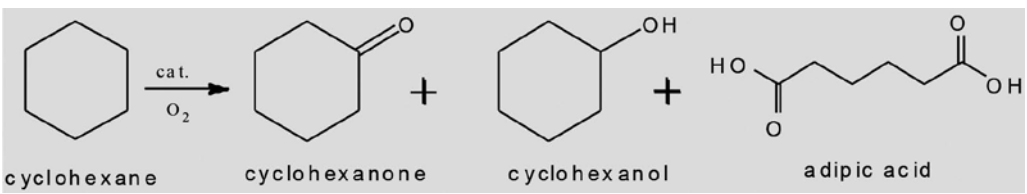

Scheme 2. Oxidation of cyclohexane with O_2 in the presence of nano-Au catalyst.

Commercial production of AA involves a two-stage process. Stage one requires oxidation of CH to create cyclohexanone (-One) and cyclohexanol (-Ol). This is done through the ketone and alcohol oil process (KA-oil) and operationalizes a cobalt or manganese catalyst at around 150°C and at 10-20 bar of air. Stage two derives AA from the KA-oil mixture by applying nitric acid as an oxidant [126]. The majority of AA is produced using this process. However, this process involves significant amount of recycling (more than 90%) of unreacted cyclohexane due to its low conversion (5–10%). The reaction is deliberately performed at such low conversion to obtain high selectivity (70–85%) of KA products. This recycling of ≥90% certainly incurs higher operation costs. Besides, there are also some additional environmental implications. Particularly, the usage of nitric acid in the second step results in the formation of NO_x by-products, which can be held responsible for smog, acid rain, and ozone depletion. Therefore, there is a need to explore new possible routes for the production of AA. This is the real motivation to uncover a more environment-friendly route using nano gold catalysts of the present study. **Scheme 3** depicts some other possible options for the production of AA. Although there are many potential options available, direct synthesis of AA from CH in a one-step process using O_2 is considered to be a more suitable option from both environment-friendly and economic points of view.

This research has also addressed oxidizing adipic acid from cyclohexane and the associated catalytic activity in addition to the oxidation of benzaldehyde from benzyl alcohol using supported AuNPs [126]. Section 5.1 outlines the type of catalysts used in this instance. The

reaction conditions applied for determining the influence of support in CH oxidation were: 10 ml CH, 20 ml solvent (acetonitrile), 0.3 g catalyst, 0.1 g TBHP, pO_2 = 10 bar, t = 4 h, 1500 rpm, T = 130°C. The reaction resulted in adipic acid (AA), cyclohexanone (-One) and cyclohexanol (-Ol). Combining ketone and alcohol products is commonly denoted as KA (as is the case with commercially producing AA from cyclohexanone and cyclohexanol). Succinic acid, CO, CO_2, and glutaric acid are expected by-products, formed in small quantities. However, these reactions are intended to produce AA.

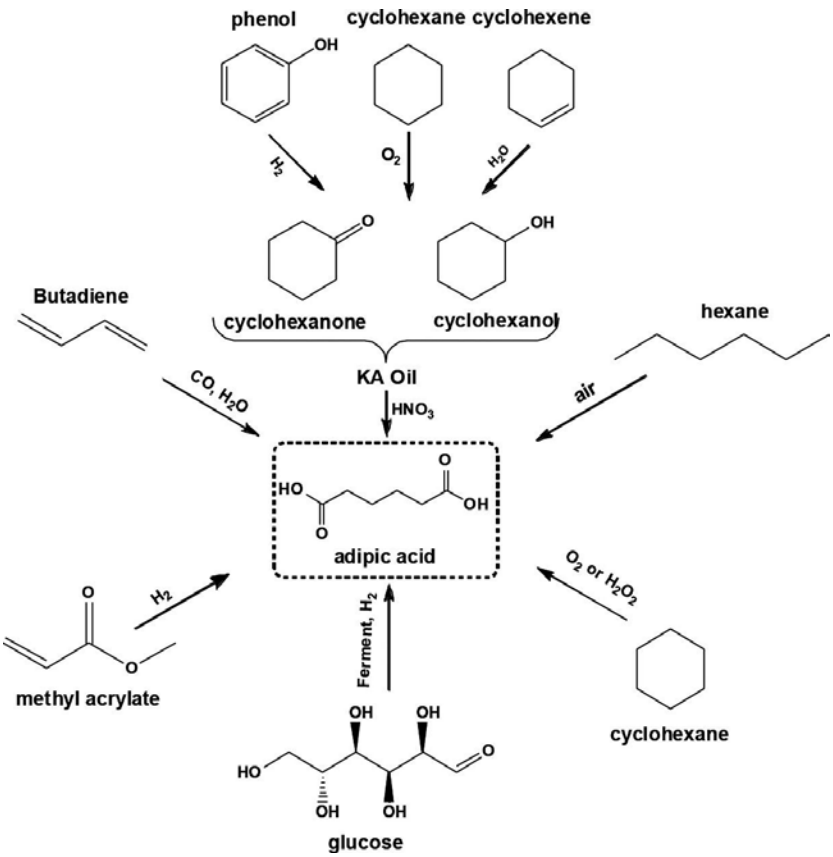

Scheme 3. Summary of the different alternative pathways for AA production.

Figure 6 depicts the impact of the nature of oxide support on CH to AA oxidation activity. It is evident from the figure that the characteristics of the supports clearly influence both the product selectivity as well as CH conversion. It is also clear that AuNPs supported on TiO_2 gave the best performance compared to other supports. Similarly, even in case of benzyl alcohol oxidation, the same Au/TiO_2 nanocatalyst was found to exhibit superior performance (**Figure 6**). The best performance of Au/TiO_2 catalyst is due to (i) the formation of small AuNPs

http://dx.doi.org/10.5772/63314

(2–3 nm), (ii) high dispersion of Au, (iii) higher active metal (Au) area, and (iv) the high surface enrichment of Au species compared to other catalysts applied in this study [126]. This finding further confirms that catalyst performance is strongly dependent on the size of Au particles. As discussed earlier, the poor catalytic performance was observed over the MgO- and CaO-supported catalysts. In addition, these catalysts also produce high amounts of unwanted by-products (including CO and CO_2), and thus they should not be considered as appropriate supports for this reaction. Conversion of CH achieved over TiO_2 was 16.4%, and the selectivity of AA was 21.6%.

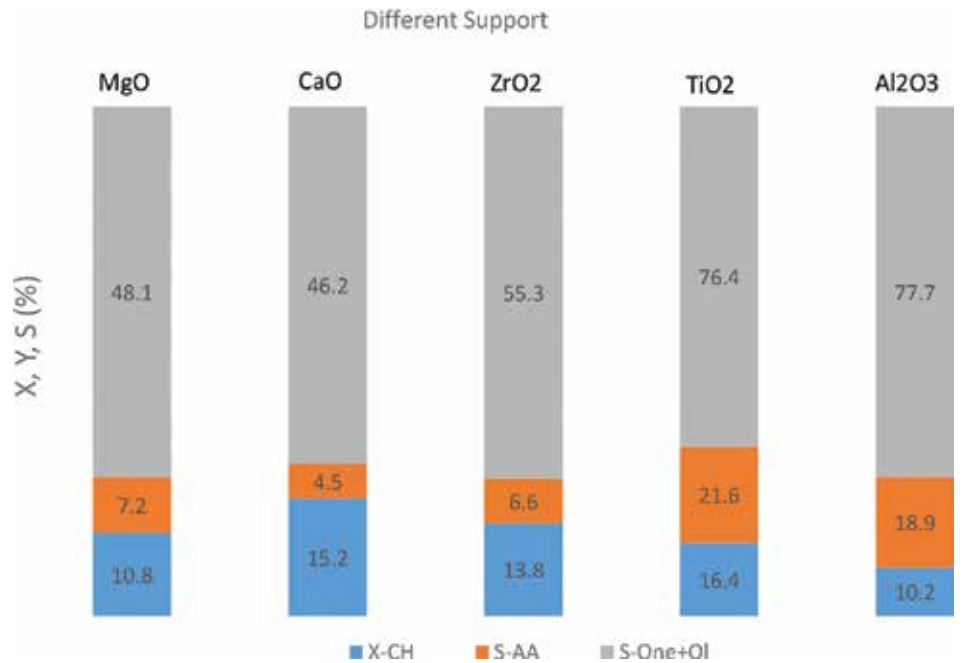

Figure 6. Effects of different oxide supports on the oxidation of cyclohexane over Au/X catalysts (*X* = MgO, CaO, ZrO_2, TiO_2, Al_2O_3). Reaction conditions: (10 ml CH, 20 ml solvent (acetonitrile), 0.3 g catalyst, 0.1 g TBHP, pO_2 = 10 bar, *t* = 4 h, 1500 rpm, *T* = 130°C). X-CH, conversion of cyclohexane; S-AA, selectivity of cyclohexane; S-One, selectivity of cyclohexanone; S-Ol, selectivity of cyclohexanol; S-Others, yields of glutaric acid, succinic acid, cyclohexylhydroperoxide, CO, and CO_2.

Moreover, we have also made attempts to find some correlations between the superior performances of AuNPs supported on TiO_2 compared to other types of catalysts. Such correlation between the Au particle size, surface gold-to-support atomic ratio (Au/SU) derived from XPS and catalytic performance is presented in **Figure 7**. It is clear from the figure that the activity results are in good agreement with the particle size of Au, and therefore the conversion of CH and selectivity to AA changed relatively in a similar way as that of Au size. Unsurprisingly, the smallest gold nanoparticles supported on TiO_2 showed the best catalytic activity. The conversion of CH decreased from 26% using Au/TiO_2 catalyst to 9% using Au/CaO. On the other hand, the Au size increased from 2 nm in case of using TiO_2 to 6–8 nm using CaO.

Moreover, the XPS results also confirmed that the surface region was indeed enriched in Au which hence the catalytic activity of gold catalyst. We can obviously observe from **Figure 7** that the gold nanoparticles supported on TiO_2 showed the highest surface Au/SU atomic ratios (SU = different supports) compared to others types of supports, and hence enhanced performance as well. In addition, supporting evidence for the beneficial effect of TiO_2 can be the high dispersion of Au and high active Au metal area. On the whole, better performance of TiO_2 is certainly due to the presence of small Au particles, high Au enrichment in the near-surface-region, high dispersion, and higher active metal area.

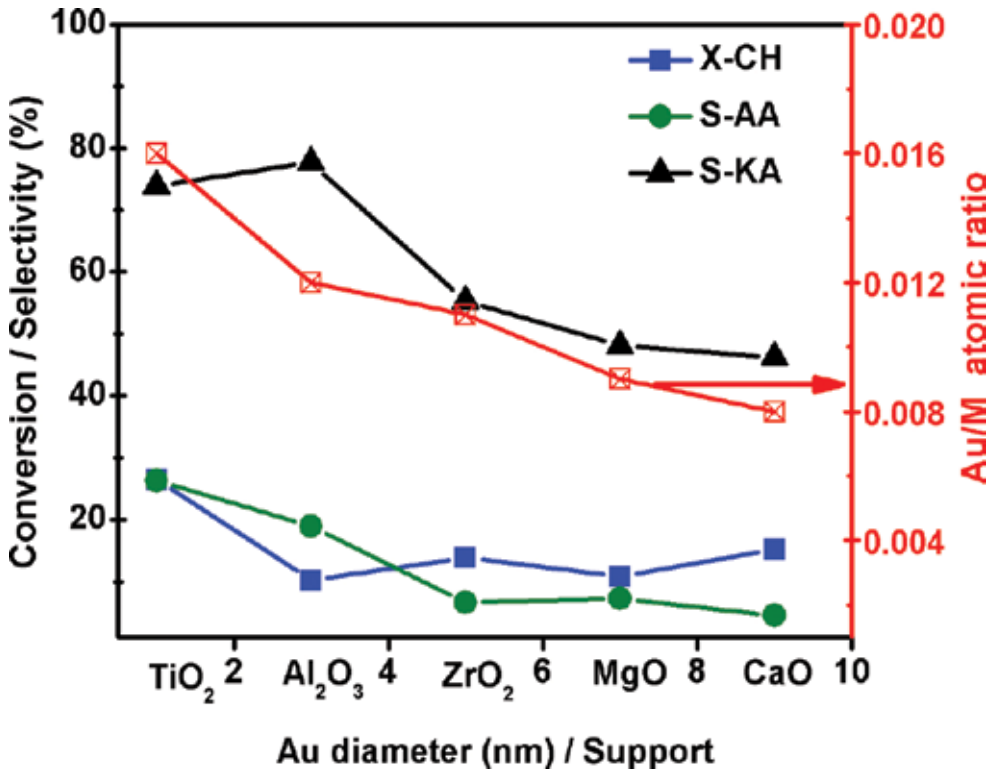

Figure 7. Correlation between cyclohexane conversion (X-CH), selectivity to adipic acid (S-AA) and to KA oil (S-KA), and catalyst properties of supported AuNPs.

5.3. Supported metal nanoparticles for dye's photodegradation

Metal nanoparticles (e.g., Au, Cu, and Ag) have recently begun to generate attention regarding their uses in electronics, optics, and the environment, and as catalysts [128–130]. One important green technology application is the use of combined M and metal oxide supports to remove dyes photocatalytically from water. Toward this end, we looked at the potential of using gold MNPs supported on TiO_2 and ZnO under UVA light irradiation to test their photocatalytic activity toward photodegradation of rhodamine B (RB) in aqueous medium [128]. The

http://dx.doi.org/10.5772/63314

procedure previously described was used to prepare the catalysts. The UV-vis absorption spectra of a 20 mg/L rhodamine B solution is demonstrated in **Figure 8a** and **b**, which shows the results before and after UVA light irradiation at 20-minute intervals and in the presence of one of two photocatalysts: Au/ZnO and Au/TiO_2. Even before introducing light irradiation, a test was deployed to determine if dye absorption transpired on the catalyst surface. According to the tests, there was a slight amount of absorption (as shown by a diminished RB concentration), which was comparable between the both photocatalysts applied. Peak absorption with Au/TiO_2 was observed to occur at 554 nm, and thereafter decreased during irradiation, until full elimination after 100 min (**Figure 8a**). Peak absorption with Au/ZnO occurred at RB 554 nm, and likewise decreased with exposure to irradiation, reaching full RB depletion at 80 min (**Figure 8b**). The former's 100-minute degradation time was slower, indicating that Au/ZnO has superior photocatalytic activity.

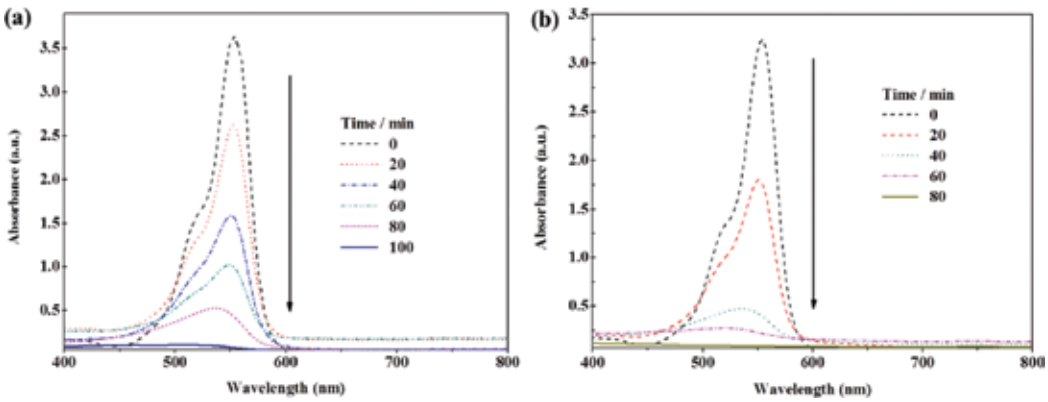

Figure 8. Absorption spectra of RB at different times after UV irradiation using Au/TiO_2 (**a**) and Au/ZnO (**b**) as AuNPs photocatalysts.

Furthermore, the degradation plot depicted in **Figure 9** shows further details, demonstrating the photocatalytic degradation of RB in aqueous medium using undoped and Au-doped photocatalysts, which is dependent on the nature of the support. For example, undoped TiO_2 and ZnO have similar RB photodegradation reactions in the first hour, with approximately 73% of the present RB dye present in the solution. Approximately 98% was achieved after 160 min, with constant efficiency following. It is possible that the photocatalytic performance was so stable beyond 160 min due to the accumulated degradation products at the photocatalyst surface. However, enhanced RB photodegradation performance was achieved by doping both TiO_2 and ZnO with 1 wt.% AuNPs. In this case, 87% degradation was achieved following 60 min with Ay/TiO_2 and 96% with ZnO in the same time. Enhanced photocatalytic degrading capability could potentially be due to AuNPs' electron buffering, which results in slower recombination of pairs of electrons and holes [131]. Degradation efficiency of Au/ZnO rose to 97% when reaction time was increased to 80 min, and remained stable at this stage. Au/TiO_2 saw the same results when reaction time was increased to 100 min. This plateau behavior is likely due to reaction product deposits on the surface of the photocatalysts.

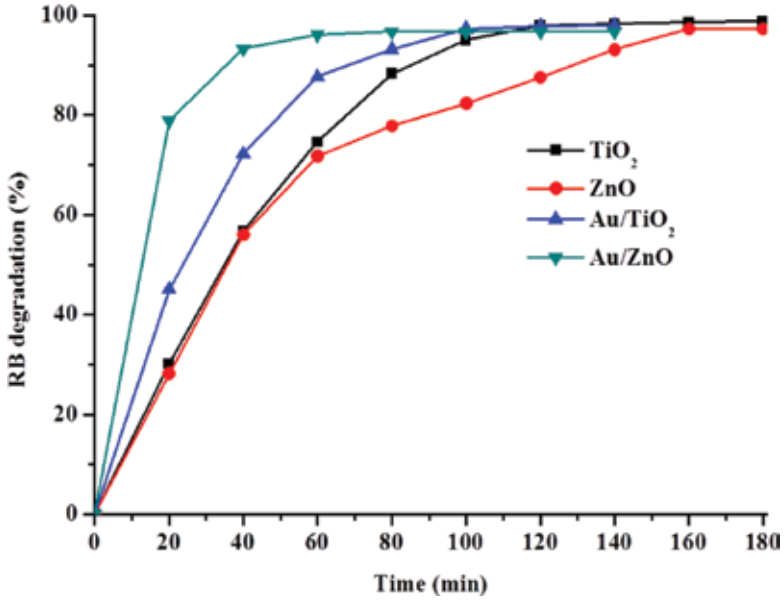

Figure 9. Photocatalytic degradation of RB under UV irradiation, catalyzed with TiO_2, ZnO, Au/TiO_2, and Au/ZnO.

6. Conclusions and outlook

Particles having the size from 1 to 100 nm are termed as nanoparticles, and in nanotechnology, small particles behave as an identical unit in both chemical and physical aspects. Supporting such metal nanoparticles is found to be a great tool where they can be used to develop different green catalytic applications. The interesting phenomenon about these materials is that their high surface area-to-volume ratio of solid-supported metal particles is essentially responsible for their catalytic properties. In this chapter, the recent reported methods for fabricating MNPs have been reviewed. However, the selection of such method is found to be dependent on the desired application. We have also shown that a deeper knowledge to understand the catalytic properties of MNPs is needed to explore the potential application of these MNPs. Therefore, different spectroscopic and microscopic techniques used to understand the catalytic parameters in MNPs have been briefly reviewed. A number of important green reactions using supported MNPs have been presented in this chapter. Quite recently, we have successfully reported that supported MNPs catalyst is an efficient catalyst for different applications such as the oxidation of cyclohexane to adipic acid. Here, one can clearly notice that the size of Au and the nature of support applied matter a lot. In this context, smaller Au particles revealed superior performance compared to their corresponding counterparts. Based on this, the Au/TiO_2 exhibited the best performance compared to other catalysts of the same series for both benzyl alcohol oxidation to benzaldehyde and cyclohexane oxidation to adipic acid. In addition, the application of supported MNPs as efficient photocatalysts was also reported.

Overall, recent advances have been made in governing metal particle morphology, size, and synthetic methodology. Prior art research demonstrates that synthetic approaches and adjustments to chemical and redox environments can result in control over the final form and morphology of nanoparticles. Using oxide carriers to synthesize stable MNPs has environment-friendly implications due to the fact that MNPs have unique properties compared to bulk or isolated atoms. When these MNPs interact successfully with the support, they may stabilize the surface and may generate Lewis sites that may catalyze certain catalytic reactions. However, the interaction degree depends upon the kind of support applied. Therefore, MNPs have varied and new environment-friendly applications. In view of this, highly unsaturated systems are considered superior as they provide larger number of active surface metal sites that may allow efficient interactions between the support and active phases. The ability to stabilize and control other MNPs (such as Pd, Rh, Pt, etc.) would be an excellent advancement, allowing concepts and reactions now possible with homogenous catalysis to be used in a heterogeneous context. However, the commercial application is limited by their activity and selectivity properties. Stability and durability of supported MNPs have implications for productivity. The research presented here was driven by determining the role of supported MNPs in various reactions taking place, either in liquid or gas phase, as well as their associated catalytic processes. Future research may address the creation of bifunctional or multifunctional MNPs, which may have implications for existing reactions or even new outputs. Furthermore, rational approaches need to be worked out in the coming years to sequence various functionalities in the direction of developing novel, attractive, and ecofriendly nanostructured metal nanoparticles for various catalytic applications.

Author details

Ahmad Alshammari[1*], V. Narayana Kalevaru[2*] and Andreas Martin[2]

*Address all correspondence to: aalshammari@kacst.edu.sa

*Address all correspondence to: narayana.kalevaru@catalysis.de

1 Materials Science Research Institute (MSRI), King Abdulaziz City for Science and Technology (KACST), Riyadh, Saudi Arabia

2 Department of Heterogeneous Catalytic Processes, Leibniz Institute for Catalysis, Rostock, Germany

References

[1] Fahlman BD. What is Materials Chemistry? New York: Springer; 2011. DOI: 10.1007/978-94-007-0693-4

[2] Nouailhat A. An Introduction to Nanoscience and Nanotechnology. New York: Wiley; 2010. DOI: 10.1002/9780470610954

[3] Astruc D. Nanoparticles and Catalysis. New York: Wiley, 2008. DOI: 10.1002/9783527621323

[4] Somorjai G, Borodko Y. Research in nanosciences–great opportunity for catalysis science. Catalysis Letters. 2001;76(1-2):1–5. DOI: 10.1023/A:1016711323302

[5] Pasquato L, Rancan F, Scrimin P, Mancin F, Frigeri C. N-methylimidazole-functionalized gold nanoparticles as catalysts for cleavage of a carboxylic acid ester. Chemical Communications. 2000;(22):2253–4. DOI: 10.1039/b005244m

[6] Haruta M, Daté M. Advances in the catalysis of Au nanoparticles. Applied Catalysis A: General. 2001;222(1):427–37. DOI: 10.1016/S0926-860X(01)00847-X

[7] Brayner R, Viau G, Bozon-Verduraz F. Liquid-phase hydrogenation of hexadienes on metallic colloidal nanoparticles immobilized on supports via coordination capture by bifunctional organic molecules. Journal of Molecular Catalysis A: Chemical. 2002;182:227–38. DOI: 10.1016/S1381-1169(01)00469-1

[8] Toshima N, Shiraishi Y, Teranishi T. Effect of additional metal ions on catalyses of polymer-stabilized metal nanoclusters. Journal of Molecular Catalysis A: Chemical. 2001;177(1):139–47. DOI: 10.1016/S1381-1169(01)00314-4

[9] Dai J, Bruening ML. Catalytic nanoparticles formed by reduction of metal ions in multilayered polyelectrolyte films. Nano Letters. 2002;2(5):497–501. DOI: 10.1021/nl0255471

[10] Pileni M. Nanosized particles made in colloidal assemblies. Langmuir. 1997;13(13): 3266–76. DOI: 10.1021/la960319q

[11] Fu X, Wang Y, Wu N, Gui L, Tang Y. Shape-selective preparation and properties of oxalate-stabilized Pt colloid. Langmuir. 2002;18(12):4619–24. DOI: 10.1021/la020087x

[12] Toshima N, Kuriyama M, Yamada Y, Hirai H. Colloidal platinum catalyst for light-induced hydrogen evolution from water. A particle size effect. Chemistry Letters. 1981;10(6):793–6. DOI: 10.1246/cl.1981.793

[13] Hirai H, Chawanya H, Toshima N. Colloidal palladium protected with poly (N-vinyl-2-pyrrolidone) for selective hydrogenation of cyclopentadiene. Reactive Polymers, Ion Exchangers, Sorbents. 1985;3(2):127–41. DOI: 10.1016/0167-6989(85)90055-8

[14] Yonezawa T, Toshima N. Mechanistic consideration of formation of polymer-protected nanoscopic bimetallic clusters. Journal of the Chemical Society, Faraday Transactions. 1995;91(22):4111–9. DOI: 10.1039/ft9959104111

[15] Toshima N, Hirakawa K. Polymer-protected bimetallic nanocluster catalysts having core/shell structure for accelerated electron transfer in visible-light-induced hydrogen generation. Polymer Journal. 1999;31:1127–32. DOI: 10.1295/polymj.31.1127

[16] Li Y, El-Sayed MA. The effect of stabilizers on the catalytic activity and stability of Pd colloidal nanoparticles in the Suzuki reactions in aqueous solution. The Journal of Physical Chemistry B. 2001;105(37):8938–43. DOI: 10.1021/jp010904m

[17] Klingelhöfer S, Heitz W, Greiner A, Oestreich S, Förster S, Antonietti M. Preparation of palladium colloids in block copolymer micelles and their use for the catalysis of the Heck reaction. Journal of the American Chemical Society. 1997;119(42):10116–20. DOI: 10.1021/ja9714604

[18] Kimling J, Maier M, Okenve B, Kotaidis V, Ballot H, Plech A. Turkevich method for gold nanoparticle synthesis revisited. The Journal of Physical Chemistry B. 2006;110(32):15700–7. DOI: 10.1021/jp061667w

[19] Swihart MT. Vapor-phase synthesis of nanoparticles. Current Opinion in Colloid & Interface Science. 2003;8(1):127–33. DOI: 10.1016/S1359-0294(03)00007-4

[20] Kruis FE, Fissan H, Peled A. Synthesis of nanoparticles in the gas phase for electronic, optical and magnetic applications—a review. Journal of Aerosol Science. 1998;29(5): 511–35. DOI: 10.1016/S0021-8502(97)10032-5

[21] Okazaki K-i, Kiyama T, Hirahara K, Tanaka N, Kuwabata S, Torimoto T. Single-step synthesis of gold–silver alloy nanoparticles in ionic liquids by a sputter deposition technique. Chem Commun. 2008;(6):691–3. DOI: 10.1039/B714761A

[22] Li S, El-Shall MS. Synthesis of nanoparticles by reactive laser vaporization: silicon nanocrystals in polymers and properties of gallium and tungsten oxides. Applied Surface Science. 1998;127:330–8. DOI: 10.1016/S0169-4332(97)00651-X

[23] Ullmann M, Friedlander SK, Schmidt-Ott A. Nanoparticle formation by laser ablation. Journal of Nanoparticle Research. 2002;4(6):499–509. DOI: 10.1023/A:1022840924336

[24] Kammler HK, Mädler L, Pratsinis SE. Flame synthesis of nanoparticles. Chemical Engineering & Technology. 2001;24(6):583–96. DOI: 10.1002/1521-4125(200106)24:6<583::AID-CEAT583>3.0.CO;2-H

[25] Stark WJ, Pratsinis SE. Aerosol flame reactors for manufacture of nanoparticles. Powder Technology. 2002;126(2):103–8. DOI: 10.1016/S0032-5910(02)00077-3

[26] Rao N, Girshick S, Heberlein J, McMurry P, Jones S, Hansen D, et al. Nanoparticle formation using a plasma expansion process. Plasma Chemistry and Plasma Processing. 1995;15(4):581–606. DOI: 10.1007/BF01447062

[27] De La Veaux SC, Zhang L. Method of producing nanoparticles using a evaporation-condensation process with a reaction chamber plasma reactor system. Google Patents; 2010.

[28] Kotov YA. Electric explosion of wires as a method for preparation of nanopowders. Journal of Nanoparticle Research. 2003;5(5-6):539–50. DOI: 10.1023/B:NANO.0000006069.45073.0b

[29] Mao Z, Zou X, Liu X, Wang X, Jiang W, editors. Study of nanopowder production by gas-embeded electrical explosion of wire. 17th International Conference on High Power Particle Beams (Beams'08) in Xi'an, Shaanxi, China.

[30] Jaworek A. Micro-and nanoparticle production by electrospraying. Powder Technology. 2007;176(1):18–35. DOI: 10.1016/j.powtec.2007.01.035

[31] Srivastava SK, Yamada R, Ogino C, Kondo A. Biogenic synthesis and characterization of gold nanoparticles by Escherichia coli K12 and its heterogeneous catalysis in degradation of 4-nitrophenol. Nanoscale Research Letters. 2013;8(1):1–9. DOI: 10.1186/1556-276X-8-70

[32] Parida UK, Bindhani BK, Nayak P. Green synthesis and characterization of gold nanoparticles using onion (Allium cepa) extract. World Journal of Nano Science and Engineering. 2011;1(04):93. DOI: 10.4236/wjnse.2011.14015

[33] Petla RK, Vivekanandhan S, Misra M, Mohanty AK, Satyanarayana N. Soybean (Glycine max) leaf extract based green synthesis of palladium nanoparticles. Journal of Biomaterials and Nanobiotechnology. 2012;3:14–19. DOI: 10.4236/jbnb.2012.31003.2011

[34] Lee JH, Ahn K, Kim SM, Jeon KS, Lee JS, Yu IJ. Continuous 3-day exposure assessment of workplace manufacturing silver nanoparticles. Journal of Nanoparticle Research. 2012;14(9):1–10. DOI: 10.1007/s11051-012-1134-8

[35] Yang H, Wang Y, Huang H, Gell L, Lehtovaara L, Malola S, et al. All-thiol-stabilized Ag44 and Au12Ag32 nanoparticles with single-crystal structures. Nature Communications. 2013;4:2422. DOI: 10.1038/ncomms3422

[36] Prieto G, Zečević J, Friedrich H, de Jong KP, de Jongh PE. Towards stable catalysts by controlling collective properties of supported metal nanoparticles. Nature Materials. 2013;12(1):34–9. DOI: 10.1038/nmat3471

[37] An K, Somorjai GA. Size and shape control of metal nanoparticles for reaction selectivity in catalysis. ChemCatChem. 2012;4(10):1512–24. DOI: 10.1002/cctc.201200229

[38] Bell AT. The impact of nanoscience on heterogeneous catalysis. Science. 2003;299(5613): 1688–91. DOI: 10.1126/science.1083671

[39] Cuenya BR. Synthesis and catalytic properties of metal nanoparticles: size, shape, support, composition, and oxidation state effects. Thin Solid Films. 2010;518(12):3127–50. DOI: 10.1016/j.tsf.2010.01.018

[40] Haruta M, Daté M. Advances in the catalysis of Au nanoparticles. Applied Catalysis A: General. 2001;222(1):427–37. DOI: 10.1016/S0926-860X(01)00847-X

[41] Haruta M. Gold as a novel catalyst in the 21st century: preparation, working mechanism and applications. Gold Bulletin. 2004;37(1-2):27–36. DOI: 10.1007/BF03215514

[42] Boudart M. Catalysis by supported metals. In: Frankenburg WG. Advances in Catalysis. 20th ed. New York: Academic Press; 1969. p. 153–66. ISSN:0360-0564

[43] Gates BC. Supported metal clusters: synthesis, structure, and catalysis. Chemical Reviews. 1995;95(3):511–22. DOI: 10.1021/cr00035a003

[44] Flytzani-Stephanopoulos M, Gates BC. Atomically dispersed supported metal catalysts. Annual Review of Chemical and Biomolecular Engineering, 2012;3:545–74. DOI: 10.1146/annurev-chembioeng-062011-080939

[45] Borodzinski A, Bonarowska M. Relation between crystallite size and dispersion on supported metal catalysts. Langmuir. 1997;13(21):5613–20. DOI: 10.1021/la962103u

[46] Hammer B, Morikawa Y, Nørskov JK. CO chemisorption at metal surfaces and overlayers. Physical Review Letters. 1996;76(12):2141. DOI: 10.1103/PhysRevLett.76.2141

[47] Dulaurent O, Bianchi D. Adsorption isobars for CO on a Pt/Al2O3 catalyst at high temperatures using FTIR spectroscopy: isosteric heat of adsorption and adsorption model. Applied Catalysis A: General. 2000;196(2):271–80. DOI: 10.1016/S0926-860X(99)00472-X

[48] Joshi AM, Tucker MH, Delgass WN, Thomson KT. CO adsorption on pure and binary-alloy gold clusters: a quantum chemical study. The Journal of Chemical Physics. 2006;125(19):194707. DOI: 10.1063/1.2375094

[49] Mustard DG, Bartholomew CH. Determination of metal crystallite size and morphology in supported nickel catalysts. Journal of Catalysis. 1982;67(1):186–206. DOI: 10.1016/0021-9517(81)90271-2

[50] Cui C, Gan L, Li HH, Yu SH, Heggen M, Strasser P. Octahedral PtNi nanoparticle catalysts: exceptional oxygen reduction activity by tuning the alloy particle surface composition. Nano Letters. 2012;12(11):5885–9. DOI: 10.1021/nl3032795

[51] Stamenkovic VR, Mun BS, Arenz M, Mayrhofer KJ, Lucas CA, Wang G, Ross PN, Markovic NM. Trends in electrocatalysis on extended and nanoscale Pt-bimetallic alloy surfaces. Nature Materials. 2007;6(3):241–7. DOI: 10.1038/nmat1840

[52] Chin YHC, King DL, Roh HS, Wang Y, Heald SM. Structure and reactivity investigations on supported bimetallic Au Ni catalysts used for hydrocarbon steam reforming. Journal of Catalysis. 2006;244(2):153–62. DOI: 10.1016/j.jcat.2006.08.016

[53] Matsumura Y, Nakamori T. Steam reforming of methane over nickel catalysts at low reaction temperature. Applied Catalysis A: General. 2004;258(1):107–14. DOI: 10.1016/j.apcata.2003.08.009

[54] Hayek K, Kramer R, Paál Z. Metal-support boundary sites in catalysis. Applied Catalysis A: General. 1997;162(1):1–15. DOI: 10.1016/S0926-860X(97)00243-3

[55] White RJ, Luque R, Budarin VL, Clark JH, Macquarrie DJ. Supported metal nanoparticles on porous materials. Methods and applications. Chemical Society Reviews. 2009;38(2):481–94. DOI: 10.1039/B802654H

[56] Jia CJ, Schüth F. Colloidal metal nanoparticles as a component of designed catalyst. Physical Chemistry Chemical Physics, 2011;13(7):2457–87. DOI: 10.1039/C0CP02680H

[57] Heck RM, Farrauto RJ. Automobile exhaust catalysts. Applied Catalysis A: General. 2001;221(1):443–57. DOI: 10.1016/S0926-860X(01)00818-3

[58] Sabatier P, Senderens JB. New synthesis of methane. Comptes Rendus Hebdomadaires des Seances de l'Academie des Sciences. 1902;134:514–516.

[59] Sabatier P, Senderens JB. Direct hydrogenation of the oxides of carbon in the presence of various finely-divided metals. Comptes Rendus Hebdomadaires des Seances de l'Academie des Sciences. 1902;134:689–91.

[60] Lange F, Armbruster U, Martin A. Heterogeneously-catalyzed hydrogenation of carbon dioxide to methane over RuNi-bimetallic catalysts. Energy Technology. 2015:3;55–62. DOI: 10/1002./ente.201402113

[61] Schoder M, Armbruster U, Martin A. Heterogen-katalysierte Hydrierung von CO2 zu Methan unter erhöhten Drücken. Chemie Ingenieur Technik. 2013:85;344–52. DOI: 10.1002/cite.201200112

[62] http://www.nobelprize.org/nobel_prizes/chemistry/laureates/1912/

[63] Guo M, Lu G. The regulating effects of cobalt addition on the catalytic properties of silica-supported Ni–Co bimetallic catalysts for CO2 methanation. Reaction Kinetics, Mechanisms and Catalysis. 2014;113(1):101–13. DOI 10.1007/s11144-014-0732-0

[64] Jackson SD, Willis J, Kelly GJ, McLellan GD, Webb G, Mather S, Moyes RB, Simpson S, Wells PB, Whyman R. Supported nickel catalysts: preparation and characterisation of alumina-, molybdena-, and silica-supported nickel, and the identification of reactive oxygen on these catalysts by exchange with isotopically labelled carbon dioxide. Physical Chemistry Chemical Physics. 1999;1:2573–80. DOI: 10.1039/A809293A

[65] Auer E, Freund A, Pietsch J, Tacke T. Carbons as supports for industrial precious metal catalysts. Applied Catalysis A: General. 1998;173(2):259–71. DOI: 10.1016/S0926-860X(98)00184-7

[66] Van de Vyver S, Geboers J, Schutyser W, Dusselier M, Eloy P, Dornez E, Seo JW, Courtine CM, Gaigneaux EM, Jacobs PA, Sels BF. Tuning the acid/metal balance of carbon nanofiber-supported nickel catalysts for hydrolytic hydrogenation of cellulose. ChemSusChem. 2012;5(8):1549–58. DOI: 10.1002/cssc.201100782

[67] Gadalla AM, Bower B. The role of catalyst support on the activity of nickel for reforming methane with CO 2. Chemical Engineering Science. 1988;43(11):3049–62. DOI: 10.1016/0009-2509(88)80058-7

[68] Chen YG, Ren J. Conversion of methane and carbon dioxide into synthesis gas over alumina-supported nickel catalysts. Effect of Ni-Al2O3 interactions. Catalysis Letters. 1994;29(1-2):39–48. DOI: 10.1007/BF00814250

[69] Sehested J. Four challenges for nickel steam-reforming catalysts. Catalysis Today. 2006;111(1):103–10. DOI: 10.1016/j.cattod.2005.10.002

[70] Ruettinger W, Ilinich O, Farrauto RJ. A new generation of water gas shift catalysts for fuel cell applications. Journal of Power Sources. 2003;118(1):61–5. DOI: 10.1016/S0378-7753(03)00062-4

[71] Li Y, Fu Q, Flytzani-Stephanopoulos M. Low-temperature water-gas shift reaction over Cu-and Ni-loaded cerium oxide catalysts. Applied Catalysis B: Environmental. 200;27(3):179–91. DOI: 10.1016/S0926-3373(00)00147-8

[72] Ratnasamy C, Wagner JP. Water gas shift catalysis. Catalysis Reviews. 2009;51(3):325–440. DOI: 10.1080/01614940903048661

[73] Song Q, Wang F, Xu J. Hydrogenolysis of lignosulfonate into phenols over heterogeneous nickel catalysts. Chemical Communications. 2012;48(56):7019–21. DOI: 10.1039/c2cc31414b

[74] Huynh TM, Armbruster U, Pohl M-M, Schneider M, Radnik J, Hoang D-L, Phan BMQ, Nguyen DA, Martin A. Hydrodeoxygenation of phenol as a model compound for bio-oil over non-noble bimetallic catalysts based on Ni. ChemCatChem. 2016;6:1940–51. DOI: 10.1002/cctc.201402011

[75] Schulz, H. Short history and present trends of Fischer–Tropsch synthesis. Applied Catalysis A: General. 1999;186(1):3–12. DOI: 10.1016/S0926-860X(99)00160-X

[76] Khodakov AY, Chu W, Fongarland P. Advances in the development of novel cobalt Fischer-Tropsch catalysts for synthesis of long-chain hydrocarbons and clean fuels. Chemical Reviews. 2007;107(5):1692–744. DOI: 10.1021/cr050972v

[77] Kim YC, Park NC, Shin JS, Lee SR, Lee YJ, Moon DJ. Partial oxidation of ethylene to ethylene oxide over nanosized Ag/α-Al 2 O 3 catalysts. Catalysis Today. 2003;87(1):153–62. DOI: 10.1016/j.cattod.2003.09.012

[78] Rojluechai S, Chavadej S, Schwank JW, Meeyoo V. Catalytic activity of ethylene oxidation over Au, Ag and Au–Ag catalysts: support effect. Catalysis Communications. 2007;8(1):57–64. DOI: 10.1016/j.catcom.2006.05.029

[79] Mortensen PM, Grunwaldt JD, Jensen PA, Knudsen KG, Jensen AD. A review of catalytic upgrading of bio-oil to engine fuels. Applied Catalysis A: General. 2011;407(1):1–19. DOI: 10.1016/j.apcata.2011.08.046

[80] Prins R, De Beer VHJ, Somorjai GA. Structure and function of the catalyst and the promoter in Co—Mo hydrodesulfurization catalysts. Catalysis Reviews – Science and Engineering. 1989;31(1-2):1–41. DOI: 10.1080/01614948909351347

[81] Babich IV, Moulijn JA. Science and technology of novel processes for deep desulfurization of oil refinery streams: a review. Fuel. 2003;82(6):607–31. DOI: 10.1016/S0016-2361(02)00324-1

[82] Wildgoose GG, Banks CE, Compton RG. Metal nanoparticles and related materials supported on carbon nanotubes: methods and applications. Small. 2006;2(2):182–93. DOI: 10.1002/smll.200500324

[83] Lightcap IV, Kosel TH, Kamat PV. Anchoring semiconductor and metal nanoparticles on a two-dimensional catalyst mat. Storing and shuttling electrons with reduced graphene oxide. Nano Letters. 2010;10(2):577–83. DOI: 10.1021/nl9035109

[84] Li XH, Antonietti M. Metal nanoparticles at mesoporous N-doped carbons and carbon nitrides: functional Mott–Schottky heterojunctions for catalysis. Chemical Society Reviews. 2013;42(16):6593–604. DOI: 10.1039/c3cs60067j

[85] Jin Z, Xiao M, Bao Z, Wang P, Wang J. A general approach to mesoporous metal oxide microspheres loaded with noble metal nanoparticles. Angewandte Chemie International Edition. 2012;51(26):6406–10. DOI: 10.1002/anie.201106948

[86] Alayoglu S, Beaumont SK, Zheng F, Pushkarev VV, Zheng HM, Iablokov V, Liu Z, Guo JH, Kruse N, Somorjai GA. CO_2 hydrogenation studies on Co and CoPt bimetallic nanoparticles under reaction conditions using TEM, XPS and NEXAFS. Topics in Catalysis. 2011;54(13-14):778–785. DOI: 10.1007/s11244-011-9695-9

[87] Satterfield CN. Heterogeneous Catalysis in Practice. New York: McGraw-Hill Companies; 1980.

[88] Akia M, Yazdani F, Motaee E, Han D, Arandiyan H. A review on conversion of biomass to biofuel by nanocatalysts. Biofuel Research Journal. 2014;1(1):16–25. DOI: 10.18331/BRJ2015.1.1.5

[89] Digman B, Joo HS, Kim DS. Recent progress in gasification/pyrolysis technologies for biomass conversion to energy. Environmental Progress & Sustainable Energy. 2009;28(1):47–51. DOI: 10.1002/ep.10336

[90] Luo Z, Zhou J. Thermal Conversion of Biomass. Handbook of Climate Change Mitigation. New York: Springer; 2012. p. 1001–42. DOI: 10.1007/978-1-4419-7991-9_27

[91] Demirbas A. Biofuels sources, biofuel policy, biofuel economy and global biofuel projections. Energy Conversion and Management. 2008;49(8):2106–16. DOI: 10.1016/j.enconman.2008.02.020

[92] Aravind P, de Jong W. Evaluation of high temperature gas cleaning options for biomass gasification product gas for solid oxide fuel cells. Progress in Energy and Combustion Science. 2012;38(6):737–64. DOI: 10.1016/j.pecs.2012.03.006

[93] Malik P, Sangwan A. Nanotechnology: a tool for improving efficiency of bio-energy. Journal of Engineering and Applied Sciences. 2012;1:37–49.

[94] Asadullah M. Barriers of commercial power generation using biomass gasification gas: a review. Renewable and Sustainable Energy Reviews. 2014;29:201–15. DOI: 10.1016/j.rser.2013.08.074

[95] Nzihou A, Stanmore B, Sharrock P. A review of catalysts for the gasification of biomass char, with some reference to coal. Energy. 2013;58:305–17. DOI: 10.1016/j.energy.2013.05.057

[96] Anis S, Zainal Z. Tar reduction in biomass producer gas via mechanical, catalytic and thermal methods: a review. Renewable and Sustainable Energy Reviews. 2011;15(5):2355–77. DOI: 10.1016/j.rser.2011.02.018

[97] Han J, Kim H. The reduction and control technology of tar during biomass gasification/pyrolysis: an overview. Renewable and Sustainable Energy Reviews. 2008;12(2):397–416. DOI: 10.1016/j.rser.2006.07.015

[98] Boerrigter H, Den Uil H, Calis H-P. Green diesel from biomass via Fischer-Tropsch synthesis: new insights in gas cleaning and process design. Citeseer; 2003. p. 371–83.

[99] Kang J, Zhang S, Zhang Q, Wang Y. Ruthenium nanoparticles supported on carbon nanotubes as efficient catalysts for selective conversion of synthesis gas to diesel fuel. Angewandte Chemie. 2009;121(14):2603–6. DOI: 10.1002/ange.200805715

[100] Hutchings G, Polshettiwar V, Asefa T. Nanocatalysis: Synthesis and Applications. New York: John Wiley & Sons; 2013.

[101] Fischer F, Tropsch H. The preparation of synthetic oil mixtures (synthol) from carbon monoxide and hydrogen. Brennstoff-Chem. 1923;4:276–85.

[102] Saxena S, Rosen M, Smith D, Ruether J. Mathematical modeling of Fischer-Tropsch slurry bubble column reactors. Chemical Engineering Communications. 1986;40(1-6):97–151. DOI: 10.1080/00986448608911693

[103] Van Der Laan GP, Beenackers A. Kinetics and selectivity of the Fischer–Tropsch synthesis: a literature review. Catalysis Reviews. 1999;41(3-4):255–318. DOI: 10.1081/CR-100101170

[104] Serp P, Corrias M, Kalck P. Carbon nanotubes and nanofibers in catalysis. Applied Catalysis A: General. 2003;253(2):337–58. DOI: 10.1016/S0926-860X(03)00549-0

[105] Ranganathan SV, Narasimhan SL, Muthukumar K. An overview of enzymatic production of biodiesel. Bioresource Technology. 2008;99(10):3975–81. DOI: 10.1016/j.biortech.2007.04.060

[106] Zheng S, Kates M, Dube M, McLean D. Acid-catalyzed production of biodiesel from waste frying oil. Biomass and Bioenergy. 2006;30(3):267–72. DOI: 10.1016/j.biombioe.2005.10.004

[107] Li J, Wang X, Zhu W, Cao F. $Zn_{1.2}H_{0.6}PW_{12}O_{40}$ nanotubes with double acid sites as heterogeneous catalysts for the production of biodiesel from waste cooking oil. ChemSusChem. 2009;2(2):177–83. DOI: 10.1002/cssc.200800208

[108] Li S, Varatharajan B, Williams F. Chemistry of JP-10 ignition. AIAA Journal. 2001;39(12):2351–6. DOI: 10.2514/3.15032

[109] Wickham DT, Cook R, De Voss S, Engel JR, Nabity J. Soluble nano-catalysts for high performance fuels. Journal of Russian Laser Research. 2006;27(6):552–61. DOI: 10.1007/s10946-006-0034-8

[110] Li S, Varatharajan B, Williams F. Chemistry of JP-10 ignition. AIAA Journal. 2001;39(12):2351–6. DOI: 10.2514/3.15032

[111] Rostrup-Nielsen T. Manufacture of hydrogen. Catalysis Today. 2005;106(1):293–6. DOI: 10.1016/j.cattod.2005.07.149

[112] Bion N, Duprez D, Epron F. Design of nanocatalysts for green hydrogen production from bioethanol. ChemSusChem. 2012;5(1):76–84. DOI: 10.1002/cssc.201100400

[113] Schlapbach L, Züttel A. Hydrogen-storage materials for mobile applications. Nature. 2001;414(6861):353–8. DOI: 10.1038/35104634

[114] Schlapbach L, Züttel A. Hydrogen-storage materials for mobile applications. Nature. 2001;414(6861):353–8. DOI: 10.1038/35104634

[115] Kasta P, Friedricha M, Girgsdiesa F, Kröhnerta J, Teschnera D, Lunkenbeina T, Behrensb M, Schlögla R. Strong metal-support interaction and alloying in Pd/ZnO catalysts for CO oxidation. Catalysis Today. 2016;260:21–30. DOI:10.1016/j.cattod.2015.05.021

[116] Grisel RJH, Nieuwenhuys BE. Selective oxidation of CO, over supported Au. Journal of Catalysis. 2001;199(1):48–58. DOI:10.1006/jcat.2000.3121

[117] Tauster SJ, Fung SC, Baker RTK, Horsley JA. Strong interactions in supported-metal catalysts. Science. 1981;211(4487):1121–5. DOI: 10.1126/science.211.4487.1121

[118] Mallat T, Baiker A. Oxidation of alcohols with molecular oxygen on solid catalysts. Chemical Reviews. 2004;104(6):3037–58. DOI: 10.1021/cr0200116

[119] Hashmi AS, GJ Hutchings. Gold catalysis. Angewandte Chemie International Edition 2006;45(47):7896–936. DOI: 10.1002/anie.200602454

[120] Prati L, Rossi M. Gold on carbon as a new catalyst for selective liquid phase oxidation of diols. Journal of Catalysis. 1998;176(2):552–60. DOI:10.1006/jcat.1998.2078

[121] Pina CD, Falletta E, Pratia L, Rossi M. Selective oxidation using gold. Chemical Society Reviews. 2008;37:2077–95. DOI: 10.1039/B707319B

[122] Carretin S, McMorn P, Johnston P, Griffin K, Kiely JC. Hutchings GJ. Oxidation of glycerol using supported Pt, Pd and Au catalysts. Physical Chemistry Chemical Physics. 2003;5:1329–36. DOI: 10.1039/B212047J

[123] Abad A, Concepción P, Corma A, Garciá HH. A collaborative effect between gold and a support induces the selective oxidation of alcohols. Angewandte Chemie. 2005;26(117):4134–7. DOI: 10.1002/ange.200500382.

[124] Enache DI, Edwards JK, Landon P, Solsona-Espriu B, Carley AF, Herzing AA, Watanabe M, Kiely CJ, Knight DW, Hutchings GJ. Solvent-free oxidation of primary alcohols

to aldehydes using Au-Pd/TiO_2 catalysts. Science. 2006;311(5759):362–5. DOI: 10.1126/science.1120560

[125] Miedziak P, Sankar M, Dimitratos N, Lopez-Sanchez JA, Carley AF, Knight DW, Taylor ST, Kiely CJ, Hutchings GJ. Oxidation of benzyl alcohol using supported gold–palladium nanoparticles. Catalysis Today. 2011;163(1):47–54. DOI:10.1016/j.cattod.2010.02.051

[126] Alshammari A, Koeckritz A, Kalevaru VN, Bagabas A, Martin A. Significant formation of adipic acid by direct oxidation of cyclohexane using supported nano-gold catalysts. ChemCatChem. 2012;4(9):1330–6. DOI: 10.1002/cctc.201200008

[127] Schuchardt U, Cardoso D, Sercheli R, Pereira R, Cruz RS, Guerreiro MC, Mandelli D, Spinace EV, Pires EL. Cyclohexane oxidation continues to be a challenge. Applied Catalysis A: General. 2001;211(1):1–17. DOI:10.1016/S0926-860X(01)00472-0

[128] Alshammari A, Bagabas A, Assulami M. Photodegradation of rhodamine B over semiconductor supported gold nanoparticles: the effect of semiconductor support identity. Arabian Journal of Chemistry. 2014, in press.

[129] Bagabas A, Alshammari A, Aboud M, Kosslick H. Room-temperature synthesis of zinc oxide nanoparticles in different media and their application in cyanide photodegradation. Nanoscale Research Letters. 2013;8(516):1–10. DOI: 10.1186/1556-276X-8-516

[130] Alshammari A, Chi L, Chen X, Bagabas A, Kramer D, Alromaeha A, Zheng J. Visible-light photocatalysis on C-doped ZnO derived from polymer-assisted pyrolysis. RSC Advances. 2015;5:27690–8. DOI:10.1039/C4RA17227B

[131] Yu H, Ming H, Gong J, Li H, Huang H, Pan K, Liu Y, Kang Z, Wei J, Wang, D. Facile synthesis of Au/ZnO nanoparticles and their enhanced photocatalytic activity for hydroxylation of benzene. Bulletin of Materials Science. 2013;36(3):367–72. DOI: 10.1007/s12034-013-0491-y

Chapter 2

Recent Highlights in Green Oxidative Chemical Processes Applied to Steroid Chemistry

Samuel M. Silvestre, M. Manuel C. Silva and
Jorge A. R. Salvador

Additional information is available at the end of the chapter

http://dx.doi.org/10.5772/62381

Abstract

Steroids and their oxidation products are widely distributed in living organisms and are important intermediates for the synthesis of many biologically active molecules. Due to their pharmacological and synthetic relevance, several oxidative chemical processes for the functionalization of the steroid nucleus have been developed. Green chemistry principles have been incorporated in some oxidative transformations of steroids, allowing significant advances in synthetic chemistry applied to these compounds. This chapter presents a selection of relevant applications of pharmaceutical green chemistry to steroid's oxidative processes. Special emphasis is given to catalytic processes encompassing heterogeneous nanocatalysts, whose application in this context is increasing over the past years. This chapter is organized according to the reaction type that includes alcohol oxidation, epoxidation of alkenes, and allylic oxidation of alkenes to enones, among other relevant oxidative transformations. Biocatalytic oxidative methods applied to steroid synthesis are not included in this review.

Keywords: green pharmaceutical chemistry, steroids, catalysis, oxidation, green technologies, nanocatalysts

1. Introduction

1.1. Basic steroid chemistry and relevance of oxygenated steroids

Steroid compounds are found in almost all living organisms [1, 2], having an important role in their vital activity [1–4]. The steroid hormones were discovered and characterized during the 1930s, and since then, it has been realized that steroid compounds can control important

physiopathological conditions, being therefore important starting point for the development of new medicines [3]. Indeed, several natural and synthetic steroids are important therapeutic options for a wide range of diseases. These include sex and corticosteroid hormones, bile acids, vitamin D derivatives, and cardiotonic steroids, among others, that have shown unique therapeutic value for a broad array of medical conditions [1]. Due to their relevance, over the last decades, hundreds of steroid compounds have been isolated from natural sources, whereas many thousands of them have been obtained synthetically [2, 4] and their study has continued until present days in both chemical and biological perspectives.The steroidal basic structure constitutes a common chemical skeleton of four fused rings, consisting of three six-membered rings and a five-membered ring [1, 2, 5]. This hydrocarbon scaffold contains 17 carbons and has the cyclopentaneperhydrophenanthrene basic structure. The four steroid rings are labeled as A, B, C and D and their carbon atoms are numbered according to the universal convention according to the IUPAC-IUB (International Union of Pure and Applied Chemistry/International Union of Biochemistry) Joint Commission on Biochemical Nomenclature [6]. Angular methyl groups at C13 and C10 are designated as 18-CH_3 and 19-CH_3, respectively, and alkyl substituents at C17 are the steroid side-chain. The 18- and 19-methyl groups stand above the plane of the steroid skeleton and, by convention, have β-configuration. Therefore, as stated, other atoms or substituents located above this plane also have β-configuration, while those below it have α-configuration (**Figure 1**) [1, 2, 5, 6].

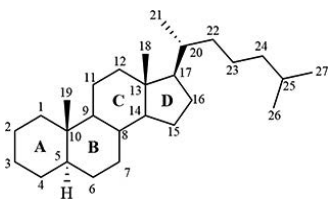

Figure 1. Chemical structure of the 5α-cholestane nucleus.

The preparation of steroids containing oxygenated functions in the steroid nucleus is of high relevance and can be performed by means of several oxidative processes. Among the large variety of available methods, the allylic oxidation and epoxidation of alkenes and the alcohol oxidation are probably the most commonly used oxidative transformations [1, 2]. In fact, the allylic oxidation of steroidal alkenes to the corresponding enones, such as Δ^5-7-ketones, is of great importance because of their significant biological properties. The diastereoselective epoxidation of steroidal alkenes is a relevant challenge because of the difficulty in the preparation of pure epoxides. This transformation is also very important not only because the epoxide moiety is of high synthetic interest for further elaboration but also because this functionality has been found in several biologically active steroids. The oxidation of steroidal alcohols is also considered in this chapter. A relevant example of high industrial interest is the transformation of Δ^5-3β-hydroxylated steroids into the corresponding Δ^4-3-ketones, a typical functionality of the major class of steroidal hormones [1, 2].

http://dx.doi.org/10.5772/62381

1.2. The green chemistry concept and green nanotechnologies

According to the Environmental Protection Agency, green or sustainable chemistry has been defined as "the design of chemical products and processes that reduce or eliminate the use or generation of hazardous substances" [7]. In fact, over the years, a large development in this field was observed and several new greener procedures are now being used in the chemical industry [8]. In the pharmaceutical industry, due to the complexity of the products involved as well as the characteristics/issues associated with their uses, the application of the green chemistry principles in the production of medicines has been an enormous challenge [8, 9]. Considering that the major sources of waste in the chemical/pharmaceutical industry are the use of stoichiometric reagents and solvent losses, and the clear solution to this problem is the development of catalytic reactions in alternative reaction media. Additionally, the possibility of recovery and reuse of the reactants/catalysts/solvents and the use of inexpensive, renewable and non-toxic materials are key issues in this context. Accordingly, over the years several greener approaches for the majority of chemical reactions have been developed [10–12].

The development of catalytic processes has been the most explored strategy in green and sustainable chemistry, avoiding the use of numerous hazardous and/or expensive stoichiometric reactants. According to their nature, catalysts can be classified as metallic, organometallic, organocatalysts and biocatalysts. On the other hand, based on their physical state, catalysts can be grouped as homogeneous and heterogeneous [10–13]. In this context, the use of heterogeneous catalysts (either metallic or non-metallic) has the important advantage of allowing their recovery and reuse [14, 15]. Furthermore, of major relevance in the pharmaceutical industry is the synthesis of organic compounds devoid of metal contamination, which can be achieved by using organo- [16, 17] and biocatalytic [18] procedures. Biocatalysis also has several advantages in the context of green chemistry, including the fact that reactions are frequently performed under mild conditions of temperature, pressure and pH and using water as solvent. Moreover, the catalyst is biodegradable and derived from renewable raw materials. Noteworthy, biocatalysis frequently leads to higher chemo-, regio- and stereoselectivities, than traditional chemical processes [10].

A special advance in green chemistry is the use of nanotechnologies. According to McKenzie and Hutchison, "Green nanoscience/nanotechnology involves the application of green chemistry principles to the design of nanoscale products, the development of nanomaterial production methods, and the application of nanomaterials" [19]. In organic chemical synthesis, the main application of this concept is the use of nanomaterials as nanocatalysts, being considered sustainable alternatives to conventional materials. In fact, the nanosized particles can offer some of the advantages of homogeneous catalysts because of an increased exposed surface area of the active component of the catalyst, which enhances dramatically the contact between reactants and catalyst. In addition, similarly to heterogeneous catalysts, their insolubility in the reaction solvents renders them easily separable from the reaction mixture, which consequently makes the product isolation stage effortless. Moreover, the activity and selectivity of nanocatalysts can be manipulated by tailoring chemical and physical properties such as size, shape, composition and morphology [20]. Due to these interesting properties, the use of nanocatalysts has been increasing over the years [21].

Solvent selection is another important issue in the development of new synthetic processes, in the chemical and pharmaceutical industries [8, 22]. Actually, the highest part of the material usage for active pharmaceutical ingredient (API) manufacture is usually constituted by solvents. In fact, it was estimated that their use consumes more than 50% of the overall energy and accounts for half of the post-treatment green-house gas emissions. Ideally, reactions should be performed without any solvent (neat conditions). However, solvents are critical for the reaction rates and selectivities and are often required for heat and mass transfer. Consequently, solvents should be readily available, non-volatile, non-flammable, non-toxic, recyclable and cheap [8, 10, 22]. Attractive solvents from both economical and environmental point of view can include water [23, 24], ionic liquids [25, 26], fluorous solvents [27] as well as supercritical fluids (e.g., supercritical CO_2) [28, 29].

Green chemistry also deals with the minimization of energy usage. In fact, the addition of energy, mostly thermal, is necessary for the majority of organic reactions. For this reason, the strategy to develop chemical transformations under mild reaction conditions has been exploring alternative energy sources such as microwaves (MW), ultrasounds and even light [11, 12, 30]. In fact, successful advances have been made over the years mainly on MW-promoted reactions [30, 31] but also on sonochemistry [30, 32] and photochemistry [33].

1.3. Scope and organization of this chapter

Due to the above referred biological and synthetic importance of steroids, several new green chemical processes for the preparation and/or functionalization of the steroid nucleus have also been developed over the years [34, 35]. In this chapter, relevant applications of green oxidative chemical processes in steroid chemistry are described. Special emphasis is given to catalytic processes involving the use of heterogeneous catalysts, including nanocatalysts. Other green approaches, such as MW technologies as well as the use of ionic liquids as solvents, are presented. This chapter is organized according to the reaction type that includes alcohol oxidation, epoxidation, allylic oxidation and miscellaneous oxidative transformations.

2. Alcohol oxidation

The most common oxidative transformation in steroid chemistry is probably the oxidation of alcohols [34, 35]. Actually, not only several important natural and synthetic steroids have carbonyl groups but also this oxidation is frequently used as an intermediary step in the preparation of a large variety of bioactive steroids. For this reason, several oxidative processes for this reaction have been developed over the years. The most employed oxidants are transition metals, particularly chromium(VI) reagents. Nonetheless, other oxygen- and halogen-based oxidants as well as other oxidizing conditions, frequently combined with suitable catalysts, have been described [34, 35].

As a relevant example, a heterogeneous catalyst described for the successful oxidation of 5α-cholestan-3β-ol to 5α-cholestanone (**Scheme 1**) was chromium exchanged zeolite (CrE-ZSM-5) combined with 70% aqueous *tert*-butyl hydroperoxide (TBHP), an oxygen-based oxidant. However, it was shown that the reaction was, at least partially, homogeneously catalyzed by

http://dx.doi.org/10.5772/62381

leached chromium [36]. Recently, metal-monocatecholate species were immobilized in a Zr(IV)-based metal-organic framework (MOF) to create new efficient heterogeneous catalysts. Within these, Cr-metalated MOFs revealed to be useful in the oxidation of a wide range of alcohols to ketones with TBHP (80% TBHP in di-*t*-butyl peroxide/water 3:2 solution). Catalysis could be achieved with very low metal loadings (0.5−1 mol %), and these MOF-based catalysts were completely recyclable and reusable [37]. In spite of the fact that 5α-cholestan-3β-ol is too large to diffuse into the pore cage of this catalyst, this steroidal alcohol was also efficiently oxidized with this system and probably the catalysis occurred on the surface of the particles. The oxidation of several alcohols, including cholesterol (**Scheme 1**), was also reported in aqueous conditions using the same oxidant and vanadyl sulfate as catalyst. Noteworthy, after completion of the oxidation and isolation of the product by extraction, the catalyst was recovered in the aqueous layer and reused in a new reaction by simply adding CH_3CN, substrate and TBHP [38]. The immobilization of a $RuCl_3$ complex in an aluminum metal-organic framework (MOF), MOF-253, by post-synthetic modification, afforded an heterogeneous catalyst (MOF-253-Ru) that was used in the oxidation of primary and secondary alcohols with $PhI(OAc)_2$ as the oxidant, under very mild reaction conditions. When applied to 5α-cholestan-3β-ol (**Scheme 1**), a fast and high-yielding reaction was observed and after 4 hours of reaction, the corresponding ketone was obtained in 89% yield. Interestingly, due to the structure of the catalyst, it seems that its pore size is large enough to accommodate this complex substrate. Moreover, the MOF-253-Ru could be successively recycled up to six times without significant loss of activity [39].

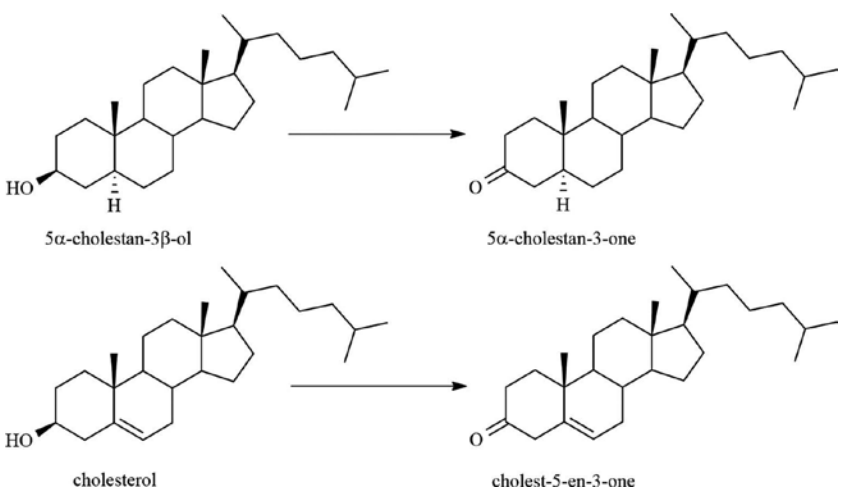

Scheme 1. Oxidation of 5α-cholestan-3β-ol and cholesterol to the corresponding 3-ketone derivatives.

Of high interest in the context of green chemistry is the use of molecular oxygen combined with recoverable and reusable heterogeneous catalysts in the transformation of alcohols to carbonyl compounds. An important example is the use of the heterogeneous Pd catalyst consisting on the palladium(II) acetate-pyridine complex supported on hydrocal-

cite in the aerobic oxidation of 5α-cholestan-3β-ol (**Scheme 1**) by air at atmospheric pressure as the sole oxidant under mild conditions. This catalyst was easily prepared using only commercially available reagents and could be reused several times [40]. Later, diverse nanocatalyts were reported to be effective in this transformation under aerobic conditions. These include gold nanoparticles immobilized in aluminum oxyhydroxide [41] or supported in hydrotalcite [42], and palladium nanoparticles entrapped in aluminum hydroxide [43]. Other steroidal alcohols including 3α-hydroxy-5α-pregnan-20-one and nandrolone were oxidized under aerobic conditions catalyzed by *in situ* generated Pd nanoparticles from $Pd(O_2CCF_3)_2$ and neocuproine. Interestingly, this reaction was performed in aqueous solvent [44]. The use of fluorinated solvents is another relevant strategy in this context not only because they can be recovered and reused, but also because of the fact that the solubilization of oxygen is favored in fluorinated solvents. A relevant example was the aerobic oxidation of 5α-cholestan-3β-ol to 5α-cholestanone by molecular oxygen (**Scheme 1**) in a fluorinated biphasic system composed by perfluorodecalin and toluene, under catalysis by palladium(II) acetate combined with a perfluoroalkylated-pyridine ligand [pyridine-3-carbaldehyde bis(3,3,4,4,5,5,6,6,7,7,8,8,9,9,10,10,10-heptadecafluorodecyl) acetal]. Of high interest is the fact that the fluorinated phase containing the active palladium species was easily separated and reused several times without significant loss of catalytic activity [45].

The use of a readily available organic compound as hydrogen acceptor can provide an interesting alternative to aerobic conditions namely by overcoming safety concerns linked to the use of flammable solvents. A relevant example of this strategy is the use of styrene as hydrogen acceptor in the oxidation of steroidal alcohols such as 3β-hydroxy-5α-androstan-17-one catalyzed by a low loading supported copper catalyst (Cu/Al_2O_3) [46]. More recently, Mitsudome et al. described the successful oxidation of 5α-cholestan-3β-ol to 5α-cholestanone promoted by two different nanocatalysts (**Scheme 1**). These included hydrotalcite-supported copper nanoparticles [47] and hydrotalcite-supported silver nanoparticles [48], which were used in combination with mesitylene or *p*-xylene as hydrogen acceptor, respectively.

Several ionic liquids can be used as compatible supports for or catalyst/reagent immobilization with the advantage of allowing its recovery and recycling. In this context, an organosulfoxide anchored on imidazolium ionic liquid scaffold was used in the oxidation of 5α-cholestan-3β-ol to 5α-cholestanone (**Scheme 1**) in 85% yield, under Swern oxidation conditions. This ionic liquid-supported reagent has the advantages of being non-volatile and odorless but also recoverable and reusable after reoxidation of the sulfide with periodic acid [49]. The oxidation of several alcohols including 5α-cholestan-3β-ol using ion-supported methyl sulfoxides and methyl sulfides through Swern and Corey-Kim reaction conditions, respectively, was also reported. Again, unpleasant odor was not detected in both procedures, and good yields and high purity of the products were achieved after straightforward work-ups. Moreover, the reactants could also be recovered and reused [50]. A similar strategy involved the use of ion-supported (diacetoxyiodo)benzenes (IS-DIB) in the presence of a catalytic amount of 2,2,6,6-tetramethylpiperidine-1-oxy radical (TEMPO) to efficiently transform a large variety of alcohols including 5α-cholestan-3β-ol (**Scheme 1**) under mild conditions. Ion-supported iodobenzenes, the co-products derived from IS-DIB in this oxidation, were recovered in good

http://dx.doi.org/10.5772/62381

yields by a simple extraction and were then re-oxidized with sodium peroxoborate, for reuse in the same transformation [51].

The preparation of oxandrolone intermediates required the oxidation of 17α-methylandrostan-3β,17β-diol, which was accomplished by means of several mild, efficient and eco-friendly oxidizing conditions involving the use of NaOCl or H_2O_2/catalytic Na_2WO_4 under phase transfer conditions [52]. The oxidation of this substrate was also studied using the environmentally benign ionic liquid [bmim][Br] and mild and inexpensive reagent 2-iodoxybenzoic acid (IBX). Interestingly, it was observed that the relative amount of oxidant determined the products obtained. In effect, using 1.2 eq. of IBX, mestanolone was the only product, however, with 2.4 eq., a 1,2-dehydrogenation occurred along with the oxidation to the carbonyl functionality, affording 17β-hydroxy-17α-methyl-Δ^1-androsten-3-one as the major product in a one-pot reaction. Moreover, by simply concentrating the filtrate under reduced pressure, the ionic liquid was recovered and effectively reused up to three times [53].

In addition to the previously described use of fluorinated solvents and ionic liquids, subcritical water may also be useful to replace environmentally unacceptable solvents in numerous organic reactions, including in oxidations of alcohols. This fact results from a dramatic decrease in solvent viscosity and an increase in substrate solubility observed with its use. Similarly to the observed with fluorinated solvents, molecular oxygen has a relevant solubility in subcritical water. In this context, Ozen and Kus reported a metal-free procedure using this solvent in several oxidations, including in the transformation of alcohols to carbonyl compounds. Under these conditions, cholesterol originated cholest-5-en-3-one (**Scheme 1**) in high yields [54].

The use of MW technology for the oxidation of alcohols to the corresponding carbonyl functions was also reported. Among other relevant substrates, diosgenin and cholesterol (**Scheme 1**) were oxidized to their Δ^5-3-ketone derivatives in high isolated yields and after 2 minutes of reaction with pyridinium chlorochromate (PCC) and under MW irradiation [55].

3. Epoxidation

Epoxysteroids, namely several withanolides and oxysterols, exhibit diverse biological activities [34, 35, 56, 57]. In addition, the epoxide functional group has high synthetic interest because the facile ring opening allows the stereoselective introduction of various functionalities into the steroidal nucleus.

Classically, the preparation of epoxysteroids involves the use of peroxacids, such as meta-chloroperoxybenzoic acid (MCPBA), usually originating α-epoxides [58]. The stoichiometric combination of $KMnO_4$ and metal salts, on the other hand, allows the successful selective synthesis of β-epoxides. Steroidal epoxides can also be prepared using other oxidative procedures involving, for example, the use of isolated or *in situ* generated dioxiranes, aziridines and peroxides, frequently combined with adequate promoters. More recently, due to their greener nature, several catalytic epoxidations have been reported as well as various procedures using more environmental friendly oxidants in combination with metal and non-metal

catalysts [34, 35]. For example, new iron- and manganese-based catalysts were recently reported to efficiently epoxidize several unsaturated steroids in combination with H_2O_2 [59–62]. In addition, the possibility of the recovery and reuse of the catalysts as well as the use of alternative solvents were also considered greener approaches to perform this transformation [34, 35].

Stereoselective syntheses of several β-epoxysteroids were described with combinations of oxidant/catalysts including 2,6-dichloropyridine *N*-oxide (DCPNO)/Ru-based catalysts and iodosylbenzene (PhIO)/Mn-porphyrins [34, 35]. In this context, among other interesting and advantageous heterogeneous catalytic procedures, the use of a polymer-supported manganese(III) porphyrin as heterogeneous catalyst and PhIO as oxidant has been reported for the β-selective epoxidation of several Δ^4- and Δ^5-steroids (**Scheme 2**) [63] Similar results were observed using DCPNO as oxidant combined with a ruthenium(II) tetrafluorophenylporphyrin (TFPP) carbonyl complex [Ru(TFPP)CO] covalently attached to functionalized silica [64] or with [Ru^{II}(F20-TPP)CO] (TPP = tetraphenylporphyrin) covalently attached to poly(ethylene glycol) [65]. Other green approach for the effective preparation of 5β,6β-epoxides from Δ^5-steroids (**Scheme 2**) involves the use of O_2 combined with a sacrificial aldehyde (Mukaiyama reaction conditions) and heterogeneous catalysts mainly bearing cobalt as the metal centre [66, 67]. Later, a SiO_2-supported Ru-monomer complex was described as catalyst for the epoxidation of cholesteryl benzoate under similar oxidative conditions [68].

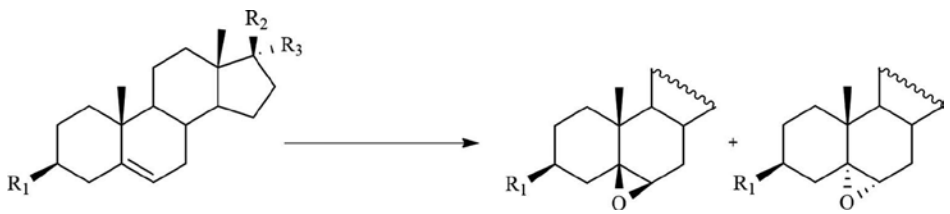

Scheme 2. Epoxidation of Δ^5-steroids affording 5β,6β- and 5α,6α-epoxides.

An alternative strategy to allow the recovery and efficient reuse of the catalysts is their use in perfluorinated compounds to mediate the oxidative reactions, being the fluorinated solvents also recoverable and reusable. Accordingly, it was reported that both 2,4-bisperfluorooctylphenyl butylselenide combined with H_2O_2 [69] and a ruthenium-pyridine-benzimidazole complex bearing perfluorinated 'ponytails' under Mukaiyama reaction conditions [70] catalyzed the epoxidation of various olefins, including 3β-chlorocholest-5-ene in a fluorous biphasic system.

The epoxidation of Δ^5-steroids (**Scheme 2**) mediated by organocatalysts has been reported as an interesting approach to obtain these biological and pharmaceutical interesting steroids avoiding the contamination with metal compounds. A representative example is the regio- and stereoselective epoxidation of cholesteryl benzoate performed with O_2 in the presence of benzhydrol catalyzed by *N*-hydroxyphthalimide (NHPI) and hexafluoroacetone. Among other epoxides, this metal-free aerobic procedure allowed the selective preparation of 5α,6α-

http://dx.doi.org/10.5772/62381

epoxycholesteryl benzoate in moderate yield [71]. Additionally, other 5β,6β-epoxysteroids (**Scheme 2**) were efficiently prepared using chiral ketones [e.g. 1,1,3(*S*),5(*R*)-tetramethyl-4-oxo-2(*R*),6(*S*)-diphenylpiperidinium triflate] as organocatalysts and Oxone™ as oxidant [72]. More recently, Dansey et al. [73] reported the application of a chiral and bulky fructose-derived ketone as catalyst also combined with Oxone™ for the regio- and stereoselective epoxidation of a diene A-homosteroid that occurred in the steroidal A-ring and afforded the corresponding β-epoxide as the only product in 35% yield [73].

The previously referred hexahaloacetones, including hexafluoroacetone, can be used as catalysts in combination with H_2O_2 for the epoxidation of several estra-5(10),9(11)-dienes to obtain the corresponding 5α,10α-epoxy derivatives (**Scheme 3**) as the major reaction products. An improvement of the α:β ratio of isomers to 7:1 was observed in the epoxidation of the substrate 3,3-ethylenedioxo-17α-(1-propynyl)estra-5(10),9(11)-dien-17β-ol using chiral ammonium salts derived from cinchona alkaloids as phase-transfer enantioselective catalysts under similar oxidation conditions [74]. Other oxidative conditions to perform this transformation (**Scheme 3**) used stoichiometric MCPBA or metal catalysts under homogeneous conditions. These included methylrhenium trioxide combined with H_2O_2 or urea-hydrogen peroxide or Fe^{II}-phthalocyanine and PhIO. However, the results were poorer than those observed with the combination of hexahaloacetones and H_2O_2 [75].

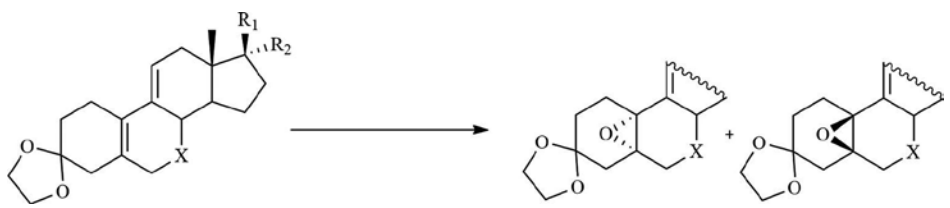

Scheme 3. Regioselective epoxidation of 3,3-ethylenedioxo-$\Delta^{5(10),9(11)}$-steroidal dienes.

Guggulsterones are natural steroids with high potential therapeutic interest namely as hypocholesterolemic agents, and therefore it is important to study their chemical reactivity including under oxidative conditions. For this purpose, the use of H_2O_2 combined with different 5,10,15,20-tetraarylporphyrinatoiron(III)chlorides (e.g., iron(III) 5,10,15,20-tetrakis(2′,6′-dichloro-3′-sulfonatophenyl)porphyrin, [$Cl_8TPPS_4Fe(III)$]) in dichloromethane as well as in the ionic liquid [bmim]BF_4 was evaluated by Singhal and Chauhan. Interestingly, in both solvents the 17,20-epoxide was formed in moderate yields along with minor hydroxylated products and it was observed that the reaction was more effective with *Z*-guggulsterone than its geometric isomer *E*-guggulsterone. In addition, the use of ionic liquid allowed the easy isolation of the products from the reaction mixture, leaving behind the water-soluble iron(III)porphyrin catalyst immobilized in it [76].

A recent and interesting example involving nanotechnologies was reported by Banerjee et al., who developed a heterogeneous Co_xO_y–N/C (x=1,3; y=1,4) catalyst composed by cobalt oxide nanoparticles with varying size along with very few large particles with a metallic Co core and an oxidic shell. This catalyst was applied to efficient epoxidation reactions of aromatic and

aliphatic olefins using TBHP as the terminal oxidant. Interestingly, among the substrates included in the study, only the linear double bond of 20-oxopregn-5-en-3β-yl *trans*-styrylates was epoxidized. This cobalt oxide catalyst can be recycled up to five times without significant loss of activity or change in structure [77].

4. Allylic oxidation

The allylic oxidation allows the synthesis of allylic alcohols, esters, ethers and α,β-unsaturated carbonyl compounds and has attracted interest over the years [78]. In the steroids field, the oxidation of alkenes to the corresponding enones, such as Δ^5-7-ketones (**Scheme 4**), is an important reaction, not only because this functionality can be found in biologically active compounds, namely in the nutraceutical 7-oxodehydroepiandrosterone, but also because of its synthetic interest, associated with the further functionalization of the intact double bond or of the carbonyl group [78–80].

Typically, the oxidation of Δ^5-steroids to Δ^5-7-ketones (**Scheme 4**) has been performed using either chromium(VI) reagents in stoichiometric conditions or with TBHP combined with metal catalysts under homogeneous conditions [34, 35]. Very recently vanadyl acetylacetonate [81] or activated manganese dioxide [82] was explored as interesting catalysts for this reaction, using a 70% aqueous solution of TBHP. In addition, this oxidant was combined with the catalysts NHPI and $Co(OAc)_2$ in another optimized protocol described by Zhao et al. [83] for the regio- and chemoselective allylic oxidation of several functionalized Δ^5-steroids.

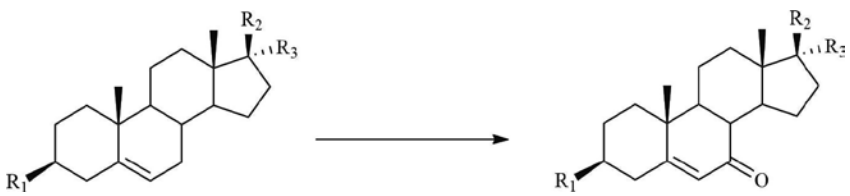

Scheme 4. Allylic oxidation of Δ^5-steroids to Δ^5-7-ketones.

Greener approaches to prepare Δ^5-7-oxosteroids from Δ^5-steroids (**Scheme 4**) involved the use of catalysts immobilized on heterogeneous supports, which may allow their recovery and reuse. In fact, several heterogeneous catalysts including $KMnO_4/SiO_2$ in benzene or chromium(VI) adsorbed on SiO_2/ZrO_2, cobalt(II), copper(II), manganese(II) and vanadium(II) immobilized on silica and $BiCl_3$/montmorillonile K-10 were described for the allylic oxidation of Δ^5-steroids in combination with TBHP as oxidant [34, 84].

The use of recyclable/reusable acetylacetone-metal catalysts modified by a pyridinium salt as co-catalysts in a NHPI-catalyzed oxidation of cholesteryl acetate by molecular oxygen under mild conditions was described. The pyridinium salt interacting with the acetylacetone ligand behaved as an electron-withdrawing group and as a co-catalyst for the decomposition of the alkyl hydroperoxides formed, allowing the relevant isolated yields. Interestingly, the catalyst

http://dx.doi.org/10.5772/62381

$[Co(acac\text{-}py)_2][Cl_2]$ could be easily recovered by a water wash method and reused at least four times with only a slight loss of catalytic activity [85].

Recently, the preparation of multifunctional core-shell nanospheres consisting of a core of metal clusters and an outer microporous silica shell was described. Interestingly, the Pd clusters encapsulated in hybrid core-shell structures exhibit exceptional size-selective catalysis in aerobic allylic oxidations of substrates. In fact, after 60 minutes, conversions of 23.1% and 9.8% were observed for cyclohexene and cholesteryl acetate, respectively, affording mainly allylic oxidation products. These reactivities can be explained by the different sizes of these substrates (cyclohexene ~0.5 nm, cholesteryl acetate ~1.91 nm), which can determine their diffusion to inside the pores of the catalyst [86].

As previously referred, synthetic transformations avoiding the use of toxic and expensive metals are especially attractive for the preparation of compounds that do not tolerate metal contamination such as APIs [87]. A relevant application of this concept was the use of household laundry bleach and aqueous TBHP at sub-ambient temperature for the oxidation of steroidal olefins (**Scheme 4**) and benzylic compounds to α,β-enones. This procedure is not only simple and economical but also has the advantage of using water as solvent [88]. Later, our group described that various Δ^5-steroids could be selectively oxidized to Δ^5-7-ketones (**Scheme 4**) by sodium chlorite associated with NHPI as catalyst in aqueous solvents, achieving good yields [35, 89].

The use of water as solvent was also described in the preparation of several steroidal Δ^4-3,6-diketones from Δ^4-3-ketones (**Scheme 5**) catalyzed by dirhodium caprolactamate $[Rh_2(cap)_4]$ and 70% TBHP in water [90]. This allylic oxidation was also carried out with 5 mol% of CrO_3 as catalyst combined with the same oxidant but using benzotrifluoride as a recoverable fluorous solvent [91].

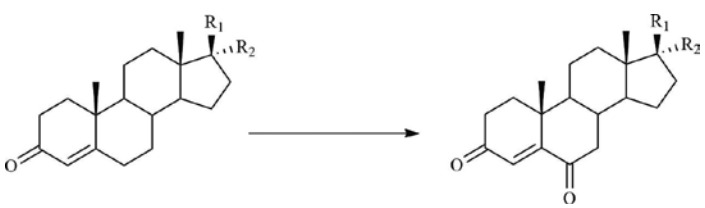

Scheme 5. Allylic oxidation of Δ^4-3-ketone steroids to Δ^4-3,6-diketones.

The oxidation of 3β-cholesteryl benzoate to the corresponding Δ^5-4-ketone derivative was also described involving the same fluorous solvent and perfluorooctylseleninic acid as catalyst along with $PhIO_2$ as oxidant. Interestingly, this catalyst could be recovered by fluorous extraction as bis(perfluorooctyl)diselenide, which served as a catalyst precursor [92].

Alternative energy sources such as light can also be useful in allylic (**Scheme 4**) and benzylic oxidation reactions. In this context, the irradiation of olefins such as cholesteryl acetate with UV light in open flasks in the presence of HgBr or *N*-bromosuccinimide originated the corresponding allylic oxidation products in high yields [93]. More recently, the same trans-

formation was performed by means of a photocatalytic system consisting on the combination of a recoverable graphitic carbon nitride (*g*-C_3N_4) and *N*-hydroxy compounds (e.g., NHPI) to activate O_2. Despite the low to moderate conversions, this mild photocatalytic strategy also has the advantages of avoiding the employment of metal derivatives or organic oxidizing agents [94].

Several electrochemical methods were applied in the oxidation of cholesterol and derivatives affording, namely, allylic acetoxylation or hydroxylation products [95, 96]. In effect, an electrochemical system for the aerobic oxidation of cholesteryl acetate induced by iron picolinate complexes was reported by Okamoto et al. Interestingly, this procedure mainly afforded 7-hydroxylated products with high stereoselectivity (α:β ratio > 100:9), despite relatively low yields [97]. Later, it was described that cholesterol can undergo direct electrochemical oxidation on platinum electrode in glacial acetic acid containing sodium perchlorate and sodium acetate as supporting electrolytes. This preparative electrolysis mainly led to 7α- and 7β-acetoxycholesterol in a 10:3 ratio. These products were also found when sodium acetate was replaced by sodium trifluoroacetate, but the stereoselectivity of the reaction was lost and the yields of the oxidized products were low to moderate [95].

5. Other oxidation reactions

Electrochemical methods were also developed and applied in the halogenation of steroids [96, 98–100], including Δ^5-steroids, to afford 5α,6β-halogenated derivatives that have high biological interest and can be useful in the protection of the double bond in synthetic chemistry. In addition, these procedures can be valuable alternatives to the use of less green reagents namely chlorine gas.

Another important oxidation reaction to which new sustainable procedures have been developed is the Baeyer-Villiger rearrangement [101]. However, within the steroidal field, this reaction is classically performed by means of peroxyacids, such as MCPBA. In this context, the use of MW irradiation to accelerate the oxidation of several steroidal ketones was described. In fact, after few minutes of reaction, the corresponding esters/lactones were successfully obtained (**Scheme 6**) [102]. A more sustainable oxidant used to perform this reaction is H_2O_2 which, in combination with the lipophilic catalyst $Ca[B(C_6F_5)_4]_2$ allowed, for example, the preparation of estrolactone from estrone in 88% yield after 4 hours of reaction [103].

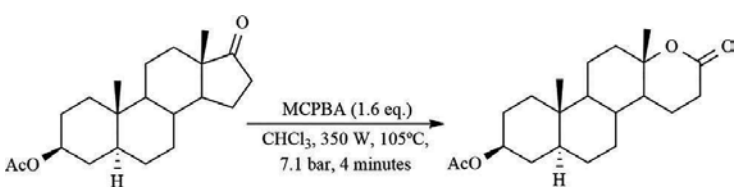

Scheme 6. Baeyer-Villiger oxidation of 17-oxo-5α-androstan-3β-yl acetate by MCPBA under MW.

http://dx.doi.org/10.5772/62381

The dihydroxylation of olefins is an important reaction because the 1,2-diol functionality is present in many synthetic and natural relevant molecules and is a very useful synthetic building block. The most efficient approach for the preparation of steroidal *syn*-diols is the direct dihydroxylation of olefins, [35, 75], whereas the *trans*-dihydroxylation of olefins occurs mainly by epoxidation and hydrolysis [104]. Recently, the Brønsted acid *p*-toluenesulfonic acid (PTSA) was described as a catalyst for the direct *trans*-dihydroxylation of olefins including cholesterol affording the 5α,6β-diol derivative in 56% yield, in aqueous media. This procedure has the advantages of being mild and metal-free and compatible with a considerable range of organic functional groups, and the catalyst could be recycled and reused [105].

Water was also used as solvent in combination with Aliquat 336 and sand for several reactions of very sparingly soluble high melting-point organic substrates, such as steroids. In this system, Aliquat 336 works as both catalyst and solvent, and its efficiency is enhanced by the moving sand under mechanical stirring. This mixture was successfully applied in the good-yield oxidation of pseudosapogenins into 16-dehydropregnenolone acetate and its analogues using H_2O_2 and catalyzed by V_2O_5 [106]. This transformation is of high impact because 16-dehydropregnenolone acetate and similar compounds are important starting materials for the preparation of several semisynthetic steroid drugs [2].

The metal-free oxidation of spironolactone-related sulfides to corresponding sulfoxides and sulfones was performed by the green oxidant H_2O_2 in the presence of the organocatalyst *N*-hydroxysuccinimide (NHS). In this high-yielding process, a full oxidation to sulfones occurred in methanol at room temperature, whereas sulfoxides could be selectively obtained using acetone as solvent under reflux temperature (example in **Scheme 7**). Both processes were compatible with the presence of sensitive groups including ketones, alkenes, hydroxyl groups and benzylic carbons under the described reaction conditions [107].

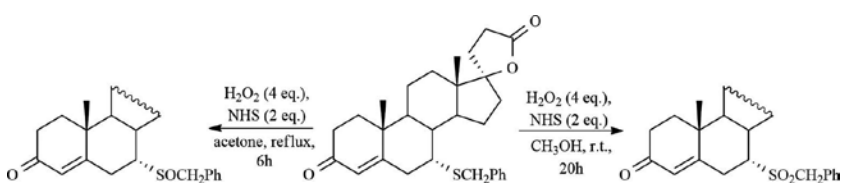

Scheme 7. Organocatalytic oxidation of 7α-(phenylmethylthio)-17-hydroxy-3-oxo-17α-pregn-4-ene-21-carboxylic acid γ-lactone by H_2O_2.

6. Conclusions and future perspectives

Currently, pharmaceutical chemistry is moving towards the incorporation of the sustainable chemistry principles into the development of new reactions and processes. In the oxidation of steroids, however, green approaches are still relatively limited and mostly involving catalytic methods. In addition, the application of nanocatalysts to steroid chemistry has started to emerge.

Considering the importance of sustainability in oxidative process research and development and the biological and synthetic relevance of oxygenated steroid compounds in medicinal chemistry, it is mandatory to increase the efforts to enlarge the scope of the new green chemistry tools, such as novel catalysts, solvents and technologies. Therefore, in the near future, it can be expected an increase in the use of greener solvents, such as water and fluorous solvents. The application of alternative energy sources, including microwaves, sonochemistry and photo irradiation, will contribute to reduce reaction times and overall energy consumption. Furthermore, the continuous replacement of stoichiometric methods by catalytic reactions, preferably avoiding metal catalysts and involving heterogeneous catalysts is also expected.

In spite of some limitations, such as the shape and complexity of steroid compounds, which are responsible for their singular chemo-, regio- and stereoselectivities, their solubility problems and their rigid molecular framework, nanocatalysts, will certainly be increasingly applied in catalytic oxidative processes namely in steroid chemistry.

Acknowledgements

JAR Salvador and MMC Silva thank University of Coimbra and SM Silvestre thanks University of Beira Interior for their financial support.

Author details

Samuel M. Silvestre[1,2], M. Manuel C. Silva[2,3] and Jorge A. R. Salvador[2,3*]

*Address all correspondence to: salvador@ci.uc.pt

1 Health Sciences Research Centre, University of Beira Interior, Covilhã, Portugal

2 Center for Neuroscience and Cell Biology, University of Coimbra, Coimbra, Portugal

3 Pharmaceutical Chemistry Laboratory, University of Coimbra, Coimbra, Portugal

References

[1] Brueggemeier RW, Li P-K. Fundamentals of steroid chemistry and biochemistry. In: Abraham DJ, editor. Burger's Medicinal Chemistry and Drug Discovery, Vol. 3. Cardiovascular Agents and Endocrines. 6th ed. New York: John Wiley & Sons; 2003. pp. 594-627. DOI: 10.1002/0471266949

[2] Lednicer D. Steroid Chemistry at a Glance. Chichester: John Wiley & Sons; 2011. 144 p. DOI: 10.1002/9780470973639

[3] Nicolaou KC, Montagnon T. Steroids & the Pill. In: Nicolaou KC, Montagnon T, editors. Molecules that changed the world. Weinheim: Wiley-VCH; 2008. pp. 79-90. ISBN: 978-3-527-30983-2

[4] Salvador JAR, Carvalho JFS, Neves MAC, Silvestre SM, Leitão AJ, Silva MMC, Sá e Melo, ML. Anticancer steroids: Linking natural and semi-synthetic compounds. Natural Product Reports. 2013; 30(2):324-374.

[5] Hill RA, Kirk DN, Makin HLJ, Murphy GM. Dictionary of Steroids. London: Chapman & Hill; 1991. ISBN-13: 978-0412270604

[6] Moss GP. Nomenclature of steroids (recommendations 1989). Pure & Applied Chemistry. 1989; 61(10):1783-1822.

[7] www.epa.gov/greenchemistry (accessed 29 January 2016).

[8] Dunn PJ. The importance of green chemistry in process research and development. Chemical Society Reviews. 2012; 41:1452-1461.

[9] Tucker JL. Green chemistry: A pharmaceutical perspective. Organic Process Research & Development. 2006; 10:315-319.

[10] Sheldon RA. Fundamentals of green chemistry: Efficiency in reaction design. Chemical Society Reviews. 2012; 41:1437-1451.

[11] Clark JH. Green chemistry: Today (and tomorrow). Green Chemistry. 2006; 8:17-21.

[12] Anastas P, Eghbali N. Green chemistry: Principles and practice. Chemical Society Reviews. 2010; 39:301-312.

[13] Busacca CA, Fandrick DR, Song JJ, Senanayake CH. The growing impact of catalysis in the pharmaceutical industry. Advanced Synthesis & Catalysis. 2011; 353:1825-1864.

[14] Ranu BC, Bhadra S, Saha D. Green recyclable supported-metal catalyst for useful organic transformations. Current Organic Synthesis. 2011; 8:146-171.

[15] Cozzi F. Immobilization of organic catalysts: When, why, and how. Advanced Synthesis & Catalysis. 2006; 348:1367-1390.

[16] Dalko PI, Moisan L. In the golden age of organocatalysis. Angewandte Chemie International Edition. 2004; 43:5138-5175.

[17] Alemán J, Cabrera S. Applications of asymmetric organocatalysis in medicinal chemistry. Chemical Society Reviews. 2013; 42:774-793.

[18] Clouthier CM, Pelletier JN. Expanding the organic toolbox: A guide to integrating biocatalysis in synthesis. Chemical Society Reviews. 2012; 41:1585-1605.

[19] Dahl JA, Maddux BLS, Hutchison JE. Toward greener nanosynthesis. Chemical Reviews. 2007; 107:2228-2269, and references cited therein.

[20] Polshettiwar V, Varma RS. Green chemistry by nano-catalysis. Green Chemistry. 2010; 12:743-754.

[21] Kalidindi SB, Jagirdar BR. Nanocatalysis and prospects of green chemistry. ChemSusChem. 2012; 5:65-75.

[22] Clark JH, Tavener SJ. Alternative solvents: Shades of green. Organic Process Research & Development. 2007; 11:149-155.

[23] Simon M-O, Li C-J. Green chemistry oriented organic synthesis in water. Chemical Society Reviews. 2012; 41:1415-1427.

[24] Hailes HC. Reaction solvent selection: The potential of water as a solvent for organic transformations. Organic Process Research & Development. 2007; 11:114-120.

[25] Siódmiak T, Marszall MP, Proszowska A. Ionic liquids: A new strategy in pharmaceutical synthesis. Mini-Reviews in Organic Chemistry. 2012; 9:203-208.

[26] Chowdhury S, Mohan RS, Scott JL. Reactivity of ionic liquids. Tetrahedron. 2007; 63:2363-2389.

[27] Fish RH. Fluorous biphasic catalysis: A new paradigm for the separation of homogeneous catalysts from their reaction substrates and products. Chemistry: A European Journal. 1999; 5:1677-1680.

[28] Cole-Hamilton DJ. Asymmetric catalytic synthesis of organic compounds using metal complexes in supercritical fluids. Advanced Synthesis & Catalysis. 2006; 348:1341-1351.

[29] Leitner W. Supercritical carbon dioxide as a green reaction medium for catalysis. Accounts of Chemical Research. 2002; 35:746-756.

[30] Baig RBN, Varma RS. Alternative energy input: Mechanochemical, microwave and ultrasound-assisted organic synthesis. Chemical Society Reviews. 2012; 41:1559-1584.

[31] Kappe CO, Pieber B, Dallinger D. Microwave effects in organic synthesis: Myth or reality?. Angewandte Chemie International Edition. 2013; 52:1088-1094.

[32] Mason TJ. Ultrasound in synthetic organic chemistry. Chemical Society Reviews. 1997; 26:443-451.

[33] Hoffmann N. Photochemical reactions as key steps in organic synthesis. Chemical Reviews. 2008; 108:1052-1103.

[34] Salvador JAR, Silvestre SM, Moreira VM. Catalytic oxidative processes in steroid chemistry: Allylic oxidation, beta-selective epoxidation, alcohol oxidation and remote functionalization reactions. Current Organic Chemistry. 2006; 10(17):2227-2257.

[35] Salvador JAR, Silvestre SM, Moreira VM. Recent developments in oxidative processes in steroid chemistry. Current Organic Chemistry. 2012; 16(10):1243-1276.

[36] Lounis Z, Riahi A, Djafri F, Muzart J. Chromium-exchanged zeolite (Cr-E-ZSM-5) as catalyst for alcohol oxidation and benzylic oxidation with *t*-BuOOH. Applied Catalysis A-General. 2006; 309(2):270-272.

[37] Fei H, Shin J, Meng YS, Adelhardt M, Sutter J, Meyer K, Cohen SM. Reusable oxidation catalysis using metal-monocatecholato species in a robust metal–organic framework. Journal of the American Chemical Society. 2014; 136:4965-4973.

[38] Sarmah G, Bharadwaj SK, Dewan A, Gogoi A, Bora U. An efficient and reusable vanadium based catalytic system for room temperature oxidation of alcohols to aldehydes and ketones. Tetrahedron Letters. 2014; 55:5029-5032.

[39] Carson F, Agrawal S, Gustafsson M, Bartoszewicz A, Moraga F, Zou X, Martín-Matute B. Ruthenium complexation in an aluminium metal-organic framework and its application in alcohol oxidation catalysis. Chemistry-A European Journal. 2012; 18:15337-15344.

[40] Kakiuchi N, Maeda Y, Nishimura T, Uemura S. Pd(II)-hydrotalcite-catalyzed oxidation of alcohols to aldehydes and ketones using atmospheric pressure of air. Journal of Organic Chemistry. 2001; 66:6620-6625.

[41] Kim S, Bae SW, Lee JS, Park J. Recyclable gold nanoparticle catalyst for the aerobic alcohol oxidation and C-C bond forming reaction between primary alcohols and ketones under ambient conditions. Tetrahedron. 2009; 65(7):1461-1466.

[42] Mitsudome T, Noujima A, Mizugaki T, Jitsukawa K, Kaneda K. Efficient aerobic oxidation of alcohols using a hydrotalcite-supported gold nanoparticle catalyst. Advanced Synthesis & Catalysis. 2009; 351(11-12):1890-1896.

[43] Kwon MS, Kim N, Park CM, Lee JS, Kang KY, Park J. Palladium nanoparticles entrapped in aluminum hydroxide: Dual catalyst for alkene hydrogenation and aerobic alcohol oxidation. Organic Letters. 2005; 7(6):1077-1079.

[44] Mifsud M, Parkhomenko KV, Arends IWCE, Sheldon RA. Pd nanoparticles as catalysts for green and sustainable oxidation of functionalized alcohols in aqueous media. Tetrahedron. 2010; 66(5):1040-1044.

[45] Nishimura T, Maeda Y, Kakiuchi N, Uemura S. Palladium(II)-catalysed oxidation of alcohols under an oxygen atmosphere in a fluorous biphase system (FBS). Journal of the Chemical Society-Perkin Transactions 1. 2000; (24):4301-4305.

[46] Zaccheria F, Ravasio N, Psaro R, Fusi A. Synthetic scope of alcohol transfer dehydrogenation catalyzed by Cu/Al_2O_3: A new metallic catalyst with unusual selectivity. Chemistry-A European Journal. 2006; 12(24):6426-6431.

[47] Mitsudome T, Mikami Y, Ebata K, Mizugaki T, Jitsukawa K, Kaneda K. Copper nanoparticles on hydrotalcite as a heterogeneous catalyst for oxidant-free dehydrogenation of alcohols. Chemical Communications. 2008; (39):4804-4806.

[48] Mitsudome T, Mikami Y, Funai H, Mizugaki T, Jitsukawa K, Kaneda K. Heterogeneous catalysis – Oxidant-free alcohol dehydrogenation using a reusable hydrotalcite-supported silver nanoparticle catalyst. Angewandte Chemie-International Edition. 2008; 47(1):138-141.

[49] He X, Chan TH. New non-volatile and odorless organosulfur compounds anchored on ionic liquids. Recyclable reagents for Swern oxidation. Tetrahedron. 2006; 62(14): 3389-3394.

[50] Tsuchiya D, Tabata M, Moriyama K, Togo H. Efficient Swern oxidation and Corey-Kim oxidation with ion-supported methyl sulfoxides and methyl sulfides. Tetrahedron. 2012; 68(34):6849-6855.

[51] Suzuki Y, Iinuma M, Moriyama K, Togo H. TEMPO-mediated oxidation of alcohols with ion-supported (Diacetoxyiodo)benzenes. Synlett. 2012; 23:1250-1256.

[52] Ginotra SK, Chhikara BS, Singh M, Chandra R, Tandon V. Efficient oxidizing methods for the synthesis of oxandrolone intermediates. Chemical & Pharmaceutical Bulletin. 2004; 52(8):989-991.

[53] Chhikara BS, Chandra R, Tandon V. IBX in an ionic liquid: Eco-friendly oxidation of 17α-methylandrostan-3β,17β-diol, an intermediate in the synthesis of anabolic oxandrolone. Tetrahedron Letters. 2004; 45(41):7585-7588.

[54] Ozen R, Kus NS. Oxidation of alcohols to carbonyl compounds, benzylic carbons to their ketones, and arenes to their quinones with molecular oxygen in subcritical water. Monatshefte Fur Chemie. 2006; 137(12):1597-1600.

[55] Chakraborty V, Bordoloi M. Microwave-assisted oxidation of alcohols by pyridinium chlorochromate. Journal of Chemical Research. 1999; (2):118-119.

[56] Guardiola F, Dutta PC, Codony R, Savage GP, editors. Cholesterol and Phytosterol Oxidation Products: Analysis, Occurrence, and Biological Effects. Champaign: AOCS Press; 2002. 394 p. ISBN: 9781439822210

[57] Kadis B. Steroid epoxides in biologic systems – Review. Journal of Steroid Biochemistry. 1978; 9(1):75-81.

[58] Matthews GJ, Hassner A. Synthesis of oxiranes, aziridines and episulfides. In: Fried J, Edwards JA, editors. Organic Reactions in Steroid Chemistry. New York: Van Nostrand Reinold Company; 1972. Vol. 2, pp. 1-21. ISBN: 13: 978-0442783396.

[59] Clemente-Tejeda D, Lopez-Moreno A, Bermejo FA. Oxidation of unsaturated steroid ketones with hydrogen peroxide catalyzed by Fe(bpmen)$(OTf)_2$. New methodology to

access biologically active steroids by chemo-, and stereoselective processes. Tetrahedron. 2012; 68:9249-9255.

[60] Clemente-Tejeda D, Bermejo FA. Oxidation of alkenes with non-heme iron complexes: Suitability as an organic synthetic method. Tetrahedron. 2014; 70:9381-9386.

[61] Bruyneel F, Letondor C, Basturk B, Gualandi A, Pordea A, Stoeckli-Evans H, Neier R. Catalytic epoxidation of alkenes by the manganese complex of a reduced porphyrinogen macrocycle. Advanced Synthesis & Catalysis. 2012; 354:428-440.

[62] Cussó O, Garcia-Bosch I, Font D, Ribas X, Lloret-Fillol J, Costas M. Highly stereoselective epoxidation with H_2O_2 catalyzed by electron-rich aminopyridine manganese catalysts. Organic Letters. 2013; 15(24):6158-6161.

[63] Du CP, Li ZK, Wen XM, Wu J, Yu XQ, Yang M, Xie RG. Highly diastereoselective epoxidation of cholest-5-ene derivatives catalyzed by polymer-supported manganese(III) porphyrins. Journal of Molecular Catalysis A-Chemical. 2004; 216(1):7-12.

[64] Zhao YC, Xiang YZ, Pu L, Yang M, Yu XQ. Highly β-selective epoxidation of the Δ^5- and Δ^4-unsaturated steroids catalyzed by the silica-supported polyhalogenated ruthenium porphyrin. Applied Catalysis A-General. 2006; 301(2):176-181.

[65] Zhang JL, Huang JS, Che CM. Oxidation chemistry of poly(ethylene glycol)-supported carbonylruthenium(II) and dioxoruthenium(VI) meso-tetrakis(pentafluorophenyl)porphyrin. Chemistry-A European Journal. 2006; 12(11):3020-3031.

[66] Dhar D, Koltypin Y, Gedanken A, Chandrasekaran S. Catalytic aerobic epoxidation of olefins by nanostructured amorphous CoO-MCM-41. Catalysis Letters. 2003; 86(4): 197-200.

[67] Silvestre SM, Salvador JAR, Clark JH. β-Selective epoxidation of Δ^5-steroids by O_2 using surface functionalised silica supported cobalt catalysts. Journal of Molecular Catalysis A-Chemical. 2004; 219(1):143-147.

[68] Tada M, Muratsugu S, Kinoshita M, Sasaki T, Iwasawa Y. Alternative selective oxidation pathways for aldehyde oxidation and alkene epoxidation on a SiO_2-supported Ru-monomer complex catalyst. Journal of the American Chemical Society. 2010; 132(2):713-724.

[69] Betzemeier B, Lhermitte F, Knochel P. A selenium catalyzed epoxidation in perfluorinated solvents with hydrogen peroxide. Synlett. 1999; (4):489-491.

[70] Ragagnin G, Knochel P. Aerobic Ru-catalyzed epoxidations in fluorous biphasic system using new fluorous benzimidazolic ligands. Synlett. 2004; (6):951-954.

[71] Iwahama T, Sakaguchi S, Ishii Y. Epoxidation of alkenes using dioxygen in the presence of an alcohol catalyzed by *N*-hydroxyphthalimide and hexafluoroacetone without any metal catalyst. Chemical Communications. 1999; (8):727-728.

[72] Yang D, Jiao GS. Highly β-selective epoxidation of Δ^5-unsaturated steroids catalyzed by ketones. Chemistry-a European Journal. 2000; 6(19):3517-3521.

[73] Dansey MV, Di Chenna PH, Veleiro AS, Kristofikova Z, Chodounska H, Kasal A, Burton G. Synthesis and $GABA_A$ receptor activity of A-homo analogues of neuroactive steroids. European Journal of Medicinal Chemistry. 2010; 45(7):3063-3069.

[74] Yang Y-X, Li Z, Chen G-R, Li Y-C. Phase-transfer catalysed enantioselective epoxidation of estra-$\Delta^{5(10),9(11)}$-diene using chiral ammonium salts derived from cinchona alkaloids. Letters in Organic Chemistry. 2010; 7:163-167.

[75] Salvador JAR, Silvestre SM, Moreira VM. Catalytic epoxidation and *syn*-dihydroxylation reactions in steroid chemistry. Current Organic Chemistry. 2008; 12(6):492-522.

[76] Singhal A, Chauhan SMS. Biomimetic oxidation of guggulsterone with hydrogen peroxide catalyzed by iron(III) porphyrins in ionic liquid. Catalysis Communications. 2012; 25:28-31.

[77] Banerjee D, Jagadeesh RV, Junge K, Pohl M-M, Radnik J, Bruckner A, Beller M. Convenient and mild epoxidation of alkenes using heterogeneous cobalt oxide catalysts. Angewandte Chemie-International Edition. 2014; 53:4359-4363.

[78] Bulman Page PC, McCarthy TJ. Oxidation adjacent to C=C Bonds. In: Trost BM, Flemming I, chief editors; Ley SV, volume editor. Comprehensive Organic Synthesis. Oxford-New York-Seoul-Tokyo: Pergamon Press; 1991. Vol. 7, pp. 83-117. ISBN: 0-08-040598-3.

[79] Arsenou ES, Fousteris MA, Koutsourea AI, Nikolaropoulos SS. 7-keto-Δ^5-steroids: Key-molecules owning particular biological and chemical interest. Mini Reviews in Medicinal Chemistry. 2003; 3(6):557-567.

[80] Parish EJ, Kizito SA, Qiu ZH. Review of chemical syntheses of 7-keto-Δ^5-sterols. Lipids. 2004; 39(8):801-804.

[81] Grainger WS, Parish EJ. Allylic oxidation of steroidal olefins by vanadyl acetylacetonate and *tert*-butyl hydroperoxide. Steroids. 2015; 101:103-109.

[82] Serra S. MnO_2/TBHP: A versatile and user-friendly combination of reagents for the oxidation of allylic and benzylic methylene functional groups. European Journal of Organic Chemistry. 2015; (29): 6472-6478.

[83] Zhao Q, Qian C, Chen X-Z. N-Hydroxyphthalimide catalyzed allylic oxidation of steroids with *t*-butyl hydroperoxide. Steroids. 2015; 94:1-6.

[84] Salvador JAR, Silvestre SM. Bismuth-catalyzed allylic oxidation using *t*-butyl hydroperoxide. Tetrahedron Letters. 2005; 46(15):2581-2584.

[85] Zhang P, Wang C, Chen Z, Li H. Acetylacetone-metal catalyst modified by pyridinium salt group applied to the NHPI-catalyzed oxidation of cholesteryl acetate. Catalysis Science & Technology. 2011; 1(7):1133-1137.

[86] Qiao Z-A, Zhang P, Chai S-H, Chi M, Veith GM, Gallego NC, Kidder M, Dai S. Lab-in-a-shell: Encapsulating metal clusters for size sieving catalysis. Journal of the American Chemical Society. 2014; 136:11260-11263.

[87] Adam W, Saha-Moller CR, Ganeshpure PA. Synthetic applications of nonmetal catalysts for homogeneous oxidations. Chemical Reviews. 2001; 101(11):3499-3548.

[88] Marwah P, Marwah A, Lardy HA. An economical and green approach for the oxidation of olefins to enones. Green Chemistry. 2004; 6(11):570-577.

[89] Silvestre SM, Salvador JAR. Allylic and benzylic oxidation reactions with sodium chlorite. Tetrahedron. 2007; 63(11):2439-2445.

[90] McLaughlin EC, Choi H, Wang K, Chiou G, Doyle MP. Allylic oxidations catalyzed by dirhodium caprolactamate via aqueous *tert*-butyl hydroperoxide: The role of the *tert*-butylperoxy radical. Journal of Organic Chemistry. 2009; 74(2):730-738.

[91] Boitsov S, Riahi A, Muzart J. Chromium(VI) oxide-catalysed oxidations by *tert*-butyl hydroperoxide using benzotrifluoride as solvent. Comptes Rendus de l'Académie des Sciences - Series IIC – Chemistry. 2000; 3(9):747-750.

[92] Crich D, Zou YK. Catalytic allylic oxidation with a recyclable, fluorous seleninic acid. Organic Letters. 2004; 6(5):775-777.

[93] Friedman N, Gorodets M, Mazur Y. Photo-oxidations of olefins and benzene derivatives. Journal of the Chemical Society D-Chemical Communications. 1971; (15):874.

[94] Zhang P, Wang Y, Yao J, Wang C, Yan C, Antonietti M, Li H. Visible-light-induced metal-free allylic oxidation utilizing a coupled photocatalytic system of *g*-C3N4 and *N*-Hydroxy compounds. Advanced Synthesis & Catalysis. 2011; 353(9):1447-1451.

[95] Kowalski J, Ploszynska J, Sobkowiak A, Morzycki JW, Wilczewska AZ. Direct electrochemical acetoxylation of cholesterol at the allylic position. Journal of Electroanalytical Chemistry. 2005; 585(2):275-280.

[96] Morzycki JW, Sobkowiak A. Electrochemical oxidation of cholesterol. Beilstein Journal of Organic Chemistry. 2015; 11:392-402.

[97] Okamoto I, Funaki W, Nakaya K, Kotani E, Takeya T. A new electrochemical system for stereoselective allylic hydroxylation of cholesteryl acetate with dioxygen induced by iron picolinate complexes. Chemical & Pharmaceutical Bulletin. 2004; 52(6):756-759.

[98] Maki S, Konno K, Ohba S, Takayama H. Stereoselective chlorination of steroidal 5,6-olefin by an electrochemical method; A convenient synthesis of blattelastanoside B. Tetrahedron Letters. 1998; 39(21):3541-3542.

[99] Milisavljević S, Vukićević RD. Electrochemical chlorination of some 5-unsaturated steroids. Journal of the Serbian Chemical Society. 2004; 69 (11):941-947.

[100] Milisavljević S, Wurst K, Laus G, Vukićević MD, Vukićević RD. Electrochemical bromination of cholest-5-enes. Steroids. 2005; 70:867-872.

[101] ten Brink GJ, Arends I, Sheldon RA. The Baeyer-Villiger reaction: New developments toward greener procedures. Chemical Reviews. 2004;104,(9):4105-4123.

[102] Borah JM, Chowdhury P. Expedited Baeyer-Villiger oxidation of steroidal ketones by microwave irradiation. Steroids. 2011; 76(12):1341-1345.

[103] Uyanik M, Nakashima D, Ishihara K. Baeyer–Villiger oxidation and oxidative cascade reactions with aqueous hydrogen peroxide catalyzed by lipophilic $Li[B(C_6F_5)_4]$ and $Ca[B(C_6F_5)_4]_2$. Angewandte Chemie - International Edition. 2012; 51:9093-9096.

[104] Yudin AK, editor. Aziridines and epoxides in organic synthesis. Weinheim: Wiley-VCH; 2006. 516 p. ISBN: 978-3-527-31213-9

[105] Rosatella AA, Afonso CAM. Brønsted acid-catalyzed dihydroxylation of olefins in aqueous medium. Advanced Synthesis & Catalysis. 2011; 353(16):2920-2926.

[106] Cui X, Li B, Liu T, Li C. A practical solution for aqueous reactions of water-insoluble high-melting-point organic substrates. Green Chemistry. 2012; 14(3):668-672.

[107] Xiong Z-G, Zhang J, Hu X-M. Selective oxidation of spirolactone-related sulfides to corresponding sulfoxides and sulfones by hydrogen peroxide in the presence of *N*-hydroxysuccinimide. Applied Catalysis A-General. 2008; 334(1-2):44-50.

Chapter 3

Metal Complexes Immobilized on Magnetic Nanoparticles

Seyed Mohsen Sadeghzadeh and Mehdi Mogharabi

Additional information is available at the end of the chapter

http://dx.doi.org/10.5772/61585

Abstract

The reusability of valuable catalysts in organic reaction without change in properties is known as an important feature in the evolution of green processes. The imobilization of metal catalysts on magnetic nanoparticles makes them recoverable and can be used as building blocks for the fabrication of various functional systems, which are applied in several fields such as catalysis, environmental remediation magnetic resonance imaging, data storage, and biotechnology. Applying magnetic nanoparticles in organic reaction as a scaffold for the immobilization of metal complexes is reviewed as well as the improvement of the methods of production and applying catalysts with magnetic properties in organic reaction.

Keywords: Recyclable catalyst, superparamagnetic nanoparticle, nanocatalyst, recyclable support matrix, magnetic separation

1. Introduction

The concept of "green chemistry" has emerged as one of the main principles of environmentally benign organic synthesis approaches. Using nanoparticles (NPs) in organic synthesis has become a subject of intense investigation. In particular, magnetic nanoparticles (MNPs) offer several advantages in clean and sustainable chemistry such as nontoxic effects, readily accessible, and retrievable. In addition, the activity and selectivity of magnetic nanocatalysts can be manipulated surface modification.

2. Green and sustainable catalysis

Green and sustainable chemistry is a philosophy of chemical research and engineering that encourages the design of products and processes, minimizing the use and generation of hazardous materials. Green catalysis as a subchapter of green chemistry but probably the most important one is associated with the synthetic protocols and reaction conditions, which plays a pivotal role in recent years toward the goal of switching to increasingly efficient and benign processes avoiding the use of volatile organic solvents, toxic reagents, hazardous and/or harsh reaction conditions, as well as challenging and time-consuming wasteful separations. Among the various principles of green chemistry, the use of alternative energy sources, benign solvents, and efficient reusable catalytic materials are contributed to the development of greener synthetic methods for a wide range of applications related to medicine, the environment, and nanoscience. In this sense, the search for environmentally benign, sustainable, and efficiently reusable alternative catalytic systems has become critical [1].

3. Homogeneous and heterogeneous catalysis

Catalysts are broadly divided into two types: homogeneous and heterogeneous. In a homogeneous catalysis, the active sites and the reactants are in the same phase, which allows for easier interaction between the components leading to better action. Homogeneous ones have other advantages such as high selectivities, high turnover numbers, and effortless optimization of activity. It is also possible to control the chemo-, regio-, and enantioselectivity of product by adapting the active molecules.

These catalysts are widely used in industrial processes, but the separation of the final product is one of the most important drawbacks of homogeneous types. After separation the homogeneous catalyst from the reaction mixture, trace amounts of are likely remains in the final product. It is essential to remove the catalyst completely and avoiding metal contamination in final products especially in the food and pharmaceutical industry. One efficient way to overcome this is the immobilization on the heterogeneous supports. Heterogenization is commonly achieved by entrapment or grafting of the active molecules on surfaces or inside the pores of a solid support such as silica, alumina, or ceria. Grafting can be achieved by covalent binding or by simple adsorption of the active catalytic molecules, but covalent binding is preferred because of it is sufficiently robust to survive the harsh reaction conditions; this binding and adsorption process not only minimizes catalyst leaching but also allows the reusability of catalyst. However, the active sites in heterogeneous catalysts are not as accessible as in a homogeneous system, and thus the activity of the catalyst may be reduced. There are many attempts to make all active sites on solid supports available for reactions, but only sites on the external surface of a porous solid support are available for reaction, and thus the overall reactivity of the catalyst system decreases. Consequently, we need a system that not only shows high activity and selectivity but also possesses the ease of separation and recovery. These goals can be achieved by nanocatalysis. Nanocatalysts bridge the gap between homogeneous and heterogeneous catalysts, preserving the desirable attributes of both systems [2].

http://dx.doi.org/10.5772/61585

4. Nanocatalysis

Nanoparticles have emerged as sustainable alternatives to conventional materials. The nanosized particles increase the exposed surface area of the component of the catalyst and enhance the contact between reactants and catalyst dramatically and mimic the homogeneous catalysts. However, their insolubility in reaction solvents makes them easily separable from the reaction mixture, which in turn makes the product isolation stage effortless. In addition, the selectivity of nanocatalyst can be manipulated by tailoring chemical and physical properties such as size, shape, composition, and morphology. One challenge is the synthesis of specific size and shape of nanocatalysts to allow the easy movement of materials in the reacting phase and control over the morphology of nanostructures to tailor their physical and chemical properties. However, the rapid advancement of nanotechnology made possible the preparation of a variety of nanoparticles with controlled size, shape, morphology, and composition [3].

5. Magnetic nanocatalysts

Nanocatalysts possess some advantages over conventional systems; however, the isolation and recovery of these nanocatalysts from the reaction mixture is not so easy, and conventional filtration methods are not efficient because of the nanosize of the catalyst. To overcome such limitations, the use of magnetic nanosupport has emerged as one of the best alternatives; their insoluble and paramagnetic nature enables easy and efficient separation of the catalysts from the reaction mixture with an external magnet. In addition, the design of the materials that are specifically needed for a particular application is possible by the control of properties, including size, shape, morphology, and dispersity. The isolation and separation of magnetic nanoparticle-supported catalysts can be achieved using an external magnet, thus offering a promising option that can meet the requirements of high accessibility with improved reusability [4]. Catalyst recovery and reusability are the two most important features for many catalytic processes; most heterogeneous systems require a filtration or centrifugation step or a time-consuming workup of the final reaction mixture to recover them, while magnetically supported nanocatalysts can be recovered with an external magnet.

5.1. Synthesis of magnetic catalysts

There are several protocols reported in the literature for preparing a wide variety of catalytic magnetic materials, some of them are discussed in the following sections. It is important to note that the practicality and cost-effectiveness of these processes have a direct effect on the sustainability of the catalytic protocols based on these materials.

5.2. Carbonaceous magnetic materials

Magnetic carbon nanoparticles were obtained from the carbonization of iron-doped polypyrrole nanoparticles [5, 6]. Carbonization was performed at 800°C and yielded microporous carbonaceous nanomaterials with approximately 4–5 wt% nitrogen. Palladium nanoparticles were subsequently deposited onto the surface of the microporous carbon using a conventional

impregnation/deposition methodology and using $Pd(NO_3)_2$ as a metal precursor in aqueous media. The synthesized material possesses a remarkably high palladium content that is comprised of homogeneously and well-dispersed PdNP on the porous surface, with a reasonably narrow particle size distribution. Carbonaceous materials and a carbon black are prepared by thermal decomposition of methane using dc thermal plasma processing, provided poorly dispersed Pd NP on the material surface [6]. Zhu et al. [7] prepared magnetic porous carbon microspheres via carbonization of chitosan microspheres containing iron precursors (a negatively charged iron oxalate) that were absorbed due to the cationic and swelling properties of chitosan. In general, this biomass-derived material possessed large surface areas and good magnetic separation properties. Interestingly, Fe Mossbauer spectroscopic experiments indicated that the temperature of carbonization affected the type of Fe species observed in the sample [8]. Thus, samples calcinated at 700°C contained γ-Fe_2O_3, Fe_3C, and α-Fe, whereas samples carbonized at 900°C and 1000°C exhibited peaks that indicated Fe_3C and α-Fe. It was claimed to result from the reaction of maghemite with carbon and subsequent decomposition into metallic Fe. Because of these promising features and the potential adsorption properties of carbon, high temperature calcinated materials were tested for the adsorption of potential pollutants in aqueous solutions. A relatively similar magnetically ordered mesoporous carbon containing super paramagnetic FePt NP [7] was prepared via a simple nanocasting route, with polyfurfuryl alcohol formed after polymerization of furfural in the channels of a mesoporous silica employed as a hard template [8] and FePt sources introduced in the framework of PFA through incipient wetness impregnation. Subsequent thermal treatment of the material in argon at 700°C and extraction of the silica rendered template-free mesoporous FePt/C materials with large surface areas and important adsorption properties.

5.3. Metal oxide-derived magnetic materials

A range of novel materials based on titanium silicate mesoporous solids have been recently reported by Barmatova et al. [9, 10]. These materials were prepared following the so-called solid core-mesoporous shell morphology synthetic approach, originally developed by Yoon et al. [11]. The novel materials composed of quasi-spherical particles covered by a titanium silicate mesoporous shell containing isolated Ti atoms were modified by previously synthesized magnetic nanoparticles. According to physicochemical studies, these iron oxide NPs were stabilized within the particle core, and thus they did not interfere with the catalytic application such as selective oxidation processes. Wang et al. [12] recently reported a facile chemical route to these interesting materials, which have photocatalytic applications. These hybrid nanoparticles have been reported to be spherical, 100 nm in diameter, and decorated with several Fe_2O_3 particles as cores distributed within the titania matrix. The silica layers intercalated between magnetic cores and titania shells. Similarly, Xu et al. [13] recently reported the preparation of a visible-light active $TiO_2/ZnFe_2O_4$ photocatalyst via conventional liquid-phase transformation using the sol-gel method. The formation of highly dispersed zinc ferrite nanoparticles (less than 5 nm in size, with imperfect crystallization) on the TiO_2 material prevented the formation of the rutile phase to some extent. The advantage of this material was the coupling of the relatively narrow band gap for $ZnFe_2O_4$ (light absorbing semiconductor) and the wide band gap of titania resulting in a semiconductor system with an enhanced

http://dx.doi.org/10.5772/61585

primary charge separation and photocatalytic activity under visible light irradiation. A magnetically recoverable material composed of palladium nanoparticles supported on hydroxyapatite-encapsulated maghemite nanocrystallites (Pd-HAP-γ-Fe_2O_3) was also reported in the dehalogenation of organic compounds with molecular hydrogen [14]. Pd deposition on the magnetic support was achieved via simple impregnation with a solution of $PdCl_2(PhCN)_2$ in acetone. Monomeric $PdCl_2$ species were grafted by chemisorption onto the PdO groups of the support, which were subsequently reduced under H_2 atmosphere to give Pd metallic MNP [15, 16]. The synthesized catalyst were used in the dechlorination of 4-chlorophenol as a model compound, with quantitative yields to products obtained in 40 min [17].

5.4. Polymer-derived magnetic materials

Polymer-derived Fe_3O_4-polyaniline-Au magnetic nanocomposites have been prepared via a two-step process [18]. In the first step, a super paramagnetic Fe_3O_4-polyaniline (PANI) with a well-defined core-shell nanostructure was synthesized using an ultrasound-assisted in situ surface polymerization method. Aniline monomers were added to an aqueous solution of carboxylic acid-functionalized Fe_3O_4 microspheres and partially reacted with the surface carboxylic groups to generate $COO^-H_3N^+$, followed by aniline polymerization [19] on the surface of particle to form the mono-dispersed Fe_3O_4-PANI core/shell structure [20]. Negatively charged discrete Au nanoparticles with particle sizes of approximately 4 nm were effectively loaded onto the positively charged magnetic support surface by electrostatic attraction. These materials were found to be catalytically active in the reduction of rhodamine B using $NaBH_4$ as a reducing agent.

6. Catalyst and application

Catalysts can be loaded onto MNP either by modification of MNP shells or by coprecipitation during the MNP synthesis, in which the functional ligands also act as stabilizers [21]. Zhu and coworkers [22] successfully immobilized the second-generation Hoveyda–Grubbs catalyst over MNPs (Scheme 1) by using the surface-modification strategy. In this procedure, commercially available MNPs were coated with orthoisopropoxystyrene ligands by covalent bonds. The reaction of the supported ligands with the second-generation Grubbs catalyst formed the supported Hoveyda–Grubbs catalyst, which displayed high activity for both self- and cross-metathesis of methyl oleate (MO).

Polshettiwar et al. [23] used silica coated nanoferrite for the synthesis of magnetically retrievable ruthenium–arene–PTA complexes (Scheme 2) and developed a simple strategy to modify a catalyst that worked efficiently for the hydration of nitriles and various isomerization reactions in aqueous media.

Philip D. Stevens and coworkers reported the use of superparamagnetic nanoparticles (Scheme 3) as a new type of matrices for supporting catalytic homogeneous Suzuki, Heck, and Sonogashira cross-coupling reactions (Scheme 4).

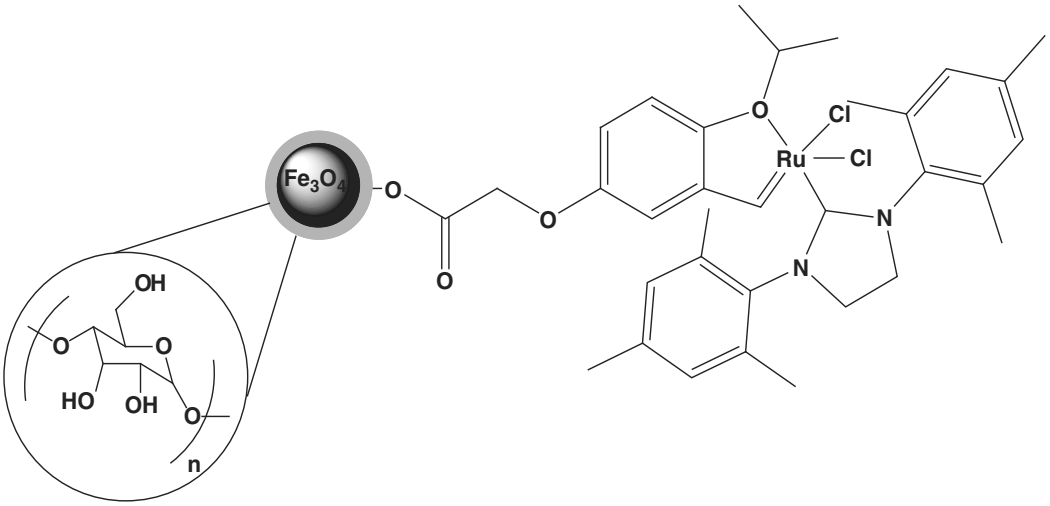

Scheme 1. Synthesis of magnetic Hoveyda–Grubbs catalyst.

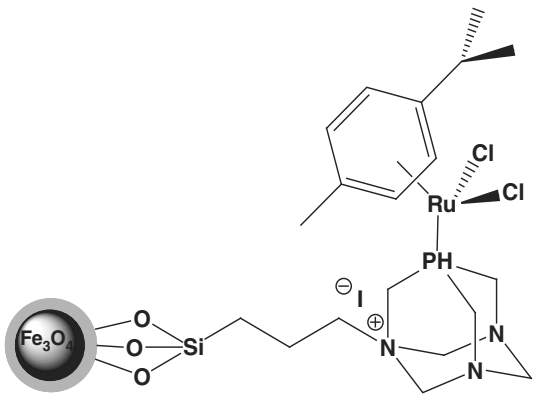

Scheme 2. Magnetically retrievable ruthenium–arene–PTA (RAPTA) complex.

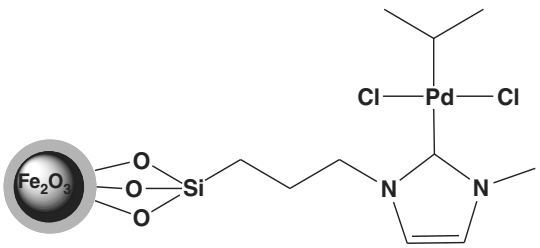

Scheme 3. Structures of maghemite nanoparticle-supported polystyrene (PS) resin-supported NHC–Pd catalyst (solid phase–Pd).

http://dx.doi.org/10.5772/61585

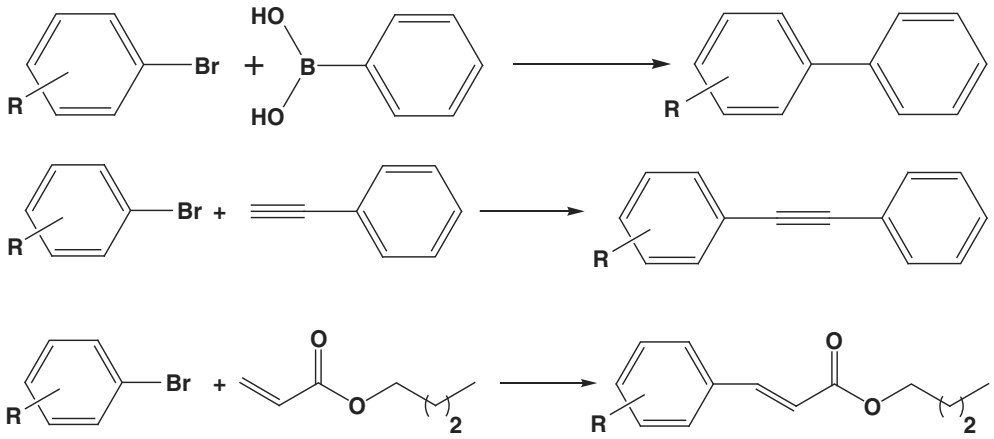

Scheme 4. Supporting catalytic homogeneous Suzuki, Heck, and Sonogashira cross-coupling reactions.

Gao et al. [24] also developed an emulsion polymerization methodology as a novel route for the immobilization of a Pd-NHC catalyst on core/shell super paramagnetic nanoparticles that consisted of a highly crystalline γ-Fe_2O_3 core and a very thin polymeric shell wall (Scheme 5).

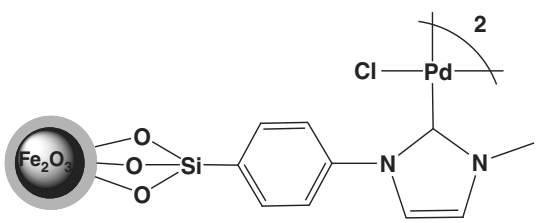

Scheme 5. Emulsion polymerization synthesis of core/shell iron oxide/polymer nanocrystals.

As-synthesized catalyst showed excellent activities in the Suzuki coupling of various aryl iodides and bromides with phenyl boronic acid, using DMF as a solvent (Scheme 6). However, the coupling of aryl chlorides was not reported for this system. The recovery of the catalysts was easily achieved by applying an external permanent magnet, and recycling of the catalytic system was examined for five consecutive rounds in the synthesis of 4-phenyltoluene from 4-iodotoluene and phenylboronic acid. No significant loss of catalytic activity consequently observed during the five consecutive reactions.

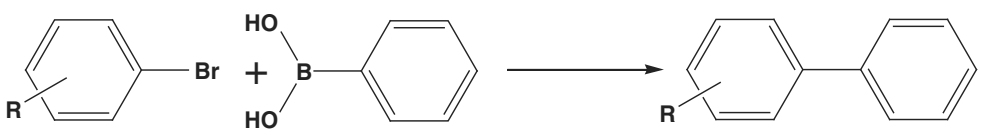

Scheme 6. Maghemite nanoparticle-supported Suzuki cross-coupling reactions.

Jin et al. [25] designed a remarkably active magnetic nanoparticle-supported (β-oxoiminato) (phosphanyl) palladium catalyst via the immobilization of a triethoxysilyl-functionalized palladium complex on the surface of robust SiO_2/Fe_3O_4 in refluxing toluene (Scheme 7).

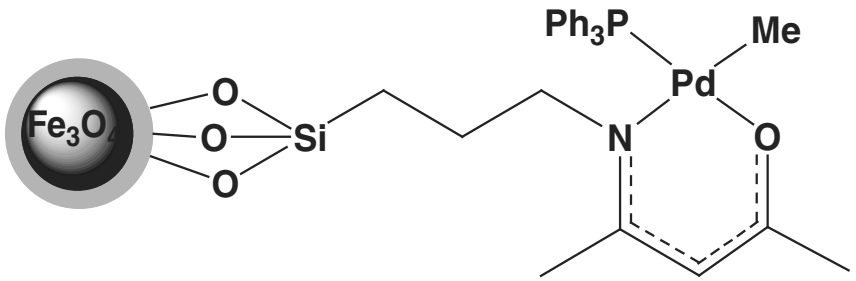

Scheme 7. Synthesis of the MNP-supported (β-oxoiminato) (phosphanyl) palladium complex.

The activity of this catalyst was evaluated in the Suzuki coupling of a series of aryl chlorides with arylboronic acid in aqueous solution and in the presence of K_2CO_3 as a base and tetra-butylammonium bromide as a phase-transfer agent. Reactions of phenylboronic acid with activated aryl chlorides led to the desired products with excellent yields after 3 h at 60°C. The system was particularly efficient for the coupling of phenylboronic acid with deactivated aryl chlorides, including 4-chloroanisole, 4-chlorotoluene, 4-chlorophenol, 2-chloroanisole, and 2-chlorotoluene (Scheme 8).

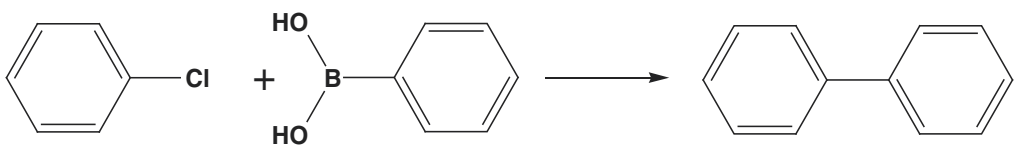

Scheme 8. Suzuki cross-coupling of deactivated aryl chlorides and phenylboronic acid.

Thiel and coworkers [26] reported trimethoxysilyl-functionalized palladium (II)-phosphine complexes on magnetic nanoparticles, which were successfully used as heterogeneous catalysts in the Suzuki reaction of aryl bromides and iodides (Scheme 9). In the presence of 1 mol% of this catalyst, the best results were obtained with Cs_2CO_3 as the base in dioxane at 80°C for 15 h (Scheme 10).

Heuze et al. [27] have synthesized a metallodendron functionalized with a dicyclohexyl-diphosphino palladium complex (Scheme 11). The grafting of this dendron onto core-shell γ-Fe_2O_3/polymer 300 nm MNPs was studied on the basis of the peptide reaction via covalent bond formation between the terminal primary amino group and the carboxyl group of the MNP polymer shell.

http://dx.doi.org/10.5772/61585

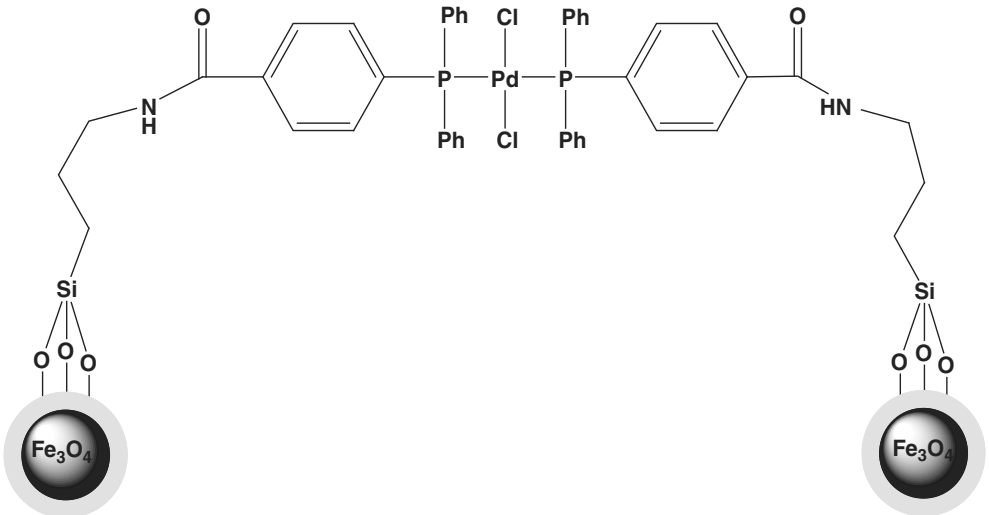

Scheme 9. Pd(II)–phosphine complexes supported on magnetic nanoparticles.

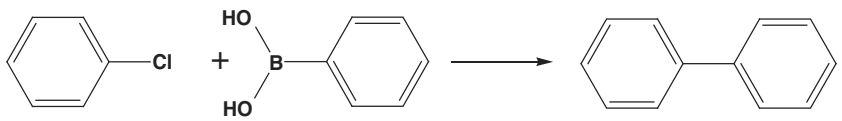

Scheme 10. Scheme 8 Suzuki coupling of bromobenzene and phenylboronic acid.

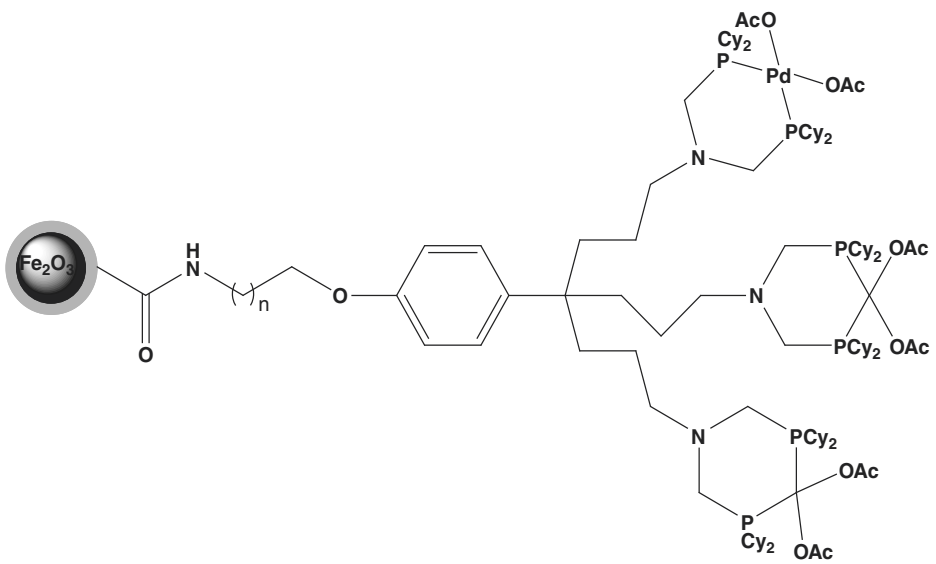

Scheme 11. Dendron-functionalized core-shell super paramagnetic nanoparticles.

This catalyst showed excellent catalytic activities for the coupling of a range of iodo and aryl bromides, which were obtained in good to excellent yields. However, the coupling of aryl chlorides with phenylboronic acid required higher catalyst loading, longer reaction times, and higher temperatures (Scheme 12).

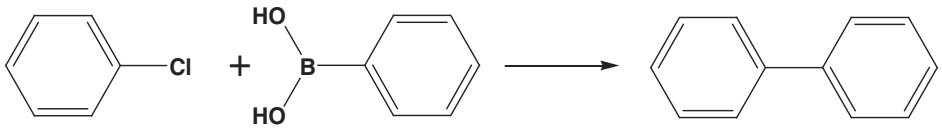

Scheme 12. Suzuki cross-couplings of aryl chlorides with phenylboronic acid using grafted MNPs.

Baig and Varma [28] synthesized a nano-FeDOPACu bimetallic catalyst (Scheme 13) and demonstrated its application for C-S coupling of aryl halides and thiophenols under microwave conditions.

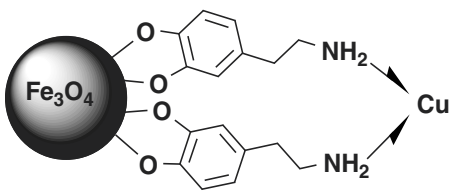

Scheme 13. Nano-Fe_3O_4-DOPA-Cu catalyst (nano-FeDOPACu).

Thiel and coworkers [29] reported an organic–inorganic hybrid catalyst, obtained by covalently anchoring [(L-L)MoO$(O_2)_2$] (LL=(3-triethoxysilylpropyl)[3-(2-pyridyl)-1-pyrazolyl]acetamide) on silica MNPs as a robust magnetically separable epoxidation catalyst (Scheme 14).

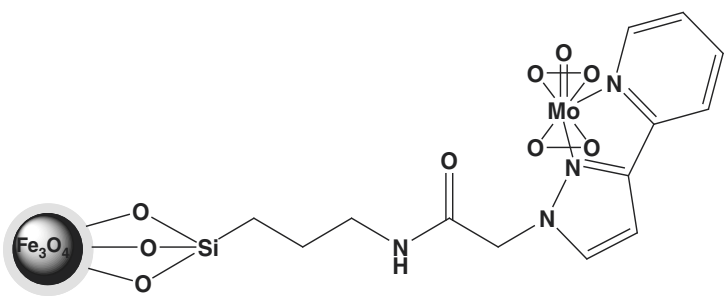

Scheme 14. Magnetic molybdenumperoxo catalyst for olefin epoxidation.

Reiser and co-workers [30] synthesized azabis(oxazoline)copper(II) complexes immobilized on magnetic silica nanoparticles, which displayed selectivities in the asymmetric benzoylation of 1,2-diols in high yields (Scheme 15).

http://dx.doi.org/10.5772/61585

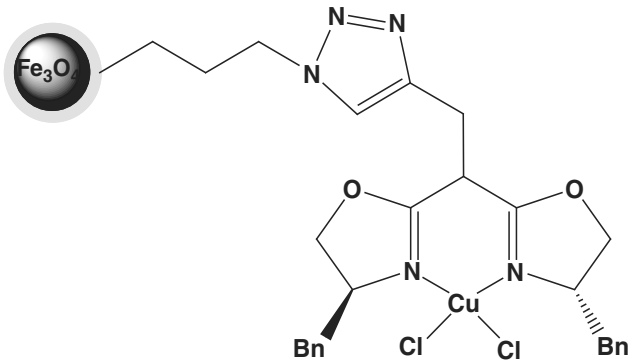

Scheme 15. Asymmetric benzoylation using magnetically separable azabis(oxazoline)copper(II) nanocatalysts.

Claesson et al. [31] employed a stable dispersion to synthesize monodisperse magnetizable colloidal silica particles functionalized with a homogeneous catalyst, i.e., PCP–pincer Pd complex (Scheme 16). This complex is known to catalyze the aldol condensation reaction between benzaldehyde and methyl isocyanoacetate to produce oxazolines (Scheme 17).

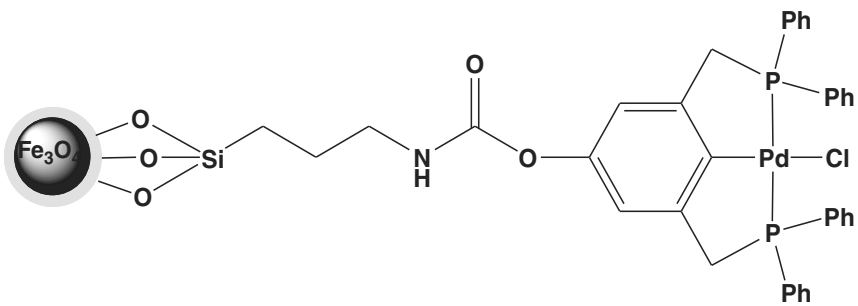

Scheme 16. PCP–pincer Pd complex-immobilized silica-coated nanocatalyst.

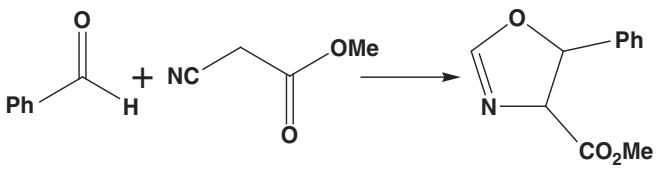

Scheme 17. Catalytic activity for cross-aldol condensation reactions.

Masteri-Farahani and Tayyebi [32] synthesized a highly efficient catalyst by covalent binding of a Schiff base ligand (*N*,*N*′-bis(3-salicylidenaminopropyl)amine) (salpr) onto the surface of silica-encapsulated magnetite nanoparticles (Si-MNPs) followed by complexation with $MoO_2(acac)_2$ (Scheme 18).

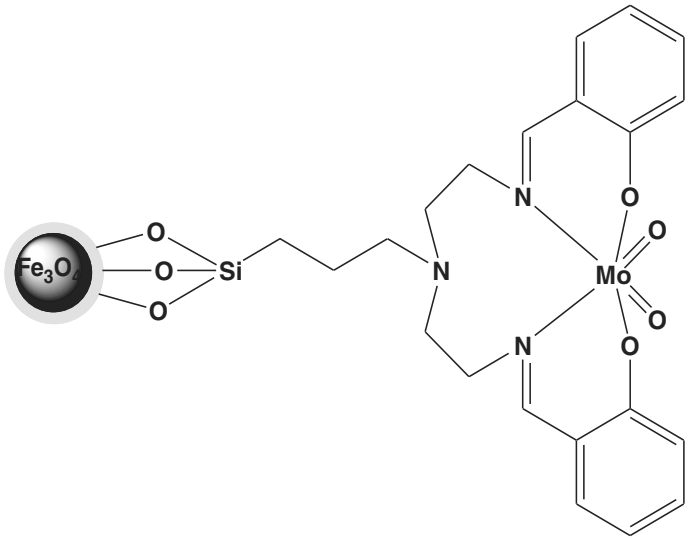

Scheme 18. MoO_2 salpr-immobilized silica-coated nanocatalyst.

The catalytic activity of the prepared MoO2salpr/SI-MNPs nanocatalyst was examined in the epoxidation of olefins with tert-butyl hydroperoxide (TBHP) and cumene hydroperoxide (CHP) (Scheme 19).

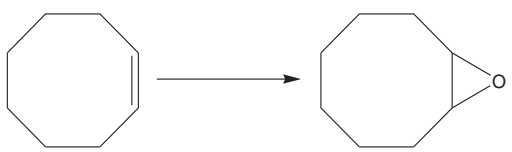

Scheme 19. Epoxidation of olefins.

Benign and economic [33] reported silica-coated magnetically recoverable Mn-porphyrin catalytic system (Scheme 20).

This catalyst is used for oxidation of industrially and biologically important substrates including olefins, saturated hydrocarbons, alcohols, and organosulfur compounds in water applying tert-butyl hydroperoxide (Scheme 21).

Sun and coworkers [34] reported organic–inorganic hybrid heterogeneous nanocatalysts via covalent anchoring of cobalt(II) or copper(II) acetylacetonate complexes ($[Co(acac)_2]$ or $[Cu(acac)_2]$) onto core–shell structured Fe_3O_4/SiO_2 previously functionalized with 3-aminopropyltriethoxysilane (APTES) (Scheme 22).

Sharma et al. [35] reported the fabrication of a highly efficient magnetically separable nanocatalyst by the covalent immobilization of a copper (II) acetylacetonate complex onto amine-functionalized silica magnetite NPs ($Cu(acac)_2$@Si-MNP) (Scheme 22).

http://dx.doi.org/10.5772/61585

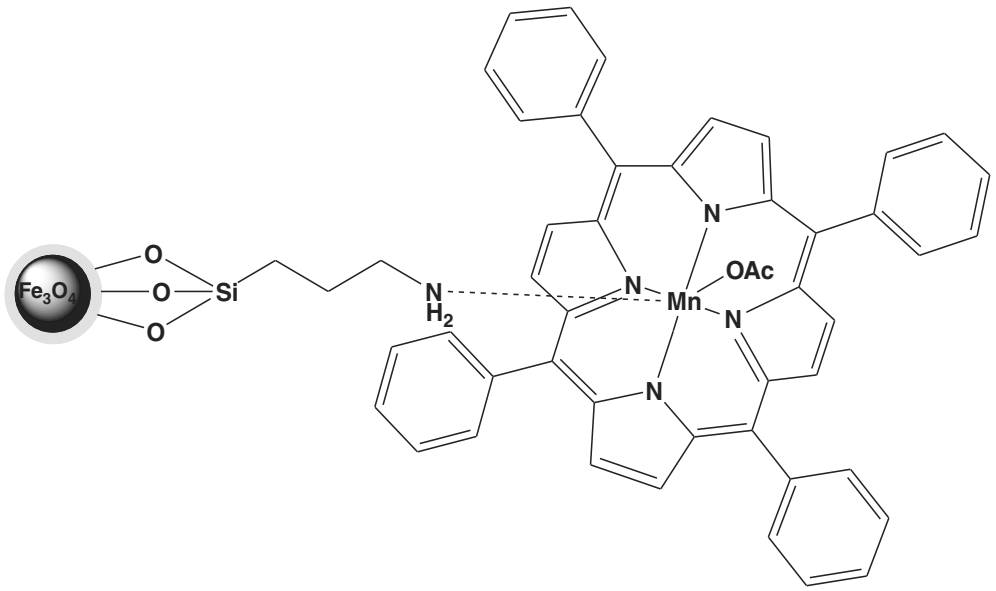

Scheme 20. Silica-coated magnetically recoverable Mn-porphyrin catalytic system.

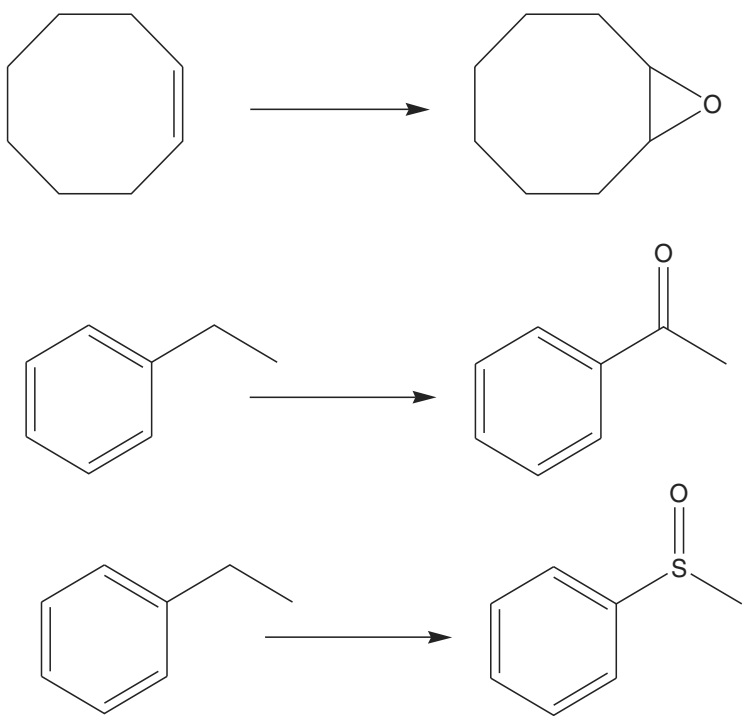

Scheme 21. Oxidation of different arenes.

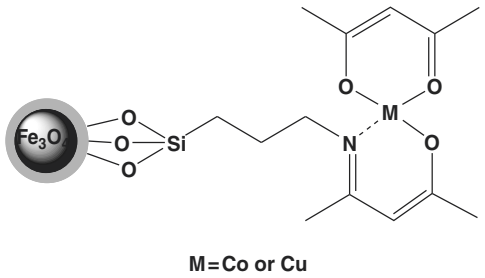

Scheme 22. Magnetically recoverable heterogeneous nanocatalysts $Fe_3O_4/SiO_2–NH_2–M$ (M=Cu or Co).

The application of the synthesized nanocomposites was examined for the degradation of various organic nitro-analogues in aqueous medium at room temperature using sodium borohydride as a source of hydrogen (Scheme 23). The reported nanocatalytic system was able to selectively reduce the nitro group even in presence of other sensitive functional groups.

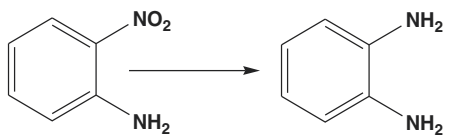

Scheme 23. $Cu(acac)_2$@Am-Si-MNPs catalyzed reduction of nitro compounds.

Byrenes et al. [36] synthesized a nanocatalyst in one step from a commercially available second-generation Grubbs catalyst by the immobilization of the homogeneous catalyst onto magnetically separable silica coated nanosized iron oxide particles (Scheme 24).

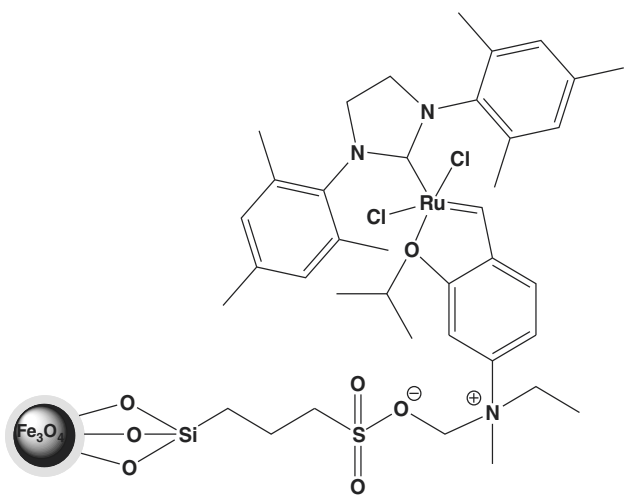

Scheme 24. Ruthenium alkylidene-immobilized silica-coated nanocatalyst.

http://dx.doi.org/10.5772/61585

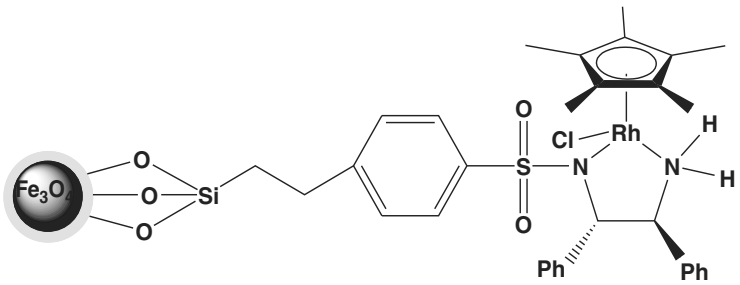

Scheme 25. Preparing magnetic catalysts through direct complexation of $[Cp^*RhCl_2]_2$ with (S,S)-TsDPEN and $[Cp^*RhCl_2]_2$ with (R,R)-TsDACH modified SiO_2-coated Fe_3O_4 nanoparticles.

Liu and coworkers [37, 38] reported a convenient method for preparing three magnetic catalysts (Scheme 25) through direct complexation of $[Cp^*IrCl_2]_2$ or $[Cp^*RhCl_2]_2$ with (S,S)-TsDPEN and $[Cp^*RhCl_2]_2$ with (R,R)-TsDACH modified SiO_2-coated Fe_3O_4 nanoparticles.

In 2004, Xu and coworkers [39] developed a simple and efficient functionalization protocol for ferrites using dopamine as an anchor. These functionalized materials with Ni-complex (Scheme 26) displayed high specificity for protein separation and excellent stability to heating and high salt concentrations.

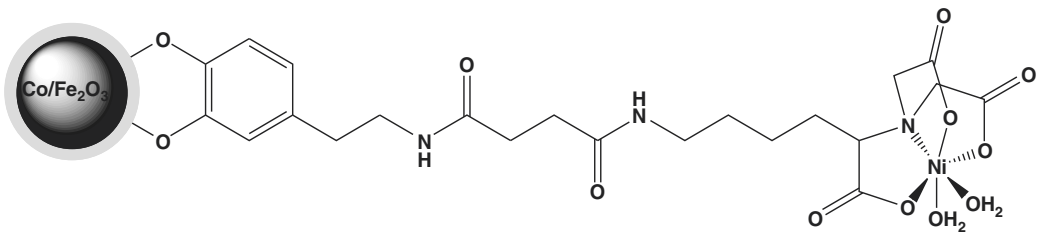

Scheme 26. Dopamine functionalization of ferrites.

Lin et al. [40] designed a magnetite nanoparticle-supported chiral catalyst by Ru-complex formation with BINAP followed by functionalization on the ferrite surfaces (Scheme 27). The catalyst could be recovered by using an external magnet and was used up to 14 times without any change in activity.

This catalyst was then used for the hydrogenation of a wide range of aromatic ketones to their corresponding secondary alcohols and exhibited high reactivity and enantioselectivity. The enantiomeric excess (ee) values were significantly higher than those of the parent homogeneous catalyst [Ru(BINAP)(DPEN)-Cl_2] and were comparable to the values of its homogeneous counterpart. The stability of the recovered catalyst was investigated in the asymmetric hydrogenation of 1-acetonaphthone. In this reaction, the catalyst could be recycled 14 times with no decrease in conversion and/or enantiomeric excess. However, the MSCs tend to aggregate slightly, presumably because the [Ru(BINAPPO3)(DPEN)Cl_2] moieties on the MNP

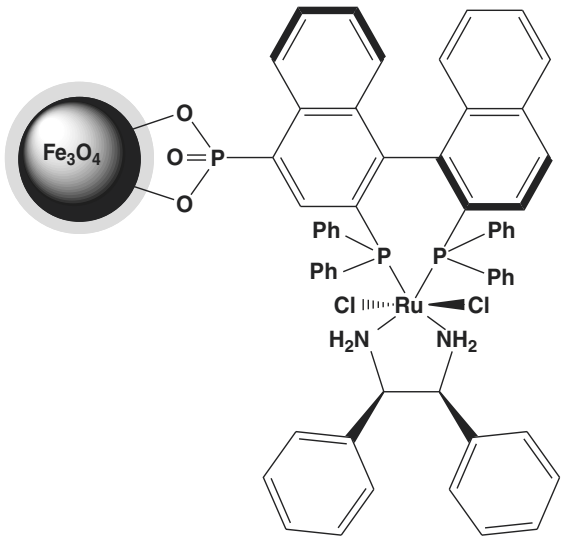

Scheme 27. Nanoparticle-supported chiral Ru-catalyst.

surfaces are less effective in preventing the aggregation of the MNPs than that of widespread coating agents such as oleic acid (Scheme 28).

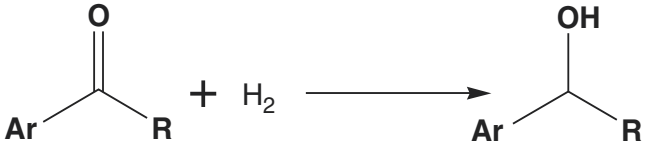

Scheme 28. Magnetite chiral Ru catalyst for asymmetric hydrogenation of aromatic ketones.

Kitamura and colleagues [41] prepared a heterogeneous deallylation catalyst by immobilizing [CpRu(η^3-C_3H_5)(2-pyridinecarboxylato]PF_6 onto silica-coated nanoferrite particles. The obtained materials showed high saturation magnetization and high levels of dispersibility with weak coercive forces. It was highly active for deallylation reactions and could operate in alcoholic solvents in the absence of any extra additives to complete the reaction (Scheme 29).

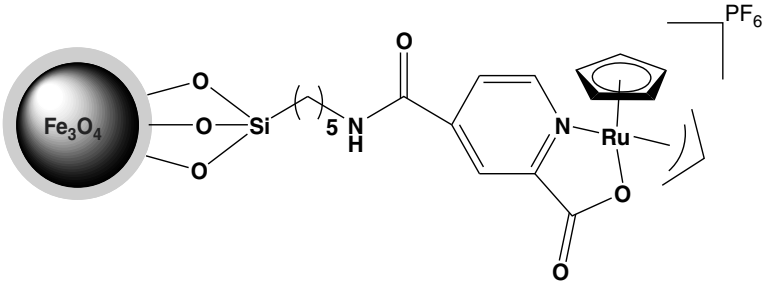

Scheme 29. Heterogeneous deallylation catalyst.

http://dx.doi.org/10.5772/61585

The catalyst was highly active for deallylation reactions (Scheme 30), and no extra additives were needed to complete the reaction. Only volatile allyl ethers were the coproducts of the reaction. The catalyst was removed using an external magnet and reused, making the protocol economical.

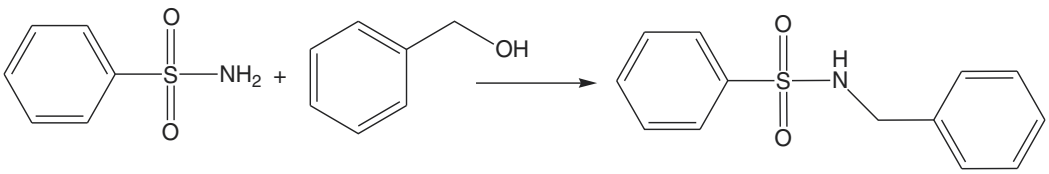

Scheme 30. Magnetically separable Ru catalyst for synthesis of sulfonamides.

Gao and colleagues [42] reported the synthesis of a novel magnetic nanoparticle-supported di(2-pyridyl)methanol palladium dichloride complex via click chemistry (Scheme 31).

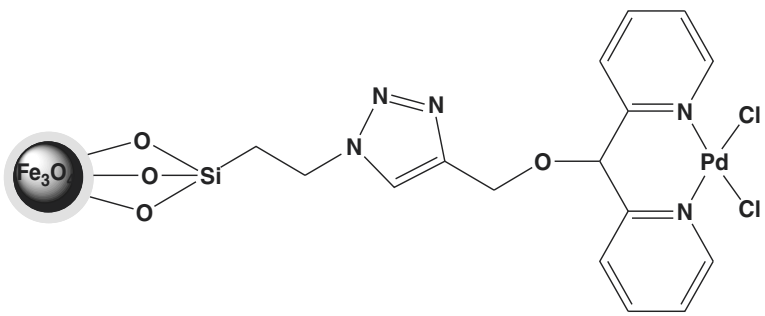

Scheme 31. Preparation of an MNP-supported Di(2-pyridyl)-methanol-Pd complex via click chemistry.

The catalyst was then initially used in the Suzuki coupling of phenylboronic acid with bromobenzene. Optimized results were achieved with a 0.2 mol% catalyst and the use of K_2CO_3 as base in DMF at 100°C. Under these conditions, fairly good to excellent yields were obtained in the coupling of aryl bromides containing electron-donating and electron-withdrawing substituents (Scheme 32).

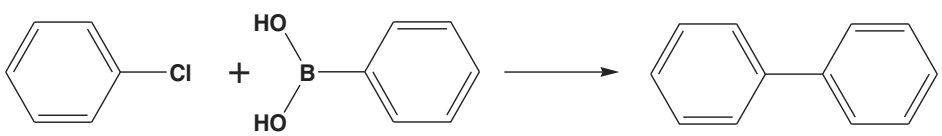

Scheme 32. Coupling reactions using MSC-supported complexes.

Interestingly, Che et al. [43] developed a novel type of Hoveyda–Grubbs catalyst by assembling magnetic nanoparticles with a Grubbs I catalyst. Scheme 33 describes the synthesis of the

magnetic nanoparticle-supported Hoveyda–Grubbs catalyst. The isopropoxystyrene derivative was first treated with glutaric anhydride in the presence of Et3N and DMAP to create 5-(4-isopropoxy-3-vinylbenzyloxy)-5-oxopentanoic acid, which was further reacted with amino-functionalized ferrite. The as-synthesized material was then coupled with a first-generation Grubbs catalyst in the presence of CuCl to produce the desired magnetic Hoveyda–Grubbs catalyst.

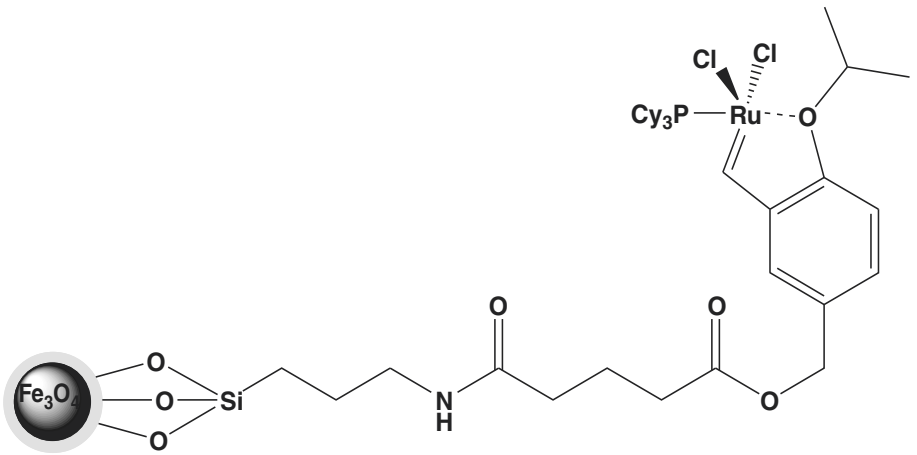

Scheme 33. Preparation of the magnetic Hoveyda–Grubbs catalyst.

Recently, Li et al. [44] synthesized a magnetite-supported copper(I)pybox magnetically retrievable catalyst (Scheme 34).

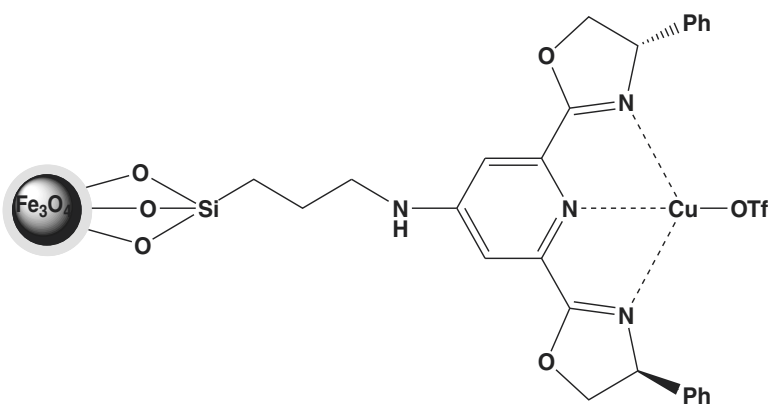

Scheme 34. Magnetite-supported copper (I) pybox.

More recently, Glorious et al. [45] reported an enantioselective allylation reaction on a magnetite-supported NHC catalyst. The immobilization of an enantiomerically pure imida-

http://dx.doi.org/10.5772/61585

zolium salt on the surface of magnetite leading to the formation of a molecular Pd complex is presented in Scheme 35.

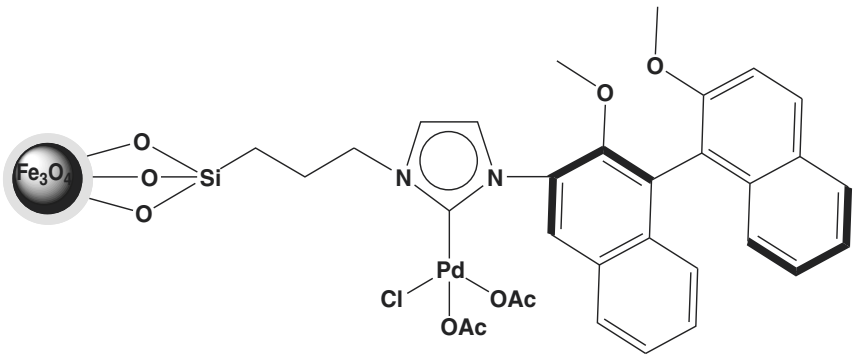

Scheme 35. Synthesis of magnetite-supported chiral NHC.

Shijie Ding et al. [46] used regular shaped Fe3O4 magnetic nanoparticles (20–30 nm) to support the catalyst for atom transfer radical polymerization (ATRP). It was tethered onto the magnetic nanoparticles (Scheme 1). The supported catalyst could mediate ATRP with a control over polymerization unattainable by heterogeneous catalysts. The separation of nanosized magnetic supports could be easily achieved by applying a magnetic field (Scheme 36).

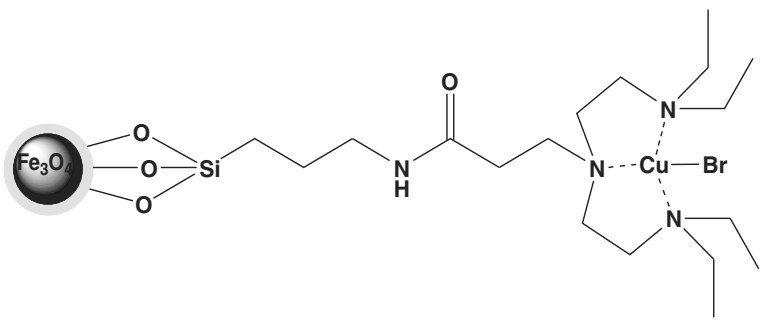

Scheme 36. Immobilization of the ligand tetraethyldiethylenetriamine (TEDETA) and the catalyst onto Fe_3O_4 magnetic nanoparticles.

The Fe_3O_4 magnetic nanoparticle-supported porphyrinato cobalt III (MNP-P) has been designed, synthesized (Scheme 37), and evaluated as a recoverable catalyst for coupling reaction of epoxide and CO_2 (Scheme 38) [47].

Barahman Movassagh et al. [48] introduced a new heterogeneous, recyclable, heat- and air-stable silica-coated magnetic nanoparticle (MNP)-supported palladium(II)-crypt and complex [Fe_3O_4/SiO_2/C22–Pd(II)] catalyst (Scheme 39) as a highly efficient catalytic system for performing the Suzuki–Miyaura reaction and S-arylation of thiols (Scheme 40).

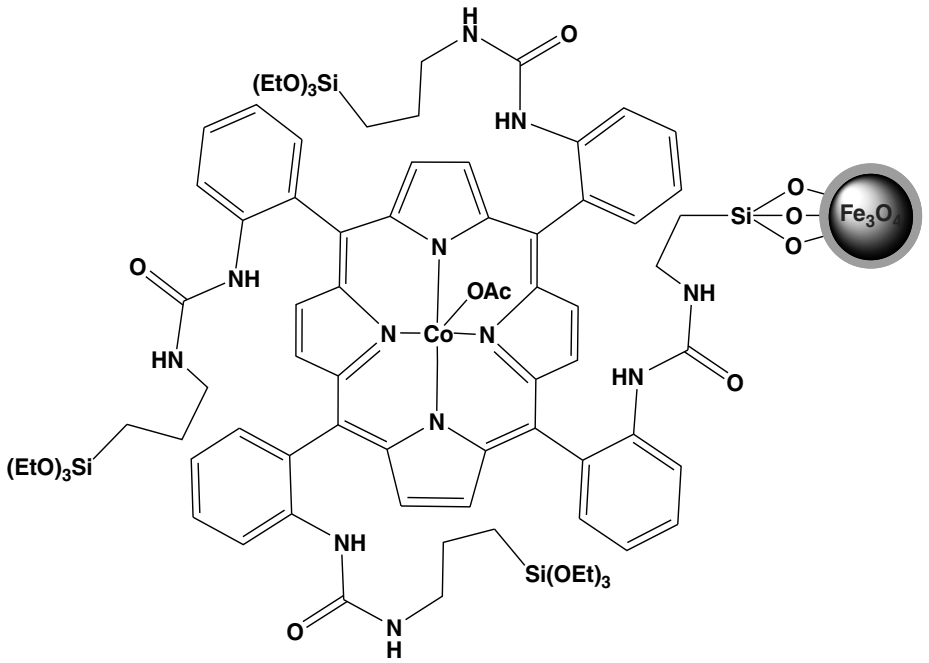

Scheme 37. The Fe_3O_4 magnetic nanoparticle-supported porphyrinato cobalt III.

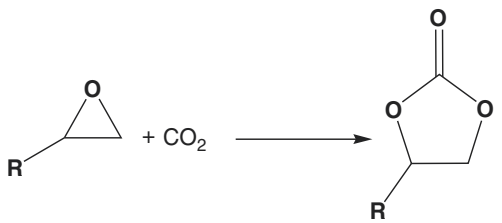

Scheme 38. Coupling reaction catalyzed by MNP-P/PTAT.

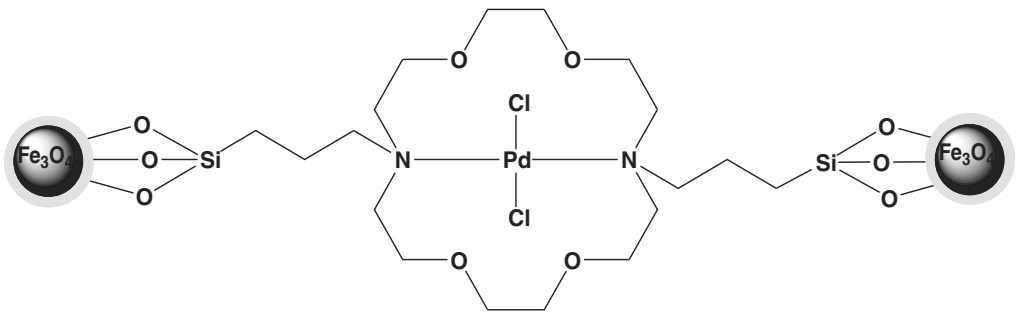

Scheme 39. Synthetic schemes of Fe_3O_4/SiO_2/C22–Pd(II) catalyst.

http://dx.doi.org/10.5772/61585

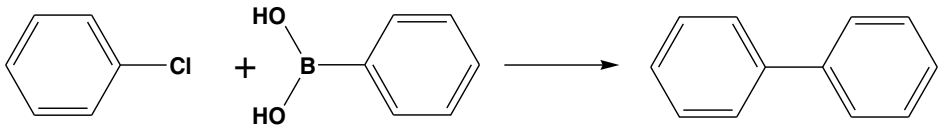

Scheme 40. Suzuki cross-couplings of aryl chlorides with phenylboronic acid using grafted MNPs.

Pinhua Li et al. [49] developed a highly active air- and moisture-stable and easily recoverable magnetic nanoparticle-supported palladium catalyst (Scheme 41) for the Suzuki, Sonogashira, and Heck reactions. A wide range of substrates was coupled successfully under aerobic conditions (Scheme 42).

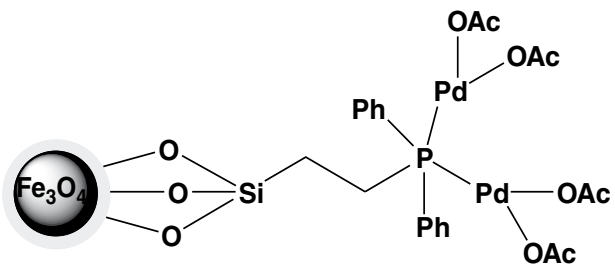

Scheme 41. Preparation of the magnetic nanoparticle-supported palladium catalyst.

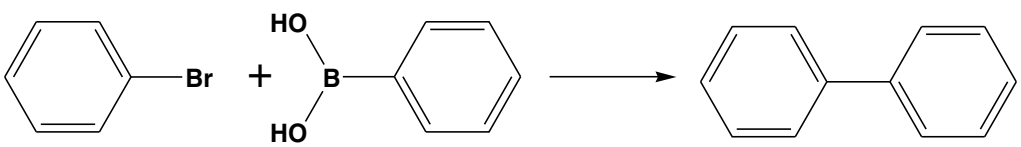

Scheme 42. Applications in Suzuki, Sonogashira, and Heck reactions.

Xingquan Xiong et al. [50] reported a green, inexpensive and scale-up synthesis of 1,4-disubstituted 1,2,3-triazoles from benzyl/alkyl halides, functional alkynes and sodiumazides in water, which were catalyzed by heterogeneous, recyclable, and commercially available Fe_3O_4-supported Cu(I) catalysts (MNPs–CuBr) via a combination of one-pot multi-component CuAAC reaction and microwave irradiation (Scheme 43).

Fe_3O_4 was successfully prepared by coprecipitation with $FeCl_2$ and $FeCl_3$ as reaction substrate, polystyrene (PS) as surfactant and aqueous NH_3 as precipitant And then the core-shell Fe_3O_4/SiO_2 nanospheres were prepared by a modified Stober method. A mild, convenient, and efficient protocol developed for the synthesis of 1- and 5-substituted 1H-tetrazoles from nitriles and amines using magnetically separable Fe_3O_4/SiO_2/ligand/Cu(II) nanoparticles as an efficient and recyclable catalyst (Scheme 44) [51].

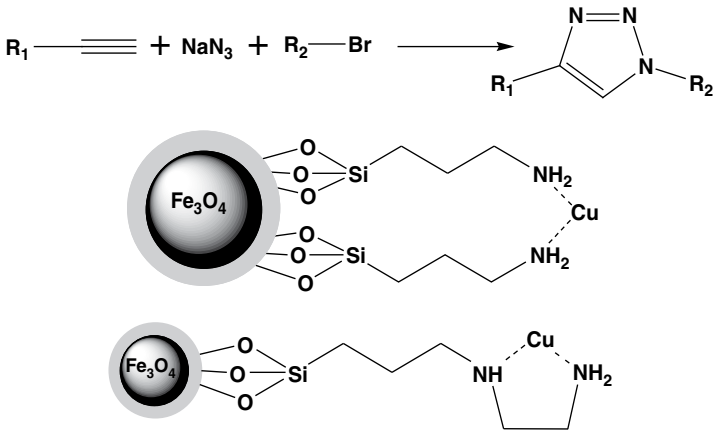

Scheme 43. MNPs–CuBr catalyzed one-pot synthesis of 1,4-disubstituted 1,2,3-triazoles in water under microwave irradiation conditions.

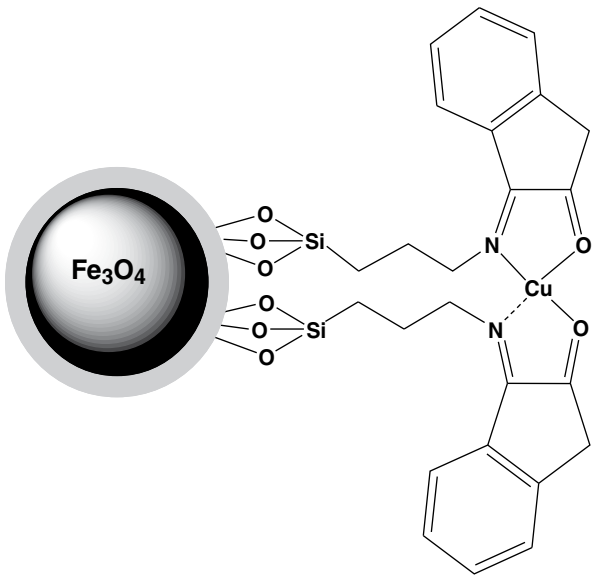

Scheme 44. Cu(II) complex functionalized Fe_3O_4/SiO_2 nanoparticle.

The immobilized copper complex was used as an efficient catalyst for synthesis of 1- and 5-substituted 1H-tetrazoles from nitriles and amines in good to excellent yields (Scheme 45).

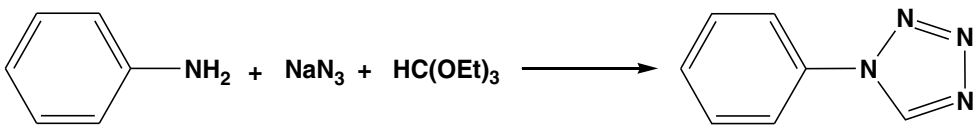

Scheme 45. Synthesis of 1- and 5-substituted 1H-tetrazoles from nitriles and amines.

http://dx.doi.org/10.5772/61585

Functionalized magnetic iron ferrite (Fe_3O_4) synthesized by complexation with various metals and applied in organic synthesis. A new Fe_3O_4 magnetic nanoparticle-supported manganese–salen complex was successfully prepared by attaching manganese acetates to a novel *N*,*N*′-bis(salicylidine)ethylenediamine ligand functionalized Fe_3O_4 (Scheme 46) [52].

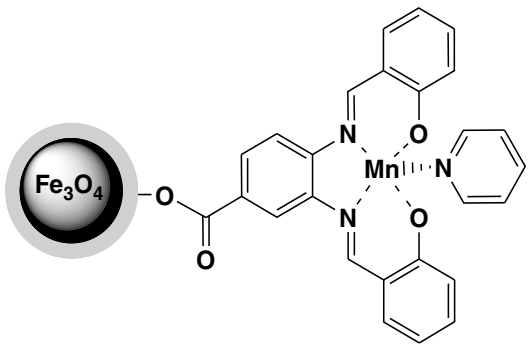

Scheme 46. Schematic illustration of the synthesis for Fe_3O_4\SiO_2\Salen\Mn nanoparticles.

This catalyst was used as a magnetically recyclable heterogeneous catalyst for the efficient one-pot synthesis of benzopyranopyrimidines from the reaction of 2-hydroxybenzaldehyde, malononitrile, and amine with high product yields (Scheme 47).

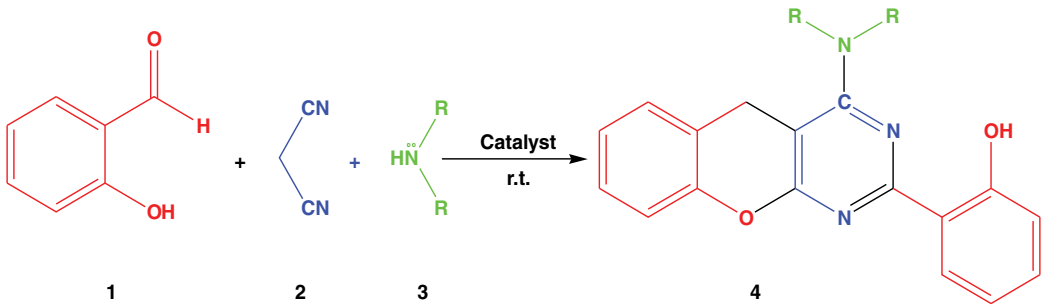

Scheme 47. Synthesis of benzopyranopyrimidines from salicylic aldehydes, malononitrile, and amine in the presence of Fe_3O_4\SiO_2\Salen\Mn MNPs.

The Fe_3O_4/SiO_2 core shell was synthesized by a simple method and then functionalized by the Schiff base complex of Mn (III), which had been obtained by the reaction between Mn (III) acetate and the Schiff base prepared from 1,2-benzenediamine and salicylaldehyde, according to Scheme 48 and its catalytic activity in the multicomponent reaction (Scheme **49**) [53].

Magnetite–polyoxometalate hybrid nanomaterials, Fe_3O_4/SiO_2/salen/Mn/IL/HPW, were prepared by grafting $H_3PW_{12}O_{40}$ on ionic liquid-functionalized Fe3O4 magnetite nanoparticles (Scheme 50) [54].

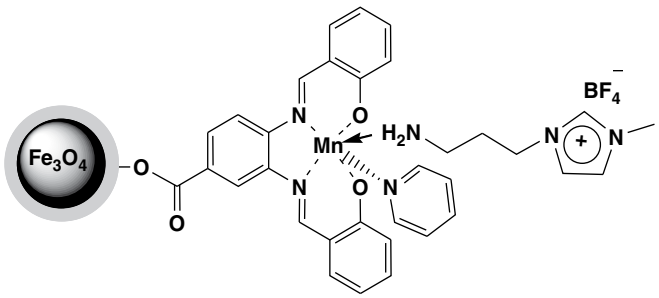

Scheme 48. Schematic illustration of the synthesis for Fe_3O_4/SiO_2/Salen/Mn/IL nanoparticles.

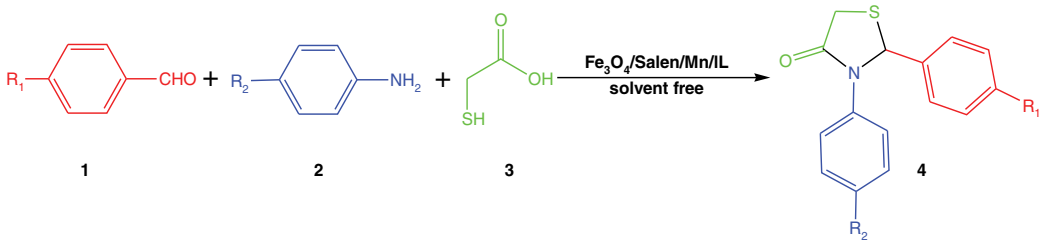

Scheme 49. Synthesis of 1,3-thiazolidin-4-one in the presence of Fe_3O_4/SiO_2/Salen/Mn/IL MNPs.

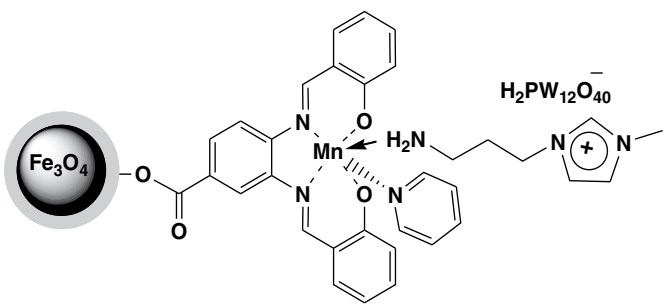

Scheme 50. Schematic illustration of the synthesis of MNPs-HPW.

This catalyst is a recoverable catalyst for the one-pot synthesis of thiazoloquinolines in high to excellent yield under solvent-free conditions (Scheme 51).

A new Fe_3O_4 magnetic nanoparticle-supported gold dipyridine complex was successfully prepared by attaching sodium tetrachloroaurate(III) hydrate to a novel dipyridine ligand functionalized Fe_3O_4. The catalyst was prepared by sonicating nanoferrites with dipyridine (which acts as a robust anchor and avoids Au(III)) in absolute MeOH, followed by addition of sodium tetrachloroaurate(III) hydrate. Material with Au(III) on the functionalized nanoferrites was obtained in excellent yield (Scheme 52), which catalyzed the 2,6-dihydropyrimido[2,1-a]isoindole derivatives (4) in aqueous media (Scheme 53) [55].

http://dx.doi.org/10.5772/61585

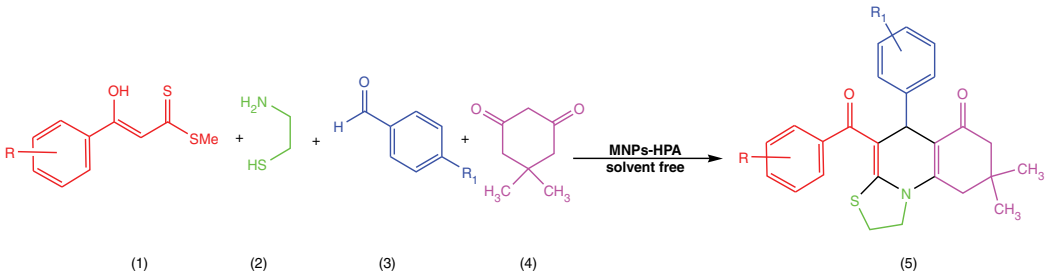

Scheme 51. Synthesis of thiazoloquinolines in the presence of MNPs-HPW.

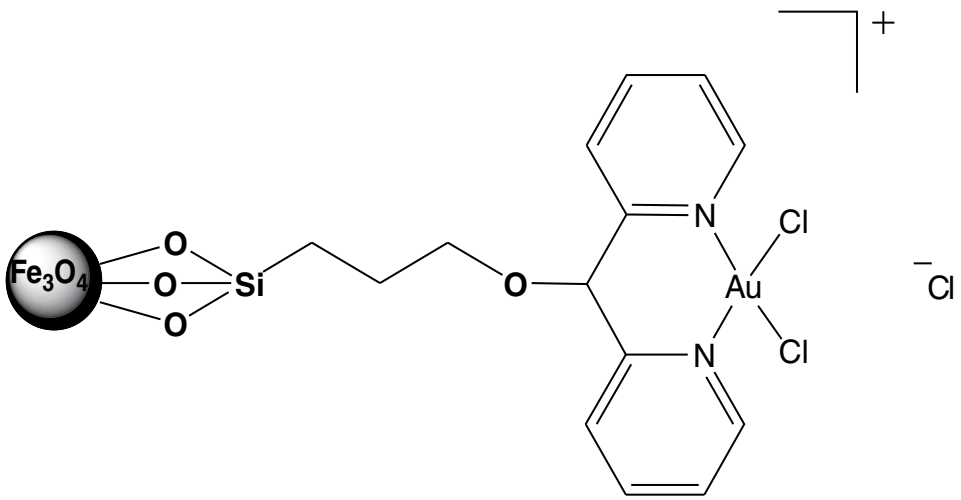

Scheme 52. It was found to be an efficient catalyst for the synthesis 2,6-dihydro[2,1-a]isoindole in aqueous medium.

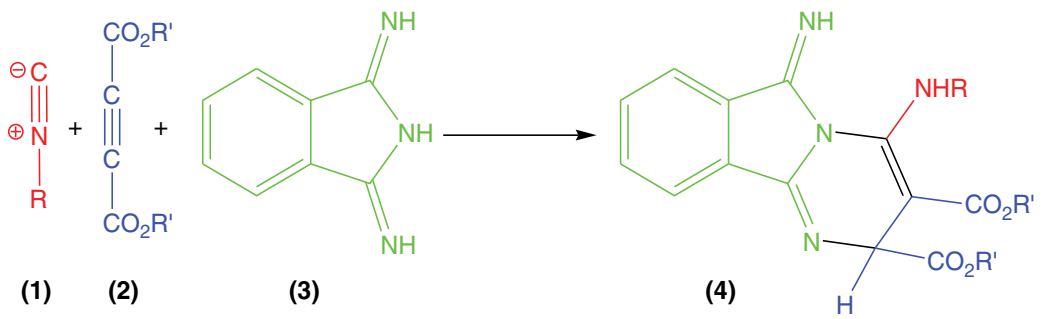

Scheme 53. Reaction pathways for the condensation of alkyl isocyanides (1) and dialkyl acetylenedicarboxylates (2) with 1,3-diimino isoindoline (3).

7. Conclusion

The heterogenization of catalysts using magnetic supports is a new direction for modern organic chemistry, which is associated with the efficient isolation, reusability, and recyling of precious catalysts or reagents. Magnetic separation not only reduces the costs of production but also prevents the production and accumulation of toxic waste. These reasons explain why the development of magnetically separable nanocatalysts is growing exponentially, with uses in sustainable and benign chemical transformations. The high-surface area and cost-effective solid supports are important features, but the main problem when using MNPs is the unwanted aggregation of tiny magnetic particles. This problem has been mitigated by grafting catalyst species onto presynthesized MNPs, as well as by the functionalization and modification of MNPs with suitable ligands, and coating or encapsulating with stabilizing materials such as silica, polymers, ionic liquids, and carbon. The application of magnetically supported catalysts may affect most types of organic reactions such as cyclo-addition, oxidation, reduction, and coupling, including their asymmetric equivalents. Major progress has been made in the synthesis and application of magnetically recoverable chiral catalysts, as well as their applications in asymmetric organic synthesis, but maintaining their persistent activity, selectivity, and asymmetric induction over a period of time is challenging due to the leaching or poisoning of the catalysts in the reaction conditions. Thus, the development of new magnetic materials, their functionalization, and the immobilization of asymmetric catalysts demand further research to overcome these problems. The particle size, size distributions, and coherent functionalization are the most important features because of their important roles in the activity and strength of catalysts. In addition, there should be an emphasis on bringing these magnetic materials closer to industrial applications by employing them in multikilogram-scale processes in a cost-effective manner. Finally, the use of magnetic nanocatalysts in continuous flow synthesis needs to be exploited. The automated recycling of magnetic nanocatalysts needs to be studied to demonstrate their usefulness as supports for use in parallel and high-throughput synthesis.

Author details

Seyed Mohsen Sadeghzadeh[1*] and Mehdi Mogharabi[2,3]

*Address all correspondence to: sadeghzadeh_sm@yahoo.com

1 Department of Chemistry, College of Sciences, Sina Masihabadi Student Research, Neishabour, Iran

2 Department of Pharmaceutical Biotechnology, Faculty of Pharmacy and Biotechnology Research Center, Tehran University of Medical Sciences, Tehran, Iran

3 Pharmaceutical Sciences Research Center, Tehran University of Medical Sciences, Tehran, Iran

http://dx.doi.org/10.5772/61585

References

[1] V. Polshettiwar, R. Luque, A. Fihri, H. Zhu, M. Bouhrara, J. M. Basset, Chem. Rev. 111 (2011) 3036.

[2] V. Polshettiwar, R. S. Varma, Green Chem. 12 (2010) 743.

[3] (a) V. Polshettiwar, R. Luque, A. Fihri, H. Zhu, M. Bouhrara, J. M. Basset, Chem. Rev. 111 (2011) 3036; (b) V. Polshettiwar, R. S. Varma, Green Chem. 12 (2010) 743; (c) S. Shylesh, V. Schunemann, W. R. Thiel, Angew. Chem., Int. Ed. 49 (2010) 3428; (d) Lu, A. H.; Salabas, E. L.; Schuth, F. Angew. Chem., Int. Ed. 46 (2007) 1222.

[4] H. Yoon, S. Ko, J. Jang, Chem. Commun. (2007) 1468.

[5] Y. Zhu, L. Zhang, F. M. Schappacher, R. Pottgen, J. Shi, S. J. Kaskel, J. Phys. Chem. C 112 (2008) 8623.

[6] Y. Zhu, E. Kockrick, S. Kaskel, T. Ikoma, N. Hanagata, J. Phys. Chem. C 113 (2009) 5998.

[7] F. Kleitz, S. H. Choi, R. Ryoo, Chem. Commun. (2003) 2136.

[8] Y. Chang, D. J. Chen, Hazard. Mater. 165 (2009) 664.

[9] M. V. Barmatova, I. D. Ivanchikova, O. A. Kholdeeva, A. N. Shmakov, V. I. Zaikovskii, M. S. Melgunov, J. Mater. Chem. 19 (2009) 7332.

[10] M. V. Barmatova, I. D. Ivanchikova, O. A. Kholdeeva, A. N. Shmakov, V. I. Zaikovskii, M. S. Melgunov, Catal. Lett. 127 (2009) 75.

[11] S. B. Yoon, J. Y. Kim, J. H. Kim, Y. J. Park, K. R. Yoon, S. K. Park, J. S. Yu, J. Mater. Chem. 17 (2007) 1758.

[12] C. Wang, L. Yin, L. Zhang, L. Kang, X. Wang, R. Gao, J. Phys. Chem. C 113 (2009) 4008.

[13] S. Xu, D. Feng, W. Shangguan, J. Phys. Chem. C 113 (2009) 2463.

[14] T. Hara, T. Kaneta, K. Mori, T. Mitsudome, T. Mizugaki, K. Ebitani, K. Kaneda, Green Chem. 9 (2007) 1246.

[15] K. Mori, T. Hara, T. Mizugaki, K. Ebitani, K. Kaneda, J. Am. Chem. Soc. 126 (2004) 10657.

[16] T. Hara, K. Mori, T. Mizugaki, K. Ebitani, K. Kaneda, Tetrahedron Lett. 44 (2003) 6207.

[17] T. Hara, T. Kaneta, K. Mori, T. Mitsudome, T. Mizugaki, K. Ebitani, K. Kaneda, Green Chem. 9 (2007) 1246.

[18] S. Xuan, Y. X. J. Wang, J. C. Yu, K. C. F. Leung, Langmuir 25 (2009) 11835.

[19] C. L. Zhu, S. W. Chou, S. F. He, W. N. Liao, C. C. Chen, Nanotechnology 18 (2007) 275604.

[20] S. Xuan, Y. X. J. Wang, K. C. F. Leung, K. Y. Shu, J. Phys. Chem. C 112 (2008) 18804.

[21] A. H. Lu, E. L. Salabas, F. Schth, Angew. Chem. 119 (2007) 1242.

[22] Y. Zhu, K. Loo, H. Ng, C. Li, L. P. Stubbs, F. S. Chia, M. Tan, S. C. Peng, Adv. Synth. Catal. 351 (2009) 2650.

[23] S. E. G. Garrido, J. Francos, V. Cadierno, J. M. Basset, V. Polshettiwar, ChemSusChem 4 (2011) 104.

[24] P. D. Stevens, J. Fan, H. M. R. Gardimalla, M. Yen, Y. Gao, Org. Lett. 7 (2005) 2085.

[25] M. J. Jin, D. H. Lee, Angew. Chem., Int. Ed. 49 (2010) 1119.

[26] Z. Yinghuai, S. C. Peng, A. Emi, S. Zhenshun, M. Lisa, R. A. Kemp, Adv. Synth. Catal. 349 (2007) 1917.

[27] D. R. Amorin, X. Wang, M. Gaboyard, R. Clerac, S. Nlate, K. Heuze, Chem. Eur. J. 15 (2009) 12636.

[28] R. B. Nasir Baig, R. S. Varma, Chem. Commun. 48 (2012) 2582.

[29] S. Shylesh, J. Schweitzer, S. Demeshko, V. Schnemann, S. Ernst, W. R. Thiel, Adv. Synth. Catal. 351 (2009) 1789.

[30] A. Schtz, M. Hager, O. Reiser, Adv. Funct. Mater. 19 (2009) 2109.

[31] E. Maria Claesson, N.C. Mehendale, R.J.M. Klein Gebbink, G. van Koten, A.P. Philipse, J. Magn. Magn. Mater. 311 (2007) 41.

[32] M. Masteri-Farahani, N. Tayyebi, J. Mol. Catal. A. Chem. 348 (2011) 83.

[33] A. Rezaeifard, P. Farshid, M. Jafarpour, G.K. Moghaddam, RSC Adv. 4 (2014) 9189.

[34] J. Sun, G. Yu, L. Liu, Z. Li, Q. Kan, Q. Huo, J. Guan, Catal. Sci. Technol. 4 (2014) 1246.

[35] R.K. Sharma, Y. Monga, A. Puri, J. Mol. Catal. A. Chem. 393 (2014) 84.

[36] M.J. Byrnes, A.M. Hilton, C.P. Woodward, W.R. Jackson, A.J. Robinson, Green Chem. 14 (2012) 81.

[37] G. Liu, H. Gu, Y. Sun, J. Long, Y. Xu, H. Li, Adv. Synth. Catal. 353 (2011) 1317.

[38] Y. Sun, G. Liu, H. Gu, T. Huang, Y. Zhang, H. Li, Chem. Commun. 47 (2011) 2583.

[39] C. Xu, K. Xu, H. Gu, R. Zheng, H. Liu, X. Zhang, Z. Guo, B. Xu, J. Am. Chem. Soc. 126 (2004) 9938.

[40] C. O. Dalaigh, S. A. Corr, Y. Gunko, S. Connon, Angew. Chem., Int. Ed. 46 (2007) 4329.

[41] T. Hirakawa, S. Tanaka, N. Usuki, H. Kanzaki, M. Kishimoto, M. Kitamura, Eur. J. Org. Chem. 6 (2009) 789.

[42] G. Lv, W. Mai, R. Jin, L. Gao, Synlett (2008) 1418.

http://dx.doi.org/10.5772/61585

[43] C. Che, W. Li, S. Lin, J. Chen, J. Zhang, J. Wu, Q. Zheng, G. Zhang, Z. Yang, B. Jiang, Chem. Commun. (2009) 5990.

[44] T. Zeng, L. Yang, R. Hudson, G. Song, A. R. Moores, C. J. Li, Org. Lett. 13 (2011) 442.

[45] K. V. S. Ranganath, A. H. Schafer, F. Glorius, ChemCatChem, 3 (2011) 1889.

[46] S. Ding, Y. Xing, M. Radosz, Y. Shen, Macromolecules 39 (2006) 6399.

[47] D. Bai, Q. Wang, Y. Song, B. Li, H. Jing, Catal Commun. 12 (2011) 684.

[48] B. Movassagh, A. Takallou, A. Mobaraki, J. Mol. Catal. A. Chem. 401 (2015) 55.

[49] P. Li, L. Wang, L. Zhang, G.W. Wang, Adv. Synth. Catal. 354 (2012) 1307.

[50] X. Xiong, L. Cai, Catal. Sci. Technol. 3 (2013) 1301.

[51] R. K. Sharma, Y. Monga, A. Puri, J. Mol. Catal. A. Chem. 393 (2014) 84.

[52] S. M. Sadeghzadeh, F. Daneshfar, M. Malekzadeh, Chin. J. Chem. 32 (2014) 349.

[53] S. M. Sadeghzadeh, M. Malekzadeh, J. Mol. Liq. 202 (2015) 46.

[54] S. M. Sadeghzadeh, RSC Adv. 5 (2015) 17319.

[55] S. M. Sadeghzadeh, RSC Adv. 4 (2014) 43315.

Chapter 4

TiO_2 Nanostructures and Nanocomposites for Sustainable Photocatalytic Water Purification

Giuseppe Cacciato, Massimo Zimbone,
Francesco Ruffino and Maria Grazia Grimaldi

Additional information is available at the end of the chapter

http://dx.doi.org/10.5772/62620

Abstract

Water, together with energy and food, has been addressed as one of the main urgent problems of humanity. The conventional wastewater treatments suffer some limitations related to the effectiveness in decontamination (mechanical filtration), in the heavy use of chemicals (chlorination), or in elevation of operational costs and energy requirements (desalination and reverse osmosis). In this sense, new materials such as nanocomposites may overcome these issues taking advantage of the peculiar properties of materials at nanoscale. Research on novel nanotechnologies must bring advances in order to contrast and prevent water scarcity and pollution. In order to be effective, these nanotechnologies should run at low operational cost, even in places unequipped by strong infrastructures and in concert with conventional cheap methodologies.

Among the alternative water purification methods, TiO_2-based photocatalysis has attracted great attention due to material stability, abundance, non-toxicity and high decontamination efficiency. In this material, electron–hole pairs generated by light absorption separate from each other and migrate to catalytically active sites at the surface of the photocatalyst. Photogenerated carriers are able to induce the decomposition of organic pollutants as well as the deactivation of bacteria and viruses. The main deficiency of this material, related to its large bandgap, is that only the UV fraction of the solar spectrum which is effective to this purpose. Several approaches have been proposed to overpass this issue and, among them, the use of metal–TiO_2 nanocomposites with proper nanostructuration seems very promising for water purification strategies.

Keywords: TiO_2, photocatalysis, water purification, nanocomposites, plasmonics

1. Introduction

Among the alternative water purification methods, TiO_2-based photocatalysis has attracted great attention due to material stability, abundance, non-toxicity and high activity [1–3]. In this material, electron–hole pairs generated by a flux of photons, separated from each other and migrated to catalytically active sites at the surface of the photocatalyst. Photogenerated carriers are able to induce the water-splitting reaction and to decompose organic pollutants. Depending on the reaction path, highly reactive species (OH •,O_2^-,H_2O_2) can be created in solution. These reactants are able to decompose and mineralize most of the organic pollutants in solution as well as destroy bacteria [2]. The main deficiency of titanium dioxide relies on its wide bandgap (~3.2 eV) that makes it inefficient for solar-driven applications. However, proper nanostructuration of titanium dioxide and metal–TiO_2 nanocomposites have been demonstrated which is able to improve its efficiency, thus making this material an ideal candidate for water purification strategies.

Photocatalytic reactions are always the result of complex and concurring processes occurring on the surface at the nanoscale [2, 4]: (i) the absorption of light creating electron–hole excitations in a thin layer of a semiconducting compound, (ii) the separation followed by (iii) the transfer of these charges to the surface in contact with water or air, (iv) their interaction with organic or inorganic molecules located on this surface through oxidation and reduction reactions, leading finally (v), the electronic semiconductor system to recover its ground state. These processes are sketched in **Figure 1**. In this figure, an energetic photon generates a e^-/h^+ pair. The carriers can recombine at a surface trap (A) or in the bulk (B); otherwise, they can interact with acceptor (C) or donor (D) species adsorbed on the surface.

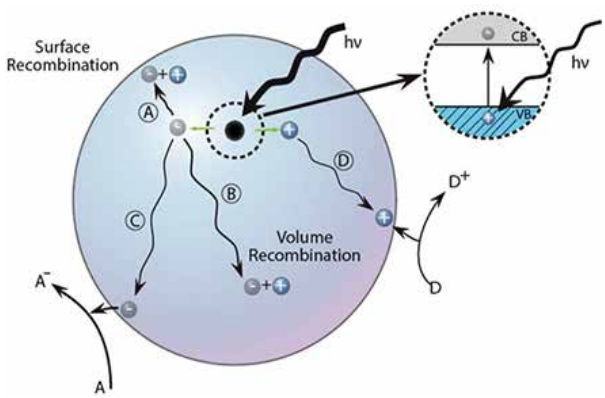

Figure 1. Schematic representation of the phenomena taking place in a semiconductor photocatalyst. The photogenerated carriers can recombine at a surface trap (A) or in the bulk (B); otherwise, they can interact with acceptor (C) or donor (D) species. Adapted with permission from Linsebigler et al. [5]. Copyright ©1995, American Chemical Society.

In **Figure 2** are reported the valence band (VB) and the conduction band (CB) positions (at pH = 0) for a range of semiconductors on a potential scale (V) versus the normal hydrogen electrode (NHE). As an example of the reactions taking place on the surface of the semiconductor, we

http://dx.doi.org/10.5772/62620

analyse more in depth the case of the water splitting. Dashed red lines in **Figure 2** represent the energy levels for the water-splitting half-reactions. For the water-splitting reaction to be thermodynamically favourable, the bandgap of the semiconductor photocatalyst should straddle these redox potentials, that is, the CB should have higher energy (more negative potential) than the hydrogen-evolution potential and the VB should be lower in energy (more positive potential) than the oxygen-evolution potential. So electrons can lower their energy being transferred to H^+ in solution and holes lower their energy being transferred to H_2O molecules through a short-circuited reaction and balancing the charges transferred to the solution. The final results are H_2 and O_2 molecules.

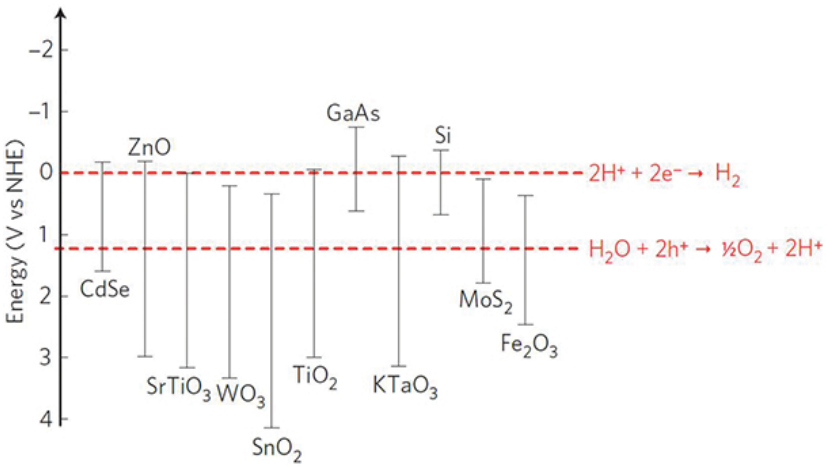

Figure 2. VB and CB for a range of semiconductors on a potential scale (V) versus the normal hydrogen electrode (NHE) at pH = 0. Redox potentials for the water-splitting half-reactions versus the NHE are also indicated by dashed red lines. Reprinted with permission from Linic et al [6]. Copyright ©2011, Macmillan Publisher Ltd.

Prior to the Honda–Fujishima effect in titanium dioxide [7], the interest in photocatalysis was centred on ZnO, which has similar CB and VB to TiO_2. The material is, however, limited by intrinsic photocorrosion upon excitation in aqueous media by the photoinduced hole weakening of Zn^{2+}–O^{2-} bonds to produce O_2 and soluble Zn^{2+} [8]. Hematite (α-Fe_2O_3) is another material that was originally thought to be an ideal photocatalyst due to its low cost, abundance and narrow bandgap for harnessing solar energy (bandgap = 2.0–2.2 eV, excitation wavelength up to 620 nm) [9]. However, the material suffers from rapid charge recombination (lifetime <10 ps) and a short charge carrier diffusion length (2–4 nm) [9]. Tungsten trioxide (WO_3) is another narrow bandgap material (bandgap = 2.7 eV) that has received fresh interest. The primary disadvantage of WO_3 lies in its low CB, which is below that required for the single-electron reduction of molecular oxygen [9]. Despite the narrow bandgap and the ideal position of VB and CB energy levels with respect to water-splitting semi-reactions potentials, CdSe (either in bulk or in quantum dot) is known to be toxic [10], thus is not suitable for pollution remediation in water.

The interest in titanium dioxide as the most studied photocatalytic material remains indisputable. This material has the advantage of being stable, abundant, non-toxic and highly active [1–3]. TiO_2 has three main polymorphs [11]: rutile (stable), anatase (metastable) and brookite (metastable). These have diverse activities for photocatalytic reactions, but the precise reasons for differing activities are a matter of debate and have not still been elucidated in detail. The most common studied phases are anatase and rutile. The commercial standard is the Aeroxide P25® (formerly Degussa P25). The P25 is a powder composed by a mixture of anatase (75%) and rutile (25%) [12]. There is a large debate in the literature claiming whether rutile or anatase is the best phase for photocatalytic reaction. Anatase seems to be more active than rutile [13], even if some studies suggest that the mixture of the two phases is the best compromise [14]. Moreover, one has to consider that, in view of decontamination strategies, the use of a photocatalyst fixed onto a substrate instead of a powder dispersed in solution may represent a clear advantage.

2. TiO_2-based photocatalysis

Photocatalysis is generally thought of as the catalysis of a chemical reaction induced by light at a solid surface. This implies that there must be at least two reactions occurring simultaneously, the first involving oxidation, from photogenerated holes, and the second involving reduction, from photogenerated electrons. Both processes must be balanced precisely in order to conserve the charge neutrality and for the photocatalyst itself not to undergo change (which is one of the basic requirements for a catalyst). In other words, photocatalysis is based on short-circuited photoelectrochemical reactions, balancing electrons and holes [2]:

$$h\upsilon \rightarrow e^- + h^+ \tag{1}$$

$$2H_2O + 4h^+ \rightarrow O_2 + 4H^+ \tag{2}$$

$$O_2 + 4H^+ + 4e^- \rightarrow 2H_2O \tag{3}$$

Because reduction or oxidation by the photoinduced charges of the reacting species involves electron transfer, these redox processes usually occur with species adsorbed to the surface. In competition with the charge carriers transfer processes, recombination takes place, either in bulk or at the surface. Retarding the recombination processes could effectively enhance the photocatalytic activity. Thereby, the presence of shallow trap centres at the surface could extend the mean lifetime of e^-/h^+ pairs. The typical timescale in photocatalytic reactions is reported in **Figure 3**.

http://dx.doi.org/10.5772/62620

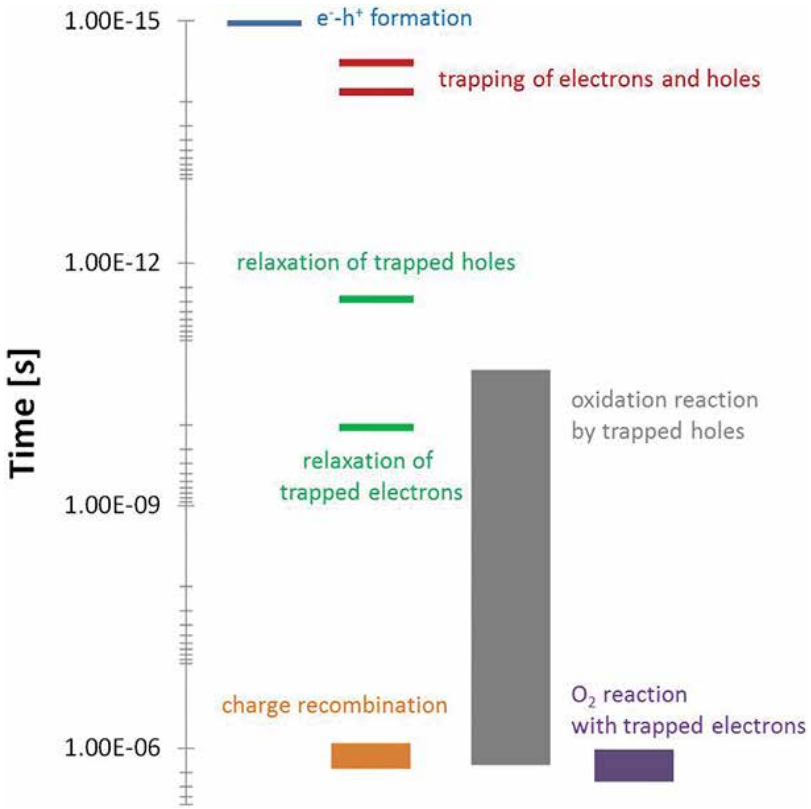

Figure 3. Time-scale in photocatalysis. Data taken 2008, Elsevier. with permission from Fujishima et al. [2].

Even in a perfect crystal, one observes the occurrence of a certain number of defects, especially at the surface. In particular, in TiO_2, the n-type behaviour is induced by the occurrence of oxygen vacancies [2]. In correspondence of these particular locations, there will be a trap centre for carriers, whose position in the band diagram will depend on the type of defect. Since h^+ are attracted by oxygen atoms in the lattice, while e^- are attracted by Ti^{4+}, one can state that defects which influence oxygen or titanium in the lattice correspond to level close to the VB or close to the CB, respectively. Actually, the most common defects in TiO_2 are represented by an oxygen vacancies and interstitial Ti [2]. The Ti^{4+} site left from this vacancy can attract an e^-, thus becoming a Ti^{3+} site. Non-coordinated Ti^{3+} on the surface is an ideal site for adsorption of oxygen [2]. Moreover, when two oxygen vacancies are close to the same Ti site on the surface, then the Ti atom can translate from its position, thus becoming an interstitial defect. Furthermore, interstitial Ti^{4+}, interacting with the oxygen of the TiO_2 lattice, is considered a trap for photogenerated holes [15].

In TiO_2 photocatalysis, surface adsorbed O_2 acts as the primary electron acceptor and no photocatalytic organic degradation is observed to occur in the absence of O_2 [4]. The reduction of O_2 has been demonstrated to be the rate-limiting step in semiconductor photocatalysis [4]. O_2 plays a critical role in enhancing photocatalysis by acting as an electron scavenger, thus

reducing e^-/h^+ pair recombination and forming highly oxidative species such as H_2O_2. These reactive oxygen species contribute to the oxidation of organic compounds by either directly attacking the organic or by producing hydrogen peroxide, which is a source of hydroxyl radicals that act as a strong oxidizer as shown in:

$$O_2 + 2e^- + 2H^+ \rightarrow H_2O_2 \rightarrow 2HO \quad (4)$$

In aqueous solutions, several different pathways have been suggested for O_2 reduction. For example, Hoffman suggested that O_2 first adsorbs to the TiO_2 surface before gaining an electron and then combines with two protons to form H_2O_2, which subsequently converts to hydroxyl species that degrade organic compounds [2, 4]. Nakamura proposed two mechanisms for this process; in the first one, an O^- on the TiO_2 surface transfers an electron to an O_2 in solution that then reacts with H^+ to form HO_2^- and eventually H_2O_2; in the second mechanism, an O_2 in solution adsorbs to a surface Ti^{4+} site by sequentially accepting two electrons and reacting with two protons to form H_2O_2 [16]. Similarly, Mattioli *et al.* suggested that O_2 accepts two electrons as it adsorbs on the TiO_2 surface and subsequently accepts two protons to form adsorbed H_2O_2, which then desorbs [17]. Surface adsorbed water or hydroxide anions act as the main hole acceptors in TiO_2 photocatalysis, although it has been suggested that certain organic materials may be directly oxidized by holes from TiO_2 [2, 4]. Indeed, holes are primary oxidizing species in photocatalytic reactions.

Most organic pollutant in water can be decomposed and mineralized on the surface of TiO_2 under UV irradiation. There are, obviously, several factors affecting the mineralization processes: light intensity, pH, ions dispersed in solution, etc. [2]. TiO_2 photocatalytic reactions reasonably follow first-order kinetics with respect to the concentration of the organic compound adsorbed, and α order with respect to light intensity [4]:

$$r = k\Gamma I^{\alpha} 5 \quad (5)$$

where r is the reaction rate, k the first-order constant, Γ the concentration of the organic compound for surface unity and I the light intensity. At high intensity $0 < \alpha < 1$, while at low intensity $\alpha = 1$.

Due to its wide bandgap, TiO_2 (either rutile or anatase) absorbs only in the UV range of the electromagnetic spectrum. However, sunlight contains a small amount of UV photons (~5%). Thus, in the last 20 years, several strategies have been developed, which devoted to increase the efficiency of titanium dioxide under visible (solar) irradiation. Among the most extensively studied methods, we cite the doping with N [18], transition metals [19] and C [20], the coupling with a narrow bandgap semiconductor quantum dots [21], the preparation of oxygen-deficient and/or hydrogen-rich TiO_x [22, 23] and the use of plasmonic metal nanostructures [6, 24]. We are interested, in particular, in these last two approaches.

http://dx.doi.org/10.5772/62620

3. Metal–TiO_2 nanocomposites

The typical response of a metal nanostructure excited by an electromagnetic wave is governed by the response of the electron gas in the metal. The simplest model describing the electron gas oscillations is similar to that of a damped harmonic oscillator. When matching the proper wavelength (frequency), it is possible to observe the so-called localized surface plasmon resonance (LSPR). LSPRs are non-propagating excitations of the conduction electrons of the nanoparticles (NPs). In the case of a spherical metal NP interacting with an incident electromagnetic wave, the response is determined by the particle polarizability [25]:

$$\alpha = 4\pi a^3 \frac{\varepsilon - \varepsilon_m}{\varepsilon + 2\varepsilon_m} \tag{6}$$

being a the particle radius, ε and ε_m the complex dielectric function of the metal and the embedding medium, respectively. The polarizability experiences a resonant enhancement under the condition that $|\varepsilon + 2\varepsilon_m|$ is a minimum, which for the case of small or slowly varying $\Im\{\varepsilon\}$ around the resonance simplifies to:

$$\Re\{\varepsilon(\omega)\} = -2\varepsilon_m \tag{7}$$

This relationship is called the Fröhlich condition and the associated mode (in an oscillating field) the *dipole surface plasmon* of the metal NP. In the quasi-static approximation ($a \ll \lambda$), a metal NP can be represented as an ideal dipole and spatial retardation effects over the particle volume can thus neglected. The scattering and absorption cross sections, calculated via the Poynting vector, are given by [25, 26]:

$$\sigma_{sca} = \frac{k^4}{6\pi}|\alpha|^2 = \frac{8\pi}{3}k^4 a^6 \left|\frac{\varepsilon - \varepsilon_m}{\varepsilon + 2\varepsilon_m}\right|^2 \tag{8}$$

$$\sigma_{abs} = k\Im\{\alpha\} = 4\pi k a^3 \Im\left\{\frac{\varepsilon - \varepsilon_m}{\varepsilon + 2\varepsilon_m}\right\} \tag{9}$$

where $k = \frac{2\pi}{\lambda}$ is the wavenumber.

For noble metals, silver and gold, in air the resonance is observed in the visible region of the electromagnetic spectrum. Indeed, the wavelength (energy) at which plasmon resonance occurs strongly depends on the metal. At a fixed electron density (i.e. for a certain metal), the plasmon resonance peak depends on the shape and on the dimension of the nanostructure [27–29].

In **Figure 4** the experimental data for Ag nanostructures having different shapes are shown. In general, it is not obvious to predict how a certain shape will influence the position of the resonance peak.

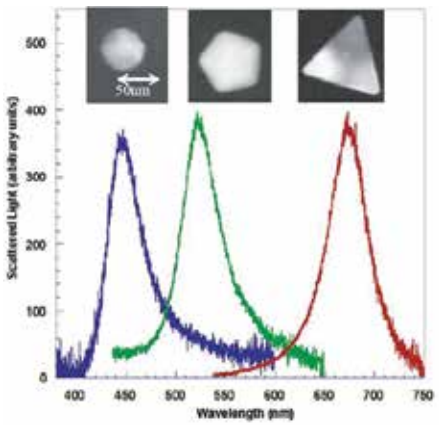

Figure 4. Experimental optical spectroscopy measurements of individual Silver nanoparticles having different shapes. Reprinted with permission from Mock et al. [28]. Copyright ©2002, AIP Publishing LLC.

However, asymmetric and complex shapes can reveal several resonances, depending on the polarization of incident light [27,30]. In **Figure 5** are reported the UV–Vis spectra of Ag nanoplatelets whose transversal size is fixed (20 nm), while the longitudinal length varies in the range between 65 and 92 nm [30]. These data are interesting since it is possible to observe two resonance peaks. The first one, located at about 400 nm, is fixed for all the samples and is related to the transversal size of the nanostructures. The second one red shifts from about 500 nm to about 650 nm and, at the same time, broaden as the longitudinal dimension increases.

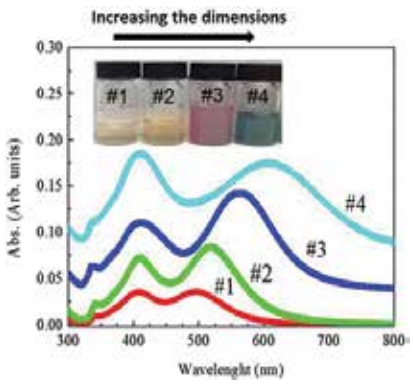

Figure 5. UV–Vis spectra of different Ag nanoplatelet solutions. The nanoplatelets have a transversal size of 20 nm and a longitudinal length in the range 65–92 nm (growing from sample #1 to sample #4). In the inset, a photograph of the corresponding solutions is shown. Reprinted with permission from Zimbone et al. [30]. Springer.

http://dx.doi.org/10.5772/62620

Two mechanisms occur as the nanostructure size increases: a red shift and a broadening of the resonance peak [31]. The first one is due to the *dynamic depolarization*: increasing particle dimensions, conduction electrons no longer move in phase, reducing the depolarization field and thus the restoring force, causing a red shift of the resonance. The second one is due to the *radiative damping*: as scattering becomes significant, this re-radiation leads to a radiative damping correction to the quasi-static polarizability and the effect of which is to significantly broaden the plasmon resonance.

The red shift and broadening of the resonance with increased NP size would generally be expected to be an advantage for solar-driven applications, since it translates in an enlarged absorption of the visible spectrum.

As already pointed out, the dielectric constant of the embedding medium also dramatically influences the plasmon resonance and its quality factor [27]. In **Figure 6** are reported the simulations of the extinction spectra of a silver sphere having diameter of 3 nm immersed in air (refractive index $n = 1$), glass ($n = 1.4$) or TiO_2 ($n = 2.7$). The simulations clearly show how the plasmon peak shifts to higher wavelengths (lower energies) as the refractive index increases. At the same time, one observes an increase of the quality factor of the resonance, due to a higher confinement of the electric field.

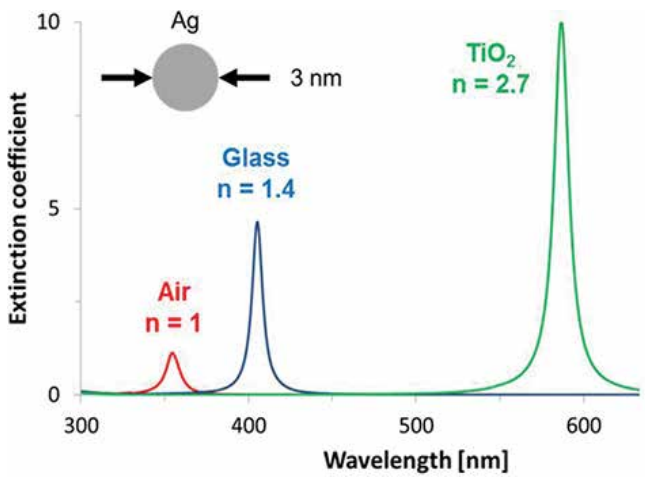

Figure 6. Simulation of the extinction spectra versus wavelength of a silver sphere having diameter of 3 nm immersed in air (red), glass (blue) or TiO_2 (green). The refractive index (at the resonance peak wavelength) of each medium is also reported.

As previously mentioned, in the neighbouring of the plasmonic metal, NP one observes a high enhancement of the electromagnetic field, in particular during the occurrence of a LSPR. Such a high rise in the intensity of the field can, in principle, lead to nonlinear effects both in the metal particle and in the embedding matrix. In **Figure 7** is reported the simulated magnitude of the electromagnetic field in the vicinity of a silver nanocube of diameter 75 nm, at a wavelength of $\lambda = 420$ nm matching the plasmon resonance [6]. The field intensity is redis-

tributed leading to a region where the field enhancement reaches a factor up to 10^3 times the incident intensity.

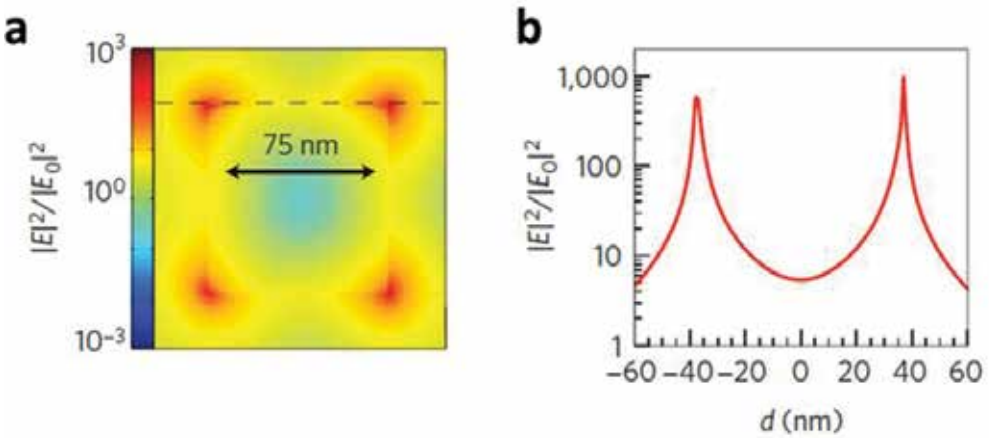

Figure 7. (a) Spatial distribution of the LSPR-induced enhancement of electric field intensity at the LSPR peak wavelength (420 nm), from a finite-difference time-domain (FDTD) simulation of a 75-nm Ag nanocube. (b) Enhancement in the electric field intensity at the LSPR peak wavelength as a function of distance *d* along the dashed line indicated in (a). Reprinted with permission from Linic et al [6]. Copyright ©2011, Macmillan Publisher Ltd.

The field enhancement is particularly strong (up to a factor 10^4 with respect to the exciting electromagnetic field) inside metal gaps, that is in the space between two metal nanostructures close (few nm) each other [32, 33].

As previously mentioned, one of the main deficiencies of TiO_2 relies on its wide bandgap. In order to enhance the material efficiency in the visible range of the electromagnetic spectrum, surface-plasmon-mediated photocatalytic activity of TiO_2 has become a hot research topic [6, 24, 34–40].

As depicted in **Figure 8**, metal nanostructures in the presence of an external exciting electromagnetic field can interact with a photoactive substrate at least in three different ways [41]:

1. the far-field component of the scattered field will induce a prolonged optical path for photons and thereby will increase the probability of absorption within the semiconductor substrate;

2. the near-field component of the field can cause an enhancement of the field intensity in the vicinity of the nanostructure, thus leading to nonlinear effects as well as local heating effects;

3. as a consequence of the metal–semiconductor junction, a direct injection of photoexcited carriers into the substrate can occur as well as a charge separation process due to the Schottky barrier.

http://dx.doi.org/10.5772/62620

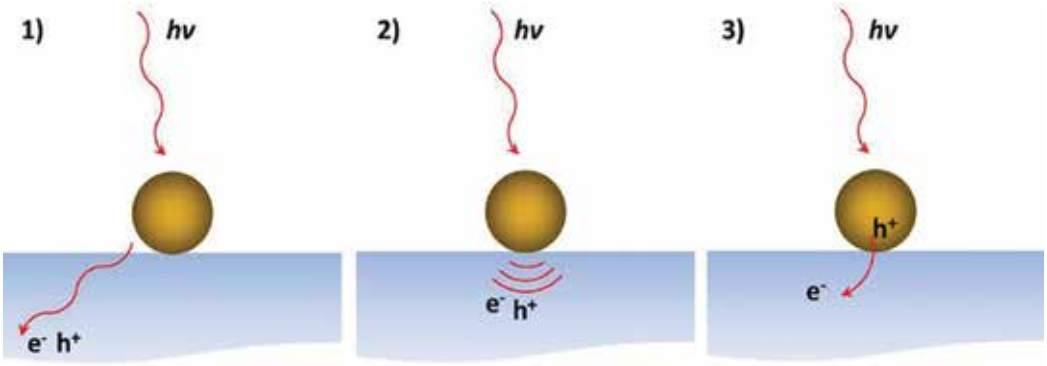

Figure 8. Schematic of different interactions between a metal nanoparticle and a photoactive substrate: (1) far-field scattering, (2) near-field scattering and (3) direct injection of photoexcited carriers into the semiconductor.

For photocatalysis, the last two effects are particularly important. The advantage of the formation of e^-/h^+ pairs, close to the semiconductor surface, is that these charge carriers are readily separated from each other and easily migrate to the surface, where they can perform photocatalytic transformations.

Experimental evidences of the improvement in the photocatalytic activity under visible irradiation have been recently reported [6, 24, 34, 42, 43]. In **Figure 9** is reported the comparison between oxygen and hydrogen evolution from solution of Ag–TiO_2 and bare TiO_2 nanocomposites upon illumination with a broadband visible source (400–900 nm, ~500 mW/cm^2, spectral peak at 580 nm) [42]. The solution was prepared mixing a colloidal solution of Ag nanocubes with nitrogen-doped TiO_2 (N–TiO_2) solution. The composite was 5% metal by weight.

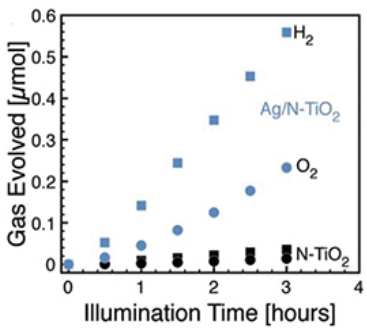

Figure 9. H_2 (squares) and O_2 (circles) production upon visible illumination of N–TiO_2 (black symbols) and Ag/N–TiO_2 (blue symbols) photocatalysts, as measured by mass spectrometry. Reprinted with permission from Ingram and Linic [42]. Copyright ©2011, American Chemical Society.

The presence of silver nanostructures is responsible for the enhancement in the activity of the photocatalyst through charge injection. According to this model, electrons near the metal Fermi

level E_f are excited to surface-plasmon (SP) states; then, after the relaxation of the plasmon oscillations, some electron can transfer to the nearby semiconductor and, at this point, activate electron-driven processes such as the hydrogen-evolution half-reaction [6, 44] (**Figure 10**).

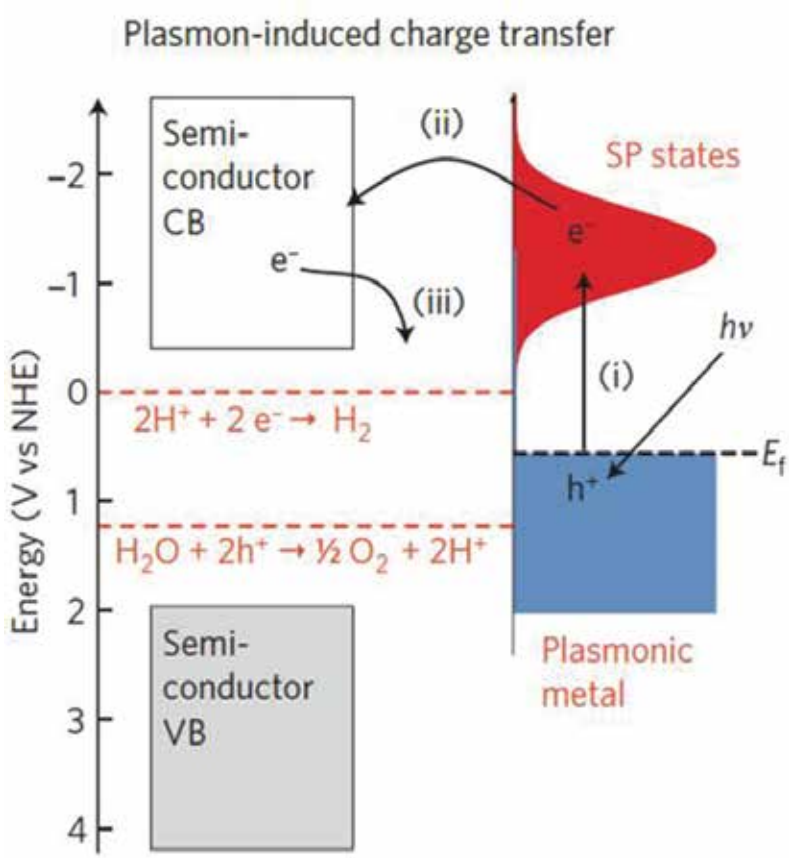

Figure 10. Mechanism of LSPR-induced charge transfer with approximate energy levels on the NHE scale. Dashed red lines refer to the water-splitting redox potentials (see **Figure 2**). Reprinted with permission from Linic et al [6]. Copyright ©2011, Macmillan Publisher Ltd.

In another experiment conducted by Liu et al. [43], the enhancement in the photoactivity of an Au–TiO_2 nanocomposite film is explained in terms of the local electric field enhancement near the TiO_2 surface, rather than by the direct transfer of charge between the two materials. According to the authors, in this case, the near-field optical enhancement increases the electron–hole pair generation rate at the surface of the TiO_2. In **Figure 11a–d** are reported the finite-difference time-domain (FDTD) simulations on a 5-nm thick Au film onto TiO_2 substrate, showing the presence and distribution of region of high electromagnetic field intensity (*hot spots*) within metal gaps. In **Figure 11e, f** are reported the experimental photocurrent measurements emphasizing the better performance of the Au–TiO_2 composite film in the spectral range of interest for LSPR in gold (red region of the visible spectra).

http://dx.doi.org/10.5772/62620

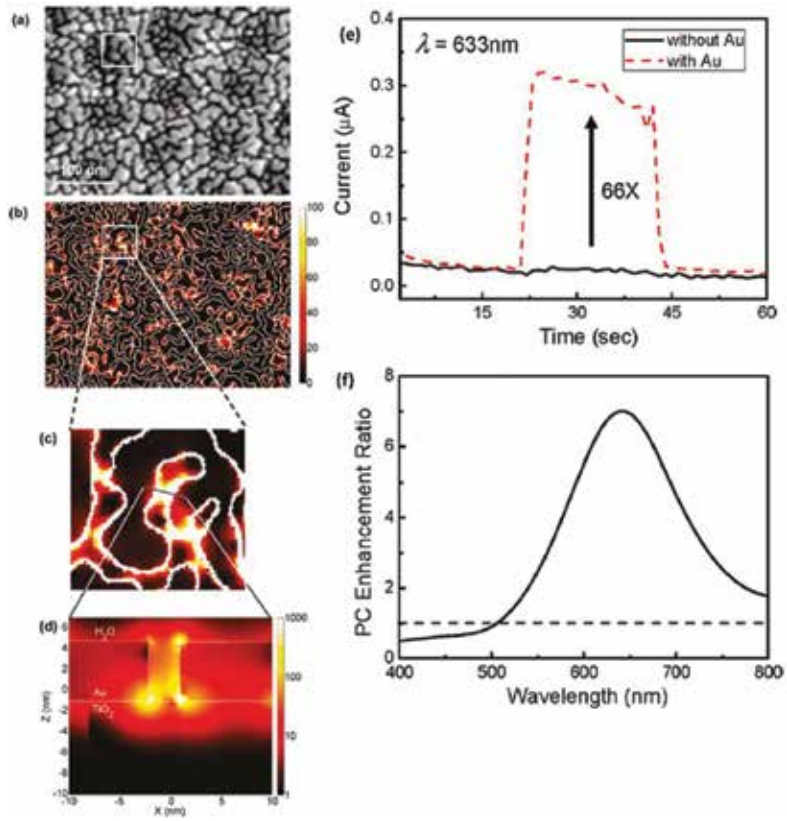

Figure 11. On the left, (a) SEM image of a 5-nm thick Au island film on TiO_2; FDTD-simulated electric field intensity, in the plane xy (b, c) and in a vertical section (d). On the right, (e) photocurrent of anodic TiO_2 with and without Au nanoparticles irradiated with λ = 633 nm light for 22 s; (f) photocurrent enhancement ratio spectrum; the dashed line refers to the bare TiO_2 (value 1). Reprinted with permission from Liu et al. [43]. Copyright ©2011, American Chemical Society.

However, it has been also proposed a photocatalytic reaction directly on the surface of the plasmon-excited metal NP [37, 44, 45]. In this picture, excited NP inject hot electrons to the states (orbitals) of the adsorbed species (reactants). It is a process similar to charge injection but without the mediation of the semiconductor material.

Whatever the process involved, it seems clear that the presence of metal nanostructures can effectively improve the efficiency under visible (solar) irradiation.

4. Optical engineering of Ag/TiO_2 nanocomposite films

4.1. Field enhancement engineering

In order to introduce the concept of field enhancement, let us consider a perfect mirror with a film of refractive index n grown on its surface. Let us consider a monochromatic wave in

normal incidence on this film. It is well known that an electromagnetic wave, passing through a film and being reflected backward, will undergo to a phase shift δ:

$$\delta = \frac{2\pi t}{\lambda_n} \tag{10}$$

where t is the film thickness and λ_n the wavelength in the medium. When measuring the reflectivity of a thin film on substrate, we obtain constructive interference for $2\delta = 2\pi m$, destructive interference for $2\delta = (2m + 1)\pi$, being m an integer. Thus, the thicknesses at which destructive or constructive interference occur are given by:

$$t = \frac{m\lambda_n}{2} \tag{11}$$

$$t = \frac{(2m+1)\lambda_n}{4} \tag{12}$$

It is worth noting that in destructive interference conditions, the electromagnetic field intensity at the air–film interface is at maximum. Indeed, in stationary state, thus considering the incident and reflected beam, we observe a node at the (perfect) mirror–dielectric interface; if we look at the intensity of the electromagnetic field ($\propto E^2$) versus the distance from the mirror, we can observe a maximum of the intensity of field at:

$$d = \frac{(2m+1)\lambda_n}{4} \tag{13}$$

Note how this distance equals the condition in Eq. (12), stating the antireflectivity conditions (i.e. destructive interference).

In **Figure 12** are shown the calculation made by Bayle et al. [46] in the case of a SiO_2/Si substrate. In this case, the wavelength in vacuum is chosen at 413 nm (in coincidence with the plasmon frequency of Ag NPs in SiO_2), the thickness of the layer is 210 nm (matching the antireflectivity conditions for the chosen wavelength), the incidence is normal. Firstly, one observes that, under these antireflectivity conditions, the intensity of the total electromagnetic field reaches the maximum at the air/SiO_2 interface. Indeed, in **Figure 12a**, the total electromagnetic field (resulting from incident and reflected electromagnetic waves) shows a maximum at the free surface of the matrix: the film thickness matches the condition (**Figure 12**), that is equal to the result in Eq. (13). This means that the film is in antireflective conditions. In **Figure 12b, c**, a layer of Ag nanocrystals (NCs) (the particles diameter 5 nm and the amount of silver equals 5×10^{16} atoms/cm^2) is placed into the oxide matrix. As it is possible to observe from the total electromagnetic field intensity, the same layer of Ag NPs can show or not an enhanced optical

http://dx.doi.org/10.5772/62620

response depending on the position, respectively, at a minimum (**Figure 12b**) or at a maximum (**Figure 12c**) of the field.

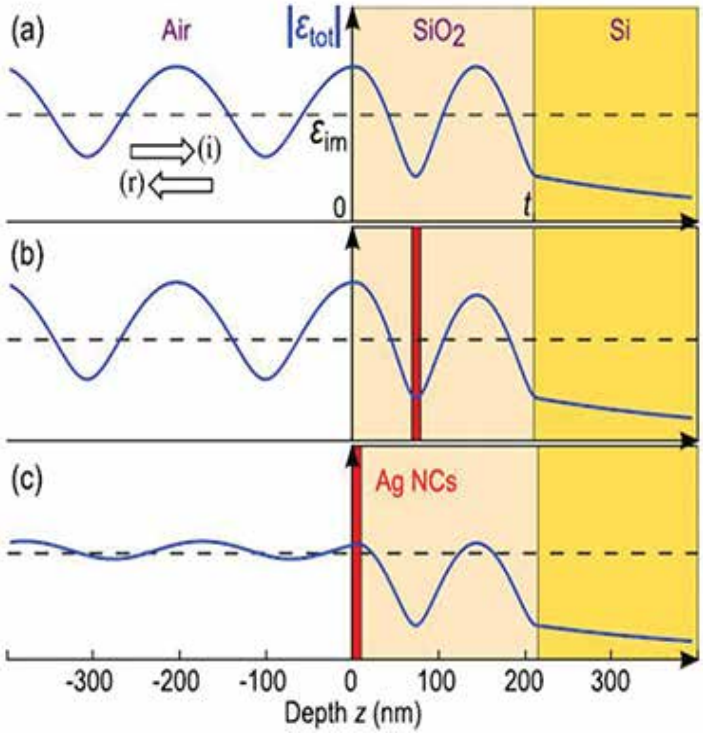

Figure 12. Variation versus depth of the amplitude of the total (incident *i* + reflected *r*) electric field $|E_{tot}|=|E_i + E_r|$: (a) without Ag NCs, (b) with a plane of Ag NCs located at a node of the electric field into the dielectric layer, and (c) with this plane located at an antinode of the electric field near the dielectric/air interface. Reprinted with permission from Bayle et al. [46]. Copyright ©2014, American Physical Society.

Therefore, engineering the architecture of the stacking layers is the key to take simultaneous advantage of spectrally and spatially LSPR but also of field enhancement. This has been recently proposed for enhanced spectroscopy and imaging by Carles et al. [47].

By choosing an appropriate thickness of a TiO_2 layer deposited on a silicon substrate, one can easily tune the spectral position of one of the antireflective minima in such a way it can match the LSPR. In particular, in **Figure 13b** is shown the extinction efficiency of a silver nanosphere (3 nm in diameter) embedded in air ($n = 1$), SiO_2 ($n \approx 1.4$) or TiO_2 ($n \approx 2.7$). We can observe how the LSPR red shifts and, at the same time, increases its quality factor as the refractive index of the embedding medium increases. This is due to the higher confinement of the electromagnetic field in high-refractive-index materials [26, 27]. In **Figure 13a** is shown the reflectance of a SiO_2 (or TiO_2)/Si heterostructure with embedded a Ag NPs layer. By choosing the proper film thickness, that is matching the antireflectivity conditions for the wavelength at which plasmon resonance occurs, it is possible to obtain an enhanced optical response from the NPs layer.

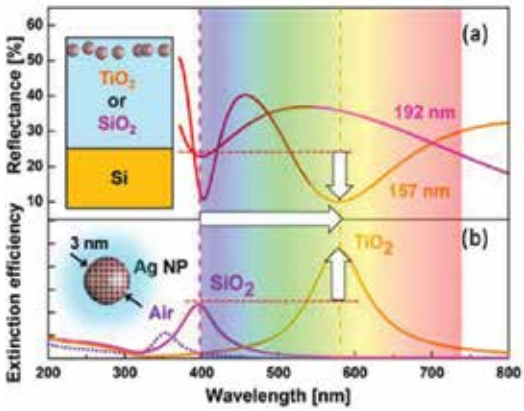

Figure 13. Theoretical simulation illustrating the tuning of anti-reflectivity condition in a TiO_2/Si heterostructure and LSPR in a silver nanoparticle of diameter D = 3 nm. Reproduced with permission from Cacciato et al. [40]. The Royal Society of Chemistry.

The aim of the work presented in this section was to take benefit of this phenomenon in multilayer stacking containing TiO_2 and embedding Ag NPs. They will be adapted to manage amplifying processes in the visible range by exploiting simultaneously the resulting optical interference phenomenon and LSPR.

4.2. TiO_2 subsurface embedded Ag NPs obtained via low energy ion beam synthesis

In our recent work [40], we demonstrated the importance of the optical engineering of the substrate supporting Ag NPs. Indeed, using low-energy ion implantation, we prepared a Ag/TiO_2 nanocomposite film showing a huge optical response when irradiated with a wavelength close to that of LSPR of Ag NPs. In **Figure 14**, a transmission electron microscopy (TEM) image of the as-implanted sample matching the field enhancement conditions is shown. A band of silver NPs 3 nm in diameter is evident few nm close to the free surface of the hosting TiO_2 matrix.

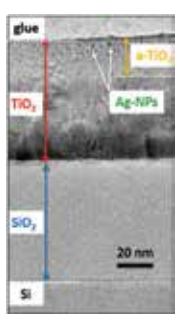

Figure 14. TEM cross-section image of Ag/TiO_2 sample, observed in bright field, showing the different stacked layers. Adapted with permission from Cacciato et al. [40]. The Royal Society of Chemistry.

http://dx.doi.org/10.5772/62620

More important, in this nanocomposite, the fingerprint of the charge injection from the NPs inside the TiO_2 matrix was revealed by means of Raman spectroscopy. In **Figure 15** are reported the Raman spectra of the Ag/TiO_2 samples under plasmon-resonant (532 nm) or out of resonance (638 nm) excitation. In order to demonstrate the importance of the optical engineering of the TiO_2 substrate, two different thicknesses were used, matching the field enhancement conditions (TiO_2 90 nm) or out of these conditions (TiO_2 165 nm). The spectra of the bare TiO_2 substrate are also reported for comparison. Focusing on the spectra in plasmon-resonant excitation, it is possible to observe the high enhancement in the response of the Ag/TiO_2 film matching the antireflective conditions (blue spectra). With respect to the bare TiO_2, which shows the characteristic peaks of rutile TiO_2 and Si, the Ag/TiO_2 spectra reveals the presence of new peaks. The peaks in the region below 200 cm^{-1} belongs to Ag phonons, as already observed in Ag nanocrystals in other dielectrics [46]. The bands at higher Raman shifts, between 650 and 900 cm^{-1}, are addressed to LO phonon–plasmon modes. This signal is absent out of resonance and without Ag NPs. These modes are due to the presence of free carriers injected in the TiO_2 matrix [40]. Similar electrons transfer from metallic NPs to a polar semiconductor is known in n- or p-doped semiconductors [48, 49] and high-Tc superconductors [50]. These modes have been also observed with IR reflectance spectroscopy in non-stoichiometric rutile [51] and anatase [52, 53].

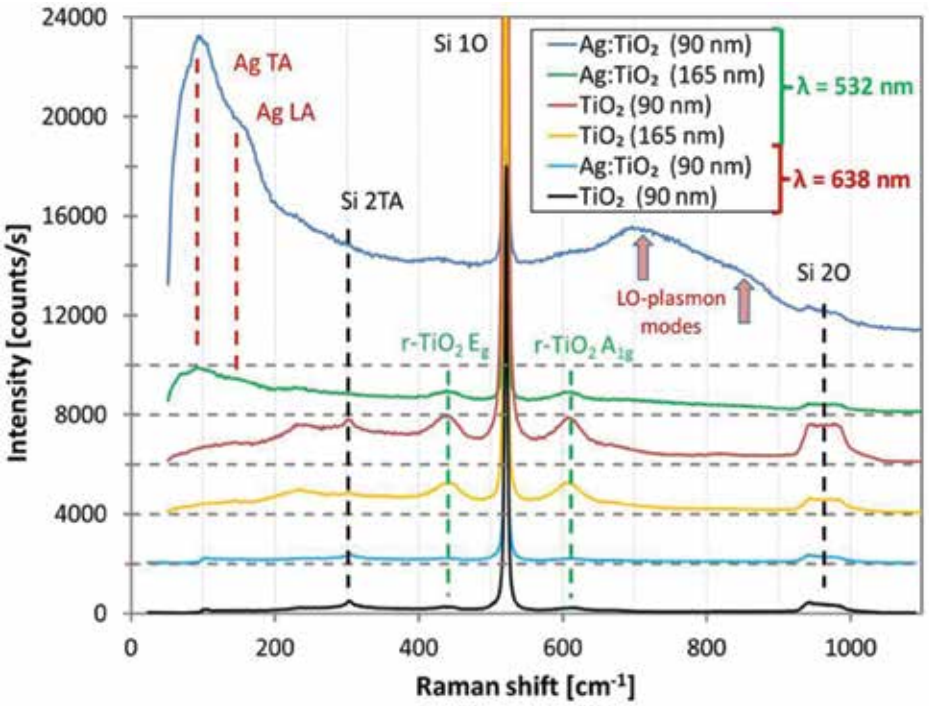

Figure 15. Raman spectra recorded on Ag/TiO_2 and bare TiO_2 of samples matching the field enhancement conditions (TiO_2 90 nm) or out of these conditions (TiO_2 165 nm) under plasmon-resonant excitation (532 nm) or out of resonance (638 nm). Reproduced with permission from Cacciato et al. [40]. The Royal Society of Chemistry.

Unfortunately, the photocatalytic tests did not show an activity enhancement induced by the implantation process and the presence of Ag NPs. On the contrary, a strong reduction was observed, probably due to charge carrier recombination on defects generated by the implantation process: the synthesis technique seems to damage irremediably the upper layer of the hosting TiO_2 matrix. Therefore, the consequent step should be to use a proper optically engineered substrate with embedded metal NPs through a technique that preserves the photoactive material. This will be the content of the next paragraph.

4.3. TiO_2/Ag/TiO_2 nanocomposite film obtained via sequential sputtering

The exposure of a photocatalytically active surface has been demonstrated of primary importance for the goal of efficient substrates for water purification [54]. At the same time, the optical engineering of the substrate can highly improve the response of the nanocomposite in the visible range, as reported in the previous paragraph. Therefore, the logical step towards solar-driven photocatalysis is to fabricate a TiO_2/AgNPs/TiO_2 multilayer using a technique that allows fine tuning of several parameters (particle size and position, thickness of each layer), while preserving the quality of the photoactive surface. For these reasons, we proposed sequential sputtering and annealing as methodology to elaborate a TiO_2/Ag/TiO_2 nanocomposite film [55]. In this case, the NPs synthesis occurs through the dewetting of the metal film. The dewetting is a process according to which the metal film deposited onto a substrate retracts under the action of the surface tension. The process is governed by the surface free energy of the metal, the substrate and the metal/substrate interface [56]. This mechanism is somehow similar to the formation of water droplets onto a hydrophobic surface. In **Figure 16** is shown a schematic representation of the steps followed to realize of the nanocomposite film: (a) realization of the TiO_2 'matrix' layer (realized for the antireflective propose), (b) deposition of the Ag film, (c) thermal annealing in order to realize the silver NPs through dewetting and (d) deposition of the TiO_2 protective layer.

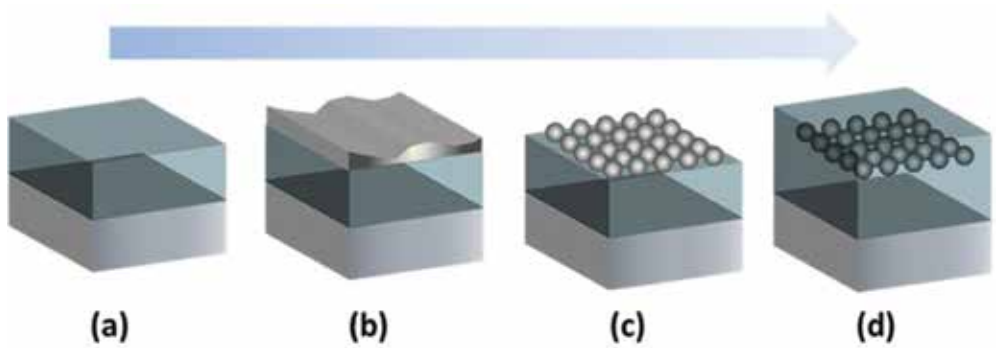

Figure 16. From left to right, schematic representation of the elaboration process: (a) TiO_2 substrate preparation, (b) Ag deposition, (c) nanostructuration via thermal annealing and (d) deposition of a TiO_2 capping layer.

A Ti film was grown by sputtering on Si <100> substrates. Polycrystalline (rutile) TiO_2 was obtained, starting from these substrates, by thermal oxidation at 600°C. Ag depositions on the

http://dx.doi.org/10.5772/62620

polycrystalline TiO_2 were carried out. A nominal thickness of d = 5 nm of Ag was deposited. After Ag depositions, samples were annealed in vacuum, at 400°C. The final 10 nm TiO_2 capping layer has been obtained via deposition of a thin Ti film followed by a thermal annealing at 400°C for 30 min in vacuum. Due to the low deposition rate, the deposited layer is already oxidized, so that the thermal annealing was required just to ensure the crystallinity of the capping layer. Anyway, this step has not influenced the underlying Ag nanostructured film.

Scanning electron microscopy (SEM) images in **Figure 17** clearly show the nanostructuration of the metal film (from **Figure 17b, c**) and then the conformal coverture of the final 10 nm thick TiO_2 layer (from **Figure 17c, d**).

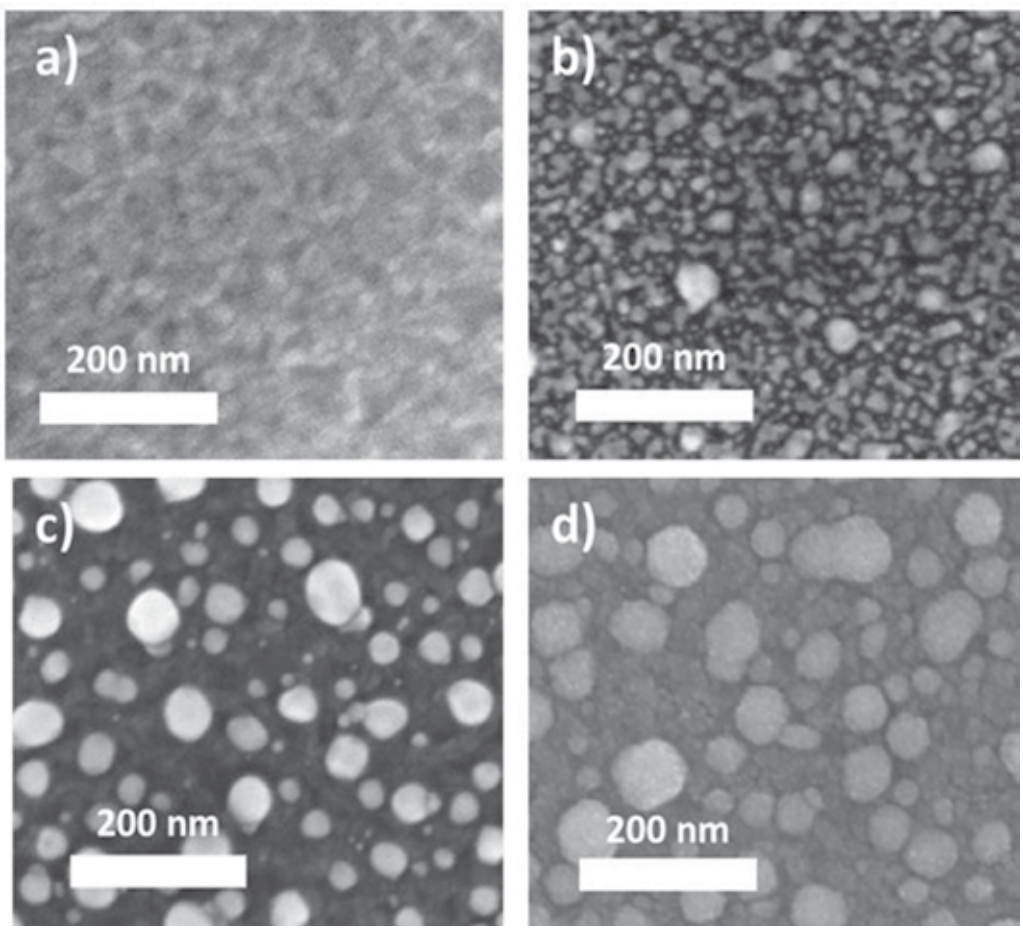

Figure 17. SEM images (plan view) of (a) the TiO_2 substrate, to (b) the Ag as deposited film, (c) the Ag/TiO_2 after annealing and finally, (d) the TiO_2 capping layer.

In order to have more insight on the photocatalysis, we tested the photoactivity of our samples by means of the discoloration of methylene blue (MB) dye. For the photocatalytic activity tests, we referred to the guidelines of the ISO 10678:2010 [57, 58]. The results of the test are summarized in **Figure 18**, where the discoloration rate normalized to the surface area is reported. We compared three samples: a TiO_2 10 nm/Ag NPs/TiO_2 190 nm nanocomposite in field enhancement conditions at the plasmon resonance wavelength of the obtained Ag NPs; a TiO_2 10 nm/Ag NPs/TiO_2 165 nm nanocomposite out of field enhancement conditions; a TiO_2 10 nm/TiO_2 165 nm whose last 10 nm where prepared in the same conditions as the capping layer of the Ag NPs of the nanocomposite samples. MB degradation occurs under irradiation; therefore, we reported also the degradation of a vessel not containing photocatalytic material as reference.

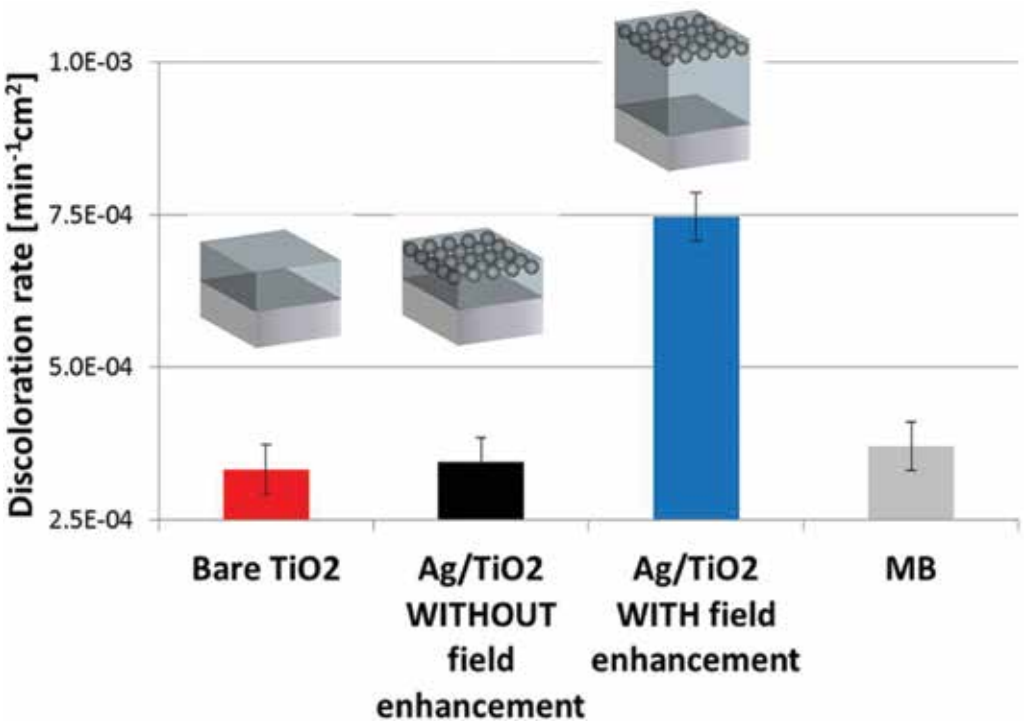

Figure 18. Discoloration test results under visible irradiation.

We observe that, as expected, TiO_2 is not active under visible illumination. The fundamental result of the test is that, despite having the same composition and superficial morphology, the two TiO_2/Ag/TiO_2 nanocomposite film show completely different behaviour. In particular, the film matching the antireflectivity conditions is able to decompose the MB dye, showing a good photocatalytic activity in the visible range, while the film outside these conditions appears to be not active. These results underline the importance of a proper optical engineering of the supporting matrix for plasmon enhanced applications.

http://dx.doi.org/10.5772/62620

4.4. Summary

We obtained an Ag/TiO_2 nanocomposite activated by visible irradiation. Such an activity, occurring at irradiation energies below the absorption threshold of titania (gap) and thus not observable in the bare TiO_2 film, has been ascribed to the presence of plasmonic metal NPs. Moreover, we observed a strong correlation between photocatalytic activity and field enhancement conditions. Therefore, we demonstrated the importance of proper film thickness engineering in order to take simultaneous advantage of plasmon resonances and optical interference. Actually, this result had been already demonstrated in [40], at least from the optical point of view. Such substrates are ideal candidates for solar-driven photocatalytic reactions. This result is actually more general and could be potentially employed in other plasmo-electronic applications (e.g. SERS,…).

5. Amorphous hydrogenated TiO_2 NPs

The second approach we want to suggest is based on the use of TiO_2 NPs. On the one hand, using NPs, the exposed surface increases of order of magnitude with respect to a photocatalytic film; on the other hand, issues related to the dispersion of the nanomaterial in the environment or to the recovery of the particles from the solution may arise.

Titanium oxides NPs can be obtained in different phases, depending on the employed synthesis method. Whereas bulk amorphous phase is generally considered to have negligible photocatalytic and antibacterial activity, recent research works pointed out the importance of the presence of an amorphous layer to boost the photocatalytic performance of TiO_2 [22]. Hydrogenated TiO_2 has attracted attention due to its optical absorption and high activity [23]. Unfortunately, the proposed synthesis method requires high pressure of hydrogen (up to 20 bar) and long annealing treatments (up to 15 days) [23]. As already mentioned, photoactivity can be ready to improved with metal grafting. Indeed, when in contact with small metal cluster, the charge separation and transfer process are faster and thermodynamically favoured [2, 59].

Recently, we proposed an alternative, industrially compatible, scalable and environmental friendly technique such as pulsed laser ablation in liquid (PLAL) for the synthesis of TiO_2 NPs in solution [58, 60]. In this work, we synthetized amorphous TiO_2 NPs characterized by a high degree of hydrogenation and high photocatalytic and antibacterial activity.

5.1. TiO_2 NPs obtained via laser ablation

The experimental details of the synthesis can be found in [58]. In **Figure 19**, representative TEM and SEM images of the TiO_2 NPs are reported. According to the electron microscopy, the particles resulted amorphous with a broad distribution in size (typical of the PLAL methodology).

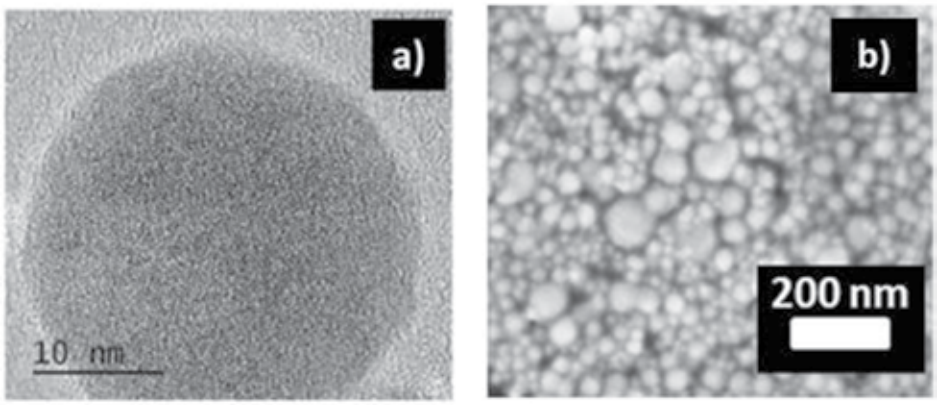

Figure 19. TEM (a) and SEM (b) images of LA-NPs. Reprinted with permission from Zimbone et al. [58]. Copyright ©2015, Elsevier.

This was further confirmed by the Raman analysis showing the characteristic convolution of peaks of the amorphous phase. In **Figure 20**, the Raman spectrum of LA-NPs is reported in comparison with the spectra of amorphous and crystalline (anatase or rutile) TiO_2.

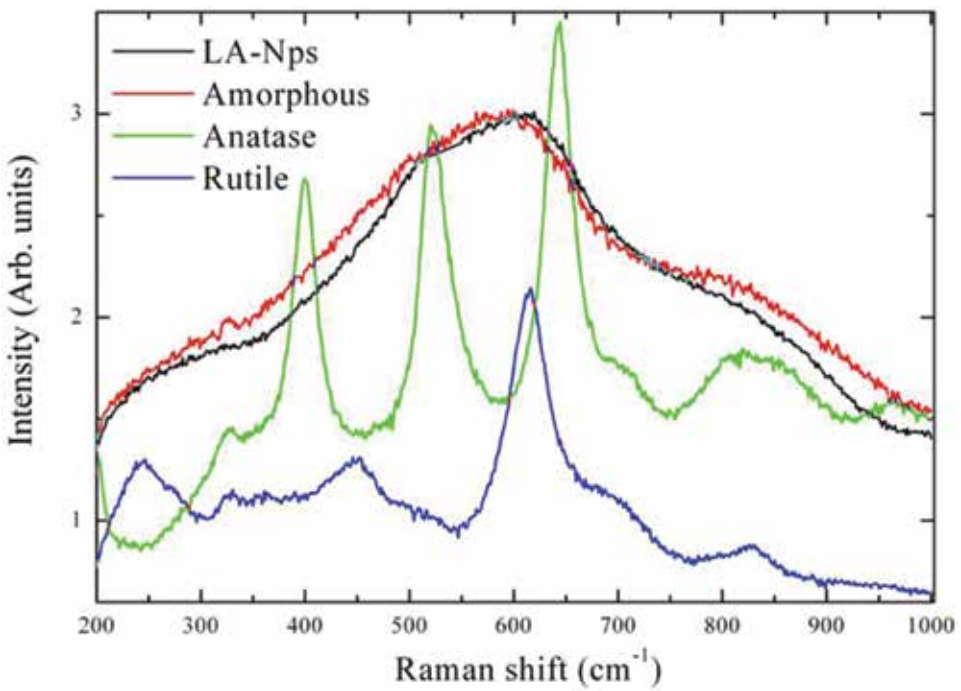

Figure 20. Raman response of LA-NPs compared with that of amorphous, rutile and anatase TiO_2 samples. Reprinted with permission from Zimbone et al. [60]. Copyright ©2016, Elsevier.

http://dx.doi.org/10.5772/62620

It is worth noting that the presence of hydroxyl groups in the TiO_2 NPs obtained via laser ablation (LA-NPs) has been evidenced by FTIR spectroscopy measurements. In **Figure 21**, the FTIR spectra of LA-NPs were compared with that of commercial TiO_2 NPs (C-NPs).

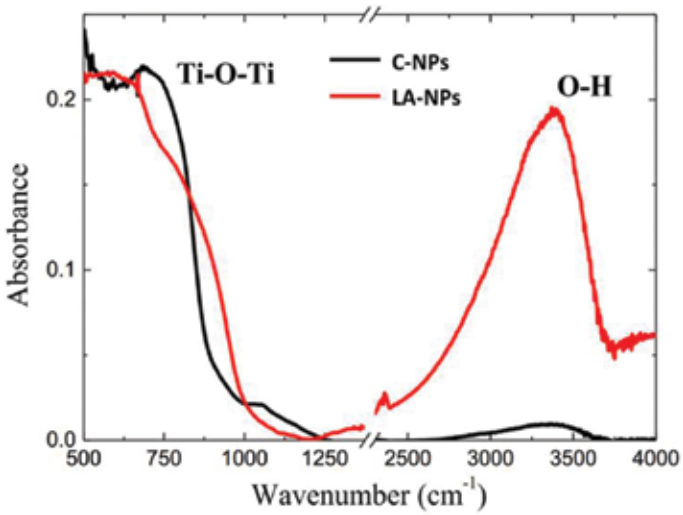

Figure 21. FTIR spectra of crystalline TiO_2 (C-NPs), and laser ablated nanoparticles (LA-NPs). Ti–O–Ti vibration and O–H stretching bands are referred in the Figure. Reprinted with permission from Zimbone et al. [60]. Copyright ©2016, Elsevier.

Hydrogen is identified by OH stretching at about 3400 cm^{-1} in FTIR spectra, as previously reported by Johnson et al. [61]. In the spectral range sampled in **Figure 21**, we clearly observe the typical absorption of TiO_2 in the 500–1000 cm^{-1} range and a strong absorption at 3000–3500 cm^{-1} due to the hydroxyl vibration. The amount of hydroxyl groups is directly related to the amount of hydrogen in or on the NPs surface [61]. In order to compare the amount of OH in LA-NPs and C-NPs, we can normalize the spectra to the TiO_2 signal in both samples. The number of hydroxyl groups in LA-NPs is found to be about one order of magnitude greater than the crystalline samples. We can state that pulsed laser ablation in water resulted in the formation of nm-sized hydrogenated TiO_2 NPs.

As reported in [58], photocatalytic activity of LA-NPs was found to be comparable to commercial crystalline NPs, while the antibacterial activity was found to be higher. These results are interpreted in terms of disorder and hydrogen inclusion in the structure of TiO_2 NPs. Interestingly, the mixture of LA-NPs with metal (Ag) NPs has been demonstrated to further improve their photocatalytic efficiency, as discussed in the next paragraph.

5.2. Ag/TiO_2 mixture

The synthesis of silver NPs (Ag-NPs) was performed by the PLAL method [55]. In **Figure 22** is shown a SEM image of the Ag-NPs. The particles appear spherical and have an average diameter of 25 ± 1 nm. From XRD, the presence of metallic Ag is confirmed.

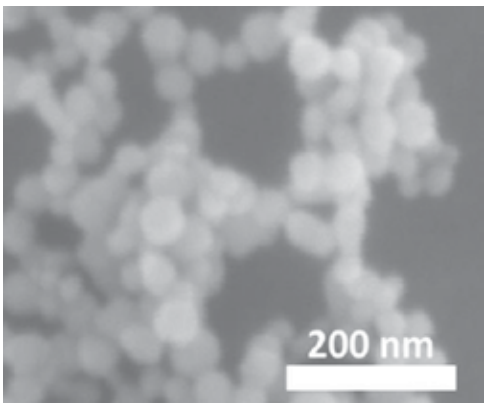

Figure 22. High magnification SEM image of laser ablated Ag nanoparticles.

In order to evaluate the effect of the Ag NPs on the photoactivity of LA-NPs, we performed MB discoloration tests [57] with a mixture of Ag-NPs and TiO_2 NPs obtained via laser ablation. We compared the resulting photocatalytic behaviour with LA-NPs without silver. In **Figure 23** are shown the absorbance spectra of MB solution in contact with LA-NPs (**Figure 23** left) and Ag–TiO_2 mixture (**Figure 23** right) versus time of irradiation. Note that in the presence of the Ag-NPs, the concentration of MB has decreased more than in the case of bare TiO_2.

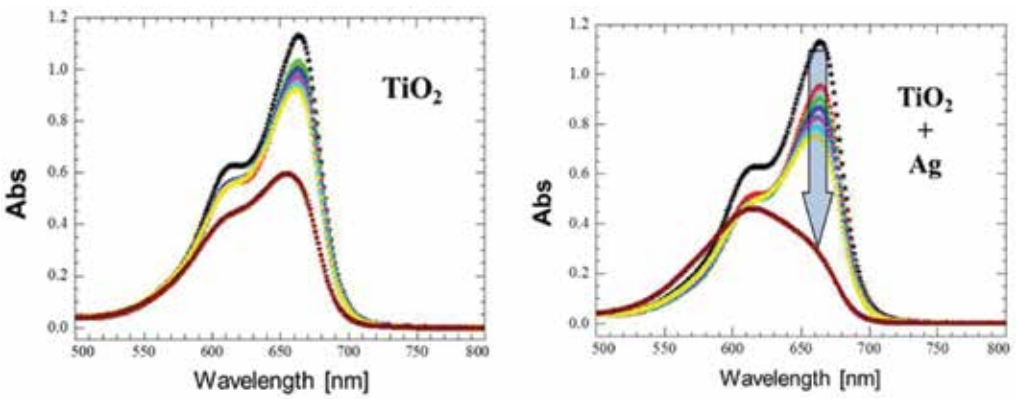

Figure 23. Absorbance of the MB solution in contact with LA-NPs (left) or a mixture of Ag and TiO_2 nanoparticles obtained by laser ablation (right) versus time.

The difference in the efficiency results more evident from **Figure 24**, where the normalized absorbance at 664 nm versus time for the two samples is reported. Note that this normalized value corresponds to the concentration of MB in solution according to $\frac{C}{C_0} = \frac{A}{A_0}$. The Ag–$TiO_2$ mixture shows clearly a better photocatalytic performance. Such enhancement is ascribable to the effect of the contact between Ag-NPs and TiO_2 LA-NPs. Indeed, the presence of a metal–

http://dx.doi.org/10.5772/62620

TiO_2 contact can effectively enhance the charge separation at the surface of NPs, thus increasing the carrier lifetime and the photocatalytic efficiency [6, 37].

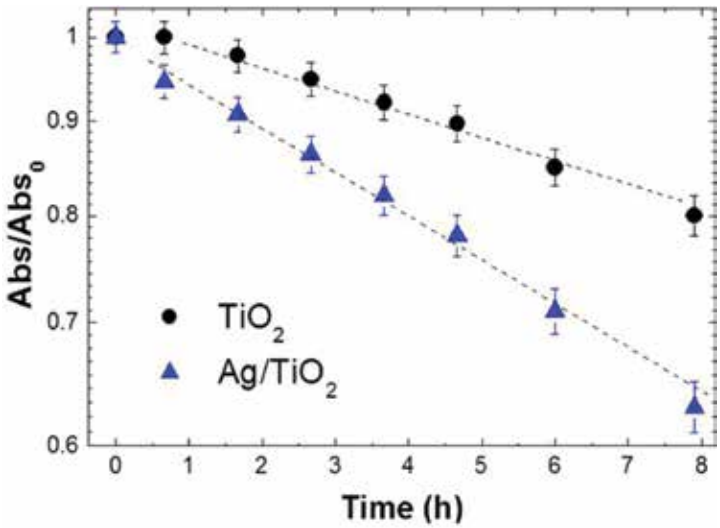

Figure 24. Normalized absorbance of the MB solution at the wavelength of 664 nm in the case of LA-NPs (black circles) and Ag–TiO_2 mixture (blue triangles) versus time.

5.3. Summary

We proposed TiO_2 NPs synthesis via PLAL as novel, environmental friendly, industrially scalable process in view of water purification strategies. Laser-ablated NPs (LA-NPs) have been found in highly disordered phase and with a high hydrogen content. Despite the amorphous phase, LA-NPs showed a photocatalytic activity similar to crystalline commercial powder and a higher antibacterial activity. This unexpected result has been explained taking into account the effects of disorder and hydrogen inclusion in the structure of TiO_2 NPs. The mixture of LA-NPs with Ag NPs obtained via laser ablation has been demonstrated to further improve the photocatalytic efficiency of TiO_2, thanks to an enhanced charge separation mechanism.

6. Conclusions

In the work presented in this chapter, two case studies have been presented: optical engineering of multilayered metal–TiO_2 thin films and TiO_2 NPs obtained via laser ablation.

In the thin film approach, we studied composite films of Ag NPs and TiO_2 for plasmon-enhanced photocatalysis. Using thermal dewetting or low-energy ion beam synthesis, metal NPs have been located at well-defined depth below the surface of a TiO_2 layer. We demon-

strated that the plasmonic effect can be effectively improved using an antireflective multilayer. This allows increasing the photon capture in a desired spectral range and enhancing this capture in a very thin layer near the surface. Photocatalytic activity has been observed under visible irradiation in multilayer Ag/TiO_2 nanocomposite samples in which the preparation procedure and stacking sequence were accurately selected. Such an activity, occurring at irradiation energies below the absorption threshold of titania (gap) and thus not observable in the bare TiO_2 film, has been ascribed to the presence of plasmonic metal NPs in field enhancement conditions. Therefore, the importance of proper film thickness engineering in order to take simultaneously advantage of plasmon resonances and optical interference has been evidenced.

In the other approach, TiO_2 NPs have been synthetized by PLAL, a novel, industrially scalable and eco-friendly technique. The LA-NPs were found to be in amorphous phase. Nevertheless, they showed a photocatalytic activity comparable to that of crystalline commercial powder and a higher antibacterial activity. This unexpected result has been explained taking into account the effects of disorder and hydrogen inclusion in the structure of TiO_2 NPs. In fact, these characteristics are reported to be responsible for the presence of superficial charge traps, which help the scavenging of electrons and, thereby, improve photocatalytic reactions. Mixing TiO_2 LA-NPs with Ag NPs has been demonstrated to further increase the photocatalytic efficiency of TiO_2, thanks to an enhanced charge separation.

Author details

Giuseppe Cacciato[1,2*], Massimo Zimbone[2], Francesco Ruffino[1,2] and Maria Grazia Grimaldi[1,2]

*Address all correspondence to: giuseppe.cacciato@ct.infn.it

1 Department of Physics and Astronomy, University of Catania, Catania, Italy

2 CNR-IMM, Catania, Italy

References

[1] Hashimoto K., Irie H., Fujishima. A. TiO_2 photocatalysis: A historical overview and future prospects. Jpn. J. Appl. Phys. 2005;44:8269–8285.

[2] Fujishima A., Zhang X., Tryk D.A. TiO_2 photocatalysis and related surface phenomena. Surf. Sci. Rep. 2008;63:515–582.

[3] Chong M.N., Jin B., Chow C.W.K., Saint C. Recent developments in photocatalytic water treatment technology: a review. Water Res. 2010;44:2997–3027.

[4] Hoffmann M.R., Martin S.T., Choi W., Bahnemann D.W. Environmental applications of semiconductor photocatalysis. Chem. Rev. 1995;95:69–96.

[5] Linsebigler A.L., Lu G., Yates J.T.Jr. Photocatalysis on TiO_2 surfaces: Principles, mechanisms, and selected results. Chem. Rev. 1995;95:735–758.

[6] Linic S., Christopher P., Ingram D.B. Plasmonic-metal nanostructures for efficient conversion of solar to chemical energy. Nat. Mater. 2011;10:911–921.

[7] Fujishima A., Honda K. Photolysis-decomposition of water at the surface of an irradiated semiconductor. Nature 1972;238:37–38.

[8] Gerischer H. Electrochemical behavior of semiconductors under illumination. J. Electrochem. Soc. 1966;113:1174–1182.

[9] Teoh W.Y., Scott J.A., Amal R. Progress in heterogeneous photocatalysis: From classical radical chemistry to engineering nanomaterials and solar reactors. J. Phys. Chem. Lett. 2012;3(5):629–639.

[10] Derfus A.M., Chan W.C.W., Bhatia S.N. Probing the cytotoxicity of semiconductor quantum dots. Nano Lett. 2004;4(1):11–18.

[11] Hanaor D.A.H., Sorrell C.C. Review of the anatase to rutile phase transformation. J. Mater. Sci. 2011;46:855–874 .

[12] Ohno T., Sarukawa K., Tokieda K., Matsumura M. Morphology of a TiO_2 photocatalyst (Degussa, P-25) consisting of anatase and rutile crystalline phases. J. Catal. 2001;203:82–86.

[13] Luttrell T., Halpegamage S., Tao J., Kramer A., Sutter E., Batzill M. Why is anatase a better photocatalyst than rutile? Model studies on epitaxial TiO_2 films. Sci. Rep. 2014;4:4043. doi:10.1038/srep04043

[14] Scanlon D.O., Dunnill C.W., Buckeridge J., Shevlin S.A., Logsdail A.J., Woodley S.M., et al. Band alignment of rutile and anatase TiO_2. Nat. Mater. 2013;12:798–801.

[15] GopalN. O., Lo H.-H., Sheu S.-C., Ke S.-C. A potential site for trapping photogenerated holes on rutile TiO_2 surface as revealed by EPR spectroscopy: An avenue for enhancing photocatalytic activity. J. Am. Chem. Soc. 2010;132:10982–10983.

[16] Nakamura R., Imanishi A., Murakoshi K., Nakato Y. In Situ FTIR studies of primary intermediates of photocatalytic reactions on nanocrystalline TiO_2 films in contact with aqueous solutions. J. Am. Chem. Soc. 2003;123:7443–7450.

[17] Mattioli G., Filippone F., AmoreBonapasta A. Reaction intermediates in the photoreduction of oxygen molecules at the (101) TiO_2 (Anatase) surface. J. Am. Chem. Soc. 2006;128:13772–13780.

[18] Asahi R., Morikawa T., Ohwaki T., Aoki K., Taga Y. Visible-light photocatalysis in nitrogen-doped titanium oxides. Science 2001;293:269.

[19] Litter M.I. Heterogeneous photocatalysis: Transition metal ions in photocatalytic systems. Appl. Catal. B 1999;23:89–114.

[20] Khan S.U.M., Al-Shahry M., Ingler W.B. Efficient photochemical water splitting by a chemically modified n-TiO_2. Science 2002;297:2243.

[21] Robel I., Subramanian V., Kuno M., Kamat P.V. Quantum dot solar cells. harvesting light energy with CdSe nanocrystals molecularly linked to mesoscopic TiO_2 films. J. Am. Chem. Soc. 2006;128(7):2385–2393.

[22] Chen X., Liu L., Yu P.Y., Mao S.S. Increasing solar absorption for photocatalysis with black hydrogenated titanium dioxide nanocrystals. Science 2011;331:746.

[23] Chen X., Liu L., Huang F. Black titanium dioxide (TiO_2) nanomaterials. Chem. Soc. Rev. 2015;44:1861.

[24] Hou W., Cronin S.B. A review of surface plasmon resonance-enhanced photocatalysis. Adv. Funct. Mater. 2013;23:1612–1619.

[25] Maier S. A. Plasmonics: Fundamentals and applications. New York: Springer; 2007.

[26] Bohren C.F., Huffman D.R. Absorption of light by small particles. New York: Wiley; 1983.

[27] Kelly K.L., Coronado E., Zhao L.L., Schatz G.C. The optical properties of metal nanoparticles: the influence of size, shape, and dielectric environment. J. Phys. Chem. B 2003;107:668–677.

[28] Mock J.J., Barbic M., Smith D.R., Schultz D.A., Schultz S. Shape effects in plasmon resonance of individual colloidal silver nanoparticles. J. Chem. Phys. 2002;116:6755.

[29] Noguez C. Surface plasmons on metal nanoparticles: the influence of shape and physical environment. J. Phys. Chem. C 2007;111:3806–3819.

[30] Zimbone M., Messina E., Compagnini G., Fragalà M.E., Calcagno L. Resonant depolarized dynamic light scattering of silver nanoplatelets. J. Nanopart. Res. 2015;17:402.

[31] Catchpole K.R., Polman A. Plasmonic solar cells. Opt. Express 2008;16(26):21793.

[32] Pavaskar P., Hsu I.-K., Theiss J., Hung W.H., Cronin S.B. A microscopic study of strongly plasmonic Au and Ag island thin films. J. Appl. Phys. 2013;113:034302.

[33] Hao E., Schatz G. C. Electromagnetic fields around silver nanoparticles and dimers. J. Chem. Phys. 2004;120:357.

[34] Awazu K., Fujimaki M., Rockstuhl C., Tominaga J., Murakami H., Ohki Y., et al. A plasmonic photocatalyst consisting of silver nanoparticles embedded in titanium dioxide. J. Am. Chem. Soc. 2008;130:1676–1680.

[35] Standridge S.D., Schatz G.C., Hupp J.T.. Distance dependence of plasmon-enhanced photocurrent in dye-sensitized solar cells. J. Am. Chem. Soc. 2009;131:8407–8409.

[36] Chen K.-H., Pu Y.-C., Chang K.-D., Liang Y.-F., Liu C.-M., Yeh J.-W., et al. Ag-nanoparticle-decorated SiO_2 nanospheres exhibiting remarkable plasmon-mediated photocatalytic properties. J. Phys. Chem. C 2012;116:19039–19045.

[37] Zhang X., Chen Y.L., Liu R.S., Tsai D.P. Plasmonic photocatalysis. Rep. Prog. Phys. 2013;76:046401.

[38] Dahl M., Liu Y., Yin Y. Composite titanium dioxide nanomaterials. Chem. Rev. 2014; 114:9853–9889.

[39] Liu E., Kang L., Yang Y., Sun T., Hu X., Zhu C., et al. Plasmonic Ag deposited TiO_2 nano-sheet film for enhanced photocatalytic hydrogen production by water splitting. Nanotechnology 2014;25:165401.

[40] Cacciato G., Bayle M., Pugliara A., Bonafos C., Zimbone M., Privitera V., et al. Enhancing carrier generation in TiO_2 by a synergistic effect between plasmon resonance in Ag nanoparticles and optical interference . Nanoscale 2015;7:13468–13476.

[41] Novotny L., Hecht B. Principles of Nano-optics. Cambridge, UK: Cambridge University Press; 2006.

[42] Ingram D.B., Linic S. Water splitting on composite plasmonic-metal/semiconductor photoelectrodes: evidence for selective plasmon-induced formation of charge carriers near the semiconductor surface. J. Am. Chem. Soc. 2011;133:5202–5205.

[43] Liu Z., Hou W., Pavaskar P., Aykol M., Cronin S.B. Plasmon resonant enhancement of photocatalytic water splitting under visible illumination. Nano Lett. 2011;11:1111–1116.

[44] Govorov A.O., Zhang H., Demir H.V., Gun'ko Y.K. Photogeneration of hot plasmonic electrons with metal nanocrystals: Quantum description and potential applications. Nano Today 2014;9:85–101.

[45] Christopher P., Xin H., Linic S. Visible-light-enhanced catalytic oxidation reactions on plasmonic silver nanostructures. Nat. Chem. 2011;3:467–472.

[46] Bayle M., Benzo P., Combe N., Gatel C., Bonafos C., Benassayag G., et al. Experimental investigation of the vibrational density of states and electronic excitations in metallic nanocrystals. Phys. Rev. B 2014;89:195402.

[47] Carles R., Farcau C., Bonafos C., Benassayag G., Bayle M., Benzo P., et al. Three dimensional design of silver nanoparticle assemblies embedded in dielectrics for raman spectroscopy enhancement and dark-field imaging. ACS Nano 2011;5:8774–8782.

[48] Mooradian A., Wright G.B. Observation of the interaction of plasmons with longitudinal optical phonons in GaAs. Phys. Rev. Lett. 1966;16:999.

[49] Mlayah A., Carles R., Landa G., Bedel E., Muñoz-Yagüe A. Raman study of longitudinal optical phonon-plasmon coupling and disorder effects in heavily Be-doped GaAs. J. Appl. Phys. 1991;69:4064–4070.

[50] Reznik D., Cooper S.L., Klein M.V., Lee W.C., Ginsberg D.M., Maksimov A.A., et al. Plane-polarized Raman continuum in the insulating and superconducting layered cuprates. Phys. Rev. B 1993;48:7624.

[51] Baumard J.F., Gervais F. Plasmon and polar optical phonons in reduced rutile TiO_{2-x}. Phys. Rev. B 1977;15:2316.

[52] Gonzalez R.J., Zallen R., Berger H. Infrared reflectivity and lattice fundamentals in anatase TiO_2s. Phys. Rev. B 1997;55:7014.

[53] Grujić-Brojčin M., ŠćepanovićM., DohčevićMitrovićZ., PopovićZ.V. Infrared study of nonstoichiometric anatase TiO_2 nanopowders. Science of Sintering 2006;38:183.

[54] Cacciato G., Ruffino F., Zimbone M., Reitano R., Privitera V., Grimaldi M.G. Au thin films nano-structuration on polycrystalline anatase and rutile TiO_2 substrates towards photocatalytic applications. Mat. Sci. Semiconduct. Proc. 2016;42:40–44.

[55] Cacciato G. Metal-TiO_2 nanocomposites towards efficient solar-driven photocatalysis [PhD thesis]. Catania; 2016.

[56] Ruffino F., Grimaldi M.G. Controlled dewetting as fabrication and patterning strategy for metal nanostructures. Phys. Status Solidi A 2015;1–23. doi:10.1002/pssa.201431755

[57] Mills A., Hill C., Robertson P.K.J.. Overview of the current ISO tests for photocatalytic materials. J. Photochem. Photobiol. A 2012;237:7–23.

[58] Zimbone M., Buccheri M.A., Cacciato G., Sanz R., Rappazzo G., Boninelli S., et al. Photocatalytical and antibacterial activity of TiO_2 nanoparticles obtained by laser ablation in water. Applied Catalysis B: Environmental 2015;165:487–494.

[59] Liu M., Inde R., Nishikawa M., Qiu X., Atarashi D., Sakai E., et al. Enhanced photoactivity with nanocluster-grafted titanium dioxide photocatalysts. ACS Nano 2014;8(7): 7229–7238.

[60] Zimbone M., Cacciato G., Buccheri M.A., Sanz R., Piluso N., Reitano R., et al. Photocatalytical activity of amorphous hydrogenated TiO_2 obtained by pulsed laser ablation in liquid. Mat. Sci. Semiconduct. Proc. 2016;40:28.

[61] Johnson O.W., De Ford J., Shaner J.W. Experimental technique for the precise determination of H and D concentration in rutile (TiO_2). J. Appl. Phys. 1973;44:3008.

Chapter 5

Nanostructured TiO_2 Layers for Photovoltaic and Gas Sensing Applications

André Decroly, Arnaud Krumpmann,
Marc Debliquy and Driss Lahem

Additional information is available at the end of the chapter

http://dx.doi.org/10.5772/62316

Abstract

Titanium dioxide (TiO_2) has been an important material for decades, combining numerous attractive properties in terms of economy (low price, large availability) or ecology (non-toxic), as well as broad physical and chemical possibilities. In the last few years, the development of nanotechnologies offered new opportunities, not only in an academic perspective but also with a view to many applications with particular reference to the environment. This chapter focuses on the many ways that allow to tailor and organize TiO_2 crystallites at the nanometre scale to make the most of this amazing material in the field of photovoltaics and gas sensing.

Keywords: titanium dioxide, solar cell, gas sensing, nanotube, anodization

1. Introduction

Titanium dioxide (TiO_2), also known as titania, has attracted a great deal of interest over the past decades because of its ability to create electron-hole pairs when absorbing light in an adequate wavelength range, taking into account that the valence and conduction bands are separated by a *ca.* 3.2 eV gap. Such a charge separation capacity makes TiO_2 a very convenient material for photovoltaic (see Section **2**) and photocatalytic applications. Basically, once an electron is excited by absorption of a photon of sufficient energy, either of the following phenomena can occur: the electron-hole pair dissociates and both charge carriers migrate toward opposite electrodes

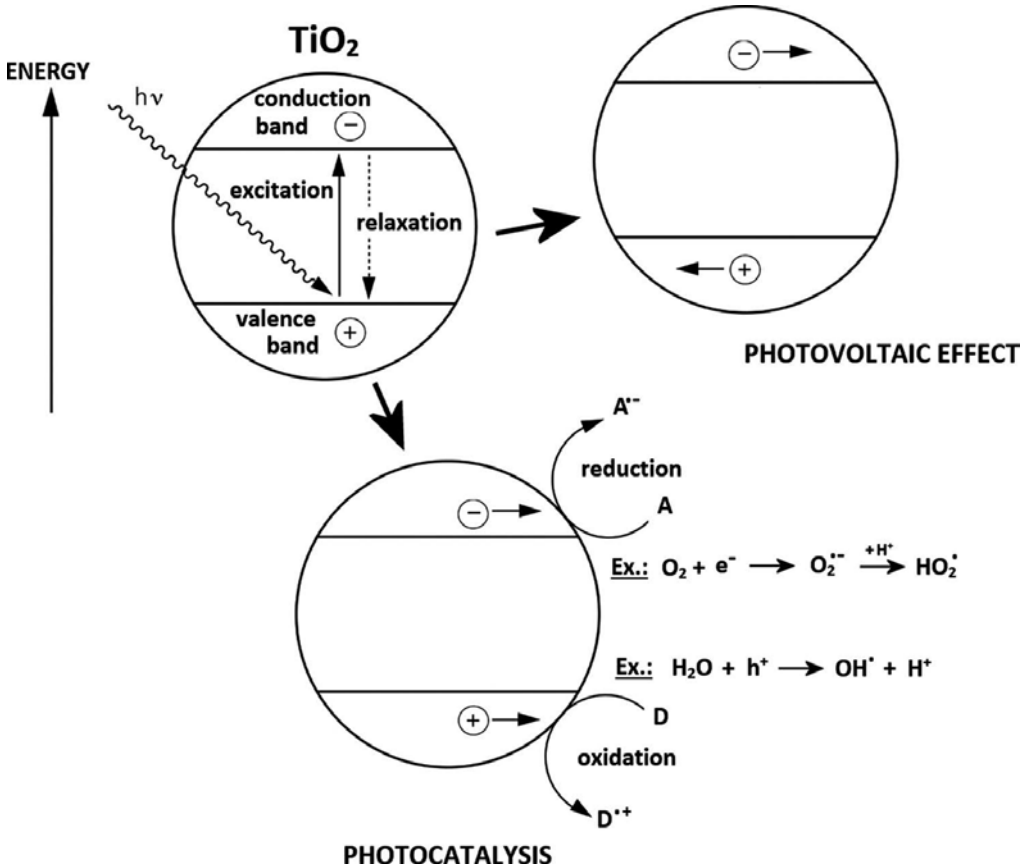

Figure 1. Schematization of either photocatalytic or photovoltaic effect following photon absorption by TiO_2.

generating a voltage that constitutes the photovoltaic effect or both charge carriers act like very active reagents in many chemical reactions what constitutes a photocatalytic effect (**Figure 1**).

Another interesting characteristic of crystalline TiO_2 is the variation of its semiconductivity because of charge transfer induced by the chemisorption of gaseous molecules onto the solid surface, making this material also very interesting for gas sensing applications (see Section **3**).

The photocatalysis field has already a very rich literature, hence it is not discussed in this chapter, despite its extreme importance, to focus on photovoltaic and gas sensing applications.

TiO_2 may crystallize in different allotropic structures, mainly anatase, rutile and brookite. Anatase is generally considered to have the best properties for the above-mentioned applications. It is metastable (or "kinetically stable") up to 550°C. Above this temperature, it transforms into the equilibrium rutile allotrope though anatase nanocrystallites (about 10 nm in size) appear to be metastable over a wider temperature range.

http://dx.doi.org/10.5772/62316

Of course, the manufacturing and optimization of a TiO_2 layer will be conducted in different ways depending on the intended application, but there is an important parameter that must be maximized in any case, which is the specific surface area. Therefore, such layers will always consist of nanocrystallites or nanostructures.

From a practical point of view, TiO_2 is also cheap, thermally and chemically stable and non-toxic (food additive E171, stated Kosher and Halal). However, in 2006, the *International Agency for Research on Cancer* (IARC) classified the titanium dioxide as possibly carcinogenic for humans.

2. TiO_2 for dye sensitized solar cells

2.1. Generalities and operating principle of a DSSC

In 1991, Professor Michael Grätzel from the *École Polytechnique Fédérale de Lausanne* (EPFL) published an article [1] describing the functioning of a new type of solar cell (called of the third generation) based on the use of a TiO_2 layer sensitized with a dye (dye-sensitized solar cell [DSSC]). This cell differs from the massive (single crystal or polycrystalline) silicon cells based on a *p-n* junction that allows an easy dissociation of the electron-hole pairs generated following photons absorption by the silicon itself (first-generation cells) or from other solar cells also based on a *p-n* junction but using thin layers of various semiconductor materials such as CdS-CdTe or CdS-$CuInSe_2$ (second-generation cells) [2].

Probably to increase their eco-attractiveness, DSSCs are now often presented as biomimetic devices inspired by photosynthesis though the comparison seems rather misleading if one looks closely. Indeed, when chlorophyll absorbs a photon, an electron-hole pair is created, which established the energy quantum needed for the photosynthetic reaction to occur. This electron-hole pair has to diffuse randomly over a long distance (and therefore with a high recombination probability) along the chlorophyll molecule antenna until it reaches the heme-like porphyrin group, which is the chemical reaction locus. Of course, neither voltage nor electrical current is produced. The role of the dye in a DSSC is completely different and is discussed thoroughly below.

Like in any solar cell, the photogenerated electron-hole pairs must readily dissociate. This is the reason why each type of solar cell is made up of two media of different conduction modes, which prevents the charge carriers once separated to recombine (too easily) so that a voltage can be generated. The TiO_2 layer is an electron conductor, and the electrolytic solution acts as an ionic conductor (**Figure 2**). An electric current is generated when the dye molecules anchored onto the surface of the TiO_2 nanoparticles absorb the incoming photons and inject the photoexcited electrons into the TiO_2 layer.

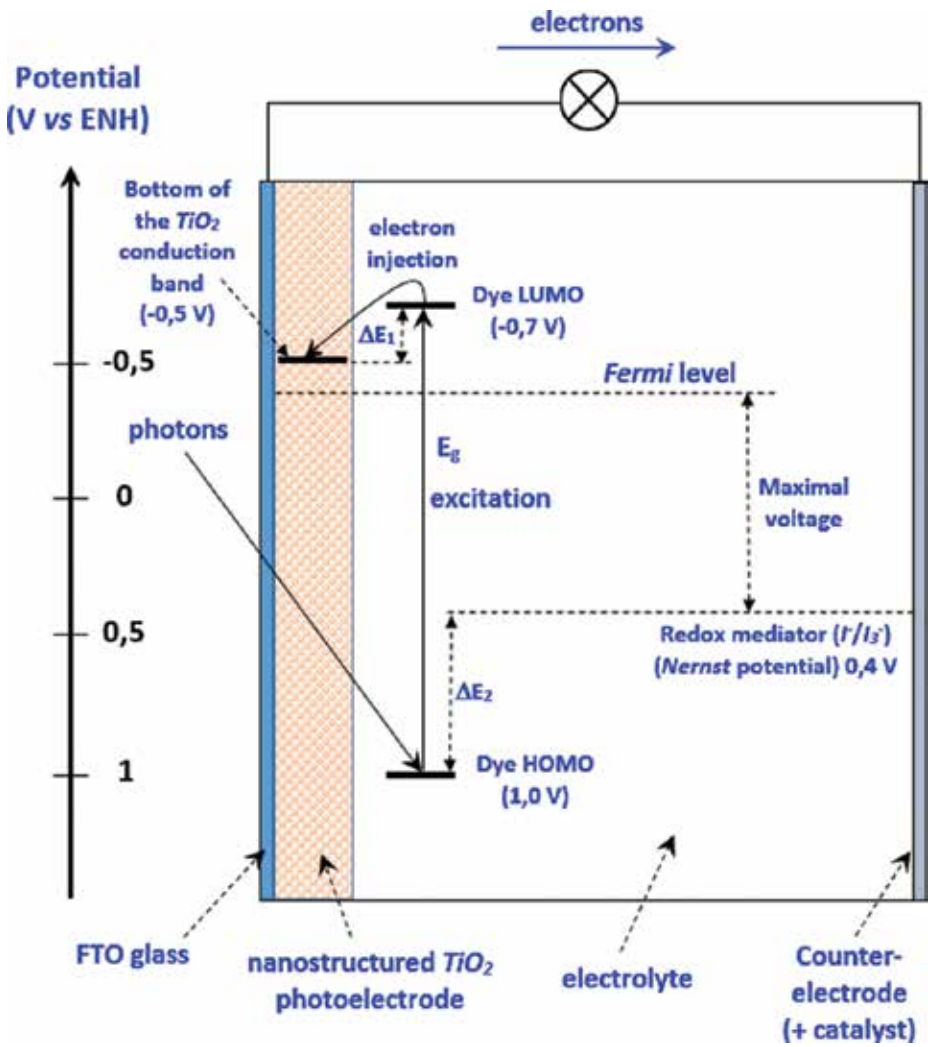

Figure 2. Functional scheme of a DSSC (thermodynamic point of view).

The function of the ionic redox couple (traditionally I_3^-/I^-) in solution is to reduce the oxidized dye molecules back to their ground state to enable continuous electron production, a process in which the reduced form of the redox couple (I^-) gets oxidized itself. The electrons are collected from the TiO_2 (photoanode) and transferred through an external circuit to the counter-electrode (cathode) where they complete the operating cycle of the cell by reducing the oxidized redox species (I_3^-) back to its original state.

Kinetic aspects are of utmost importance: electron injection from the dye into the TiO_2 conduction band must be much faster than the dye relaxation, electron transport into the TiO_2 must be faster than electron trapping or recombination and the reduction of the dye by the reduced ion in solution must not be a rate-limiting step (**Figure 3**).

http://dx.doi.org/10.5772/62316

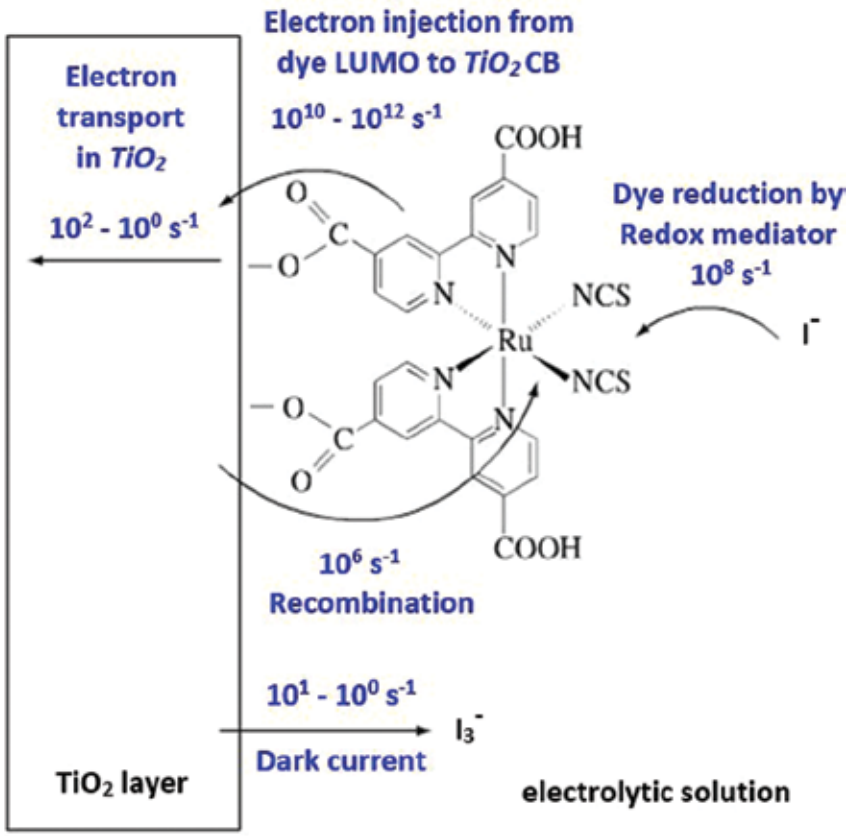

Figure 3. Functional scheme of a DSSC (kinetic point of view).

Nevertheless, since TiO_2 has a wide band gap (3.2 eV), only the most energetic photons ($\lambda <$ 400 nm, i.e., about 5 % of the total amount of photons) are able to induce a charge separation, thereby leading to a very poor conversion efficiency if TiO_2 was used alone. The dye, thus, allows to harvest photons on a wider wavelength range (up to 920 nm, for instance) [3] so as to raise the photocurrent, and therefore the efficiency of the cell. So, unlike the cells of first and second generations, the vast majority of electron-hole pairs are not generated by the material (here TiO_2) itself, but following the dye excitation. As outlined above, a very large specific surface area is therefore needed to increase the amount of dye molecules chemically grafted onto the TiO_2 surface.

Each component of the cell has undergone many developments since 1991 [4]:

- The electrodes: both electrodes must obviously be conducting but at least one must be transparent, and it is best to choose the TiO_2 photoanode to be exposed directly to the light so as to avoid great absorption of photons by the counter electrode (cathode) and the

electrolytic solution. So the TiO_2 layer should always be deposited onto a transparent conducting oxide (TCO) like an indium-tin oxide (ITO) coating onto a glass substrate. Nowadays, the classical ITO is progressively replaced by FTO (fluorine-doped tin oxide), which presents a lower sheet resistance, a better thermal resistance and avoids the use of indium whose long-term availability is uncertain. The ultimate goal would be to use flexible electrodes (conductive polymer films), but their low long-term stability, especially when exposed to UV-light, is a drawback;

- The redox couple: the Nernst potential of the mediator must be little less negative than the dye HOMO potential (**Figure 2**) so that the reduction of the oxidized molecule is thermodynamically promoted, but some other redox couples may be used (Co^{3+}/Co^{2+}, for instance) instead of the classical (I^-/I_3^-);

- The solvent: the role of the solvent is obviously to solubilize the redox species and let them cycle between the cathode and the dye molecules, but liquid solvents (ethylene glycol, for instance) may have some drawbacks (dye desorption, leakage, etc.). Therefore, the aim is now to replace the liquid electrolytic solution by a solid-hole transport material (HTM) such as P3HT and Spiro-OMeTAD. Unfortunately, using a HTM instead of a liquid electrolyte leads to lower cell performance mainly because of low hole mobility;

- The dye: of course, the dye has a key role in the conversion process. It must (1) have a high photon absorption efficiency (or IPCE [incident photon to current conversion efficiency]) on a wide wavelength range, (2) be densely chemisorbed onto the TiO_2 surface, (3) be chemically stable for a long time (even if it spends a part of its "life" in an oxidized state), (4) have a LUMO whose potential is a little less negative than the bottom of the TiO_2 conduction band (**Figure 2**) and (5) have a convenient gap between the HOMO and the LUMO (taking into account that a wide gap will lead to a higher voltage but a lower current and vice-versa if the gap is narrower). One possible perspective would be to use block copolymers acting as HTM, the part of which chemisorbed onto the TiO_2 also acting as a dye (work in progress).

Nevertheless, the rest of this section focuses on the TiO_2 layer. The first prototypes were using TiO_2 nanoparticles (10–20 nm) in liquid suspensions and deposited by some simple processes such as the "doctor blade" technique. Sometime later, the dip-coating and the sol-gel techniques starting from a titanium alkoxide aqueous solution were combined to produce well-controlled TiO_2 layers made up of anatase nanocrystallites after thermal treatment. Nevertheless, these deposits were completely disorganized and of rather poor conductivity because of high contact resistance at the grain boundaries. This electrical resistance favored the electrons recombination leading to great loss of efficiency. An improvement was brought by combining the templating techniques to the previous ones (**Figure 4**): surfactant molecules were used to organize the TiO_2 layer and, therefore, to create higher conductivity channels inside the layer (**Figure 5**). However, this process was still not sufficient and the conductivity of the TiO_2 layer remained one of the main weak spots of DSSC.

http://dx.doi.org/10.5772/62316

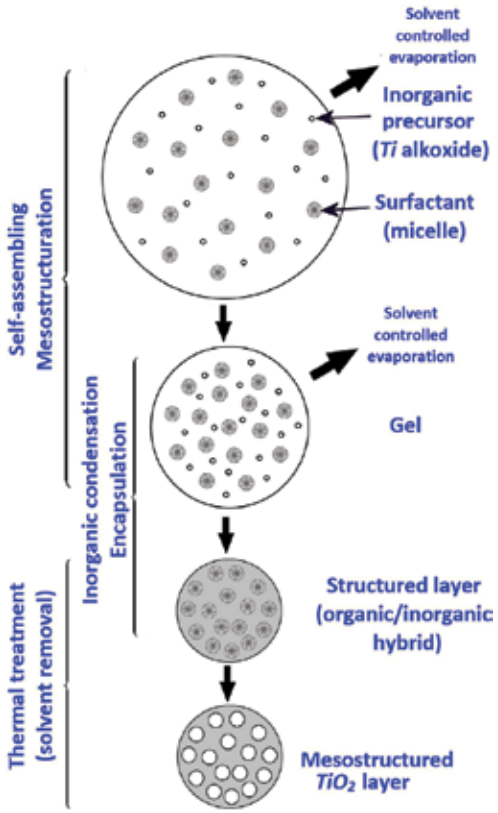

Figure 4. Scheme of the dip-coating + sol-gel + templating technique.

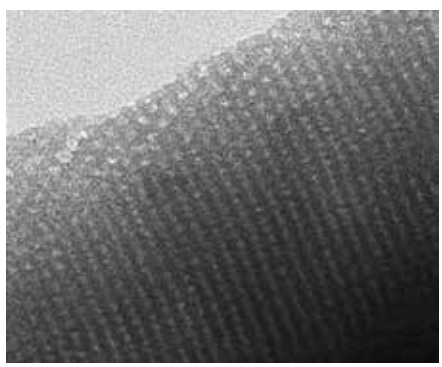

Figure 5. TiO_2 layer constituted by nanocrystallites obtained by the dip-coating + sol-gel + templating technique (with kind permission of the GREENMAT-LCIS Department, ULg, Belgium).

The last step is currently to produce "one-dimensional" (1-D) crystallites in the form of TiO_2 nanotube array (TNA or TiO_2 – NTA) [5] (**Figure 6**). Such a structure combines good specific surface area and high conductivity. It can be obtained by anodization of metallic titanium in well-defined experimental conditions that are discussed later.

2.2. Techniques and recent developments

2.2.1. Overview

Anodization is the oxidation of a metal, forced by a potential difference willingly induced between an anode (the metal to oxidize) and a cathode (classically Pt), in an electrolytic bath. The positive potential set at the anode induces the metal oxidation, whereas the cathode reaction is water reduction that leads to hydrogen evolution.

Anodization can lead to either dense or porous structures, depending on the anodization conditions (especially the bath composition). Nanotubular structures are well-known for anodized aluminum oxide, but anodization also makes it possible to elaborate nanostructured layers of several metal oxides (WO_3, Fe_xO_y, ZrO_2, etc.) [6], including TiO_2. The obtained structure depends on numerous parameters such as applied potential, bath composition, temperature and anodization time. Therefore, a good knowledge of the impact of these parameters allows a precise morphological control of the anodized layer.

As explained before, nanotubular structures are of particular interest in various fields, including photovoltaics. To obtain those porous nanostructures, anodization has to be carried out in a medium with the ability to dissolve the formed oxide. For titanium, fluoride ions are the most efficient, forming a TiF_6^{2-} complex. Initially, aqueous solutions of HF or fluoride salts were used, but because of the high reactivity of these compounds with TiO_2, only small nanotube lengths were achieved. Anodization in organic electrolytes has then been investigated to get longer nanotubes and smoother aspect of the layers. In this case, a small amount of water (at least 0.18% [7]) is added as a source of oxygen. Classical organic solvents such as glycerol, dimethyl sulfoxide or ethylene glycol have been used to produce nanotube layers of dozens (even hundreds) of micrometres on a Ti foil.

The formation mechanism of these nanotubes is quite well known and has been described on several occasions [6, 8]. Focusing on the electrochemical reactions, it can be summarized as follows: at the anode, the main reaction is the oxidation of titanium:

$$Ti \rightarrow Ti^{4+} + 4\,e^{-} \tag{1}$$

This oxidation leads to the formation of titanium dioxide, by a hydrated intermediate:

$$Ti^{4+} + 4\,OH^{-} \rightarrow Ti(OH)_4 \tag{2}$$

http://dx.doi.org/10.5772/62316

$$Ti(OH)_4 \rightarrow TiO_2 + H_2O \tag{3}$$

Equation (2) shows that titanium oxidation goes with a decreasing pH, which favours the formation of nanotubes by increasing the dissolution rate at the bottom of the tubes. It is worth noting the presence of a side reaction of oxygen evolution taking place at the anode, which can impact the quality of the structure (especially for the anodization of thin films, as shown below):

$$2\,H_2O \rightarrow O_2 + 4\,H^+ + 4e^- \tag{4}$$

At the cathode, the reaction is water reduction, with hydrogen evolution:

$$4\,H^+ + 4\,e^- \rightarrow 2\,H_2 \tag{5}$$

And the overall equation is:

$$Ti + 2\,H_2O \rightarrow TiO_2 + 2\,H_2 \tag{6}$$

To get a porous structure, a compound that can chemically dissolve the formed titanium dioxide is needed. This is achieved by fluoride ions forming a complex:

$$TiO_2 + 6\,F^- + 4\,H^+ \rightarrow TiF_6^{2-} + 2\,H_2O \tag{7}$$

It is the competition between reactions (3) and (7), that is, between the electrochemical formation of the oxide and its chemical dissolution by the fluorides that mostly determine the structure of the anodized layer. The anodized TiO_2 is generally amorphous, and this is detrimental to the charge transport properties of the nanotubular layer. Therefore, a thermal treatment around 450°C is commonly used to crystallize it into anatase (the most suited TiO_2 polymorph for photovoltaics).

2.2.2. Anodization parameters

The first important parameter to consider is the bath composition. As said previously, it mainly consists of an organic solvent with usually 1–5 wt% of water as a source of oxygen and 0.1–5 wt% of fluorides from NH_4F or HF.

The anodization process is mostly carried out in potentiostatic mode because the control of the morphological properties is easier than in galvanostatic mode [9]. The applied voltage has an important impact on the nanotube diameter. Several studies have shown a linear relationship

between the tube diameter and the applied voltage in the 10 to 60 V range [10, 11], allowing to tune the nanotube diameter from approximately 20 nm (10 V) to 120 nm (60 V).

In organic electrolytes, the nanotube length increases with the anodization duration, as the chemical dissolution is much lower than the electrochemical growth of the tubes. Therefore, nanotubes of several hundreds of micrometres can be achieved on Ti foil by a very long anodization time [12]. However, very long nanotubes are not especially suited for photovoltaic applications because the electron diffusion length in dye-sensitized solar cells is commonly a few micrometres. Longer nanotubes only increases charge recombination and finally decreases the cell efficiency.

The anodization temperature is another key parameter in the anodization process. In the case of titanium anodization, most studies are carried out at room temperature (20–25°C). On the one hand, a higher temperature obviously increases the kinetics of the reactions (which means a higher growth rate), but this is not the only effect. It also favours water oxidation (side reaction) and an increase of the tube diameter, which is disadvantageous. On the other hand, a low temperature anodization provokes an important increase of the wall thickness of the nanotubes and, consequently, reduces the porosity of the structure (and hence the specific surface area). This is also undesirable as a high specific surface area is required for the dye to adsorb and get high efficiency DSSCs. The structures obtained at 5, 20 and 30°C are shown in **Figure 6**.

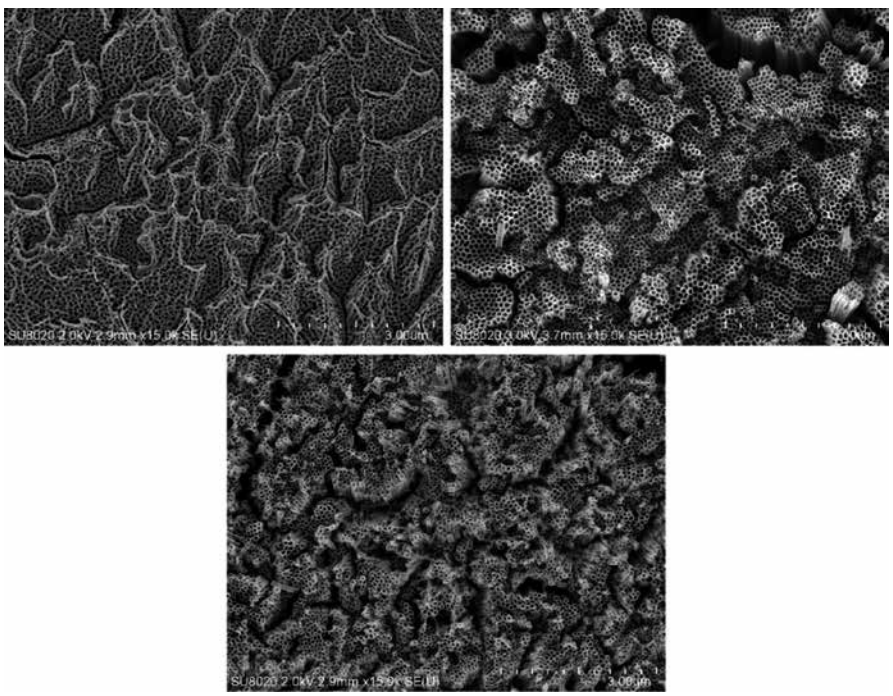

Figure 6. TNAs obtained by anodization at 40 V in a bath at 5°C (top left), 20°C (top right) and 30°C (bottom).

http://dx.doi.org/10.5772/62316

2.2.3. Anodizing a TiO_2 thin film

In order to get a transparent photoelectrode made of TNA on a conducting substrate, a Ti thin film is sputtered onto a FTO glass substrate. This film is then anodized to fully convert the dense titanium into titania nanotubes. The need for an adherent, homogeneous and dense film requires the use of magnetron (or sometimes rf) sputtering, since a simple evaporation leads to insufficient adherence and a delamination of the Ti film during anodization [13]. Some studies have pointed out that substrate preheating allows a better adherence of the film, therefore this kind of thin film is often deposited with a substrate preheated around 400°C [14, 15]. Another method is to apply a bias, so the growing Ti film is hit by more energetic ions [16]. Using these methods, several micrometres thick Ti layers can be obtained on FTO glass.

When anodization is performed on a thin Ti film on a transparent substrate to make a transparent electrode, the nanotube length is no longer linked to the anodization duration but to the thickness of the Ti film, as the anodization is carried out until the complete metal oxidation and hence the full transparency of the film are obtained. It is worth noting that the expansion factor (the ratio between the TNA film thickness and the initial Ti film thickness) varies from 1.3 to 2.5 approximately, depending on the anodization parameters (especially the applied voltage).

Another specificity of anodizing thin films on FTO glass is the role of the substrate. In this case, the anodization is carried out until the full oxidation of the Ti film is achieved, which means that there can be interactions between the electrolyte and the substrate at the end of the anodization process. The main problem is the side reaction of water oxidation (Equation (4)) taking place at the substrate–electrolyte interface, evolving oxygen. This reaction is known as a side reaction even on Ti foils but remains secondary compared with the oxidation of Ti. In this case, at the substrate–electrolyte interface, it is the only reaction and it can lead to a sufficiently intense bubbling to destructure the TNA film and provoke local delamination, even at low anodization potentials.

Knowing this side reaction is not a problem on Ti foils or on isolating substrates (such as conventional glass), there are mainly two ways to address the delamination problem. The first one is to stop anodization as soon as any contact between the substrate and the electrolyte is detected (bubbles appears), thus leaving a few nanometres of non-oxidized Ti that are oxidized during the thermal treatment of crystallization. The second is to prevent any contact between the FTO glass and the electrolyte by adding a compact underlayer of TiO_2 on which oxygen evolution is less favoured than on a highly conducting substrate such as FTO, but that is conducting enough to transport the electrons in the solar cell. Consequently, the thickness of that underlayer is chosen similar to the thickness of conventional blocking layers in DSSCs (50–100 nm). This compact underlayer is deposited by reactive sputtering just before the metallic Ti deposition, the transition between TiO_2 and Ti being triggered by switching off the oxygen admission in the vacuum chamber. The process of anodization of thin films with and without an underlayer is shown in **Figure 7**.

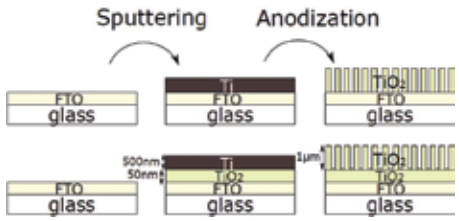

Figure 7. Schematized process to elaborate TNAs on conducting glass with and without underlayer.

2.2.4. Impact of a TiO_2 underlayer

A first impact of sputtering a compact TiO_2 underlayer is a better adherence of the film, allowing to sputter the Ti without preheating the substrate. This is a significant gain of productivity, probably by ensuring a higher chemical affinity between the metallic Ti and the substrate. Another impact is on the regularity of the nanostructure. Indeed, from a microscopic point of view, the introduction of this underlayer has little impact on the nanotubes morphology. However, from a macroscopic point of view, it induces considerable improvements of homogeneity (reducing edge effects, for example). This is especially important for samples of larger size and as pointed out earlier, it prevents delamination, allowing a complete anodization at different applied potentials. SEM cross-sectional view of nanotubes on FTO glass with a TiO_2 underlayer is shown in **Figure 8a** and top views at different potentials of anodization (with tube diameters from 30 to 60 nm) are shown in **Figure 8b**, **8c** and **8d**.

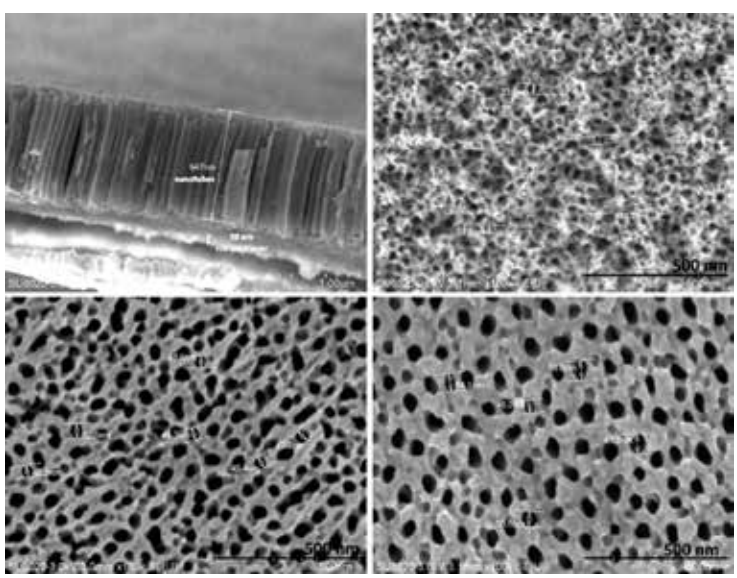

Figure 8. SEM views of TNAs: (top left) cross-sectional, (top right and bottom) top views at 20, 30 and 40 V, respectively.

http://dx.doi.org/10.5772/62316

Another important parameter for a photoelectrode is its transparency, as any absorption by the defects in the TiO_2 is parasitic and will not be converted in electricity (recombination). The transmittance of the photoelectrodes based on TNAs are shown in **Figure 9** and compared with classical photoelectrodes with the same TiO_2 thickness (about 1 μm). If the transmittance of commercial nanoparticles is the highest (around 80% in average in the 450–850 nm range), it is worth noting the great difference between the TNA elaborated with and without an underlayer (73–75% and 63–68% in average, respectively). The lower transmittance observed without an underlayer indicates that the residual Ti left to avoid delamination at the end of the anodization process is not completely oxidized by the thermal treatment or it creates other absorbing defects. A complete oxidation by anodization is therefore encouraged, and this can only be done with an underlayer to prevent delamination. Moreover, this oxidation by the thermal treatment is known for creating a resistive layer under the nanotubes (especially on Ti foils). A complete anodization allows avoiding this resistive layer, and therefore an improvement in the electron transport properties can be observed for the samples with a TiO_2 underlayer.

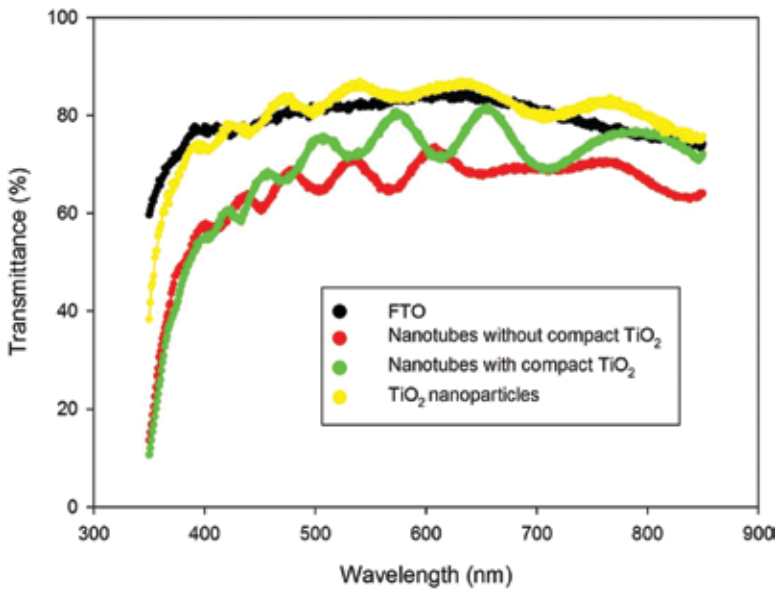

Figure 9. Transmittance of the photoelectrodes based on TNAs.

3. TiO_2 for gas sensing

3.1. Overview and principles

TiO_2 is a member of the large family of the semiconducting metal oxides used for chemical gas sensors applications [17, 18]. The detection principle is based on the conductivity change of

those materials when they are in contact with certain gases. When a gas is adsorbed onto the surface, and if the interaction is strong enough (meaning chemisorption), an electron transfer between the semiconductor and the adsorbed species takes place resulting in an increase (decrease) of the charge carrier concentration in the semiconductor and as a consequence an increase (decrease) of the conductivity. As there is an equilibrium between the gas concentration in the atmosphere and the adsorbed quantity, a direct relation is expected between the conductivity change and the gas concentration. This phenomenon can be observed with organic or inorganic semiconductors.

The general scheme of such a sensor is presented in **Figure 10**.

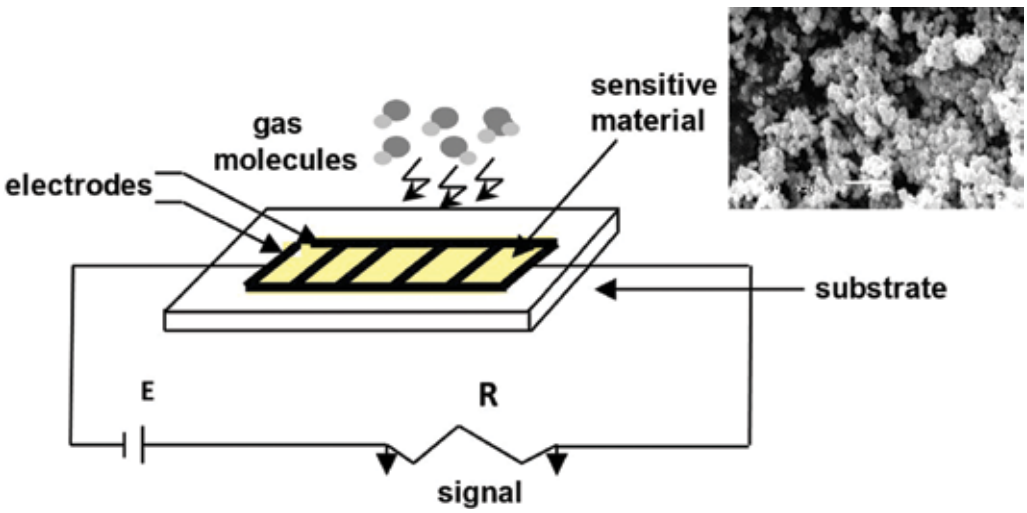

Figure 10. Scheme of a semiconductor sensor.

The sensor acts just like a variable resistance and is often called chemoresistive sensor or chemoresistor.

As the detection principle deals with chemisorption and surface reactions with the gas, an activation energy is generally needed. Otherwise, the response to the gas and the recovery are too slow or even no response is observed. That is why a heating element is usually added on the substrate (very often in the form of a coil).

Historically, the effect of gases on semiconductors was discovered by Brattain and Bardeen. Already in 1953, they observed that Ge samples modified their resistance, depending on the atmosphere they were in contact with [19]. Later in the 1960s, Seiyama [20], using a zinc oxide (ZnO) thin film, was able to demonstrate that gas sensing is possible with simple electrical devices. He studied a simple chemoresistive device sensitive to propane based on ZnO thin films, operating at 485°C. Taguchi [21] fabricated and patented the first chemoresistive gas sensor device for practical applications using tin dioxide (SnO_2) as the sensitive material. This led to the foundation of the company *Figaro Inc* whose first main product was alarms for

http://dx.doi.org/10.5772/62316

explosive gases. This paved the way to intense researches to extend the principle to numerous applications of the semiconductor gas sensors.

Because of their simplicity, low cost, small size and ability to be integrated into electronic devices, chemical sensors have been the object of an extensive work as they have a big potential in all kinds of applications: industrial emission control, household security, vehicle emission control and environmental monitoring, agricultural, biomedical, and so on [22–27].

Although organic materials are potentially very attractive because they can be more easily modified than inorganic materials and thereby their performances "tailored", they encountered considerably less success than the inorganic semiconductors, especially metal oxides. The main reasons are the bad long-term stability, and it is often impossible to use them at temperatures at which gas–solid interactions proceed rapidly and reversibly.

The detection mechanism for metal oxide is represented in **Figure 11** [18–28].

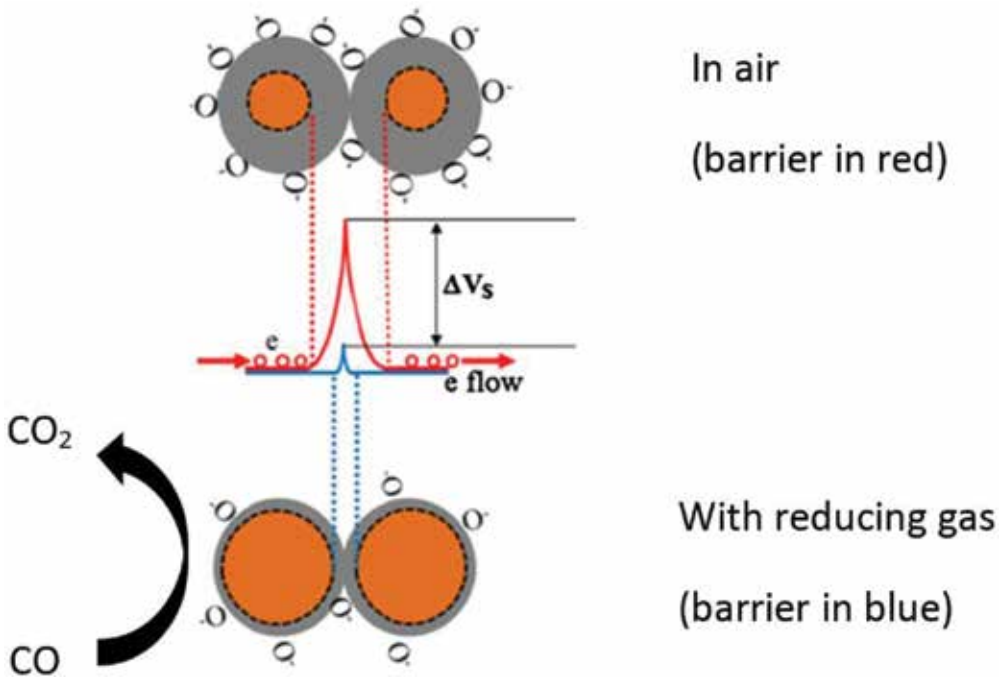

Figure 11. Detection mechanism for metal oxide sensors.

Taking the example of an *n*-type semiconductor, in air, oxygen will be adsorbed at the surface of the oxide. An electron transfer occurs from the oxide to the oxygen leading to the formation of oxygen ions O_2^-, O^- or O^{2-}. The nature of the ion depends on the temperature. The consequence is that the surface of the crystals is depleted, a potential barrier appears and the conductivity is decreased. Very often, the sensitive films are constituted of grains in contact

and the potential barrier will modulate the transfer of electrons between the grains and so the overall conductivity.

So for *n*-type semiconductors, the global conductance can be expressed as follows [29, 30]:

$$G = k \cdot \sigma_b \cdot \exp\left(\frac{-e \cdot V_s}{k_b \cdot T}\right)$$

with

- G, conductance of the sensitive layer;
- k, geometrical factor (including thickness of the sensitive layer, length, width of the electrodes);
- $\sigma_{b,}$ bulk conductivity;
- V_s, potential at the surface.

This formula is established assuming the electron transfer limitation by the surface potential.

Adsorption of the gases can modify this potential leading to conductivity changes. For instance, reduction of the oxygen pressure in the atmosphere means reduction of the adsorbed oxygen surface concentration leading to an increase of the conductivity.

In general, for *n*-type semiconductors, the contact with reducing gases (CO, H_2, CH_4, etc.) will increase the conductivity. Indeed, reducing gases can react with adsorbed oxygen, thereby releasing the trapped electrons that increase the charge carrier concentration. For oxidizing gases (NO_2, Cl_2, O_3, etc.), their adsorption will cause an increase of the barrier because of the trapping of electrons. For *p*-type semiconductors, the effects are opposite.

The nature of the oxide is a key factor for the choice of the sensitive layer for a given gas but the defects at the surface of the material play an important role as they are adsorption centres for gases. So the control of the surface is a major concern for gas sensing.

The most studied metal oxides for gas sensing as *n*-type semiconductors are SnO_2, ZnO, In_2O_3, WO_3 and TiO_2, whereas NiO, Cr_2O_3 and CuO are the most studied as *p*-type semiconductors.

The main drawbacks of these sensors remain the lack of selectivity because of the fact that the interaction between the semiconductor and the target gas is not always specific, and the need to heat the sensitive layer to rather high temperatures leading to increased power consumption. The current developments strive to reduce these drawbacks by studying a lot of other materials and by exploiting the opportunities provided by the new nanoscale technologies. Nanoscience, enabling controllable manipulation of matter at the molecular level, has become a precious tool for innovations in materials processing. A smaller size and so lower power consumption, greater sensitivity and better selectivity are expected. For instance, it is quite clear that grain-size reduction at nanometric scale can enhance the detection properties of metal oxides gas sensors.

http://dx.doi.org/10.5772/62316

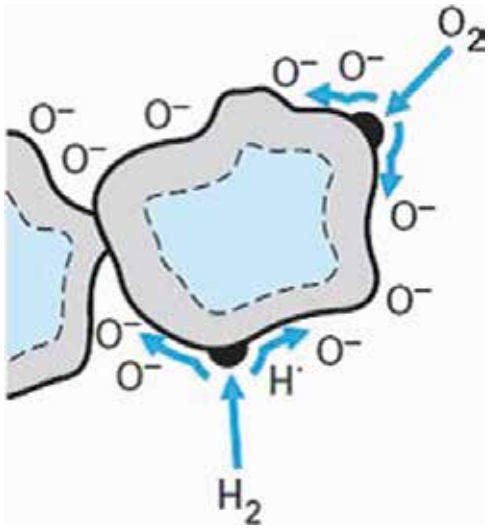

Figure 12. Spill over mechanism with hydrogen enhancing the oxidation rate.

Adding suitable promoters (metal particles, foreign metal oxide, ions, etc.) on the metal oxide layer is a common way of enhancing the sensing characteristics of metal oxide gas sensors [31, 32]. For instance, Pt promotes the gas-sensing reaction by the spill-over mechanism (massively exploited for heterogeneous catalysis). Pt clusters catalyse the dissociation of the gases, favouring the reactions with the adsorbed oxygen species. **Figure 12** shows the mechanism with hydrogen. The result is an increase of the sensitivity to hydrogen and a lowering of the working temperature.

TiO_2 is particularly attractive for gas sensors because of its cross-sensitivity to humidity lower than other metal oxides than other metal oxides [33]. Among the other applications, TiO_2 has been largely investigated as a sensing layer in resistive oxygen gas sensors operating at medium-high temperatures for automotive air/fuel ratio (A/F) control. The first titania gas sensors were developed in the late 1970s and early 1980s. The first application was the detection of the stoichiometric A/F ratio for engines [34]. Indeed, the sensor resistance was increased by orders of magnitude around the stoichiometric A/F, making it a very useful device for these applications. It was a competitor to the classical *Lambda* probe based on a solid state electrochemical cell.

Depending on the application of interest and availability of fabrication methods, different surface morphology and configurations of the metal oxides have been achieved, including single crystals, thin films, thick films and one dimensional (1-D) nanostructures [35–37]. Among all these, following the same trend as for photovoltaics, 1-D nanostructures have recently attracted much attention because of their potential applications in gas sensors [38]. 1-D nanostructures are particularly suited to this application because of their high surface-to-volume ratio as well as their good chemical and thermal stabilities [39, 40]. This chapter focuses on these materials and in particular, TiO_2.

3.2. Techniques and recent developments

The purpose is not to perform a comprehensive research survey in this chapter. There are already many excellent review articles on the topic of chemoresistive gas sensors [17, 41–45], but the aim is to give an overview of the use of nanostructured TiO_2 in the gas sensing field.

The development of fabrication methods for producing 1-D nanostructures has been the object of an intense research in the field of nanoscience and nanotechnology [37, 44, 46]. Several metal oxides such as ZnO, SnO_2, TiO_2, In_2O_3, WO_3, $AgVO_3$, CdO, MoO_3, CuO, TeO_2 and Fe_2O_3 have been investigated for gas sensing. However, according to our findings [47], 1-D structures are not always preferable for all gases. Several routes (chemical or physical) have been investigated for 1-D metal-oxide nanostructures for gas sensing applications. Arafat et al. [36] give a good summary of these routes. The most important ones are explained in this chapter focusing on TiO_2.

The sensor's response to a given gas can be enhanced by the modification of both surface states and bulk properties of the 1-D metal-oxide nanostructures. These modifications can be achieved by either depositing nanoparticles on the nanostructure's surface or coating and doping with impurities or even cover them with organic molecules [48, 49]. Sensors utilizing these types of surface and bulk property modifications showed higher sensitivity compared with unmodified systems. The functionalization can be performed in a second step after the synthesis of the 1-D structures or in one step during their formation.

Another trend is to use organized nanostructures as porous templates for the deposition of a sensitive material. This was done for instance with polypyrrole on TiO_2 for NH_3 detection [50] and was studied in our lab for the fabrication of molecularly imprinted polymers (MIP) based on polypyrrole electropolymerized in TiO_2 nanotubes for aldehydes detection.

3.3. Growth of TiO_2 nanostructures

The synthesis methods of 1-D TiO_2 nanostructures can be divided into two groups: solid-state etching and wet processing routes. The solid-state etching process includes nanocarving by H_2 gas, UV lithography and dry plasma etching [51, 52]. The wet processing route is, by far, more popular as it does not need complex equipment. The wet processing route includes hydrothermal synthesis, electrospinning and anodization.

Different surface morphologies such as nanotube arrays, branched nanotubes, coated nanotubes, nanoparticle added nanotubes, nanobelts, nanofibres and nanowires of TiO_2 can be obtained, depending on the synthesis method and the process parameters. Generally, the process ends with an annealing phase to define and stabilize the crystal structure. Depending on the starting materials and process conditions, the crystal structure of TiO_2 nanostructures varies from anatase, rutile and brookite to lepidocrocite.

The morphology of the nanostructures can be altered by combining two different processes. As an example, branched nanotubes can be obtained by the combination of anodization and hydrothermal processes [53].

http://dx.doi.org/10.5772/62316

As an example of wet processing route to obtain pure TiO_2, let us cite Rout et al. [54] describing TiO_2 nanowires obtained by hydrothermal process using $TiCl_3$ solution in HCl and saturated NaCl. The mixture was put in a *Teflon*-lined autoclave and heated at 200°C for 2 hours. After washing with water and alcohol and drying in vacuum, 1-D nanostructures with diameters of 20–80 nm and lengths of 100–800 nm were obtained. The crystal structure was found to be rutile.

A one-step functionalization and synthesis method of TiO_2 nanotubes by hydrothermal processing covered with Pd and Pt nanoparticles was detailed by Han et al. [48]. In this case, commercial anatase TiO_2 powder and $PdCl_2$ or H_2PtCl_6 were dispersed in an aqueous solution of NaOH and charged into a *Teflon*-lined autoclave at 150°C for 12 hours. The precipitates were separated by filtration, washed with dilute HCl and water and finally dried at 120°C, yielding Pd-Pt-TiO_2. The resulting nanotubes were 100 nm in diameter with a lepidocrocite-type phase.

A two-step method is illustrated by Hu et al. [55] with Ag clusters on TiO_2 nanobelts. The nanobelts were prepared via an alkaline hydrothermal process using commercial TiO_2 powders, NaOH, HCl and deionized water. The obtained $H_2Ti_3O_7$ nanobelts were annealed at 600°C for 1 hour to obtain crystalline TiO_2 nanobelts. The surface of the TiO_2 nanobelts was coarsened by adding H_2SO_4 into $H_2Ti_3O_7$ aqueous solution under magnetic stirring followed by heating at 100°C for 12 hours. The obtained phase of TiO_2 nanobelt was anatase. For the preparation of Ag nanoparticle-TiO_2 nanobelts, the as-prepared TiO_2 nanobelts obtained by hydrothermal route were dispersed into $AgNO_3$ and ethanol solution. Taking advantage of a photoreduction process, the solution was illuminated with a 20 W ultraviolet lamp under magnetic agitation.

Electrospinning was exploited by Landau et al. [56] to synthesize TiO_2 nanofibres. Biao et al. [49] describe a method to prepare Cu-doped TiO_2 nanofibres by electrospinning in one step.

A very elegant method that is used for both gas sensing and photovoltaics is anodization as described earlier (see Section **2.2**).

Varghese et al. [57] used a platinum foil as a cathode and titanium foil as an anode at an anodization potential of 12 V and 20 V between the electrodes. The electrolyte consisted of 0.5% hydrofluoric acid in water. The samples were then annealed at 500°C in pure oxygen for 6 hours. The nanotubes were approximately 400 nm in length with a 46–76 nm diameter. A barrier layer with a thickness of 50 nm was formed in between the nanotubes and foil. Nanotubes fabricated using 20 V had an average pore diameter of 76 nm with a wall thickness of 27 nm, while samples anodized at 12 V had an average pore diameter of 46 nm with a wall thickness 17 nm. Anatase concentrated on the walls of the nanotubes and rutile in the barrier layer [58].

Lu et al. [59] also synthesized TiO_2 nanotube arrays by anodization of a titanium foil in a NH_4F and $(NH_4)_2SO_4$ aqueous solution. The titanium foil was used as an anode under a constant potential of 20 V (for 2 hours at room temperature) and the cathode was a platinum foil too. The as-prepared amorphous TiO_2 nanotube arrays were annealed at 450°C in air for 2 hours to obtain anatase phase. The resulting nanostructure had an outer and inner diameter of 150 nm and 110 nm, respectively, with length of approximately 2.3 μm. As usual, the

nanotube dimensions could be varied in the anodization process by changing both the pH of the electrolyte and the electrode voltage [60]. Paulose et al. [60] prepared nanotube arrays by anodization of titanium foils in an aqueous solution containing sodium hydrogen sulfate monohydrate, potassium fluoride and sodium citrate tribasic dihydrate. It was seen that the pore diameter depended on the anodization voltage, whereas the nanotube length depended on both the electrolyte pH and anodization voltage. Hu et al. [53] also synthesized TiO_2 nanotube arrays by the anodization approach. A titanium foil was cleaned by soap, acetone and isopropanol and used as an anode. The cathode was a platinum foil. The anodization solution contained NH_4F and dimethyl sulfoxide. The anodization was conducted at a 45 V constant potential for 9 hours. The obtained amorphous TiO_2 nanotube arrays were annealed at 400°C for 1.5 hours. The resulting nanotubes were 350 nm in diameter and 3.5 μm in length with a wall thickness of 10 nm. The branched TiO_2 nanotubes were obtained through a modification process on TiO_2 nanotubes array by hydrothermal methods [53]. The as-prepared TiO_2 nanotube arrays were immersed in a solution containing HCl with constant stirring at 25°C for 15 minutes. Titanium (IV) isopropoxide was dropped into the solution under constant stirring for 1 hour, and then the beaker was sealed and heated at 95°C for 9 hours with slight stirring. After the reaction, the reactant was cooled to room temperature and washed with ethanol and distilled water. The as-prepared branched TiO_2 nanotube arrays were annealed in a muffle furnace at 400°C for 2 hours. It was observed that TiO_2 nanocrystal nucleus formed on the rough surfaces of the TiO_2 nanotubes with special bamboo structures with a larger and rougher surface area. Similarly, P25 (a commercial photocatalyst from *Degussa*, Germany) coated TiO_2 nanotube arrays were synthesized by the hydrothermal approach on the uncoated TiO_2 nanotube arrays [53]. In this process P25 was added to distilled water and then mixed vigorously by magnetic stirring and ultrasonicating, followed by transferring into a Teflon-lined autoclave. The treatment at 80–120°C for 12 hours was carried out to coat P25 on the TiO_2 nanotube arrays. After washing with distilled water, the P25 coated TiO_2 nanotube arrays were annealed at 400°C for 2 hours in air.

3.4. Sensing performance of TiO_2 1-D nanostructures

The sensitivity of nanowire arrays on silica fabricated by Francioso et al. [52] according to a solid-state process was studied for ethanol sensing. It was seen that the sensitivity of the sensor (defined as the ratio I_{EtOH}/I_{air}) was approximately 50 at 550°C for 2% ethanol. Comparing these results with the response of TiO_2 thin film, the nanowire array showed higher sensitivity towards ethanol. The response is less than 10 in the case of TiO_2 thin film for the same concentration.

Gönüllü et al. [61] studied the impact of doping the surface of TiO_2 nanotubes. TNA for NO_2 detection at high temperature were obtained by anodization. They showed the cross-sensitivity with CO was almost cancelled after doping compared with pure TiO_2 nanotubes.

Hu et al. [55] synthesized four types of TiO_2 nanobelts (TiO_2 untreated nanobelts, TiO_2 surface-coarsened nanobelts, Ag nanoparticles-TiO_2 untreated nanobelts and Ag nanoparticles-TiO_2 surface-coarsened nanobelts) for the detection of ethanol vapour according to the above-

http://dx.doi.org/10.5772/62316

mentioned hydrothermal process. The best performance is obtained for Ag nanoparticles-TiO_2 surface-coarsened nanobelts. The response (defined as the ratio R_{air}/R_{gas}) was about 100 at 200°C for 500 ppm ethanol. The optimum working temperature was in the range of 200–250°C. The response and recovery for ethanol were very short (a few seconds).

Landau et al. [56] measured the sensitivity of TiO_2 nanofibres obtained by electrospinning towards NO_2 gas. These nanofibres showed a good sensitivity at low concentrations of CO and NO_2 in air. The sensor was more sensitive at 300°C than at 400°C (sensitivity to 250 ppb NO_2 (defined as the ratio R_{gas}/R_{air}) was 74.3 at 300°C and 3.3 at 400°C).

Biao et al. [49] compared the sensitivity of Cu-doped and undoped TiO_2 nanofibres also by electrospinning for CO detection. It was observed that Cu-doped TiO_2 nanofibres showed much higher sensitivity compared with pure TiO_2 nanofibres. The sensitivity of Cu-doped TiO_2 nanofibres was approximately 21, which is 17 times larger than pure TiO_2 at 300°C for 100 ppm CO (temperature of maximum sensitivity). The response and recovery times are 4 and 8 seconds, respectively. Moreover, the Cu-doped TiO_2 presented a higher selectivity towards CH_4, CH_3OH, C_2H_5OH, H_2 and NO.

Lu et al. [59] synthesized an amorphous TiO_2 nanotube array for the detection of O_2 using the anodization process. The sensitivity of amorphous TNA approximately increased with increasing temperature, but exhibited non-reproducible behaviour with a very poor recovery above 180°C. However, at 100°C, high sensitivity, excellent recovery and a linear relationship with oxygen concentration was observed. Other metal-oxide sensors such as Ga_2O_3 thin film (~1.5) [62], nanoscale TiO_2 thick film (~1.5) [63] and $SrTiO_3$ thick film (~6.5) [64] showed lower responses towards oxygen at 100°C. Crystalline TiO_2 is highly advantageous for H_2, CO, NO_2 and CH_4 detection [65–67] but for oxygen, crystalline TiO_2 exhibits a very poor recovery [57, 59]. That is why, as for photovoltaics, TiO_2 is usually annealed in air or oxygen atmosphere at high temperature to form a crystalline structure more favourable for gas sensing.

TNA on Ti foil obtained by the anodization process described by Varghese et al. [57] were tested for H_2 sensing. They were able to detect H_2 at temperatures as low as 180°C. The sensitivity of TiO_2 nanotubes increased with increasing temperature showing a variation of three orders in magnitude of resistance to 0.1% of H_2 at 400°C. As always, the response time decreased with increasing temperature. At 290°C the response time was typically 3 min. The sensors showed high selectivity to H_2 compared with CO, CO_2 and NH_3. TiO_2 nanotubes with a smaller pore diameter (46 nm) had higher sensitivity than larger pore diameters (76 nm) towards H_2 gas. The high sensitivity of the nanotubes to H_2 was due to the highly active surface states on the nanotube walls, high surface area of the nanotube architecture and the ordered geometry of the tube-to-tube electrical connections. Han et al. [48] showed that Pt and Pd nanoparticles on TiO_2 nanotubes had a response almost twice that of pure TiO_2 nanoparticles or nanotubes. As usual, the sensitivity goes through a maximum at 25°C. The rate of reaction on the catalytic surface is probably the fastest at this temperature, resulting to a large change of conductivity. This also suggests that the higher response of Pt and Pd nanoparticle-TiO_2 is due to the higher number of adsorption sites or the catalytic surface area. Another possible reason for the enhanced response of Pt and Pd nanoparticle-TiO_2 nanotubes is due to increased

adsorption of hydrogen on the TiO_2 nanotube surface that facilitates the hydrogen oxidation reaction by the Pd and Pt catalysts.

Comparing the sensitivity of anatase and rutile nanostructures, it was stated that anatase shows high sensitivity towards reducing gases such as H_2 and CO [68–70]. The reason would be that the diffusing hydrogen atoms go to the interstitial sites [70, 71] and as the c/a (lattice parameters along c-axis and a-axis) ratio of anatase is almost four times that of rutile, anatase lattice accommodates hydrogen more easily and hence has a higher sensitivity to hydrogen.

3.5. TiO_2 used as a porous template

TiO_2 can also be used as a porous support for the deposition of an organic sensitive layer as described by Wang et al. [50] for the case of ammonia detection with polypyrrole. Polypyrrole (PPy) is a well-known organic semiconductor that was studied for gas detection, in particular NH_3 and VOC. The problem with PPy films is that they are rather non-porous leading to low surface-to-volume ratio and low sensitivity.

To increase this surface-to-volume ratio, Wang et al. [50] proposed to synthesize PPy on a very porous TiO_2/ZnO nanofibre network (diameter of the fibres ~100 nm). The nanofibres were obtained by electrospinning. The TiO_2/ZnO nanofibre network was dipped into a $FeCl_3$ alcoholic solution for 30 minutes. After drying, it was exposed to saturated pyrrole vapours at room temperature for 5 hours, resulting in a thin PPy covering the nanofibres. The obtained material showed a good sensitivity for NH_3 in the ppm concentration range although the response time was still long (15 minutes).

TiO_2 nanotube arrays can be used as a sacrificial template for the preparation of nanowires or nanotubes materials. This is inspired by the new trends in photovoltaic applications of TNA.

In the example detailed below, it was done with polypyrrole for formaldehyde detection. The sensitive polymer is a molecularly imprinted polymer (MIP) based on the polymerization of a mixture of pyrrole and polypyrrole-3-carboxylic acid. Formaldehyde, the target gas, is used as the template for the formation of the MIP. The formation of MIP films by electropolymerization is simple but leads to low porosity films that show a weak sensitivity to formaldehyde. To increase the specific surface area of the polypyrrole, it was synthesized by electrodeposition in an anodized TiO_2 matrix. After getting rid of the TNA by dissolution in NH_4F solution, porous polypyrrole is obtained with high specific surface area.

The anodization was performed on Ti foils cleaned with isopropanol and treated with 1M nitric acid for 30 minutes. The foil was used as the anode and a platinum electrode as the cathode in an electrochemical bath filled with 500 mL ethylene glycol, 10 mL water and 1.7 g NH_4F. A 40 V voltage is applied for 4 hours. After washing with water and drying, the foil is annealed in air at 475°C for 2 hours. Regularly spaced nanotubes with diameter 80–90 nm and wall thickness 7–9 nm were obtained (**Figure 13**).

http://dx.doi.org/10.5772/62316

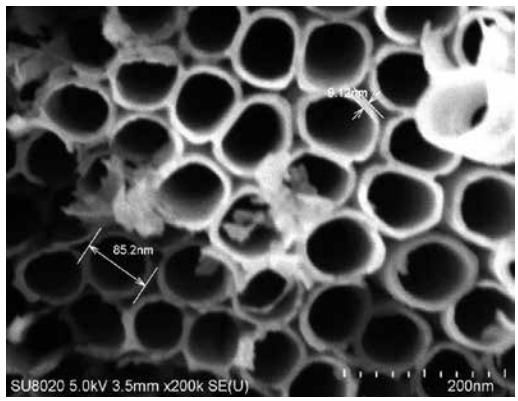

Figure 13. TiO_2 nanotubes used for the synthesis of polypyrrole based MIP.

The obtained anodized Ti is then used as anode for the electrodeposition of the conducting polymer.

The electropolymerization is carried out as follows:

Working electrode: TNA

Counter electrode: Platinum

Reference electrode: Ag/AgCl

Composition of the bath: 50 mL acetonitrile | 0.614 g $NaClO_4$ | 0.17 g sodium dodecylsulfate (SDS) | 0.335 g pyrrole | 55 mg pyrrole-3 carboxylic acid | 10 mL formaldehyde solution (37% in water).

Deposition mode: pulsed 1000 cycles 2 V pulses for 0.1 second | −0.3 V for 0.04 seconds.

By so doing, the nanotubes are covered with the polymer, as shown in **Figure 14**.

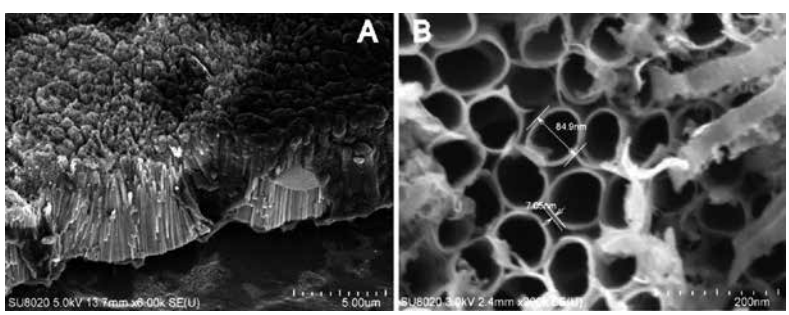

Figure 14. Growth of the polymer in the TiO_2 nanotubes.

After dissolution of the TiO_2 matrix, the porous polymer is obtained (**Figure 15**).

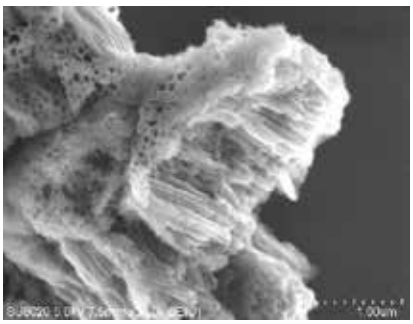

Figure 15. Obtained sensitive polymer after removal of the TiO_2 matrix.

The crushed polymer is deposited by drop coating on a polyimide substrate fitted with interdigitated silver electrodes (electrode width 100 μm, spacing 100 μm, length 20 mm and 20 fingers).

Figure 16 shows the evolution of the resistance of the sensitive polymer after exposure to formaldehyde in humid air (60% at 22°C).

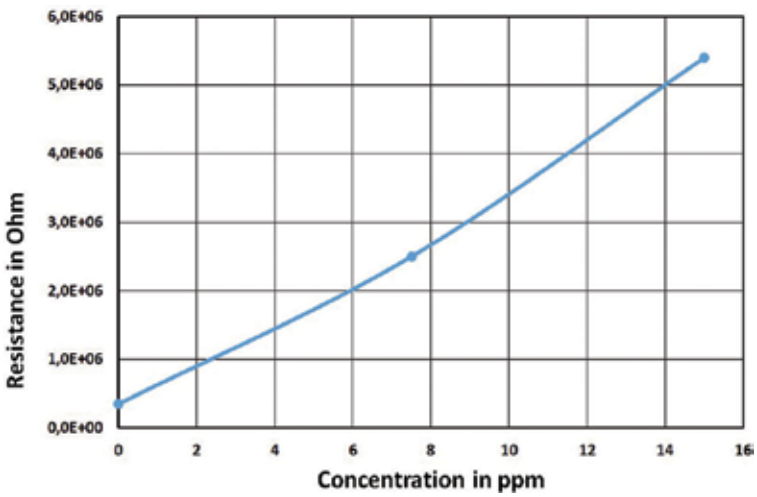

Figure 16. Evolution of the resistance of the porous MIP film when exposed to formaldehyde in humid air.

The same substrate fitted with a continuous film deposited by electropolymerization in the same conditions gives a response three times lower.

4. Conclusion

As can be seen in this chapter, the potentialities of TiO_2 and, in particular, the 1-D nanostructures are very attractive. Due to its unique combination of chemical, electronic and optical

properties, TiO_2 has become one of the major components in the third generation of solar cells and various possible variations (doping, hydrothermal synthesis, hybrid materials, etc.) expand the horizon. On the other hand, the applications of TiO_2 in gas detection are numerous and the interest for this material is growing. One can expect a lot of developments with TiO_2 as sensitive material for chemoresistors, leading to better performances in terms of sensitivity, selectivity and durability.

Acknowledgements

The authors thank the *Région Wallonne* and the *Fédération Wallonie-Bruxelles* for funding (RW: *Photocell*, *Nanorod* and *Captindoor* projects; FWB: Madsscells project). A.K. also thanks FRIA for a grant.

Author details

André Decroly[1*], Arnaud Krumpmann[1], Marc Debliquy[1] and Driss Lahem[2]

*Address all correspondence to: andre.decroly@umons.ac.be

1 University of Mons, Mons, Belgium

2 Materia Nova, Mons, Belgium

References

[1] O'Regan B, Grätzel M. A low-cost, high-efficiency solar cell based on dye-sensitized colloidal TiO_2 films. Nature 1991;353:737–740. DOI: 10.1038/353737a0

[2] Luque A, Hegedus S, editors. Handbook of Photovoltaic Science and Engineering. 2nd ed. Chichester: Wiley; 2011. 1132 p. DOI: 10.1002/978047974704

[3] Grätzel M. Conversion of sunlight to electric power by nanocrystalline dye-sensitized solar cells. Journal of Photochemistry and Photobiology A. 2004;164(1-3):3–14. DOI: 10.1016/j.jphotochem.2004.02.023

[4] Kalyanasundaram K, editor. Dye-Sensitized Solar Cells. 1st ed. Lausanne: EPFL Press; 2010. 320 p.

[5] Polizzotti A, Schual-Berke J, Falsgraf E, Johal M. Investigating new materials and architectures for Grätzel cells. In: Fthenakis V, editor. Third Generation Photovoltaics. 1st ed. Rijeka: InTech; 2012. pp. 111–140. DOI: 10.5772/28223

[6] Kowalski D, Kim D, Schmuki P. TiO_2 nanotubes, nanochannels and mesosponge: Self-organized formation and applications. Nano Today 2013;8:235–264. DOI: 10.1016/j.nantod.2013.04.010

[7] Raja KS, Gandhi T, Misra M. Effect of water content of ethylene glycol as electrolyte for synthesis of ordered titania nanotubes. Electrochemistry Communications 2007;9:1069–1076. DOI: 10.1016/j.elecom.2006.12.024

[8] Regonini D, Bowen CR, Jaroenworaluck A, Stevens R. A review of growth mechanism, structure and crystallinity of anodized TiO_2 nanotubes. Materials Science and Engineering Reports 2013;74:377–406. DOI: 10.1016/j.mser.2013.10.001

[9] Taveira LV, Macak JM, Sirotna K, Dicka LFP, Schmuki P. Voltage oscillations and morphology during the galvanostatic formation of self-organized TiO_2 nanotubes. Journal of the Electrochemical Society 2006;153:B137–B143. DOI: 10.1149/1.2172566

[10] Regonini D, Satkab A, Jaroenworaluck A, Allsopp DWE, Bowen CR, Stevens R. Factors influencing surface morphology of anodized TiO_2 nanotubes. Electrochimica Acta. 2012;74:244–253. DOI: 10.1016/j.electacta.2012.04.076

[11] Valota A, Curioni M, Leclere DJ, Skeldon P, Falaras P, Thompson GE. Influence of applied potential on titanium oxide nanotube growth. Journal of the Electrochemical Society 2010;157:K243–K247. DOI: 10.1149/1.3494155

[12] Shankar K, Mor GK, Prakasam HE, Yoriya S, Paulose M, Varghese OK. Highly-ordered TiO_2 nanotube arrays up to 220 μm in length: Use in water photoelectrolysis and dye-sensitized solar cells. Nanotechnology. 2007;18:065707. DOI: 10.1088/0957-4484/18/6/065707

[13] Mor GK, Varghese OK, Paulose M, Grimes CA. Transparent highly ordered TiO_2 nanotube arrays via anodization of titanium thin films. Advanced Functional Materials 2005;15:1291–1296. DOI: 10.1002/adfm.200500096

[14] Sadek AZ, Zheng H, Latham K, Wlodarski W, Kalantar-Zadeh K. Anodization of Ti thin film deposited on ITO. Langmuir. 2009;25:509–514. DOI: 10.1021/la802456r

[15] Biswas S, Shahjahan M, Hossain MF, Takahashi T. Synthesis of thick TiO_2 nanotube arrays on transparent substrate by anodization technique. Electrochemistry Communications 2010;12:668–671. DOI: 10.1016/j.elecom.2010.03.002

[16] Varghese OK, Paulose M, Grimes CA. Long vertically aligned titania nanotubes on transparent conducting oxide for highly efficient solar cell. Nature Nanotechnology 2009;4:592–597. DOI: 10.1038/nnano.2009.226

[17] Neri G. First fifty years of chemoresistive gas sensors. Chemosensors. 2015;3(1):1-20. DOI: 10.3390/chemosensors3010001

[18] Moseley PT, Norris J, Williams D. Techniques and Mechanisms in Gas Sensing. 1st ed. CRC Press; 1991. 408 p.

[19] Brattain WH, Bardeen J. Surface properties of germanium. Bell System Technical Journal. 1953;32(1):1–41. DOI: 10.1002/j.1538-7305.1953.tb01420.x

[20] Seiyama T, Kato A. A new detector for gaseous components using semiconductor thin film. Analytical Chemistry 1962;34(11):1502–1503. DOI: 10.1021/ac60191a001

[21] Taguchi N. Gas Detecting Devices. U.S. Patent 3,631,436. 28 December 1971.

[22] Seiyama T, editor. Chemical Sensor Technology (Vol. 1). Amsterdam: Elsevier; 1988.

[23] Yamazoe N. New approaches for improving semiconductor gas sensors. Sensors and Actuators B: Chemical. 1991;5(1-4):7–19. DOI: 10.1016/0925-4005(91)80213-4

[24] Shimizu Y, Egashira M. Basic aspects and challenges of semiconductor gas sensors. MRS Bulletin. 1999;24(6):18–24. DOI: http://dx.doi.org/10.1557/S0883769400052465

[25] Yamazoe N. Toward innovations of gas sensor technology. 2005;108(1-2):2–14. DOI: 10.1016/j.snb.2004.12.075

[26] Fierro JLG, editor. Metal Oxides: Chemistry and Applications. Boca Raton: CRC Press; 2006.

[27] Aleixandre M, Gerboles M. Review of small commercial sensors for indicative monitoring of ambient gas. Chemical Engineering Transactions. 2012;30:169–174. DOI: http://publications.jrc.ec.europa.eu/repository/handle/JRC75718

[28] Bârsan N, Hübner M, Weimar U. Conduction mechanisms in SnO_2 based polycrystalline thick film gas sensors exposed to CO and H_2 in different oxygen backgrounds. Sensors and Actuators B: Chemical. 2011;157(2):510–517. DOI: 10.1016/j.snb.2011.05.011

[29] Bârsan N, Tomescu A. Calibration procedure for SnO_2-based gas sensors. Thin Solid Films. 1995;259(1):91–95. DOI: 10.1016/0040-6090(94)06415-6

[30] Niebling G, Schlachter A. Qualitative and quantitative gas analysis with non-linear interdigital sensor arrays and artificial neural networks. Sensors and Actuators B: Chemical. 1995;247(1-3):289–292. DOI: 10.1016/0925-4005(94)01603-F

[31] Yamaura H, Tamaki J, Moriya K, Miura N, Yamazoe N. Highly selective CO sensor using indium oxide doubly promoted by cobalt oxide and gold. Journal of the Electrochemical Society. 1997;144(6):158–160.

[32] Matsuura Y, Takahata K, Matsuura S. Denki Kagaku. 1990;58:1154.

[33] Tricoli A, Righettoni M, PratsinisSE. Minimal cross-sensitivity to humidity during ethanol detection by SnO_2-TiO_2 solid solutions. Nanotechnology. 2009;20(31):315502. DOI: 10.1088/0957-4484/20/31/315502

[34] Cederquist A, Gibbons E, Meitzler A. Characterization of zirconia and titania engine exhaust gas sensors for air/fuel feedback control systems. SAE Technical Paper. 1976;760202. DOI: 10.4271/760202

[35] Kolmakov A, Moskovits M. Chemical sensing and catalysis by one-dimensional metal-oxide nanostructures. Materials Research. 2004;34:151–180. DOI: 10.1146/annurev.matsci.34.040203.112141

[36] Arafat MM, Dinan B, Akbar SA, Haseeb ASMA. Gas sensors based on one dimensional nanostructured metal-oxides: A review. Sensors. 2012;12(6):7207-7258. DOI: 10.3390/s120607207

[37] Thong LV, Hoa ND, Le DTT, Viet DT, Tam PD, Le AT, Hieu NV. On-chip fabrication of SnO2-nanowire gas sensor: The effect of growth time on sensor performance. Sensors and Actuators B: Chemical. 2010;146(1):361–367. DOI: 10.1016/j.snb.2010.02.054

[38] Huang MH, Mao S, Feick H, Yan H, Wu Y, Kind H, Weber E, Russo R, Yang P. Room-temperature ultraviolet nanowire nanolasers. Science. 2001;292(5523):1897–1899. DOI: 10.1126/science.1060367

[39] Yang Z, Li LM, Wan Q, Liu QH, Wang TH. High-performance ethanol sensing based on an aligned assembly of ZnO nanorods. Sensors and Actuators B: Chemical. 2008;135(1):57–60. DOI: 10.1016/j.snb.2008.07.016

[40] Wan Q, Li QH, Chen YJ, Wang TH, He XL, Li JP, Lin CL. Fabrication and ethanol sensing characteristics of ZnO nanowire gas sensors. Applied Physics Letters. 2004;84:3654–3656. DOI: http://dx.doi.org/10.1063/1.1738932

[41] Göpel W, Hesse J, Zemel JN, editors. Sensors set: A comprehensive survey. VCH; 1995. DOI: 10.1002/9783527619269

[42] Kim HJ, Lee JH. Highly sensitive and selective gas sensors using p-type oxide semiconductors: Overview. Sensors and Actuators B: Chemical. 2014;192(1):607–627. DOI: 10.1016/j.snb.2013.11.005

[43] Huang XJ, Choi YK. Chemical sensors based on nanostructured materials. Sensors and Actuators B: Chemical. 2007;122(2):659–671. DOI: 10.1016/j.snb.2006.06.022

[44] Jimenez-Cadena G, Riu J, Xavier Rius F. Gas sensors based on nanostructured materials. The Analyst. 2007;132(11):1083–1099. DOI: 10.1039/b704562j

[45] Yamazoe N, Shimanoe K. Receptor function and response of semiconductor gas sensor. Journal of Sensors. 2009;ID 875704. DOI: http://dx.doi.org/10.1155/2009/875704

[46] Min Y, Tuller HL, Palzer S, Wöllenstein J, Böttner H. Gas response of reactively sputtered ZnO films on Si-based micro-array. Sensors and Actuators B: Chemical. 2003;93(1-3):435–441. DOI: 10.1016/S0925-4005(03)00170-9

[47] Boudiba A, Zhang C, Umek P, Bittencourt C, Snyders R, Olivier MG, Debliquy M. Sensitive and rapid hydrogen sensors based on Pd–WO_3 thick films with different morphologies. International Journal of Hydrogen Energy. 2013;38(5):2565–2577. DOI: 10.1016/j.ijhydene.2012.11.040

[48] Han CH, Hong DW, Kim IJ, Gwak J, Han SD, Singh KC. Synthesis of Pd or Pt/titanate nanotube and its application to catalytic type hydrogen gas sensor. Sensors and Actuators B: Chemical. 2007;128(1):320–325. DOI: 10.1016/j.snb.2007.06.025

[49] Biao W, Dong ZY, Ming HL, Sheng CJ, Li GF, Yun L, Jun WL. Improved and excellent CO sensing properties of Cu-doped TiO_2 nanofibers. Chinese Science Bulletin. 2010;55(3):228–232. DOI: 10.1007/s11434-009-0727-9

[50] Wang Y, Jia W, Strout T, Schempf A, Zhang H, Li B, Cui J, Lei Y. Ammonia gas sensor using polypyrrole-coated TiO_2/ZnO nanofibers. Electroanalysis. 2009;21(12):1432–1438. DOI: 10.1002/elan.200904584

[51] Yoo S, Akbar SA, Sandhage KH. Nanocarving of titania (TiO_2): A novel approach for fabricating chemical sensing platform. Ceramics International. 2004;30(7):1121–1126. DOI: 10.1016/j.ceramint.2003.12.085

[52] Francioso L, Taurino AM, Forleo A, Siciliano P. TiO_2 nanowires array fabrication and gas sensing properties. Sensors and Actuators B: Chemical. 2008;130(1):70–76. DOI: 10.1016/j.snb.2007.07.074

[53] Hu A, Cheng C, Li X, Jiang J, Ding R, Zhu J, Wu F, Liu J, Huang X. Two novel hierarchical homogeneous nanoarchitectures of TiO_2 nanorods branched and P25-coated TiO_2 nanotube arrays and their photocurrent performances. Nanoscale Research Letters. 2011;6(91):2–6. DOI: 10.1186/1556-276X-6-91

[54] Rout CS, Kulkarni GU, Rao CNR. Room temperature hydrogen and hydrocarbon sensors based on single nanowires of metal oxides. Journal of Physics D: Applied Physics 2007;40(9):2777–2782. DOI: 10.1088/0022-3727/40/9/016

[55] Hu P, Du G, Zhou W, Cui J, Lin J, Liu H, Liu D, Wang J, Chen S. Enhancement of ethanol vapor sensing of TiO_2 nanobelts by surface engineering. ACS Applied Materials & Interfaces 2010;2(11):3263–3269. DOI: 10.1021/am100707h

[56] Landau O, Rothschild A, Zussman E. Processing-microstructure-properties correlation of ultrasensitive gas sensors produced by electrospinning. Chemistry of Materials. 2009;21(1):9–11. DOI: 10.1021/cm802498c

[57] Varghese OK, Gong D, Paulose M, Ong KG, Grimes CA. Hydrogen sensing using titania nanotubes. Sensors and Actuators B: Chemical. 2003;93(1-3):338–344. DOI: 10.1016/S0925-4005(03)00222-3

[58] Varghese OK, Gong D, Paulose M, Grimes CA, Dickey EC. Crystallization and high-temperature structural stability of titanium oxide nanotube arrays. Journal of Materials Research. 2003;18(1):156–165. DOI: http://dx.doi.org/10.1557/JMR.2003.0022

[59] Lu HF, Li F, Liu G, Chen Z-G, Wang D-W, Fang H-T, Lu GQ, Jiang ZH, Cheng H-M. Amorphous TiO_2 nanotube arrays for low-temperature oxygen sensors. Nanotechnology. 2008;19(40):405504. DOI: 10.1088/0957-4484/19/40/405504

[60] Paulose M, Varghese OK, Mor GK, Grimes CA, Ong KG. Unprecedented ultra-high hydrogen gas sensitivity in undoped titania nanotubes. Nanotechnology. 2005;17(2): 398–402. DOI: http://dx.doi.org/10.1088/0957-4484/17/2/009

[61] Gönüllü Y, Haidry AA, Saruhan B. Nanotubular Cr-doped TiO_2 for use as high-temperature NO_2 gas sensor. Sensors and Actuators B: Chemical. 2015;217:78–87. DOI: 10.1016/j.snb.2014.11.065

[62] Ogita M, Higo K, Nakanishi Y, Hatanaka Y. Ga_2O_3 thin film for oxygen sensor at high temperature. Applied Surface Science. 2001;175-176:721–725. DOI: 10.1016/S0169-4332(01)00080-0

[63] Gao L, Li Q, Song Z, Wang J. Preparation of nano-scale titania thick film and its oxygen sensitivity. Sensors and Actuators B: Chemical. 2000;71(3):179–183. DOI: 10.1016/S0925-4005(00)00612-2

[64] Hu Y, Tan OK, Cao W, Zhu W. A low temperature nano-structured $SrTiO_3$ thick film oxygen gas sensor. Ceramics International. 2004;30(7):1819–1822. DOI: 10.1016/j.ceramint.2003.12.068

[65] Varghese OK, Gong DW, Paulose M, Ong KG, Dickey EC, Grimes CA. Extreme changes in the electrical resistance of titania nanotubes with hydrogen exposure. Advanced Materials. 2003;15(7-8):624–627. DOI: 10.1002/adma.200304586

[66] Han KR, Kim CS, Kang KT, Koo HJ, Kang DI, Jingwen H. Study on sensing properties of tin oxide CO gas sensor with low power consumption. Sensors and Actuators B: Chemical. 2002;81(2-3):182–186. DOI: 10.1016/S0925-4005(01)00950-9

[67] Ruiz AM, Sakai G, Cornet A, Shimanoe K, Morante JR, Yamazoe N. Cr-doped TiO_2 gas sensor for exhaust NO_2 monitoring. Sensors and Actuators B: Chemical. 2003;93(1-3): 509–518.

[68] Akbar SA, Younkman LB. Sensing mechanism of a carbon monoxide sensor based on anatase titania. Journal of the Electrochemical Society. 1997;104(5):1750–1753. DOI: 10.1149/1.1837673

[69] Savage NO, Akbar SA, Dutta PK. Titanium dioxide based high temperature carbon monoxide selective sensor. Sensors and Actuators B: Chemical. 2001;72(3):239–248. DOI: 10.1016/S0925-4005(00)00676-6

[70] Birkefeld LD, Azad AM, Akbar SA. Carbon monoxide and hydrogen detection by anatase modification of titanium dioxide. Journal of the American Ceramic Society. 2005;75(11):2964–2968. DOI: 10.1111/j.1151-2916.1992.tb04372.x

[71] Bates JB, Wang JC, Perkins RA. Mechanisms for hydrogen diffusion in TiO_2. Physical Review B. 1979;19(8):4130-4139. DOI: 10.1103/PhysRevB.19.4130

Chapter 6

Anodic Nanostructures for Solar Cell Applications

Jia Lin, Xiaolin Liu, Shu Zhu and Xianfeng Chen

Additional information is available at the end of the chapter

http://dx.doi.org/10.5772/62396

Abstract

As a versatile, straightforward, and cost-effective strategy for the synthesis of self-organized nanomaterials, electrochemical anodization is nowadays frequently used to synthesize anodic metal oxide nanostructures for various solar cell applications. This chapter mainly discusses the synthesis of various anodic TiO_2 nanostructures on foils and as membranes or powders, and their potential use as the photoanode materials based on foils, transparent conductive oxide substrates, and flexible substrates in dye-sensitized solar cell applications, acting as dye-loading frames, light-harvesting enhancement assembly, and electron transport medium. Through the control and modulation of the electrical and chemical parameters of electrochemical anodization process, such as applied voltages, currents, bath temperatures, electrolyte composition, or post-treatments, anodic nanostructures with controllable structures and geometries and unique optical, electronic, and photoelectric properties in solar cell applications can be obtained. Compared with other types of nanostructures, there are several major advantages for anodic nanostructures to be used in solar cells. They are (1) optimized solar cell configuration to achieve efficient light utilization; (2) easy fabrication of large size nanostructures to enhance light scattering; (3) precise modulation of the electrochemical processes to realize periodic nanostructured geometry with excellent optical properties; (4) unidirectional electron transport pathways with suppressed charge recombination; and (5) large surface areas by modification of nanostructures. Due to the simple fabrication processes and unique properties, the anodic nanostructures will have a fascinating future to boost the solar cell performances.

Keywords: anodic nanostructures, membranes, scattering, photonic crystals, thermal stability, surface area

1. Introduction

1.1. Anodic oxides

The electrochemical anodization of anodic oxides is conducted with two-electrode or three-electrode configurations in an electrochemical cell, with the targeted metals as the working electrode (anode) and usually Pt/carbon as the counter electrode (cathode). The electrolytes used are typically fluoride-containing organic or aqueous solutions. A voltage is applied between the two electrodes to fabricate various nanostructures on the anodic metal surface. The anodic oxides feature the self-organized configurations with regular and open structures, such as tubes, pores, channels, bundles, powders, and various tailored shapes. The formation mechanism of oxide nanostructures is of great concern. For tube arrays, the possible processes are as follows: (1) The first step is the tube initiation. The tube growth initiates at some preferable positions on the metal surface that can provide both high local electric field and narrow channel-like surface morphology. It has been indicated that the morphological instability of the initial oxide surface layer causes the formation of pores [1]. Hence the surface state of the starting metal substrate can significantly influence the surface morphology of the anodic oxides, such as pore size distribution, regularity, and shapes. (2) The second step is the tube growth. One most accepted view is that the oxidation of the metal with the assistance of electric field forms a compact thin oxide layer (barrier layer) on the surface [2]. The thin oxide layer is also partially dissolved under the assistance of electric field. The oxidation and dissolution happen simultaneously. When the oxide growth rate at the metal/oxide interface equals to the oxide dissolution at the oxide/electrolyte interface, the thickness of the compact oxide layer keeps unchanged. Then the compact layer at the oxide/metal interface moves towards the inner part of the metals and the oxide nanostructures form into the metals.

Due the advantages such as simplicity, high efficiency, and low cost of electrochemical anodization, it has been utilized to fabricate various wide band gap metal oxide nanostructures, such as titanium oxide (TiO_2), aluminum oxide (Al_2O_3), hafnium oxide, zirconium oxide, niobium oxide, tantalum oxide, tungsten oxide, and their alloys. Among them, the most widely studied anodic oxides are Al_2O_3 and TiO_2. For Al_2O_3, usually nanoporous structures can be obtained, which can be used as filters and templates. TiO_2 nanotube structure was first reported by Zwilling in 1999 by electrochemical anodization of Ti metal in aqueous fluoride containing electrolyte [3, 4]. Recent studies have indicated that the nanotube morphology is in fact converted from nanopores by dissolution of the oxides at the interpore region. Due to the unique properties, TiO_2 nanotubes have been utilized in dye-sensitized solar cells (DSSCs), perovskite solar cells, quantum dot solar cells, photocatalysis, batteries, supercapacitors, electrochromic devices, sensors, drug release, and cell differentiation applications. In this chapter, we mainly discuss the fabrication of TiO_2 nanotubes and the design and improvement of DSSCs.

The electrochemical anodization is a highly controllable technique. The growth of anodic TiO_2 nanostructures can be influenced by many key anodization parameters, such as applied voltages, currents, bath temperatures, post treatments, and kinds of electrolyte. The

http://dx.doi.org/10.5772/62396

control of the complex oxidation formation and chemical etching of the oxides can be realized during the anodization process, to establish the balance between the oxidation and dissolution. As a result, the morphology, regularity, growth rate, size, length, wall smoothness, and single or double walled nanotubes can be artificially designed. For example, fast growth of nanotubes can be realized in an electrolyte-containing lactic acid, which is desirable for industry production [5]. The nanotubes with lengths ranged from several 100 nm to 1000 μm have been fabricated [6]. Furthermore, by in-situ doping with various non-metal or metal elements in the electrolytes containing additives, visible light response of the anodic oxides can be obtained. The control of anodic nanostructures will greatly influence their physical and chemical properties, and their performances in various devices.

1.2. Solar cell applications

The development of low-cost new-generation solar cells has attained broad attention recently. Dye-sensitized solar cell (DSSC) is a kind of photoelectrochemical cell with the advantages of low cost, simple synthesis, large area, and high stability. Since the first report by O'regan and Grätzel with 7.1% efficiency [7], the highest efficiency of above 13% has been achieved [8]. In DSSCs, typically TiO_2 nanoparticles are used as the photoanode material, which are coated on transparent conductive oxide (TCO) substrates to form porous networks. The dye sensitizers are adsorbed on the surface of nanoparticles to harvest incident light. The dyes are surrounded by liquid redox electrolytes, which can reduce the oxidized dyes and accept electrons from the counter electrode. In the photon-to-electricity conversion process, the light absorption and the charge transport are two separate processes. The electron-hole pairs are separated by the heterojunctions with different work functions. No obvious built-in electric field exists in DSSCs, and the electrons go through the TiO_2 network by diffusion. Inspired by the development of DSSCs, other types of sensitized solar cells such as quantum dot (QD)/semiconductor sensitized solar cells and perovskite solar cells have been introduced. For QD systems, by adjusting the size of QDs, the band gaps can be tuned [9]. Furthermore, by using QDs, multiple exciton generation effect exists [10]. The perovskite solar cells are a new type of solar cell devices. Due to the high absorption efficiency and broad absorption range of perovskite materials, the efficiency has been above 20% recently [11].

For solar cell applications, the anodic nanostructured materials are usually used to replace TiO_2 nanoparticles to fabricate the photoanodes. In DSSCs, the photoanodes mainly play two important roles. First, the nanostructures provide large specific internal surface areas for the anchoring of dyes. Second, the nanostructures provide the charge diffusion pathways to transport the injected charges to the outer circuit. As a result, the morphology, structure, crystal structure, and surface state of anodic nanostructures can determine the performance of DSSCs based on these photoanodes, including loading of dyes, light harvesting, charge transport, recombination, and collection, and finally power conversion efficiency.

2. Solar cell configuration

2.1. 1D TiO_2 nanotubes

The nanoparticle photoanodes in DSSCs have the randomly distributed sizes, and loosely and irregularly packed structures. As a result, the injected electrons encounter a large amount of nanoparticles (about 10^3 to 10^6 as estimated) when diffuse through the photoanodes. The real path for electrons to travel before reaching the substrate is very long. This increases the probability of electron recombination loss at the oxide/electrolyte interface. One-dimensional (1D) nanostructures, such as nanotubes, nanowires, nanofibers, and nanorods, can provide the directional electron diffusion, which shortens the electron pathways, and are proved to have better collection efficiency [12]. By electrochemical anodization, various 1D nanostructures have been developed, and one very important nanostructure is TiO_2 nanotubes. The first attempt to use TiO_2 nanotubes to replace nanoparticles in DSSCs is reported by Schmuki et al. [13], and afterwards various reports have been emerging. The electron recombination rate in TiO_2 nanotubes is found to be very slow, with much larger electron lifetime (more than 10 times) than TiO_2 nanoparticles [14]. Thus, anodic TiO_2 nanotubes are very promising for high performance solar cells.

2.2. Free-standing membranes

Usually, the anodic nanotubes are grown on the Ti metal foil substrate, which is opaque. When directly utilizing TiO_2 nanotubes on foils in DSSCs, back-side illumination cell configuration is needed [15]. That is to say, the solar light enters the solar cell from the counter electrode. As a result, the light would be reflected by counter electrode that is coated with a thin layer of catalyst, and also be absorbed by dark redox electrolyte before it can be absorbed by dyes loaded on the anodic nanostructures. It has been estimated that about approximately 30–40% light energy would be lost by using this back-side illumination configuration [16]. To realize the front-side light illumination and to fabricate transparent electrode for broad applications, the anodic TiO_2 nanotubes should be fabricated on the TCO substrates.

One strategy is the direct growth of TiO_2 nanotubes by anodizing the sputtered or thermal evaporated thick Ti metal films on TCO substrates. However, there exist two problems. One is that the synthesis of thick and high-quality metal films on TCO substrate is very difficult, with complex and expensive procedures. The other is that the anodization oxidation process would lead to the increase of the TCO substrate resistance, the weak connection between the anodic oxide films and the substrate, and even the peeling off of the oxide films from the substrate. The low electric conductivity will result in the efficiency loss of solar cells.

The more promising method is to peel the anodic oxide layer off the metal substrate to obtain free-standing membranes, and transfer them onto TCO substrate. Various strategies such as ultrasonication separation, solvent evaporation, selective metal dissolution, and chemical-assisted separation have been proposed to peel off the films, but the procedure is complex and need careful handling. Furthermore, to obtain open bottom structure for effective tube filling

http://dx.doi.org/10.5772/62396

and flow through application, usually additional chemical etching steps of tube bottoms are needed.

To obtain high-quality free-standing membranes with simple synthesis procedures and tunable bottom morphologies, the self-detaching method has been proposed [17]. The as-formed anodic oxide layer is thermally treated at a certain temperature, and anodized again in the same electrolyte. After a short time, the oxide layer can be peeled off from the substrate without any post-treatment procedure. If the as-formed oxide layer is subjected to heat treatment at a low temperature (e.g., 200°C), the detached layer is amorphous and shows a black color. After annealing, the layer becomes crystallized and transparent (**Figure 1a**). For high temperature-treated layer (e.g., 400°C), the tubes are crystallized in the anatase phase before detachment. As a result, the detached layer is already transparent without subsequent annealing (**Figure 1b**). The detachment is probably because of the difference in mechanical and chemical stability between the top anodic layer (which we try to peel off) and the newly formed layer underneath the top layer [18]. Furthermore, according to the heat treatment temperatures during the detachment, the free-standing oxide layer can have open tube bottoms (200°C, **Figure 1c-f**) or closed bottom ends (400°C). It should also be noted that during the detaching anodization, elevating the bath temperature can facilitate the layer detachment and promote the formation of open bottoms. This elevated temperature can reduce the electrolyte viscosity and enhance the filed-assisted chemical dissolution at the tube bottom. Also, the strategy is a green technology without the use of corrosive solution and ensures continuous production [19].

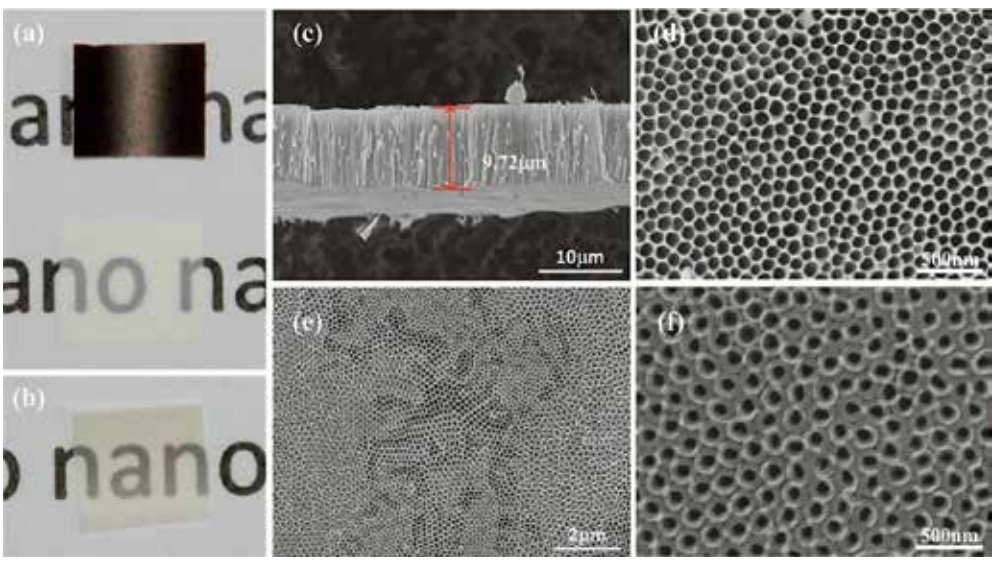

Figure 1. The photographs of (a) the detached 200°C-treated oxide layer with open bottoms before and after annealing and (b) the detached 400°C-treated oxide layer with closed bottoms. SEM images of the detached 200°C-treated oxide layer with (c) the cross-sectional view, (d) the top view, (e) the bottom view showing the open morphology, and (f) the enlarged bottom view. Reprinted with permission from Lin et al. [17].

2.3. Front-side illumination

The above-mentioned detached free-standing membranes can be used in DSSCs to achieve front-side illumination solar cell configuration, improving the light utilization efficiency. The detached oxide layer is transferred and adhered onto the TCO substrate by a thin layer of TiO_2 nanoparticles, and then sintered to enhance the connectivity (**Figure 2a**). For this detaching and transfer method, the solar cell efficiency is much higher (about 1.75 times) than on foil, due to the improvement of illumination configuration [20]. Furthermore, it has been found that tube bottom morphology also affects the solar cell efficiency. The solar cell based on tubes with open bottoms shows a better performance than that with closed bottoms, with an efficiency improvement of 17.7%. The photographs of the two kinds of photoanodes before annealing can be seen in **Figure 2b**. The removal of the tube bottom and the barrier layer can induce more dye loading of the tubes and less light scattering of the bottom caps. Furthermore, the open bottoms can facilitate the diffusion of redox electrolyte and thus reduce the recombination probability of electrons with the oxidized ions in the electrolyte [21]. Other solar cell configurations utilizing detached membranes include the bottom down or bottom-up structures and combination of nanoparticle/nanotube layers, which can be designed as required. Besides the free-standing films, nanotube powders can also be used to achieve the front-side illumination configuration, which is discussed in Section 3.

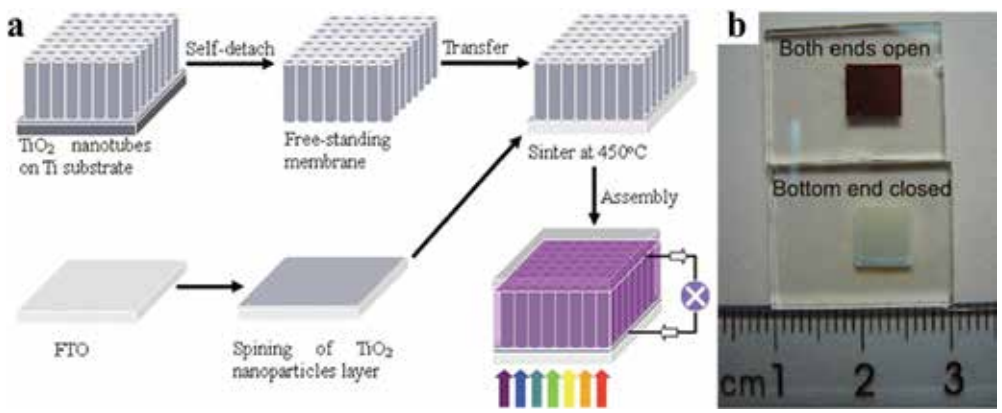

Figure 2. (a) Scheme of the fabrication procedure of front-side illuminated DSSCs using detached nanotube layers. (b) The photographs of the oxide layers with open and closed bottoms adhered onto FTO substrates. Reprinted with permission from Lin et al. [20].

3. Light scattering

3.1. Scattering effect

The widely used dyes in DSSCs commonly have high absorption efficiencies only within a narrow wavelength region, with low response for the red- and near-infrared light. Simply

http://dx.doi.org/10.5772/62396

increasing the thickness of photoelectrode film to enhance the absorption of photons will cause the increase of resistance and recombination loss. Therefore, it is essential to develop light scattering structures to increase the photon absorption opportunity by dye molecules in the weak absorption regions. As a common optical phenomenon, light scattering effect could extend the optical traveling length of incident light, so as to improve the light-harvesting efficiency and to achieve high performances. Based on Mie theory, to achieve efficient light scattering, the size of scattering centers should be comparable to the wavelength of the incident light. As a consequence, scattering structures with various morphologies have been introduced.

In general, there are three different photoelectrode configurations to combine light scattering centers. The first one is the mixed structure, for which large particles such as scattering centers are embedded into the photoelectrode films (**Figure 3a**). The scattering centers in such structure could introduce multiple scattering in the light absorption layer. However, the large particles would unavoidably cause the loss of dye adsorption because of the low surface area. The second one is the double layered structure, for which the light scattering layer is placed on the top of the nanocrystalline film (**Figure 3b**). Adding the scattering layer on the top could ensure sufficient dye loading. However, the light scattering would be weaker than in the mixed structure. The third one is the photoelectrode composed of hierarchical nanostructures with dual functions (**Figure 3c**). There have been many studies on the fabrication of such hierarchical nanocrystallite aggregates. The intensive light scattering could be guaranteed without much loss of specific surface area, but the preparation process is much more complicated. As a result, to achieve prominent light scattering and thus high DSSC performance, we should overcome the drawbacks of these structures.

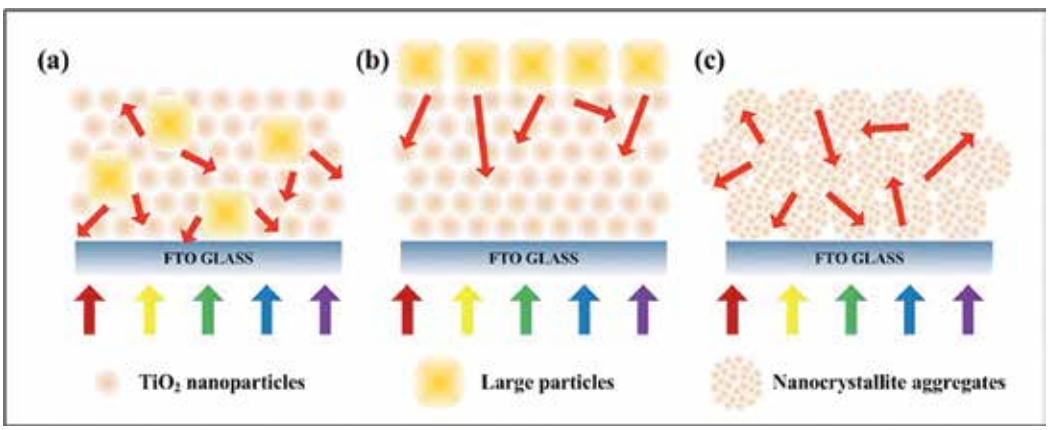

Figure 3. The schematic and light chart of the light scattering structures.

3.2. Conventional scattering centers

The large TiO_2 particles with diameters of about 200–400 nm are commonly used as light scattering centers, which can be simply mixed into the photoelectrode films to increase the light harvesting efficiency. In the early studies, Grätzel et al. have found that when TiO_2 nanoparticles are hydrothermally prepared at 250°C (normally below 230°C), the nanoparticle film would become translucent because of the spontaneous particle agglomeration [22]. Subsequently, the fabrication of large TiO_2 particles with high crystallinity has been paid more and more attention.

Besides nanoparticles, solid spheres fabricated by facile hydrothermal method also exhibit light scattering effect. However, the large particles or spheres usually suffer from low surface area for dye loading, which would affect the light harvesting. To overcome the weakness of low surface area, TiO_2 spheres with rough surfaces have been synthesized. Also, mesoporous spheres with dual functions have been fabricated by nanocrystallite clustering, which are dominant in light scattering without the loss of surface area for dye-uptake. The hollow spheres are an alternative candidate for light scattering centers because of their larger surface area and better infiltration of electrolyte. Recently, core-shell microspheres have gradually emerged and become very promising scattering center. The core-shell structure could not only provide large light scattering, but also confine the light inside the spheres.

3.3. TiO_2 nanotubes powders

Apart from the above structures, 1D nanostructures could also serve as light scattering centers, such as nanorods, nanofibers, nanotubes, and their aggregates. For example, the light-to-electricity conversion yield of 6.08% has been achieved by blending of large TiO_2 nanorods (800 nm) and small nanorods (20–40 nm) on the top of small nanorod films, benefit from the low charge transport resistance and high light scattering effect [23]. TiO_2 nanofibers have been readily fabricated by simple electrospinning and applied in DSSCs as photoanode films [24]. The mixture of 1D nanostructures with nanoparticles could make a significant improvement of the performance of DSSCs also because of the combined effect of strong light scattering, abundant dye-loading amounts, and the improvement of electron transport properties.

TiO_2 nanotube arrays with 1D nanostructure have been found to have prominent light scattering effect, with the combination of superior electron transport when applied in DSSCs [14, 25]. Due to the formation of large crystalline grains and existence of nanotube bundles, the TiO_2 nanotubes could generate effective light scattering. Lee et al. [26] obtained TiO_2 nanotube powders and coated the powders on the top of the nanocrystalline film, and attained noticeable increment of light harvesting.

The mixed structures of nanotubes and nanoparticles have also been explored in many studies. Embedding nanotube powders inside the nanoparticle film can (1) promote the permeation of liquid electrolyte, (2) increase the electron transport in the photoanode, and (3) introduce the scattering effect of nanotubes, which would be profitable for high perform-

http://dx.doi.org/10.5772/62396

ance DSSCs. Lin et al. have fabricated TiO_2 nanotubes by anodic growth and involved ultrasonic separation of the resulted nanotubes to obtain TiO_2 nanotube powders (**Figure 4a**) [27]. To reduce the electron trap states, the nanotube powders are thermally treated at a high annealing temperature (650°C) to enhance crystallinity (the details are discussed in Section 5). The hybrid photoanodes can be formed by mixing these highly crystallized nanotube powders with TiO_2 nanoparticles (**Figure 4b**). By adjusting the weight ratio of the nanotube powders, the performance of DSSCs could be optimized and the highest efficiency of 6% has been achieved.

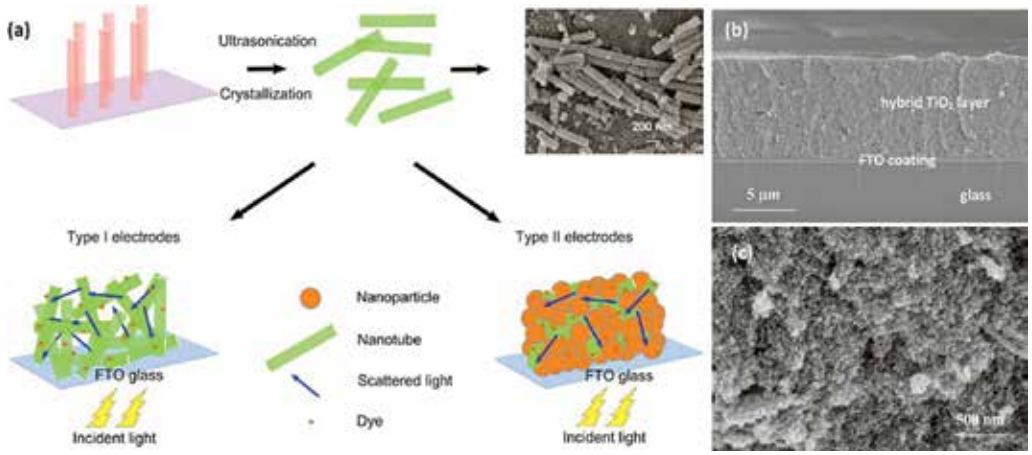

Figure 4. The schematic of the fabrication procedures of nanotube powders, nanotube electrode, and hybrid electrode. (b, c) The cross-sectional views of the hybrid photoanode with nanotubes embedded in nanoparticles. Reprinted with permission from Lin et al. [27].

3.4. Large nanotubes

Generally, the diameter of nanotubes fabricated by conventional electrochemical anodization is about 100 nm, which is obviously smaller than the wavelength of visible light. The large diameter nanotubes of size comparable to the visible light wavelength (500 nm or above) can be synthesized under high-voltage anodization. For example, by anodization at a high voltage of 180 V in an organic electrolyte containing lactic acid (aged for 10 hours), large nanotubes with top diameter of 300 nm and bottom diameter of 500 nm have been fabricated (**Figure 5a,b**) [28]. The resulting nanotube membranes are transferred onto a thick TiO_2 nanocrystalline film to act as the light scattering layer (**Figure 5c,d**). The large diameter nanotubes show a superior scattering property, and the photoanode incorporated with large nanotubes on top is nearly opaque in visible light (**Figure 5e**). By introducing the large diameter nanotube membranes, the performance of DSSCs has been greatly improved, which is 19% higher than that without scattering layer, and 11% higher than that using normal nanotubes (100 nm) as the scattering layer (**Figure 5f**).

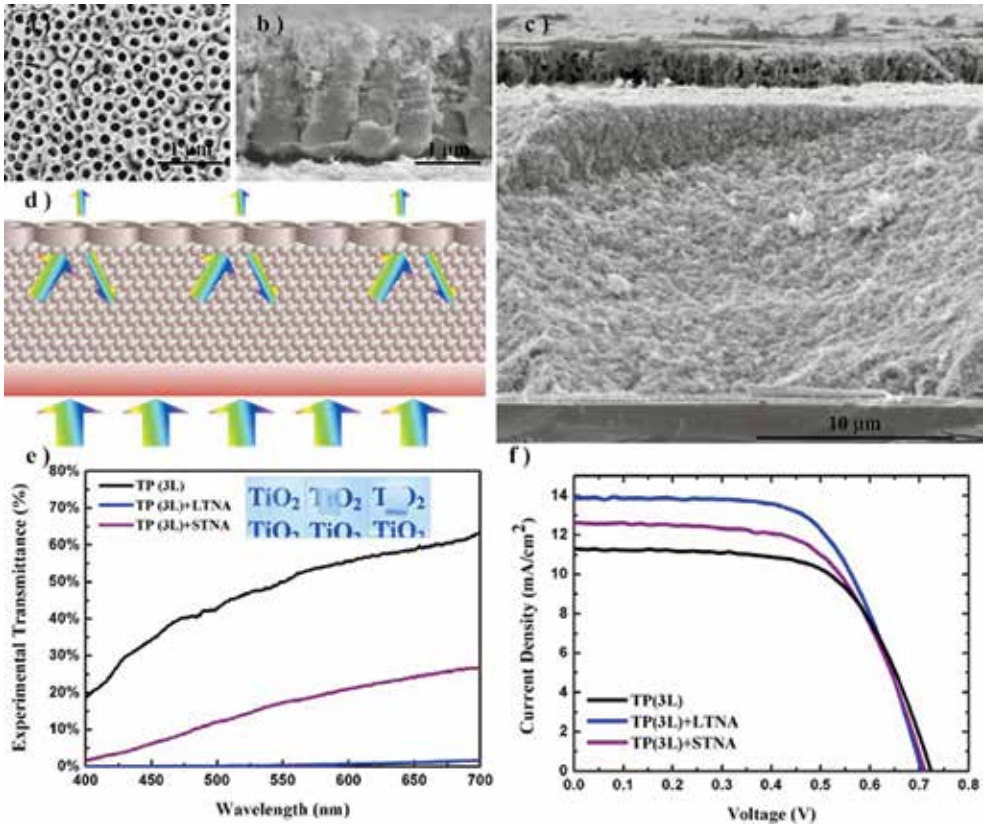

Figure 5. SEM images of large diameter nanotubes with (a) the top view and (b) the cross-sectional view. (c) SEM image and (d) schematic of double-layered photoanode using large nanotubes as the scattering layer. (e) The transmittance spectra of the photoanodes without scattering layer (TP(3L)), with normal nanotubes (TP(3L) + STNA), and with large nanotubes (TP(3L) + LTNA) as scattering layers. (f) Photocurrent-voltage curves of the DSSCs based on these photoanodes. Reprinted with permission from Liu et al. [28].

To enhance the functionality of the photoanodes of DSSCs, the multi-stacked photoanodes have also been developed by integration of three or more various TiO_2 architectures [29, 30]. For TiO_2 nanotubes, the similar multi-layered structures have been fabricated (**Figure 6a**), based on the study of large diameter nanotubes [31]. First, bi-layered TiO_2 nanotube membrane with top large nanotubes (~540 nm) and underlayer normal nanotubes (~130 nm) has been fabricated by two-step anodization in different kinds of electrolytes (**Figure 6b**). Secondly, the bi-layered membrane is transferred onto a layer of TiO_2 nanoparticles for building photoanodes. The three layers are stacked together with gradually decreased sizes from top to bottom. For this type of multi-layered photoelectrode, layers with different tailored nanostructures play different roles on the performance of the DSSCs. By optimizing the thickness and synergistic effects of each layer (**Figure 6c**), large amounts of dye adsorption, reduced recombination during the electron diffusion, and efficient light scattering can be simultaneously guaranteed. DSSCs based on the multi-functional photoanode shows a photoelectric efficiency as high as 6.52%.

http://dx.doi.org/10.5772/62396

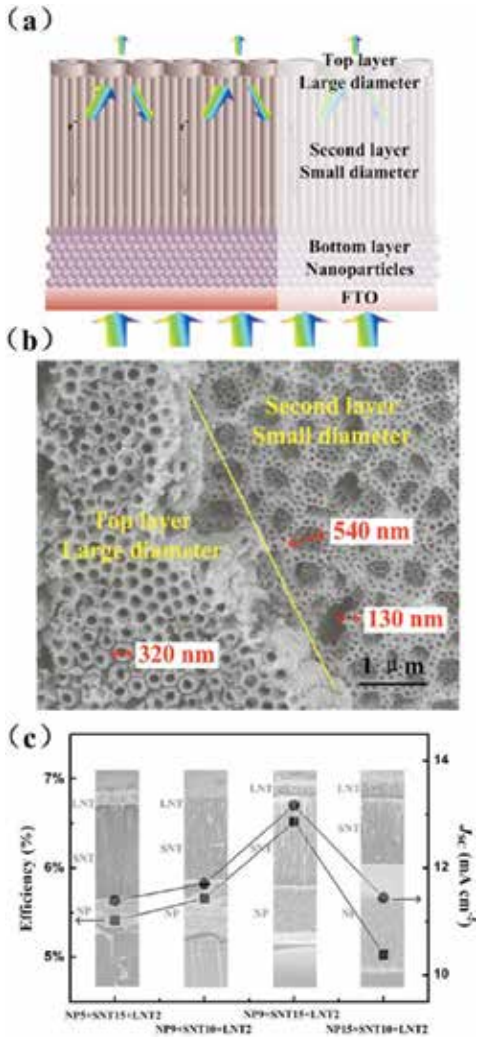

Figure 6. (a) The schematic of the multi-layered photoanode with top layer large diameter nanotubes (LNT), second layer normal nanotubes (SNT), and bottom layer nanoparticles (NP). (b) SEM image of the bilayered nanotube membrane. (c) The solar cell efficiencies based on multi-layered photoanodes with different layer thicknesses. Reprinted with permission from Liu et al. [31].

4. Photonic crystal structures

4.1. Photonic crystal effect

As illustrated above, the improvement of light harvesting is very important to enhance the solar cell performances. Besides light scattering centers, the photonic crystals (PCs), including one-dimensional (1D), two-dimensional (2D), and three-dimensional (3D) structures, can also

be used to enhance the light harvesting. PCs are the optical materials with periodically changed refractive index. By adding PCs on the top of nanocrystalline film, PCs will greatly influence the light behavior inside the photoanode, to reflect the light, which would transmit through the photoanode back to the photoanode if the light is in the band gap of PCs, reabsorbed by dye molecules. The possible mechanisms of PC effect are photon localization, special photon behavior at the band edge, and light reflection.

The PC structures can be fabricated by various strategies, such as self-assembly, lithography, and laser writing. For example, TiO_2–SiO_2 nanoparticle alternate layers have been deposited onto TiO_2 nanoparticle mesoporous layer by spin-coating to act as 1D PCs [32]. The fabrication of such multi-layers, however, needs complex processing procedures. Using soft-lithographic technique, 2D PCs with high periodicity have been produced, to enhance the photocurrent generation in DSSCs [33]. 3D PCs usually consist of opal/inverse opal structures from PS spheres [34–36], which can provide a complete photonic band gap and large enhancement in light harvesting.

4.2. Anodic photonic crystals

For PC applications, the excellent regularity of anodic nanostructures is required. The porous and tube structures by electrochemical anodization have the inherent 2D periodicity. Due to the high periodicity, porous Al_2O_3 nanostructures have been applied as 2D PCs for applications such as lasing and light-emitting diode [37, 38]. However, for TiO_2 nanotubes, due to the randomness of tube initiation, the regularity is not so satisfactory. To obtain highly ordered arrays, focused ion beam (FIB) sculpting has been used to achieve the patterned metal surface prior to anodization, which can guide the subsequent nanotube growth. This technique has been largely studied by Lu et al. [39], both on Ti and Al metals, and various kinds of patterns have been produced. The regularity can well meet the requirement of PCs, but the main problem is that the fabrication procedure is complex and time-consuming, which is not suitable for large-scale production. By using the so-called two-step or multi-step anodization [40], the dips formed by the first-step anodization on the metal surface can also act as the template to guide the tube growth, improving the tube regularity to a certain extent.

4.3. TiO_2 nanotube 3D photonic crystals

Usually, the anodized TiO_2 nanotubes have the smooth tube walls (**Figure 7a**). By the constant voltage anodization in certain electrolytes, the random and spontaneous current oscillation can lead to the formation of small ripples on the tube walls (**Figure 7b**). Inspired by this phenomenon, the fabrication of regular 1D nanostructures along the tube axis has been proposed. For Al_2O_3, Lee et al. [41, 42] tried to fabricate 3D ordered nanoporous structure by mild and hard anodization in two different electrolytes. Periodic voltage anodization (cyclic anodization or pulse voltage anodization) has also been used to fabricate branched nanostructures for PCs [43]. The key point to induce the structure change along the longitudinal direction is the abruption of the established steady growth state of anodic nanostructures. TiO_2 possesses higher refractive index ($n \sim 2.7$) than Al_2O_3 ($n \sim 1.7$), more suitable to be used as structural color materials to realize the complete bandgap. Hence, the strategies to induce ordered periodic

http://dx.doi.org/10.5772/62396

structure along the TiO_2 tube axis have been greatly concerned. The bamboo-type TiO_2 nanotubes have been achieved by the periodic or pulse voltage anodization [44], which have certain longitudinal periodicity. However, due to the unstable nanotube growth rate under constant voltage anodization, the periodic voltage can only fabricate the structures with short range regularity. Furthermore, the structural parameters and thus PC characteristics cannot be preciously adjusted.

To realize the strict control of regularity, the periodic structures along the longitudinal direction can be fabricated by periodic current anodization [45]. Because the applied current is directly related to the growth rate of anodic oxide, the steady current can ensure the uniformity of the oxide growth and the control of the interrupt of current can lead to the periodic structures along the axis. During the current pause, the oxide growth stops, but the chemical dissolution continues, resulting in the structural difference on the tube walls (**Figure 7c**). Unlike the smooth or rippled tube wall morphologies, the tube segments can be clearly observed with the concave shaped interfaces. In the range of about 20 periods from top to bottom, the distance between segments (period length) is almost the same, revealing excellent long-range regularity (**Figure 7d**).

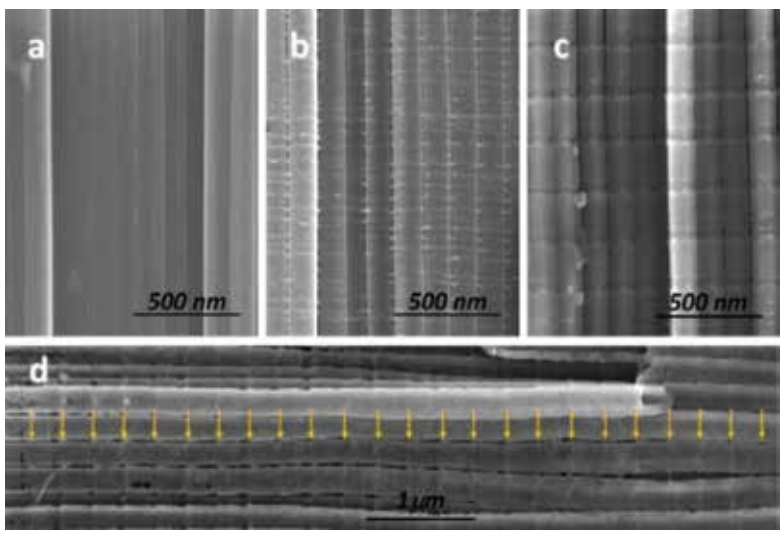

Figure 7. The cross-sectional SEM image of the periodic structures with (a) smooth, (b) rippled, and (c) periodic tubes with concave interfacial morphologies. (d) The periodic structures along the tube axis with long-range regularity (period length: 292 nm). Reprinted with permission from Lin et al. [45].

As discussed above, due to the higher reflective index, TiO_2 is more suitable photonic material than Al_2O_3. By using periodic current-pulse sequences, the photonic features of TiO_2 nanotubes, including period length, interfacial morphology, period number, and type of period (periodic, quasiperiodic, or aperiodic), can be precisely and continuously modulated by the anodization parameters. The periodic nanotube films (after detachment) with different period lengths show different colors and transparencies (**Figure 8a**), and corresponding different

reflection spectra (**Figure 8b**). Furthermore, the structural color of the nanostructured film is not static. The film with fixed period structure shows different colors with different light incident and viewing angles (**Figure 8c**).

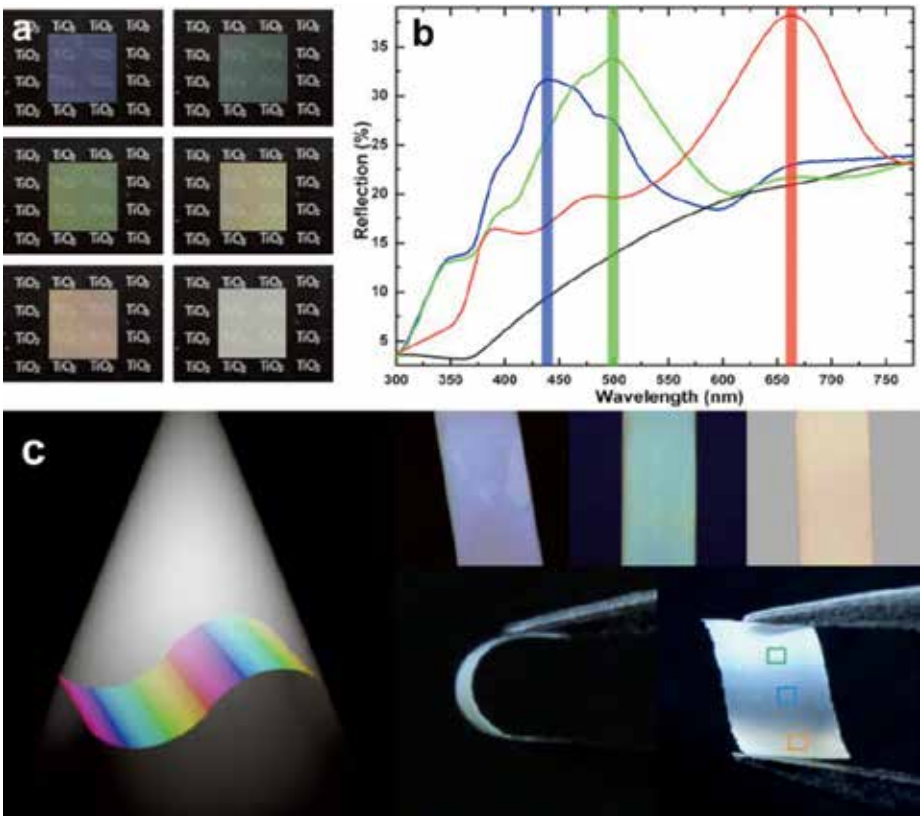

Figure 8. The optical images of the colorful films, from purple to red. (b) The reflection spectra of the colorful films, showing the bandgaps. (c) The change of film colors with different incident and viewing angles and the flexibility of the colorful films. Reprinted with permission from Lin et al. [45].

TiO_2 nanotube PCs have been coupled directly to nanotube layers in DSSCs by a single step [46]. Also the thin PC membrane can be placed on the top of nanocrystalline TiO_2 layers as semi-transparent photoanode for DSSCs [47]. During the design of the solar cells, we should consider the match between the bandgap of PC structures and the incident light spectrum, to maximize the solar cell light harvesting. Thus, the different PCs with different band structures are designed and coupled to DSSCs. When using N719 dye as light absorber, it is found that DSSCs coupled with 150 nm periodic structure show the best performance. The advantages of the strategy using the above 3D nanotube PCs in solar cells are (1) tunable photonic structure, (2) controllable fabrication process, (3) easy integration by direct fabrication of both light absorbing layer and PC layer tubes by a single-step anodization or by membrane transfer, (4) tight mechanical and electrical connection between the light absorbing layer and PC layer,

http://dx.doi.org/10.5772/62396

facilitating the charge transport, (5) interconnected two layers at the interface region, facilitating the electrolyte infiltration, and (6) easy fabrication of large area, transparent, and flexible PC films.

5. Electron properties

5.1. Substrate effect

In DSSCs, the widely used model describing the diffusion process in the TiO_2 electrode is the multiple trapping model. During the electron transport, the electron undergoes the trapping and detrapping processes by the trap states. To enhance the charge collection and thus efficiency, the fast transport and slow recombination of electrons are required. It has been reported that the order of the nanomaterials can greatly influence the electron property. For disordered nanoparticles, there exist numerous particle–particle interfaces. While for nanotubes, electrons transport along the tube axis, which would lead to higher electron transport rate [48, 49]. However, in anodic tubes, the transport is not as fast as expected. Various studies have been devoted to investigating the possible underlying mechanism. The widely accepted view is that there exist a large amount of trap states in tubes, as compared with nanoparticles, which suppress the electron transport [14, 50, 51]. The trap states, usually oxygen vacancies or Ti^{3+} ions, are most likely originated from non-crystallized amorphous regions, grain boundaries, and the impurities induced during the anodization process.

The improvement of tube crystallinity by high temperature annealing is supposed to be useful for the reduction of the trap densities. However, usually the substrate effect exists during annealing of anodic oxides on metal substrate. That is to say, the metal substrate can greatly affect the crystal phase and nanostructure of the oxide film layer during the annealing process. For TiO_2 nanotubes on Ti, rutile phase can be detected at a low annealing temperature of 400–450°C. Furthermore, the nanotubes are gradually condensed at high temperatures, and finally the porous structure is fully destroyed at about 700–800°C. This is due to the fact that the Ti foil can be directly oxided to the rutile phase during high temperature annealing, forming a thin and compact oxide layer at the oxide/metal interface region, and gradually becomes thicker [52]. This rutile layer will initiate the crystal phase and structure transformation of the upper TiO_2 layer, from the bottom to the top. The substrate effect exists at different annealing conditions, and even more severe when the annealing temperature increases [53–55]. Thus, anodic oxide films on metal foils can only be crystallized at a relatively low annealing temperature for DSSC applications. The high temperature annealing would cause the destruction of nanostructure and increase of resistance, both of which deteriorate the solar cell performance.

5.2. Highly crystallized nanotubes

To realize the high temperature annealing and thus highly crystallized TiO_2 nanotubes for DSSCs, the substrate effect should be eliminated. This can be realized by annealing of free-standing TiO_2 nanotube membranes before the attachment of the membrane onto the TCO

substrate. For membranes without metal substrate, the substrate effect does not exist, and the crystallization behavior is completely different. There have been several attempts to anneal membranes at high temperatures [56–58]. The initiation temperature of phase transformation and structure densification becomes much higher. The main problem is that during the high temperature annealing, the membrane is inclined to curling and cracking, due to the low quality of the membranes fabricated by various strategies. By optimizing the self-detaching anodization process as discussed in Section 2, high-quality TiO_2 nanotube membranes can be obtained. The membranes can withstand the high temperature annealing up to 700°C and the hollow, porous, and ordered structure is maintained (**Figure 9a–e**) [59], although the crystallites in the tube walls gradually become larger (**Figure 9f**).

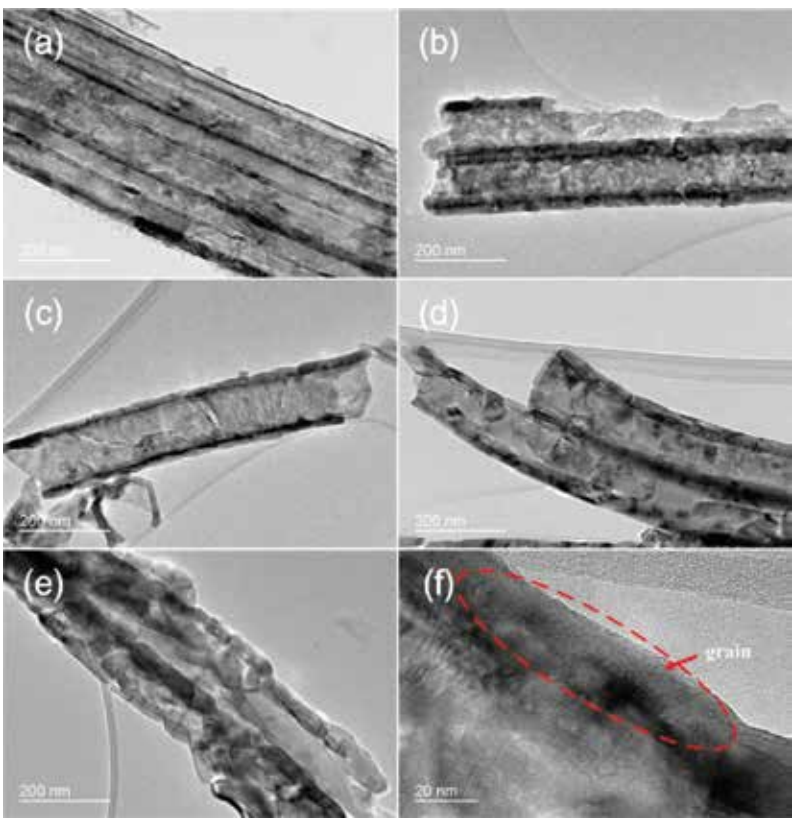

Figure 9. TEM images of tube membranes annealed at (a) 400, (b) 500, (c) 600, (d) 700, and (e) 800°C. (f) HRTEM view of the grain in the tube walls annealed at 700°C. Reprinted with permission from Lin et al. [59].

The TiO_2 nanotube membranes with high crystallinity have been used as the photoanode in DSSCs (**Figure 10a**). The electron transport is found to be enhanced significantly because of the reduction of the impurity and defects and thus the electron trap states. As a result, the electron diffusion length is much longer in the highly crystallized nanotube membranes (**Figure 10b**). Despite the lower surface area and thus lower dye loading amount, a significantly

http://dx.doi.org/10.5772/62396

improved solar cell efficiency of 7.81% has been obtained for 700°C annealed sample. The high temperature annealing for enhancement of crystallinity can also be used to fabricate flexible DSSCs. For such type of solar cells, the high temperature annealing is also not applicable because the flexible substrate (usually PET or PEN) cannot withstand high temperatures. For membranes, the high temperature annealing is completed before the transfer of nanotubes to the flexible substrate. Thus, the conductivity and quality of flexible substrate are not influenced by the high temperature annealing process. The only problem is how to keep the membrane adhered tightly to the flexible substrate, ensuring the electron transport pathways [60].

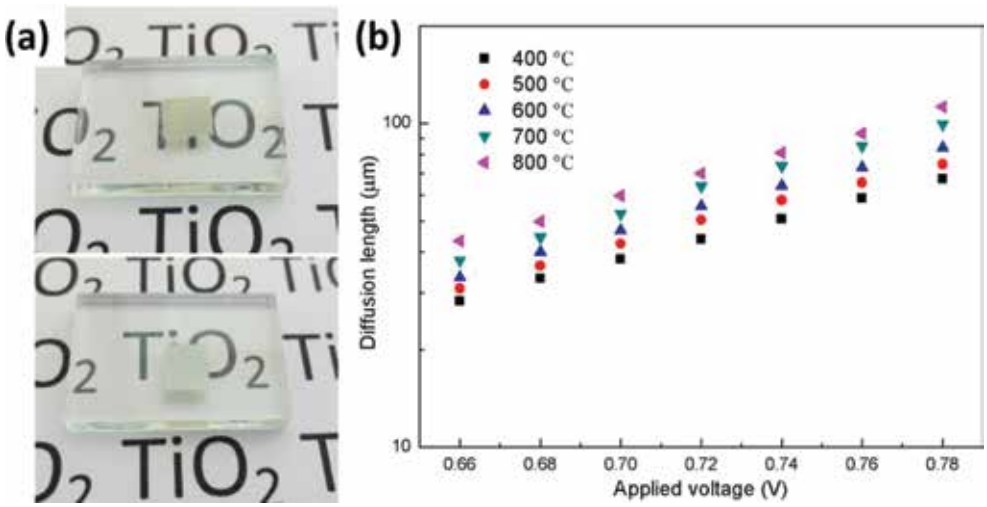

Figure 10. (a) The photographs of photoanodes consisting nanotube membranes annealed at 400 and 700°C. (b) The variation of diffusion length in DSSCs as a function of annealing temperature. Reprinted with permission from Lin et al. [59].

6. Surface areas

6.1. Small size nanotubes

Anodic TiO_2 nanotubes usually have low specific surface areas (BET surface area ~20 m^2/g), as compared with other nanomaterials. For normal hexagonal closely packed nanotube arrays, due to the compact and ordered structure, large tube size, and smooth tube wall, the internal surface area is limited. When the nanotubes are applied in DSSCs as the photoanode material, the light cannot be fully absorbed, leading to low light harvesting efficiency. To increase the surface area, the most common strategy is the decoration of small diameter nanoparticle on the hollow tube inner or outer surface by $TiCl_4$ treatment or immersion filling, to fabricate tube/particle mixed structure. The synthesis of bi-layered structure consisting of both tube layer and nanoparticle layer, double-walled nanotubes, and bamboo type tubes with rings or ripples on tube outer walls are all benefit for the improvement of surface areas.

Fabrication of small diameter but large thickness tube layer is another strategy to increase the surface area. Typically the small diameter tubes are very short [61], and thus the surface area per electrode area is still very low. The attempt has been focused on the fabrication of high aspect ratio tubes with small diameters and large thicknesses, increasing the dye loading amount per electrode area. In usual anodization conditions, it has been found that the outer diameter of TiO_2 nanotubes is proportional to the anodization voltage within a certain range, but inversely proportional to the bath temperature. By anodization at a low voltage and a high temperature, the diameter can be greatly reduced. When the bath temperature increases from 20 to 50°C, the outer diameter can be decreased from 93 to 75 nm [62]. On the other hand, the high bath temperature can promote the growth of anodic nanotubes, leading to the small tubes with large thicknesses, which can provide enough surface area for dye anchoring.

6.2. Water immersion treatment

Besides the in-situ anodization strategies, post-treatment method can also be used to tune the geometry and structure of nanotubes and guarantee the sufficient surface area for dye adsorption. By simple water immersion of as-grown TiO_2 nanotubes at room temperature (about 1–3 days) or hot water immersion, the tube wall morphology can be changed in a controllable way [63]. This is only useful for as-formed tubes before annealing, which are amorphous. The water treatment leads to the formation of hybrid-walled tubes with outer wall unchanged (smooth tubes) while inner wall converted to small nanoparticles (**Figure 11a,b**). The TEM image clearly shows that in the hybrid structure, the tube outer wall consists elongurated nanocrystallites along the tube axis with lengths of dozens of nanometers to several hundred nanometers (**Figure 11c**). The small nanoparticles existing in the inner wall have the average crystal size of about 11 nm. The hybrid structure of the tube wall after water treatment appears to be similar to the filling or decoration of tube inner part with small nanoparticles. But it is apparently different than after water treatment, the solid tube wall appears to become thinner. This can be explained by the fact that in hybrid tubes, the nanoparticles in the inner wall are, in fact, converted from the tube wall. The formation of particles consumes the tube wall.

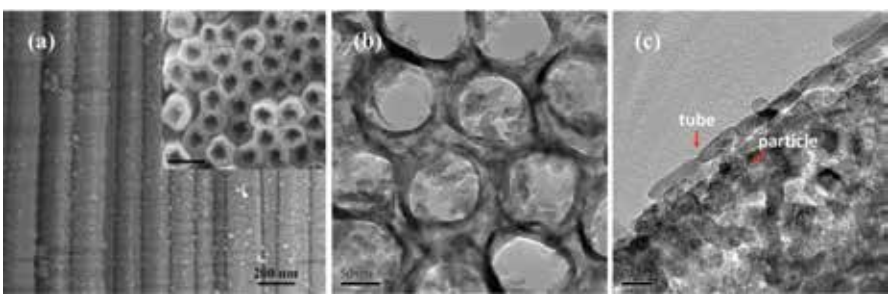

Figure 11. (a) The cross-sectional SEM images of the hybrid tubes by water immersion treatment. The insert is the top view. (b, c) TEM images of the hybrid structure consisting tubes and particles. Reprinted with permission from Lin et al. [63].

http://dx.doi.org/10.5772/62396

During the water immersion process, the inner wall is inclined to be converted to nanoparticles. Normally the tube wall fabricated in organic electrolyte consists of inner and outer shells. The inner shell contains a large amount of carbon, which is originated from the anodization electrolyte in the anodization process [64]. Due to the different chemical compositions of the two shells, the inner walls are more easily to be converted by water to nanoparticles. This is a simple but effective way to enhance the tube roughness. Also along with the structure change, partial phase transition of nanotubes from amorphous to anatase has been observed. But if the tubes are annealed (>200°C), the tubes are stable, and the water immersion cannot cause any structural change even for a long time. It has been reported that the TiO_2 dissolution/precipitate process in water would cause the rearrangement of the construction unit of TiO_2, leading to the spontaneous variation of crystal structure and morphology [65, 66].

As discussed above, the conversion of the inner tube wall to nanoparticles can enhance the tube roughness and lead to the full utilization of the tube hollow space, increasing the internal surface area of anodic nanotubes, while keeping the tubular morphology unchanged. That is to say, the unique properties of tubes can be maintained, such as more convenient dye adsorption and electrolyte infiltration, short electron diffusion path, and slow electron recombination. After the subsequent annealing, the hybrid nanostructures are applied in DSSCs. The BET surface area increases with increasing immersion time. Before treatment, the BET surface area is about 20.1 m^2/g, and increases to 39.9 and 42.7 m^2/g after 2 and 3 days immersion, respectively. The 3 days water treated sample has a BET surface area about 2.1 times larger than normal tubes. Accordingly, the photoanode dye loading amount increases by 38.9% and 57.8% as compared with normal tubes. An optimized efficiency of 6.06% is obtained, improved by about 33%. Due to the maintenance of tubular structure, the water treatments do not affect the electron recombination property. This is beneficial for the improvement of the DSSC efficiency as compared with previous report that the nanotubes decorated with nanoparticles showed decreased electron lifetimes [67, 68].

7. Conclusion remarks

This chapter discusses about the fabrication of anodic nanostructures by electrochemical anodization and their application in dye-sensitized solar cells to enhance the power conversion efficiency. The solar cell configurations can be optimized by free-standing anodic membranes to maximize the light utilization. By using large-sized nanotubes, due to the light scattering effect, the full interaction of the incident light with the absorbing layer can enhance the light harvesting of the solar cells. For periodic structures, the interface of the period is typically voids, resulting in the required periodic modulation of the refractive index for photonic crystals, which show the tunable photonic bandgaps, a property very attractive for light harvesting. By fabrication of high-quality membranes, highly crystallized nanotube membrane can be obtained, which can provide superior electron collection properties in solar cells. The surface areas of nanotubes can be increased by using high-aspect-ratio nanotubes and tube wall modification. The solar cells equipped with the proposed anodic nanostructures are expected to show excellent device performances, valuable for practical applications.

Author details

Jia Lin, Xiaolin Liu, Shu Zhu and Xianfeng Chen*

*Address all correspondence to: xfchen@sjtu.edu.cn

Shanghai Jiao Tong University, Shanghai, China

References

[1] Hebert K.R., Albu S.P., Paramasivam I., Schmuki P. Morphological instability leading to formation of porous anodic oxide films. Nature Materials. 2011; 11 (2): 162–166.

[2] Macak J., Tsuchiya H., Ghicov A., Yasuda K., Hahn R., Bauer S., et al. TiO_2 nanotubes: Self-organized electrochemical formation, properties and applications. Current Opinion in Solid State and Materials Science. 2007; 11 (1): 3–18.

[3] Zwilling V., Aucouturier M., Darque-Ceretti E. Anodic oxidation of titanium and TA6V alloy in chromic media. An electrochemical approach. Electrochimica Acta. 1999; 45 (6): 921–929.

[4] Zwilling V., Darque-Ceretti E., Boutry-Forveille A., David D., Perrin M.-Y., Aucouturier M. Structure and physicochemistry of anodic oxide films on titanium and TA6V alloy. Surface and Interface Analysis. 1999; 27 (7): 629–637.

[5] So S., Lee K., Schmuki P. Ultra-fast growth of highly ordered anodic TiO_2 nanotubes in lactic acid electrolytes. Journal of the American Chemical Society. 2012; 134 (28): 11316–11318.

[6] Paulose M., Prakasam H., Varghese O., Peng L., Popat K., Mor G., et al. TiO_2 nanotube arrays of 1000 μm length by anodization of titanium foil: Phenol red diffusion. The Journal of Physical Chemistry C. 2007; 111 (41): 14992–14997.

[7] O'regan B., Grätzel M. A low-cost, high-efficiency solar cell based on dye-sensitized colloidal TiO_2 films. Nature. 1991; 353 (6346): 737–740.

[8] Mathew S., Yella A., Gao P., Humphry-Baker R., Curchod B.F., Ashari-Astani N., et al. Dye-sensitized solar cells with 13% efficiency achieved through the molecular engineering of porphyrin sensitizers. Nature Chemistry. 2014; 6 (3): 242–247.

[9] Kongkanand A., Tvrdy K., Takechi K., Kuno M., Kamat P.V. Quantum dot solar cells. Tuning photoresponse through size and shape control of CdSe-TiO_2 architecture. Journal of the American Chemical Society. 2008; 130 (12): 4007–4015.

[10] Sambur J.B., Novet T., Parkinson B. Multiple exciton collection in a sensitized photovoltaic system. Science. 2010; 330 (6000): 63–66.

[11] Zhou H., Chen Q., Li G., Luo S., Song T.-b., Duan H.-S., et al. Interface engineering of highly efficient perovskite solar cells. Science. 2014; 345 (6196): 542–546.

[12] Law M., Greene L.E., Johnson J.C., Saykally R., Yang P. Nanowire dye-sensitized solar cells. Nature Materials. 2005; 4 (6): 455–459.

[13] Macák J.M., Tsuchiya H., Ghicov A., Schmuki P. Dye-sensitized anodic TiO_2 nanotubes. Electrochemistry Communications. 2005; 7 (11): 1133–1137.

[14] Zhu K., Neale N.R., Miedaner A., Frank A.J. Enhanced charge-collection efficiencies and light scattering in dye-sensitized solar cells using oriented TiO_2 nanotubes arrays. Nano Letters. 2007; 7 (1): 69–74.

[15] Paulose M., Shankar K., Varghese O., Mor G., Hardin B., Grimes C. Backside illuminated dye-sensitized solar cells based on titania nanotube array electrodes. Nanotechnology. 2006; 17 (5): 1446–1448.

[16] Kim J.Y., Noh J.H., Zhu K., Halverson A.F., Neale N.R., Park S., et al. General strategy for fabricating transparent TiO_2 nanotube arrays for dye-sensitized photoelectrodes: Illumination geometry and transport properties. ACS Nano. 2011; 5 (4): 2647–2656.

[17] Lin J., Chen J., Chen X. Facile fabrication of free-standing TiO_2 nanotube membranes with both ends open via self-detaching anodization. Electrochemistry Communications. 2010; 12 (8): 1062–1065.

[18] Macak J., Aldabergerova S., Ghicov A., Schmuki P. Smooth anodic TiO_2 nanotubes: annealing and structure. Physica Status Solidi (a). 2006; 203 (10): R67–R69.

[19] Wang D., Liu L. Continuous fabrication of free-standing TiO_2 nanotube array membranes with controllable morphology for depositing interdigitated heterojunctions. Chemistry of Materials. 2010; 22 (24): 6656–6664.

[20] Lin J., Chen J., Chen X. High-efficiency dye-sensitized solar cells based on robust and both-end-open TiO2 nanotube membranes. Nanoscale Research Letters. 2011; 6 DOI: 10.1186/1556-276x-6-475.

[21] Yip C.-T., Guo M., Huang H., Zhou L., Wang Y., Huang C. Open-ended TiO_2 nanotubes formed by two-step anodization and their application in dye-sensitized solar cells. Nanoscale. 2012; 4 (2): 448–450.

[22] Barbe C.J., Arendse F., Comte P., Jirousek M., Lenzmann F., Shklover V., et al. Nanocrystalline titanium oxide electrodes for photovoltaic applications. Journal of the American Ceramic Society. 1997; 80 (12): 3157–3171.

[23] Kuo P.-L., Jan T.-S., Liao C.-H., Chen C.-C., Lee K.-M. Syntheses of size-varied nanorods TiO_2 and blending effects on efficiency for dye-sensitized solar cells. Journal of Power Sources. 2013; 235: 297–302.

[24] Yang L., Leung W.W.F. Application of a bilayer TiO_2 nanofiber photoanode for optimization of dye-sensitized solar cells. Advanced Materials. 2011; 23 (39): 4559–4562.

[25] Zheng Q., Kang H., Yun J., Lee J., Park J.H., Baik S. Hierarchical Construction of self-standing anodized titania nanotube arrays and nanoparticles for efficient and cost-effective front-illuminated dye-sensitized solar cells. ACS Nano. 2011; 5 (6): 5088–5093.

[26] Lee K.S., Kwon J., Im J.H., Lee C.R., Park N.-G., Park J.H. Size-tunable, fast, and facile synthesis of titanium oxide nanotube powders for dye-sensitized solar cells. ACS Applied Materials & Interfaces. 2012; 4 (8): 4164–4168.

[27] Lin J., Zheng L., Liu X., Zhu S., Liu Y., Chen X. Assembling of a high-scattering photoelectrode using a hybrid nano-TiO_2 paste. Journal of Materials Chemistry C. 2015; 3 (26): 6645–6651.

[28] Liu X., Guo M., Cao J., Lin J., Tsang Y.H., Chen X., et al. Large-diameter titanium dioxide nanotube arrays as a scattering layer for high-efficiency dye-sensitized solar cell. Nanoscale Research Letters. 2014; 9 (1): 1–5.

[29] Wu W.-Q., Xu Y.-F., Rao H.-S., Su C.-Y., Kuang D.-B. Multi-stack integration of three-dimensional hyperbranched anatase titania architectures for high-efficiency dye-sensitized solar cells. Journal of the American Chemical Society. 2014; 136: 6437–6445.

[30] De Marco L., Manca M., Giannuzzi R., Belviso M.R., Cozzoli P.D., Gigli G. Shape-tailored TiO_2 nanocrystals with synergic peculiarities as building blocks for highly efficient multi-stack dye solar cells. Energy & Environmental Science. 2013; 6 (6): 1791–1795.

[31] Liu X., Guo M., Lin J., Chen X., Huang H. Design of multi-layered TiO_2 nanotube/nanoparticle hybrid structure for enhanced efficiency in dye-sensitized solar cells. RSC Advances. 2014; 4 (85): 45180–45184.

[32] Colodrero S., Mihi A., Häggman L., Ocana M., Boschloo G., Hagfeldt A., et al. Porous one-dimensional photonic crystals improve the power-conversion efficiency of dye-sensitized solar cells. Advanced Materials. 2009; 21 (7): 764–770.

[33] Ok M.-R., Ghosh R., Brennaman M.K., Lopez R., Meyer T.J., Samulski E.T. Surface patterning of mesoporous niobium oxide films for solar energy conversion. ACS Applied Materials & Interfaces. 2013; 5 (8): 3469–3474.

[34] Guldin S., Hüttner S., Kolle M., Welland M., Müller-Buschbaum P., Friend R., et al. Dye-sensitized solar cell based on a three-dimensional photonic crystal. Nano Letters. 2010; 10: 2303–2309.

[35] Chen J.I., von Freymann G., Kitaev V., Ozin G.A. Effect of disorder on the optically amplified photocatalytic efficiency of titania inverse opals. Journal of the American Chemical Society. 2007; 129 (5): 1196–1202.

[36] Lee S.-H ...., Abrams N.M., Hoertz P.G., Barber G.D., Halaoui L.I., Mallouk T.E. Coupling of titania inverse opals to nanocrystalline titania layers in dye-sensitized solar cells. The Journal of Physical Chemistry B. 2008; 112 (46): 14415–14421.

[37] Masuda H., Yamada M., Matsumoto F., Yokoyama S., Mashiko S., Nakao M., et al. Lasing from two-dimensional photonic crystals using anodic porous alumina. Advanced Materials. 2006; 18 (2): 213–216.

[38] Ryu S., Park J., Oh J., Long D., Kwon K., Kim Y., et al. Analysis of improved efficiency of InGaN light-emitting diode with bottom photonic crystal fabricated by anodized aluminum oxide. Advanced Functional Materials. 2009; 19 (10): 1650–1655.

[39] Chen B., Lu K. Influence of patterned concave depth and surface curvature on anodization of titania nanotubes and alumina nanopores. Langmuir. 2011; 27 (19): 12179–12185.

[40] Lin J., Chen X. Synthesis of high-aspect-ratio, top-open and ultraflat-surface TiO_2 nanotubes through double-layered configuration. Physica Status Solidi (RRL)-Rapid Research Letters. 2012; 6 (1): 28–30.

[41] Lee W., Scholz R., Gösele U. A continuous process for structurally well-defined Al_2O_3 nanotubes based on pulse anodization of aluminum. Nano Letters. 2008; 8 (8): 2155–2160.

[42] Lee W., Schwirn K., Steinhart M., Pippel E., Scholz R., Gösele U. Structural engineering of nanoporous anodic aluminium oxide by pulse anodization of aluminium. Nature Nanotechnology. 2008; 3 (4): 234–239.

[43] Wang B., Fei G., Wang M., Kong M., Zhang L. Preparation of photonic crystals made of air pores in anodic alumina. Nanotechnology. 2007; 18 (36): 365601.

[44] Kim D., Ghicov A., Albu S.P., Schmuki P. Bamboo-type TiO_2 nanotubes: Improved conversion efficiency in dye-sensitized solar cells. Journal of the American Chemical Society. 2008; 130 (49): 16454–16455.

[45] Lin J., Liu K., Chen X. Synthesis of periodically structured titania nanotube films and their potential for photonic applications. Small. 2011; 7 (13): 1784–1789.

[46] Yip C.-T., Huang H.T., Zhou L.M., Xie K.Y., Wang Y., Feng T.H., et al. Direct and seamless coupling of TiO_2 nanotube photonic crystal to dye-sensitized solar cell: A single-step approach. Advanced Materials. 2011; 23 (47): 5624–5628.

[47] Guo M., Xie K.Y., Lin J., Yong Z.H., Yip C.-T., Zhou L.M., et al. Design and coupling of multifunctional TiO_2 nanotube photonic crystal to nanocrystalline titania layer as semitransparent photoanode for dye-sensitized solar cell. Energy & Environmental Science. 2012; 5 (12): 9881–9888.

[48] Kuang D.B., Brillet J., Chen P., Takata M., Uchida S., Miura H., et al. Application of highly ordered TiO_2 nanotube arrays in flexible dye-sensitized solar cells. ACS Nano. 2008; 2 (6): 1113–1116.

[49] Shankar K., Bandara J., Paulose M., Wietasch H., Varghese O.K., Mor G.K., et al. Highly efficient solar cells using TiO_2 nanotube arrays sensitized with a donor-antenna dye. Nano Letters. 2008; 8 (6): 1654–1659.

[50] Richter C., Schmuttenmaer C.A. Exciton-like trap states limit electron mobility in TiO_2 nanotubes. Nature Nanotechnology. 2010; 5 (11): 769–772.

[51] Jennings J.R., Ghicov A., Peter L.M., Schmuki P., Walker A.B. Dye-sensitized solar cells based on oriented TiO_2 nanotube arrays: Transport, trapping, and transfer of electrons. Journal of the American Chemical Society. 2008; 130 (40): 13364–13372.

[52] Zhu K., Neale N.R., Halverson A.F., Kim J.Y., Frank A.J. Effects of annealing temperature on the charge-collection and light-harvesting properties of TiO_2 nanotube-based dye-sensitized solar cells. The Journal of Physical Chemistry C. 2010; 114 (32): 13433–13441.

[53] Liu L.J., Chan J., Sham T.K. Calcination-induced phase transformation and accompanying optical luminescence of TiO_2 nanotubes: An X-ray absorption near-edge structures and X-ray excited optical luminescence study. The Journal of Physical Chemistry C. 2010; 114 (49): 21353–21359.

[54] Varghese O.K., Gong D.W., Paulose M., Grimes C.A., Dickey E.C. Crystallization and high-temperature structural stability of titanium oxide nanotube arrays. Journal of Materials Research. 2003; 18 (1): 156–165.

[55] Allam N.K., Grimes C.A. Effect of rapid infrared annealing on the photoelectrochemical properties of anodically fabricated TiO_2 nanotube arrays. The Journal of Physical Chemistry C. 2009; 113 (19): 7996–7999.

[56] Ma Q., Liu S.J. Significantly enhanced structural and thermal stability of anodized anatase nanotube arrays induced by tensile strain. Electrochimica Acta. 2011; 56 (22): 7596–7601.

[57] Wang J., Zhao L., Lin V.S.Y., Lin Z.Q. Formation of various TiO_2 nanostructures from electrochemically anodized titanium. Journal of Materials Chemistry. 2009; 19 (22): 3682–3687.

[58] Fang D., Luo Z.P., Huang K.L., Lagoudas D.C. Effect of heat treatment on morphology, crystalline structure and photocatalysis properties of TiO_2 nanotubes on Ti substrate and freestanding membrane. Applied Surface Science. 2011; 257 (15): 6451–6461.

[59] Lin J., Guo M., Yip C.T., Lu W., Zhang G., Liu X., et al. High temperature crystallization of free-standing anatase TiO_2 nanotube membranes for high efficiency dye-sensitized solar cells. Advanced Functional Materials. 2013; 23 (47): 5952–5960.

[60] Zhu S., Liu X., Lin J., Chen X. Low temperature transferring of anodized TiO 2 nanotube-array onto a flexible substrate for dye-sensitized solar cells. Optical Materials Express. 2015; 5 (12): 2754–2760.

[61] Park J., Bauer S., von der Mark K., Schmuki P. Nanosize and vitality: TiO_2 nanotube diameter directs cell fate. Nano Letters. 2007; 7 (6): 1686–1691.

[62] Liu X., Lin J., Chen X. Synthesis of long TiO_2 nanotube arrays with a small diameter for efficient dye-sensitized solar cells. RSC Advances. 2013; 3 (15): 4885–4889.

[63] Lin J., Liu X., Guo M., Lu W., Zhang G., Zhou L., et al. A facile route to fabricate an anodic TiO_2 nanotube-nanoparticle hybrid structure for high efficiency dye-sensitized solar cells. Nanoscale. 2012; 4 (16): 5148–5153.

[64] Albu S.P., Ghicov A., Aldabergenova S., Drechsel P., LeClere D., Thompson G.E., et al. Formation of double-walled TiO_2 nanotubes and robust anatase membranes. Advanced Materials. 2008; 20 (21): 4135–4139.

[65] Wang D.A., Liu L.F., Zhang F.X., Tao K., Pippel E., Domen K. Spontaneous phase and morphology transformations of anodized titania nanotubes induced by water at room temperature. Nano Letters. 2011; 11 (9): 3649–3655.

[66] Liao Y.L., Que W.X., Zhong P., Zhang J., He Y.C. A facile method to crystallize amorphous anodized TiO_2 nanotubes at low temperature. ACS Applied Materials & Interfaces. 2011; 3 (7): 2800–2804.

[67] Pan X., Chen C.H., Zhu K., Fan Z.Y. TiO_2 nanotubes infiltrated with nanoparticles for dye sensitized solar cells. Nanotechnology. 2011; 22 (23): 235402.

[68] Wang S.H., Zhang J.B., Chen S., Yang H.T., Lin Y., Xiao X.R., et al. Conversion enhancement of flexible dye-sensitized solar cells based on TiO_2 nanotube arrays with TiO_2 nanoparticles by electrophoretic deposition. Electrochimica Acta. 2011; 56 (17): 6184–6188.

Chapter 7

"Green" Quantum Dots: Basics, Green Synthesis, and Nanotechnological Applications

Carlos A. Martínez Bonilla and
Vladimir V. Kouznetsov

Additional information is available at the end of the chapter

http://dx.doi.org/10.5772/62327

Abstract

Nanotechnological development of new materials involves the discovery or design of materials at small length scales with controlled physical and chemical properties than can be tuned or modified in function of their applications. One of the most suitable examples of nanoparticles used for this purpose are *quantum dots*, a type of colloidal fluorescent semiconducting nanocrystalline material that has the possibility, due to its unique optical and electronic properties, to be used in numerous technological applications such as biosensing, in vivo imaging techniques, photovoltaics, nanomedicine, molecular pathology, and drug delivery. Thus, there are almost endless possibilities for quantum dots materials. In spite of the fast advance in the search of quantum dots with better nanomaterial performance, environmentally benign and sustainable production is still lacking. Although the use of these materials is developing promptly, there is increasing concern that these materials might pose potential risks to human health. Herein, we discuss principal properties of quantum dots, including their functional architecture and toxicity, and review the main studies about "green" quantum dots synthesis to be aligned with green nanotechnology approach for nontoxic, cleaner, safer, and more responsible processes. The organometallic colloidal synthesis and the aqueous colloidal synthesis, as well as their drawbacks and benefits, are conferred. Recent advances in technological and biological quantum dots–based applications are also discussed in this chapter.

Keywords: nanoparticles, greener/quantum dots, fluorescence, "green" synthesis, in vivo/in vitro imaging, QDs-based solar cells

1. Introduction

Nanotechnology and nanomaterials, two closely related research fields, have become the central axis of world technological development [1, 2]. While nanosciences study the properties of

matter at nanoscale (in particular, size-dependent properties), nanotechnology has the ability to manipulate nanoparticles as building blocks for specific applications [3]. In the past 20 years, nanomaterials science had a rapid development, thereby opening up new opportunities for materials design in scientific, technological, and industrial applications [4, 5]. Such advance, a runaway race, can be counterproductive. It means that environmentally benign and sustainable process could be bypassed due to the almost endless possibilities of nanoscale materials. As consequence of this worldwide tendency, the "green nanotechnology" (GN) appears as a new promising research field. This concept seeks to provide energy, clean water, medical help, and a good environment in a sustainable way [6]. In this context, industrial revolution planted in the earth a notion about the unsustainable development, and nowadays the humankind is still suffering its legacy. Then, the so-called green process (synthesis, production, and disposition) represents an alternative for nongreen technologies, stating that it is possible to make it cleaner, safer, and faster with a neutral or positive balance for environment.

Currently, the huge challenge for new scientists is to reveal the nanoscale world discovering new knowledge, developing new characterization tools, and producing devices with great properties and applications. Importantly, a new generation of highly efficient technology is being developed employing quantum dots (QDs) as building block material [7–9]. Since their first discovery in glass crystals in 1980 by Russian physicist Alexey Ekimov [10], systematic progress has been achieved going from nanolithographic preparations to successful synthesis of colloidal QDs with size-dependent properties [11]. To understand the unique properties of QDs, we review in detail the following aspects: physicochemical properties, related toxicity, and recent technological applications, giving a special attention to the synthetic methods, including "green" approaches.

2. Physicochemical properties of QDs

Among all nanoparticles classified by their size, QDs arise as the key semiconductor material in the emerging nanomaterials area. QDs are luminescent solid-state, crystalline nanostructures composed of atoms of groups II–VI (CdSe, ZnS, and CdTe), groups III–V (InP and InAs), and groups IV–VI (PbSe and PbS) of the periodic table. Technically, these materials have structural features between the isolated atoms and the bulk macroscopic materials as a consequence of their nanoscale ranging from 1 to 10 nm. At this level, physical, chemical, and electronic properties change dramatically because of *quantum effects*, consequence of *quantum confinement*. This behavior is related to the electronic migration in semiconductor nanocrystals. Once the light absorption is over, electrons (e^-) and holes (h*) generated perceive each other due to Coulomb attraction and an electron-hole pair called exciton is formed. The average physical separation between the electron and hole represents the *exciton Bohr radius*, which is typical for each material. If the size of semiconducting material is becoming increasingly smaller, it means when it is closer to the natural scale of its *exciton Bohr radius*, quantitation of states became present. In other words, continuous energy levels change into discrete ones (**Figure 1 a**).

http://dx.doi.org/10.5772/62327

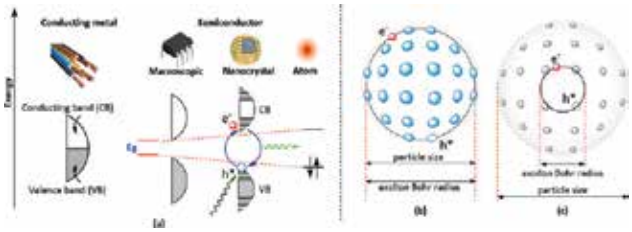

Figure 1. Schematic representation of energy levels in macroscopic, nanocrystal and atomic semiconducting materials (**a**), and related dimensions of exciton Bohr radius and particle size (**b**, **c**). Adapted with the permission from Alivisatos [12].

In this context, a discrete level refers to finite separation between energy levels due to the quantum confinement effects of electrons and holes in QDs with smaller sizes than its exciton Bohr radius (**Figure 1 b, c**). These QDs display physicochemical properties, such as high photostability, broad absorption spectra, narrow and symmetric emission spectra, slow excited state decay rates, and broad energy absorption cross sections. Their emission colors depend on their size, chemical composition, and surface chemistry and can be tuned from the ultraviolet to the visible wavelengths. QDs have nanoproperties in all three dimensions, whereas other nanoparticles as nanowire or single thin layers have ordinary properties along the wire and two dimensions, respectively.

On the other hand, respect to their functional architecture, QDs consist of an inorganic core responsible for the fundamental optical properties and semiconducting character, a layer or shell of another semiconductor material responsible for passivation of active QD-core surface and capping ligands. In almost all cases, the shell has a greater band gap than the core material. The growing of a very thick, defect-free shell is the best solution to render optical properties avoiding loss of quantum yield (QY), photobleaching, and blinking, which are typical drawbacks of QD-core material due to surface chemistry and chemical environment [13]. Additionally, the shell plays two crucial roles, one as physical barrier separating the core from its surrounding medium and other in the defect state saturation, a process related with dangling bonds at the core surface and crystalline defects suppression. Finally, capping agents or ligands are important components in nanomaterials, especially in QDs [14]. The nature of QDs' capping ligands is related with synthetic methods and final applications. For instance, long chain organophosphorates, primary amines, carboxylic acids, alcohols, and thiols are common ligands employed in QDs synthesis. Amines, alcohols, and carboxylic acids can offer the possibility of bioconjugation, a process that involves the linking of biomolecules (peptides, carbohydrates, virus, DNA fragments, and natural products) through electrostatic or hydrophobic interactions and covalent coupling [15]. In general, ligands provide colloidal stability, control particle morphology, and particle size distribution and stop uncontrolled growth and agglomeration. Nowadays, ligands are the key parameters in the design of QDs mainly because their electronic structure contributes to the final solubility, electronic and optical profiles of contemplated nanoparticle [16]. The physicochemical properties of designed QDs are directly related with nature and final assembly of core/shell/ligands, as depicted in **Figure 2**.

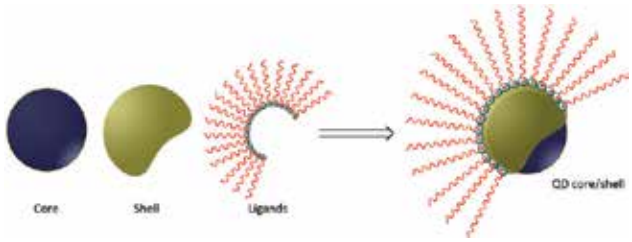

Figure 2. Basic architecture of core/shell/ligands in QDs.

In biomedical research, high fluorescence is the most attracting property of QDs [17]. This type of nanocrystals exhibits broad absorption spectrum; it extends in some cases up to the ultraviolet (UV) region. QDs have size-tunable fluorescence emission from visible to infrared in the electromagnetic spectrum. In other words, multiple QDs with same chemical composition can emit different colors depending on their size. Typically, smaller dots have larger energy band gap yielding a blue shifting of their absorption bands, so smaller QDs emit blue light. In contrast, bigger dots have smaller energy band gaps resulting in a red shifting and the emission of red light (**Figure 3**).

This is an important feature for biological applications because it allows simultaneous excitation of multicolor QDs with a single light source. Furthermore, high-quality QDs have large molar extinction coefficients (0.5–5× 10^6 M^{-1} cm^{-1}) and narrow and symmetric emission spectra. These features are ideal qualities for ultrasensitive and multiplexing applications in biosensing [18].

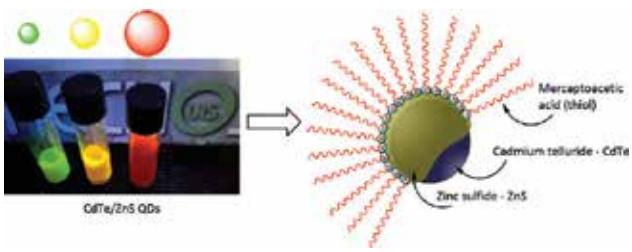

Figure 3. Emission colors of ZnS-capped CdTe QDs excited under a UV lamp (365 nm).

3. Toxicity of QDs

We now describe the task that must be overcome in QDs research to advance toward mainstream environmental and biological applications: QDs' toxicity. Cadmium-based QDs are the most studied nanoparticles in biosensing and intracellular or in vivo applications showing remarkable results [15]. CdSe and CdTe are the two of the most extensively studied QDs. However, several research groups have demonstrated the extremely toxic profile of Cd and other heavy metals such as In, Hg, and Pb, even under extended periods of time [19, 20]. This

http://dx.doi.org/10.5772/62327

toxicity is related to the leaching of Cd from the core into the cellular environment, resulting cellular death due to the DNA damaging properties of components in mention (**Figure 4**).

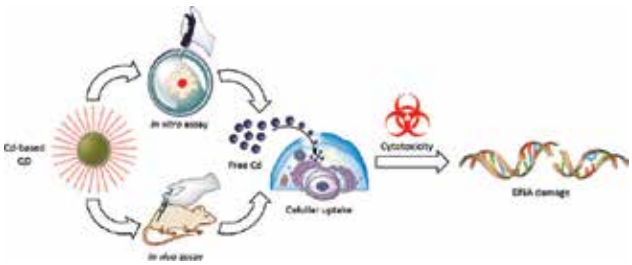

Figure 4. Schematic representation of cytotoxicity—DNA damage—due to the leaching of Cd from the core into the cellular environment.

Neurological and genitourinary toxicities are also related with Cd leaching. Moreover, previous studies showed that ultimate destination of QDs' decomposition final products remains unclear. In particular, careful methods are being developed for cytotoxicity assessment of nanoparticles, especially QDs [21]. Conventional methods used for drugs or chemicals, in some cases, are inappropriate because they obviate physicochemical characteristics, such as size, color, superficial defects, nature of capping ligand, and intracellular associations. Nowadays, one of the most promising in vivo model systems for toxicity studies, *Danio rerio* or zebrafish, has being used as evaluating biomaterial for nanotoxicity assessment in QDs [22].

A special condition of QDs in cell culture is associated with cytotoxicity assessment. An increase of QDs' toxicity is detected when UV illumination is used for their location; this condition is related with UV irradiation energy, which is close to that of a covalent chemical bond and promotes the dissolution of semiconductor particles in a process known as photolysis [23]. In contrast, under absence of UV irradiation, QDs with stable capping ligands (e.g., polymeric coating) seem to be nontoxic to cells and animals [24]. Among all physical and chemical properties of QDs, the hydrodynamic diameter (hd) define in vivo behavior of these nanocrystals [25]. Particles with hd smaller than <5.5 nm are rapidly and efficiently eliminated from the mice through renal clearance. This hd value suggests a limit to be consider in property-based design QDs to achieve an acceptable biocompatibility. In environmental applications, acute toxicity has been found as the main drawback due to the formation of reactive oxygen species (ROS) [26].

Although, several efforts have been made to reduce QDs' toxicity keeping optical and physical properties unaltered. Basically, QDs' core protection can, to some degree, control the toxicity related to metal ions leakage. Shell growth (ZnS, CdS, or polymeric capping) is the most applied alternative to largely alleviated cellular damage. Enhancing stability and surface modification are other approaches in the challenge to overcome QDs toxicity. One of the most promising superficial modifications is the coating with suitable water-soluble organic ligand/biomolecules, such as biotin, folic acid, peptides, bovine serum albumin, antibodies, and DNA [27].

These biomolecules act like biorecognition agents in the cellular media–promoting biocompatibility. With difficult cellular recognition and continuing demand for more biocompatible QDs as the signal reporter in biosensing, new emerging alternatives known as "greener" QDs are in the spotlight of current biological research. This current research field has shifted its emphasis toward the fabrication of cadmium-free QDs, such as silicon, carbon/graphene, Ag_2Se, and Ag_2S QDs (**Figure 5**) [28, 29].

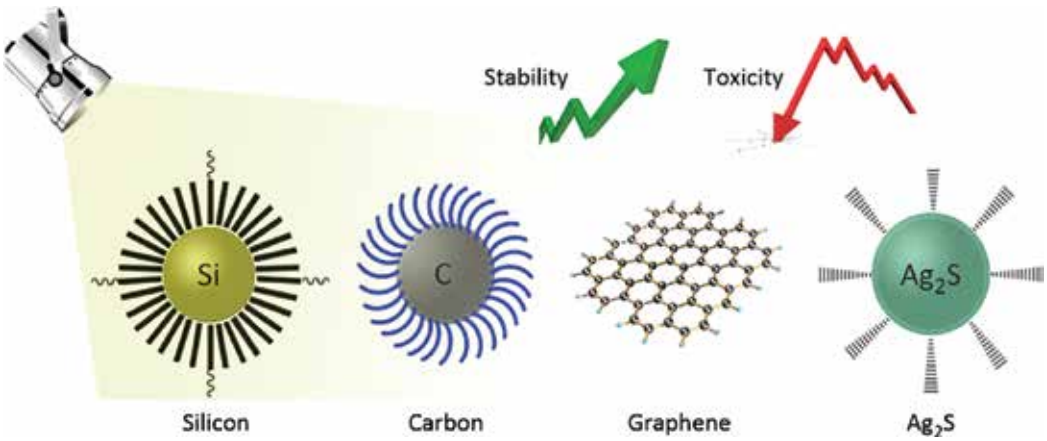

Figure 5. Emerging QDs in response to the constant demand of more stable and less toxic nanoparticles.

With the possibility that GN offers to design/make and build "green" from the beginning, there is no doubt that there will be more "greener" QDs available in the future.

4. "Green" synthesis of QDs

The search for environmentally friendly and reliable processes for nanomaterials production is an active topic in GN. Synthesis of nanomaterials with highly monodispersion, crystallinity, shape control, and narrow size distribution plays a critical role in QD-based applications. In the beginning of QDs' nanotechnology era, preparation was based mainly on physical methods, and the main goal was high-purity products. After 20 years, essential studies about the mechanisms of QDs formation have improved current synthetic methods, encouraging innovative routes for the synthesis of nanocrystals with controlled size and shape. Currently, there are two synthetic procedures (others use minor variations of these two methods) to produce QDs (**Figure 6**). Each method exploits different aspects of chemistry to produce QDs with the desired optical properties like high QY, narrow fluorescence emission, broad absorption profile, and stability against photobleaching [30].

The first procedure is an organometallic colloidal synthesis (OCS; **Figure 6a**) at high temperature (HT), which makes use of high boiling point organic solvents, such as tri-n-octylphosphine oxide (TOPO), trioctylphosphine (TOP), or hexadecyl amine (HAD), three of which are

http://dx.doi.org/10.5772/62327

containing long alkyl chains. OCS was developed by Murray's et al. in the early 1980s and rapidly become in a seminal work [11]. In a typical synthesis for high-quality QDs, elevated temperatures (≈300°C) are used in junction with coordinating solvents (TOPO or HAD) and metal/chalcogenide precursors (OCS;**Figure 6a**). Basically, coordinating solvent serves as a solvent and as a ligand and is commonly a mixture of surfactants such as TOP/TOP and HAD. During synthesis process, these ligands attach their terminal functional groups (phosphines, phosphine oxides, and amines) to the QDs surface leaving the ligand alkyl chains directed away from the surface. As consequence, a long alkyl chain monolayer is formed resulting in QDs highly hydrophobic and only soluble in nonpolar solvents, such as toluene, chloroform, and hexane. A deep look into OCS reveals the thermic decomposition at HT of organometallic precursors (TOPO-Cd and TOP-Se, in CdSe synthesis) previously formed in a process known as pyrolysis [31]. An experimental requirement for this method is related with the need to be carried out in an inert atmosphere together with quick hot injection of metallic precursors. Discussions about the influence of hot injection in OCS have been reported recently [32], it is concluded that QDs prepared through hot injection had higher QY but poor sensing attributes compared to QDs synthesized at room temperature.

Despite great performance of QDs prepared by OCS, these syntheses involve the use of nongreen conditions, hazardous chemicals, and high energy requirements. As example, extremely toxic/pyrophoric/volatile metallic precursor, dimethylcadmium ($Cd(Me)_2$), and chalcogenides vapor phase compounds, such as H_2Te, are employed in these syntheses. In this field, the only way to develop process as "green" synthesis is to adapt benign synthesis approaches that use mild reaction condition and nontoxic reaction precursors or reaction media, achieving the desired product in the highest yield possible and preventing unwanted waste. In response to this trend, easier and greener approaches have been developed for OCS replacing the highly toxic and volatile Cd precursor for a cheaper and more stable cadmium sources, such as $Cd(Ac)_2$ [33], CdO [34], and $CdCl_2$ [35]. Additionally, solvents such as glycerol and paraffin have been shown to decrease nanoparticle toxicity when are used in OCS [36, 37].

Moreover, the greenest approach for OCS includes the use of environmentally renewable raw materials as solvents and coordinating agents, such as oleic acid [38], castor [39], and olive oil [40]. These are three remarkable green alternatives of renewable materials employed in QD synthesis avoiding the need for the use of air-sensitive, toxic, and expensive chemicals, such as TOP, TOPO, or HDA.

The second procedure is an aqueous colloidal synthesis (ACS; **Figure 6b**). ACS appears in response to the needs of TOP/TOPO-QDs solubilization for biological applications. Usually, the hydrophobic layer in TOP/TOP-QDs is substituted by hydrophilic molecules, such as amines, polyhydroxy alcohols, and especially thiols, through cap exchange in liquid phase. This superficial modification brings in most cases significant decrease in QDs' photoluminescence [41]. To overcome this problem, ACS involves the direct aqueous synthesis of QDs using the less toxic and most biocompatible solvent—water. In a typical ACS, heavy metal precursor (e.g., $CdCl_2$, $Cd(NO_3)_2$, and $Cd(CH_3COO)_2$) is easily dissolved in water and coordinated by the hydrophilic agents such as thioglycolic acid (TGA), mercaptosuccinic acid (MPA), glutathione

(GSH), and L-cysteine (L-Cys). A basic version of ACS was first investigated by Gao and co-workers [42].

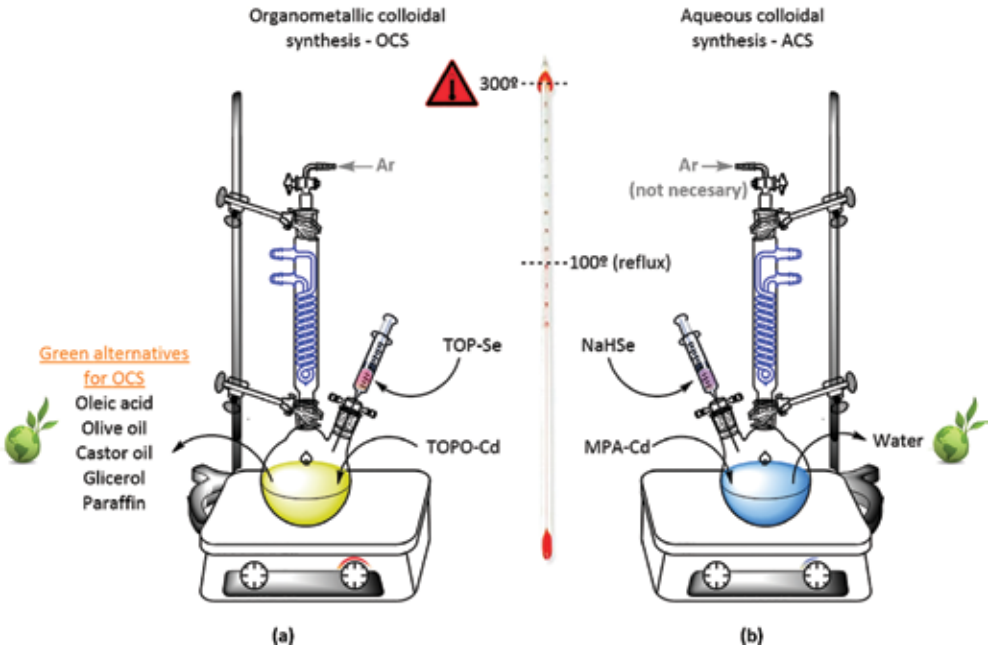

Figure 6. Schematic representation for two main QD synthesis methods, OCS (**a**) and ACS (**b**) in CdSe QD preparation.

In ACS, chalcogen precursor can be freshly prepared in aqueous medium before using in the reaction. NaHE (E=Se, Te) produced from the chemical reduction of selenium (Se) or tellurium (Te) in presence of sodium borohydride ($NaBH_4$), and Na_2SeO_3 from the reaction of Na_2SO_3 solution with Se are common sources employed in QDs ACS. Rigorous inert atmosphere is not necessary because precursors like Na_2SeO_3 are stable at open-air conditions [43]. After precursor injection or addition, crude reaction is refluxed (92–95°C) to promote QD growth. This is an example of low operating temperatures compared with the necessary 300°C for OCS; there are even reports for ACS at room or freezing temperature [44, 45]. During synthesis process, thiol-type capping agents attach their functional group –SH to the QD surface leaving the hydrophilic groups available for subsequent bioconjugation processes [46]. Additionally, compared with the organic-based synthesis, ACS is preferred as key procedure for QD preparation in biological studies as they exhibit good reproducibility and low toxicity and are less expensive and environment friendly, resembling many of the goals pursued by GN [47]. Initially, quality of QDs prepared by ACS was relatively low (low QY and large size distribution) compared to OCS. Nevertheless, continuous efforts and experimental improvements in the field allowed the discovering QDs with equal or better properties than organic-based synthetized QDs [48]. Parameters such as type of capping agent, precursor's source, heavy metal/chalcogenide/capping agent molar ratio, and shells thickness define final properties of QDs [49].

http://dx.doi.org/10.5772/62327

The reaction medium, a crucial feature that in most cases determines the quality of QDs, has been subjected to a green approach; alternatives, such as micellar synthesis and green solvents, have been investigated achieving outstanding results [50]. The energy input for QD synthesis, commonly used over years, was direct thermal energy; despite this, the successful synthesis of widespread nanomaterials using microwave [51], ultrasound [52], and hydrothermal [53]/mechanical [54, 55]/electrochemical [56] energy has increased particular attention. The utilization of these techniques allows the preparation of high quality and nearly monodispersed QDs from appropriate molecular precursors. In particular, microwave chemistry offers unique opportunities to significantly increase the rate of nanoparticle formation, while not compromising on the high-quality and narrow-size distributions needed for these nanomaterials to be further used in other areas.

Nowadays, the greenest approach in nanoparticle preparation is plant/microorganism-mediated biosynthesis, a field of recent development able to produce highly fluorescent QDs at ambient conditions by biological organism like plants and fungus in the presence of appropriated substrates [57]. A heavy metal concentration in plants and microorganisms affects their growth, morphology, membranes, enzymes, and DNA, and in most cases high concentration causes cellular death. In spite of effects in mention, biological organisms exposed to toxic concentrations of heavy metals such as Cd, In, or Pb have developed tolerance mechanism through detoxification by enzymatic oxidation or reduction of heavy metals to less toxic forms or covalent modifications [58].

An efficient and environmentally friendly method of plant-based biosynthesis of CdS QDs using hairy root culture of the flowering plant *Linaria maroccana L.* has been developed [59]. Several studies suggest that the broad range of natural products, such as alkaloids, terpenoids, phenols, flavanoids, tannins, and quinines, are involved in redox process and could mediate the synthesis of nanoparticles [60]. Microorganisms such as fungi (*Fusarium oxysporum* [61] and *Saccharomyces cerevisiae*) [62] or bacteria (*Escherichia coli*) [63] have been employed to synthesize CdSe, CdTe, and CdS QDs, respectively.

5. Nanotechnological applications of QDs

Nanotechnological applications of QDs represent one of the most important challenges in nanomaterial science. The exploitation of unique QD properties opens the door for endless applications [64]. The primary applications of QDs are in energy-efficient lighting [65], solar photovoltaic [66], and biological imaging [67, 68].

In recent years, energy-efficient lighting has been enthusiastically investigated in regard to the unique properties of colloidal QDs, positioning it as one of the most promising emitters for next-generation displays and lighting devices [69]. As a demonstration of nanotechnological development, light emitting diode (LED) technology has been a breakthrough innovation in this lighting revolution, enabling efficient and high-power devices with prolonged lifetimes. The first demonstration of QDs-based LEDs (QDsLEDs) by Alivisatos et al. in 1994 opened the door to a continuous development improving step-by-step the structure of ideal device [70]. The performance of QDsLED devices has been rapidly improved, as a result of technological

development and the accumulation of fundamental knowledge [71]. Compared with conventional LED and organic LED (OLEDs) technologies, QDsLEDs may offer many advantages in terms of color purity, stability, and production cost while still achieving similar levels of efficiency. Emission from the QDsLEDs can be easily tuned by varying the size of the QDs without changing their processing properties; this feature allows producing different QDs emissions over a broad wavelength range replaying the device fabrication procedure, covering the visible and near-infrared regions. Recently, deep-blue [72], green [73], and red [74] QDsLEDs have shown maximum external quantum efficiency (ηEQE) of 7.1, 12.6, and 18–20%, respectively (**Figure 7**); these are performance values comparable to those of OLEDs. However, to reduce the manufacture complexity in the synthesis (one-pot or two-pot synthesis approaches) and device architecture (conventional/inverted assembly or solution/vacuum deposition), unification of the total procedure is needed to achieve full-color displays with the highest efficiency for each color.

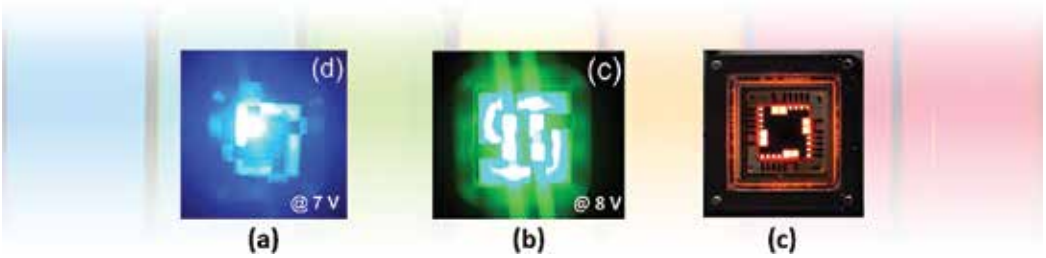

Figure 7. Photograph of (**a**) deep-blue, (**b**) green, and (**c**) red QDsLED devices. Adapted with the permission from Colvin et al. [71], Ki Bae et al. [72], and Yang et al. [73], respectively.

Keeping in mind the GN alignments, QDsLED devices for light harvesting have significant potential in terms of saving energy with a projected reduction of 50% in the electricity consumption occurring due to lighting [75].

In solar photovoltaics, several characteristics make QDs an attractive option for the development of QDs-based solar cells (QDsSCs) [76]. In QDs, the band gap can be tailored to absorb light in the whole solar spectrum, which is a crucial feature for solar applications. Also, the enhanced impact ionization leads to multiple exciton generation for each photon absorbed, characteristic that favors high and stable photocurrent generation [77]. Works by Kamat and Bawendi are the two of the most important sources of experimental and technological improvements; these groups have developed a deep knowledge in the field for nearly 10 years of continuous research. In 2014, Kamat [78] reported a detailed and concise review of QDsSCs, which highlighted the recent advances in size- and shape-selective synthesis and design of QDsSCs with photoconversion efficiencies greater than 5% (**Figure 8**). However, it was recalled that to make QDsSCs competitive with other existing thin film or polycrystalline photovoltaic technologies; it is important to overcome kinetic barriers for charge transfer at semiconductor interfaces.

http://dx.doi.org/10.5772/62327

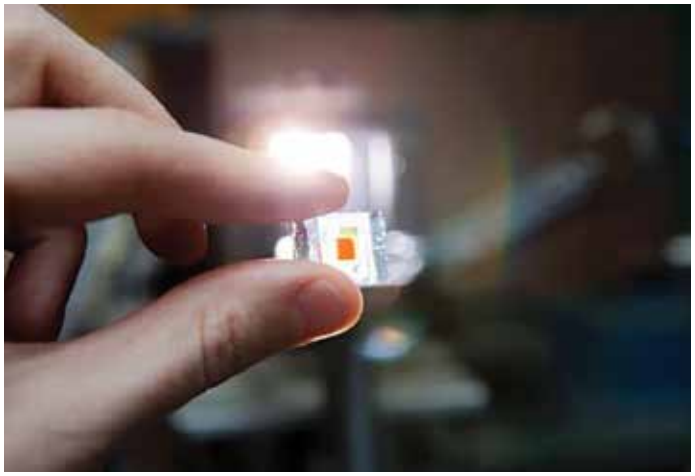

Figure 8. Example of QDsSCs developed in Professor Kamat's group (for more information visit: http://chemistry.nd.edu/people/prashant-kamat/).

On the other hand, Bawendi [79] reported a room temperature solution process for high efficiency, low-temperature fabrication, and good atmospheric stability of SCs composed of ZnO/PbS QDs. These improvements were possible through delicate band alignment engineering of the QD layers through the use of different ligand treatments achieving a photoconversion efficiency of 8.55%. Greener approaches, such as $CuInE_2$ (E=S, Se) QDs, have been reported, in spite of high absorbing capacity and low toxicity, this SCs have shown lower efficiencies (<6.79 %) [80]. Photovoltaic applications of QDs open the possibility of development of light-harvesting structures, one of the most important fields in GN. Actually, the maximum efficiency theoretically predicted for QDs-sensitized solar cells (QDs-SSCs) is 44%, this value is higher than that for dye-sensitized solar cells (DSSC) using organic sensitizers (33.5 %) and for traditional Si solar cells (35%) [81].

Finally, in the biological imaging field, QDs can act as exogenous probes in the study of biological samples, cells culture, and animal models. Due to the high stability as fluorophore and long fluorescence lifetime, QDs are used in in vivo imaging, in vitro diagnostics, drug delivery, and photodynamic therapy [68]. Fluorescence imaging technology is well established in research and medicine for biological imaging and clinical diagnostics; however, the nanotechnological improvement that QDs offer may help to overcome the persistent limitations of traditional organic dyes and genetically engineered fluorescent proteins, such as narrow excitation spectrum, broad and asymmetrical emission spectra, low photobleaching threshold, rapid lifetime decay, and low QY [82]. As we described in previous sections, QDs can be conjugated to biological molecules retaining their photophysical properties without alteration of the function of these biomolecules itself. Among bioconjugation methods, adsorption, electrostatic interaction, and covalent linkage are the most commonly used [83]. After bioconjugation process, modified QDs are used as fluorescent biological labels for cellular and molecular imaging. Basically, the main studies can be separated into *in vitro* and *in vivo* imaging. For *in vitro* imaging, fixed and living cells cultures are employed to the specific

labeling of proteins and structures [84]. These techniques are helpful to understand the process in molecular cell biology associated with the protein and gene expression in cells. Also, immunohistochemical detection of single or various molecules of interest can be accomplished using primary and secondary antibodies. DNA and RNA mapping can be developed in cellular environment with QDs using the well-established fluorescent *in situ* hybridization [85]. In living cells culture, QDs are able to help in the understanding of dynamic cellular (*e.g.*, cell tracking) and *in vivo* molecular interactions over prolonged periods at high resolution. For *in vivo* imaging, ideal coating for QDs must be designed and applied to mitigate or nullify the toxic profile of the core. One of the most interesting *in vivo* studies is cancer studies [86, 87]. Generally, QDs are attached to tumor-specific antibodies acting as cell marker in preliminary ultrasensitive cancer diagnosis. Promising studies are being developed using QDs in photodynamic therapy, a therapy that uses a photosensitizer or photosensitizing agents (like QDs) and a particular type of light to generate ROS that kills nearby cells [88].

6. Conclusions

Nanotechnology offers the opportunity to find solutions to global issues that affect society at all levels, such as disease recognition, cleaner water, and sustainable energy needs. Through continue research and development of deep knowledge in the field of nanosciences and nanotechnology, the problems and processes of life are now being revealed step by step. However, findings, improvements, and joint efforts will have a realistic impact on everyone's life if we are able to make it *green*. It means, stops being *potential* and develop complete eco-friendly process applying sustainable technologies, a responsibility that lies on the hands and minds of scientist and engineers today. QD-related nanomaterials should be produced and applied more efficiently to exploit all their unique properties in chemistry, biology, and physics.

Actually, the aqueous colloidal synthesis and organisms-mediated synthesis are considered "greener" methods of QD production; they offer appropriated materials with tailored properties for specific applications. In the near future, there is no doubt that scientists and engineers will provide a sustainable and economical approach for production of QDs, avoiding the use of *quotes* in the word "*green*" to make it completely *green*.

Additionally, the on-going fruitful collaborations between several disciplines involving biotechnology, photonics, nanomedicine, toxicology, physics, engineering, and others may place QDs' development as a breakthrough in this worldwide nanorevolution. QDs, with their intense luminosity and high photostability, are the best candidate for these types of research.

Acknowledgements

This work has been supported from the Colombian Institute for Science and Research (COLCIENCIAS), projects No. RC-0572-2012 and No. RC-0346-2013. Carlos A. Martínez Bonilla thanks VIE of Universidad industrial de Santander (Colombia) for the financial support.

Author details

Carlos A. Martínez Bonilla and Vladimir V. Kouznetsov*

*Address all correspondence to: kouznet@uis.edu.co

Organic and Biomolecular Chemistry Laboratory, Industrial University of Santander, Parque Tecnológico Guatiguará, Piedecuesta, Colombia.

References

[1] Smith G.B., Granqvist C.G. Green Nanotechnology: Introduction and Invitation. In: Smith G.B., Granqvist C.G., editors. Green Nanotechnology: Solutions for Sustainability and Energy in the Built Environment. 1st ed. Boca Raton, FL: Taylor & Francis Group; 2010. pp. 1–4. DOI: 10.1201/EBK1420085327-2

[2] Parak W.J., Nel A.E., Weiss P.S. Grand Challenges for Nanoscience and Nanotechnology. ACS Nano. 2015; 9 (7):6637–6640. DOI: 10.1021/acsnano.5b04386

[3] Mulvaney P. Nanoscience vs Nanotechnology--Defining the Field. ACS Nano. 2015; 9 (3):2215–2217. DOI: 10.1021/acsnano.5b01418

[4] Yin Y., Talapin D. The Chemistry of Functional Nanomaterials. Chem. Soc. Rev. 2013; 42 (7):2484–2487. DOI: 10.1039/c3cs90011h

[5] Rao C.N.R., Cheetham A.K. Science and Technology of Nanomaterials: Current Status and Future Prospects. J. Mater. Chem. 2001; 11 (12):2887–2894. DOI: 10.1039/B105058N

[6] Basiuk V.A., Basiuk E.V., editors. Green Processes for Nanotechnology. 1st ed. Mexico DF, MX: Springer; 2015. 434 p. DOI: 10.1007/978-3-319-15461-9

[7] Hines D., Kamat P.V. Recent Advances in Quantum Dot Surface Chemistry. ACS Appl. Mater. Interfaces. 2014; 6 (5):3041–3057. DOI: 10.1021/am405196u

[8] Karakoti A.S., Shukla R., Shanker R., Singh S. Surface Functionalization of Quantum Dots for Biological Applications. Adv. Colloid Interface Sci. 2015; 215:28–45. DOI: 10.1016/j.cis.2014.11.004

[9] Lim S.Y., Shen W., Gao Z. Carbon Quantum Dots and Their Applications. Chem. Soc. Rev. 2015; 44 (1):362–381. DOI: 10.1039/C4CS00269E

[10] Ekimov A.I., Efros A.L., Onushchenko A.A. Quantum Size Effect in Semiconductor Microcrystals. Solid State Commun. 1985; 56 (11):921–924. DOI: 10.1016/S0038-1098(85)80025-9

[11] Murray C.B., Norris D., Bawendi M.G. Synthesis and Characterization of Nearly Monodisperse CdE (E=S, Se, Te) Semiconductor Nanocrystallites. J. Am. Chem. Soc. 1993; 115 (4):8706–8715. DOI: 10.1021/ja00072a025

[12] Alivisatos A.P. Semiconductor Clusters, Nanocrystals, and Quantum Dots. Science. 1996; 271 (5251):933–937. DOI: 10.1126/science.271.5251.933

[13] Neo D.C.J., Cheng C., Stranks S.D., Fairclough S.M., Kim J.S., Kirkland A.I., Smith J.M., Snaith H.J., Assender H.E., Watt A.A.R. Influence of Shell Thickness and Surface Passivation on PbS/CdS Core/Shell Colloidal Quantum Dot Solar Cells. Chem. Mater. 2014; 26:4004–4013. DOI: 10.1021/cm501595u

[14] Loef R., Houtepen A.J., Talgorn E., Schoonman J., Goossens A. Study of Electronic Defects in CdSe Quantum Dots and Their Involvement in Quantum Dot Solar Cells. Nano Lett. 2009; 9(2):856–859. DOI: 10.1021/nl803738q

[15] Frasco M.F., Chaniotakis N. Bioconjugated Quantum Dots as Fluorescent Probes for Bioanalytical Applications. Anal. Bioanal. Chem. 2010; 396(1):229–240. DOI: 10.1007/s00216-009-3033-0

[16] Green M. The Nature of Quantum Dot Capping Ligands. J. Mater. Chem. 2010; 20(28): 5797–5809. DOI: 10.1039/C0JM00007H

[17] Liu X., Luo Y. Surface Modifications Technology of Quantum Dots Based Biosensors and Their Medical Applications. Chinese J. Anal. Chem. 2014; 42(7):1061–1069. DOI: 10.1016/S1872-2040(14)60753-2

[18] Hoshino A., Fujioka K., Oku T., Suga M., Sasaki Y.F., Ohta T., Yasuhara M., Suzuki K., Yamamoto K. Physicochemical Properties and Cellular Toxicity of Nanocrystal Quantum Dots Depend on Their Surface Modification. Nano Lett. 2004; 4(11):2163–2169. DOI: 10.1021/nl048715d

[19] Peynshaert K., Manshian B.B., Joris F., Braeckmans K., De Smedt S.C., Demeester J., Soenen S.J.. Exploiting Intrinsic Nanoparticle Toxicity: The Pros and Cons of Nanoparticle-Induced Autophagy in Biomedical Research. Chem. Rev. 2014; 114(15): 7581-7609. DOI: 10.1021/cr400372p

[20] Chen N., He Y., Su Y., Li X., Huang Q., Wang H., Zhang X., Tai R., Fan C. The Cytotoxicity of Cadmium-Based Quantum Dots. Biomaterials. 2012; 33(5):1238–1244. DOI: 10.1016/j.biomaterials.2011.10.070

[21] Su Y., Peng F., Jiang Z., Zhong Y., Lu Y., Jiang X., Huang Q. Biomaterials *In Vivo* Distribution , Pharmacokinetics , and Toxicity of Aqueous Synthesized Cadmium-Containing Quantum Dots. Biomaterials. 2011; 32(25):5855-5862. DOI: 10.1016/j.biomaterials.2011.04.063

[22] Duan J., Yu Y., Li Y., Yu Y., Li Y., Huang P., Zhou X., Peng S., Sun Z. Developmental Toxicity of CdTe QDs in Zebrafish Embryos and Larvae. J. Nanoparticle Res. 2013; 15(7): 1–11. DOI: 10.1007/s11051-013-1700-8

[23] Su Y., He Y., Lu H., Sai L., Li Q., Li W., Wang L., Shen P., Huang Q., Fan C. The Cytotoxicity of Cadmium Based, Aqueous Phase - Synthesized, Quantum Dots and Its Modulation by Surface Coating. Biomaterials. 2009; 30(1):19-25. DOI: 10.1016/j.biomaterials.2008.09.029

[24] Ballou B., Lagerholm B.C., Ernst L.A., Bruchez M.P., Waggoner A.S. Noninvasive Imaging of Quantum Dots in Mice. Bioconjug. Chem. 2004; 15(1):78-86. DOI: 10.1021/bc034153y

[25] Choi H.S., Liu W., Misra P., Tanaka E., Zimmer J.P., Itty Ipe B., Bawendi M.G., Frangioni J.V. Renal Clearance of Quantum Dots. Nat. Biotechnol. 2007; 25(10):1165–1170. DOI: 10.1038/nbt1340

[26] Van Aken B. Gene Expression Changes in Plants and Microorganisms Exposed to Nanomaterials. Curr. Opin. Biotechnol. 2015; 33:206–219. DOI: 10.1016/j.copbio.2015.03.005

[27] Selim K.K., Xing Z.C., Choi M.J., Chang Y., Guo H., Kang I.K. Reduced Cytotoxicity of Insulin-Immobilized CdS Quantum Dots Using PEG as a Spacer. Nanoscale Res. Lett. 2011; 6(1):528. DOI: 10.1186/1556-276X-6-528

[28] Murphy C.J. Sustainability as an Emerging Design Criterion in Nanoparticle Synthesis and Applications. J. Mater. Chem. 2008; 18(19):2173–2176. DOI: 10.1039/B717456J

[29] Zhang Z., Zhang J., Chen N., Qu L. Graphene Quantum Dots: An Emerging Material for Energy-Related Applications and beyond. Energy Environ. Sci. 2012; 5(10):8869–8890. DOI: 10.1039/C2EE22982J

[30] Farkhani M.S., Valizadeh A. Review: Three Synthesis Methods of CdX (X=Se, S or Te) Quantum Dots. IET Nanobiotechnol. 2014; 8(2):59–76. DOI: 10.1049/iet-nbt.2012.0028

[31] Dabbousi B.O., Rodriguez-Viejo J., Mikulec F.V., Heine J.R., Mattoussi H., Ober R., Jensen K.F., Bawendi M.G. (CdSe)ZnS Core-Shell Quantum Dots: Synthesis and Characterization of a Size Series of Highly Luminescent Nanocrystallites. J. Phys. Chem. B. 1997; 101(46):9463–9475. DOI: 10.1021/jp971091y

[32] Mir I.A., Das K., Rawat K., Bohidar H. B. .Hot Injection versus Room Temperature Synthesis of CdSe Quantum Dots: A Differential Spectroscopic and Bioanalyte Sensing Efficacy Evaluation. Colloids Surfaces A Physicochem. Eng. Asp. DOI: 10.1016/j.colsurfa.2016.01.002

[33] Qu L., Peng Z.A., Peng X. Alternative Routes toward High Quality CdSe Nanocrystals. Nano Lett. 2001; 1(6):333–337. DOI: 10.1021/nl0155532

[34] Peng Z.A., Peng X. Formation of High-Quality CdTe, CdSe, and CdS Nanocrystals Using CdO as Precursor. J. Am. Chem. Soc. 2001; 123(1):183–184. DOI: 10.1021/ja003633m

[35] Ge C., Xu M., Liu J., Lei J.; Ju H. Facile Synthesis and Application of Highly Luminescent CdTe Quantum Dots with an Electrogenerated Precursor. Chem. Commun. 2008;4:450–452. DOI: 10.1039/B714990E

[36] Gao B., Shen C., Yang Y., Yuan S. Green Synthesized CdSe Quantum Dots Capped by 3-Mercaptopropionic Acid. In: Oral, A.Y, Bahsi Z.B., Ozer M., editors. International Congress on Energy Efficiency and Energy Related Materials (ENEFM2013). 1st ed. Antalya, Turkey: Springer; 2014. p. 9–17. DOI: 10.1007/978-3-319-05521-3

[37] Yordanov G.G., Yoshimura H., Dushkin C.D. Synthesis of High-Quality Core–shell Quantum Dots of CdSe-CdS by Means of Gradual Heating in Liquid Paraffin. Colloid Polym. Sci. 2008; 289(8):1097–1102. DOI: 10.1007/s00396-008-1886-y

[38] Vasiliev R.B., Dorofeev S.G., Dirin D.N., Belov D.A., Kuznetsova T.A. Synthesis and Optical Properties of PbSe and CdSe Colloidal Quantum Dots Capped with Oleic Acid. Mendeleev Commun. 2004; 14(4):169–171. DOI: 10.1070/MC2004v014n04ABEH001970

[39] Kyobe J.W., Mubofu E.B., Makame Y.M.M., Mlowe S., Revaprasadu N. CdSe Quantum Dots Capped with Naturally Occurring Biobased Oils. New J. Chem. 2015; 39(9):7251–7259. DOI: 10.1039/C5NJ01460C

[40] Sapra S., Rogach A.L., Feldmann J. Phosphine-Free Synthesis of Monodisperse CdSe Nanocrystals in Olive Oil. J. Mater. Chem. 2006; 16(33):3391–3395. DOI: 10.1039/B607022A

[41] Bruchez M.Jr. Semiconductor Nanocrystals as Fluorescent Biological Labels. Science. 1998; 281(5385):2013–2016. DOI: 10.1126/science.281.5385.2013

[42] Gao M., Kirstein S., Möhwald H., Rogach A.L., Kornowski A., Eychmüller A., Weller H. Strongly Photoluminescent CdTe Nanocrystals by Proper Surface Modification. J. Phys. Chem. B. 1998; 102(43):8360–8363. DOI: 10.1021/jp9823603

[43] Zhu H., Sun M., Yang X. A Simple Selenium Source to Synthesize CdSe via the Two-Phase Thermal Approach. Colloids Surfaces A Physicochem. Eng. Asp. 2008; 320:74–77. DOI: 10.1016/j.colsurfa.2008.01.031

[44] Primera-Pedrozo O.M., Arslan Z., Rasulev B., Leszczynski J. Room Temperature Synthesis of PbSe Quantum Dots in Aqueous Solution: Stabilization by Interactions with Ligands. Nanoscale. 2012; 4(4):1312–1320. DOI: 10.1039/c2nr11439a

[45] Sun Q., Fu S., Dong T., Liu S., Huang C. Aqueous Synthesis and Characterization of TGA-Capped CdSe Quantum Dots at Freezing Temperature. Molecules. 2012; 17(7): 8430–8438. DOI: 10.3390/molecules17078430

[46] Smith A.M., Duan H., Mohs A.M., Nie S. Bioconjugated Quantum Dots for *In Vivo* Molecular and Cellular Imaging. Adv. Drug Deliv. Rev. 2008; 60(11):1226–1240. DOI: 10.1016/j.addr.2008.03.015

[47] Biju V., Itoh T., Ishikawa M. Delivering Quantum Dots to Cells: Bioconjugated Quantum Dots for Targeted and Nonspecific Extracellular and Intracellular Imaging. Chem. Soc. Rev. 2010; 39(8):3031–3056. DOI: 10.1039/B926512K

[48] Xiao Q., Huang S., Su W., Chan W. H., Liu Y. Facile Synthesis and Characterization of Highly Fluorescent and Biocompatible N-Acetyl-L-Cysteine Capped CdTe/CdS/ZnS Core/shell/shell Quantum Dots in Aqueous Phase. Nanotechnology. 2012; 23(49):1–10. DOI: 10.1088/0957-4484/23/49/495717

[49] Hines, M.A, GuyotSionnest P. Synthesis and Characterization of Strongly Luminescing ZnS- Capped CdSe Nanocrystals. J. Phys. Chem. 1996; 100(2):468–471. DOI: 10.1021/jp9530562

[50] Sathyamoorthy R., Manjuladevi V., Sudhagar P., Senthilarasu S., Pal U. Surfactant-Assisted Room-Temperature Synthesis of CdSe Nanoclusters. Mater. Chem. Phys. 2007; 105(1):20–24. DOI: 10.1016/j.matchemphys.2007.04.008

[51] He Y., Lu H.T., Sai L.M., Su Y.Y., Hu M., Fan C.H., Huang W., Wang L.H. Microwave Synthesis of Water-Dispersed CdTe/CdS/ZnS Core-Shell-Shell Quantum Dots with Excellent Photostability and Biocompatibility. Adv. Mater. 2008; 20(18):3416–342. DOI: 10.1002/adma.200701166

[52] Bao Y., Li J., Wang Y., Yu L., Wang J., Du W., Lou L., Zhu Z., Peng H., Zhu J. Preparation of Water Soluble CdSe and CdSe/CdS Quantum Dots and Their Uses in Imaging of Cell and Blood Capillary. Opt. Mater. 2012; 34(9):1588–1592. DOI: 10.1016/j.optmat.2012.03.033

[53] Han H., Francesco G.D., Maye M.M. . Size Control and Photophysical Properties of Quantum Dots Prepared via a Novel Tunable Hydrothermal Route. J. Phys. Chem. C. 2010; 114(45):19270–19277. DOI: 10.1021/jp107702b

[54] Tsuzuki T., McCormick P.G. Synthesis of CdS Quantum Dots by Mechanochemical Reaction. Appl. Phys. A Mater. Sci. Process. 1997; 65(6):607–609. DOI: 10.1007/s003390050629

[55] Sain S., Pradhan S.K. Mechanochemical Solid State Synthesis of (Cd0.8Zn0.2)S Quantum Dots: Microstructure and Optical Characterizations. J. Alloys Compd. 2011; 509(10):4176–4184. DOI: 10.1016/j.jallcom.2011.01.035

[56] Li S., Zhao H., Tian D. Aqueous Synthesis of Highly Monodispersed Thiol-Capped CdSe Quantum Dots Based on the Electrochemical Method. Mater. Sci. Semicond. Process. 2013; 16 (1):149–153. DOI: 10.1016/j.mssp.2012.05.013

[57] Zhou J., Yang Y., Zhang C. Toward Biocompatible Semiconductor Quantum Dots: From Biosynthesis and Bioconjugation to Biomedical Application. Chem. Rev. 2015; 115(21): 11669–11717. DOI: 10.1021/acs.chemrev.5b00049

[58] Nies D.H. Resistance to Cadmium, Cobalt, Zinc, and Nickel in Microbes. Plasmid. 1992; 27(1):17–28. DOI: 10.1016/0147-619X(92)90003-S

[59] Borovaya M.N., Naumenko A. P., Matvieieva N.A., Blume Y.B., Yemets A.I. Biosynthesis of Luminescent CdS Quantum Dots Using Plant Hairy Root Culture. Nanoscale Res. Lett. 2014; 9(1):686. DOI: 10.1186/1556-276X-9-686

[60] Rai M., Posten C., editors. Green Biosynthesis of Nanoparticles - Mechanisms and Applications. 1st ed. Wallingford, UK: CAB International; 2013. 216 p. DOI: 10.1079/9781780642239.0000

[61] Kumar S.A., Ansary A.A., Ahmad A., Khan M.I. Extracellular Biosynthesis of CdSe Quantum Dots by the Fungus, *Fusarium Oxysporum*. J. Biomed. Nanotechnol. 2007; 3 (2):190–194. DOI: 10.1166/jbn.2007.027

[62] Bao H., Lu Z., Cui X., Qiao Y., Guo J., Anderson J.M., Li C.M. Extracellular Microbial Synthesis of Biocompatible CdTe Quantum Dots. Acta Biomater. 2010; 6(9):3534–3541. DOI: 10.1016/j.actbio.2010.03.030

[63] Mi C., Wang Y., Zhang J., Huang H., Xu L., Wang S., Fang X., Fang J., Mao C., Xu S. Biosynthesis and Characterization of CdS Quantum Dots in Genetically Engineered *Escherichia Coli*. J. Biotechnol. 2011; 153(3–4):125–132. DOI: 10.1016/j.jbiotec.2011.03.014

[64] Nath D., Banerjee P. Green Nanotechnology - A New Hope for Medical Biology. Environ. Toxicol. Pharmacol. 2013; 36(3):997–1014. DOI: 10.1016/j.etap.2013.09.002

[65] Shirasaki Y., Supran G.J., Bawendi M.G., Bulovic V. Emergence of Colloidal Quantum-Dot Light-Emitting Technologies. Nat. Photonics. 2012; 7(1):13–23. DOI: 10.1038/nphoton.2012.328

[66] Emin S., Singh S.P., Han L., Satoh N., Islam A. Colloidal Quantum Dot Solar Cells. Sol. Energy. 2011; 85(6):1264–1282. DOI: 10.1016/j.solener.2011.02.005

[67] Jamieson T., Bakhshi R., Petrova D., Pocock R., Imani M., Seifalian A.M. Biological Applications of Quantum Dots. Biomaterials. 2007; 28(31):4717–4732. DOI: 10.1016/j.biomaterials.2007.07.014

[68] Li J., Zhu J.J. Quantum Dots for Fluorescent Biosensing and Bio-Imaging Applications. Analyst. 2013; 138(9):2506–2515. DOI: 10.1039/c3an36705c

[69] Sun Q., Wang Y.A., Li L.S., Wang D., Zhu T., Xu J., Yang C., Li Y. Bright, Multicoloured Light-Emitting Diodes Based on Quantum Dots. Nat. Photonics. 2007; 1(12):717–722. DOI: 10.1038/nphoton.2007.226

[70] Colvin V.L., Schlamp M.C., Alivisatos A.P. Light-Emitting Diodes Made from Cadmium Selenide Nanocrystals and a Semiconducting Polymer. Nature. 1994; 370(6488): 354–357. DOI: 10.1038/370354a0

[71] Ki Bae W., Kwak J., Park J.W., Char K., Lee C., Lee S. Highly Efficient Green-Light-Emitting Diodes Based on CdSe@ZnS Quantum Dots with a Chemical-Composition Gradient. Adv. Mater. 2009; 21(17):1690–1694. DOI: 10.1002/adma.200801908

[72] Yang Y., Zheng Y., Cao W., Titov A., Hyvonen J., Manders J.R., Xue J., Holloway P.H., Qian L. High-Efficiency Light-Emitting Devices Based on Quantum Dots with Tailored Nanostructures. Nat. Photonics. 2015; 9:259–266. DOI: 10.1038/nphoton.2015.36

[73] Lee K.H., Lee J.,H., Song, W.S., Ko, H., Lee, C., Lee, J.H., Yang, H. Highly Efficient, Color-Pure, Color-Stable Blue Quantum Dot Light-Emitting Devices. ACS Nano. 2013; 7(8):7295–7302. DOI: 10.1021/nn402870e

[74] Lee K.H., Lee J.H., Song W.S., Ko H., Lee C., Lee J.H., Yang H. Over 40 cd/A Efficient Green Quantum Dot Electroluminescent Device Comprising Uniquely Large-Sized Quantum Dots. ACS Nano. 2014; 8(5):4893–4901. DOI: 10.1021/nn500852g

[75] Irvine-Halliday D., Peon R. Solid-State Lighting: The Only Solution for the Developing World. Int. Soc. 2006. DOI: 10.1117/2.1200601.0056

[76] Hod I., Zaban A. Materials and Interfaces in Quantum Dot Sensitized Solar Cells: Challenges, Advances and Prospects. Langmuir. 2014; 30(25): pp. 7264–7273. DOI: 10.1021/la403768j

[77] Jun H.K., Careem M. A., Arof A.K. Quantum Dot-Sensitized Solar Cells-Perspective and Recent Developments: A Review of Cd Chalcogenide Quantum Dots as Sensitizers. Renew. Sustain. Energy Rev. 2013; 22:148–167. DOI: 10.1016/j.rser.2013.01.030

[78] Kamat P.V., Christians J.A., Radich J.G. Quantum Dot Solar Cells: Hole Transfer as a Limiting Factor in Boosting the Photoconversion Efficiency. Langmuir. 2014; 30(20): 5716–5725. DOI: 10.1021/la500555w

[79] Chuang C.H.M., Brown P.R., Bulovic V., Bawendi M.G. Improved Performance and Stability in Quantum Dot Solar Cells through Band Alignment Engineering. Nat. Mater. 2014; 13(8):796–801. DOI: 10.1038/nmat3984

[80] Li W., Pan Z., Zhong X. CuInSe2 and CuInSe2 –ZnS Based High Efficiency "green" Quantum Dot Sensitized Solar Cells. J. Mater. Chem. A. 2015; 3(4):1649–1655. DOI: 10.1039/C4TA05134C

[81] Duché D., Drouard E., Simon J., Escoubas L., Torchio P., Le Rouzo J., Vedraine S. Light Harvesting in Organic Solar Cells. Sol. Energy Mater. Sol. Cells. 2011; 95:S18–S25. DOI: 10.1016/j.solmat.2010.12.008

[82] Abbasi E.; Kafshdooz T.; Bakhtiary M., Nikzamir, N.N., Nikzamir N.N., Nikzamir, M., Mohammadian, M., Akbarzadeh, A. Biomedical and Biological Applications of Quantum Dots. Artif. Cells, Nanomedicine, Biotechnol. 2015. DOI: 10.3109/21691401.2014.998826

[83] Vu T.Q., Lam W.Y., Hatch E.W., Lidke D.S. Quantum Dots for Quantitative Imaging: From Single Molecules to Tissue. Cell Tissue Res. 2015; 360(1): pp. 71–86. DOI: 10.1007/s00441-014-2087-2

[84] Jin Z., Hildebrandt N. Semiconductor Quantum Dots for *In Vitro* Diagnostics and Cellular Imaging. Trends Biotechnol. 2012; 30(7):394–403. DOI: 10.1016/j.tibtech.2012.04.005

[85] Bentolila L.A., Weiss S. Single-Step Multicolor Fluorescence in Situ Hybridization Using Semiconductor Quantum Dot-DNA Conjugates. Cell Biochem. Biophys. 2006; 45(1):59–70. DOI: 10.1385/CBB:45:1:59

[86] Gao X., Yang L., Petros J. A., Marshall F.F., Simons J.W., Nie S. *In Vivo* Molecular and Cellular Imaging with Quantum Dots. Curr. Opin. Biotechnol. 2005; 16(1):63–72. DOI: 10.1016/j.copbio.2004.11.003

[87] Biju V., Mundayoor S., Omkumar R.V., Anas A., Ishikawa M. Bioconjugated Quantum Dots for Cancer Research: Present Status Prospects and Remaining Issues, Biotechnol. Adv. 2010; 28(2):199–213. DOI: 10.1016/j.biotechadv.2009.11.007

[88] Juzenas P., Chen W., Sun Y.P., Coelho M.A.N., Generalov R., Generalova N., Christensen I.L. Quantum Dots and Nanoparticles for Photodynamic and Radiation Therapies of Cancer. Adv. Drug Deliv. Rev. 2008; 60(15):1600–1614. DOI: 10.1016/j.addr.2008.08.004

Chapter 8

Recent Advances in Environment-Friendly Alkyd Nanocomposites Towards "Greener" Coatings

Eram Sharmin, Fahmina Zafar, Nahid Nishat and Sharif Ahmad

Additional information is available at the end of the chapter

http://dx.doi.org/10.5772/62448

Abstract

Alkyd nanocomposites have attracted great attention in the field of heavy duty coating materials. This is due to the synergistic action of both alkyds (flexibility, biodegradability, compatibility, good gloss retention, durability, weathering resistance) and nanofillers (large surface area to volume ratio). Alkyd nanocomposites show good physico-mechanical, physico-chemical, anticorrosive, and antimicrobial performances and thermal stability, with application as anticorrosive, anti-fog, self-cleaning, self-healing, and antimicrobial coatings. In view of present drives and legislations towards environment-friendly coatings, alkyds have undergone modifications as waterborne, high solids, hyperbranched "greener" nanocomposites. The present chapter deals with a brief overview of alkyds, recent advances in environment-friendly alkyd nanocomposite coatings, and the effects of nanofillers on the performance (physico-mechanical, chemical/corrosion resistance, thermal stability, and others) of "greener" alkyd nanocomposite coatings.

Keywords: alkyds, nanocomposites, coatings, physico-mechanical, chemical resistance, thermal stability

1. Introduction

Alkyd resins are the most versatile vegetable seed oil (VSO)-based polymeric binders find applications paints and coatings industry. They are polyester-based materials modified with oil or oil derived fatty acids. Alkyd resins owe their wide applications to their versatility and capability to engineer a wide variety of acceptable properties in terms of usage by the Coat-

ings industry. Alkyds now account for approximately half of all the resins consumed in the field of protective coatings [1–6]. Chemically, alkyd resins have been defined as reaction product of condensation polymerization of polyhydric alcohol, polybasic acid, and monobasic fatty acid (saturated or unsaturated; **Figure 1**). They are best classified according to the amount of fatty acid and phthalic anhydride present (**Table 1**) [1].

Content	Type			
	Short alkyd	**Medium alkyd**	**Long alkyd**	**Very long alkyd**
Fatty acid content	30–42	43–54	55–68	>68
Phthallic anhydride	37	30–37	20–30	<20

Table 1 Alkyd classification.

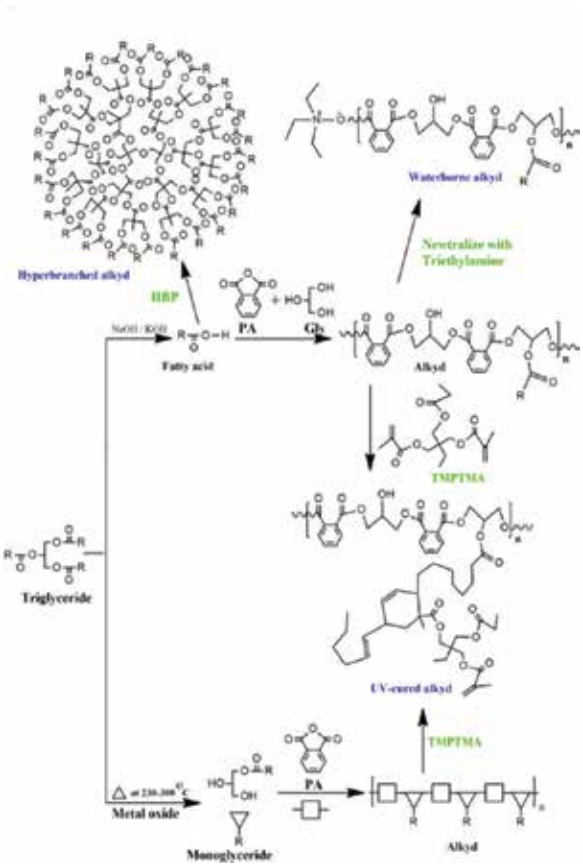

Figure 1. Alkyd synthesis, where R=fatty acid chain (saturated or unsaturated). Where PA:Phthalic anhydride, Gly:Glycerol and TMPTMA: Trimethylolpropane Trimethacrylate.

The reaction of alkyd (**Figure 1**) is based on three basic fundamental building blocks:

i. VSO or corresponding fatty acids (in percentage): linseed (linolenic/linoleic 40/35), soybean (linoleic/oleic 55/28), tall (fatty acid/rosin 50/40), castor (ricinoleic/linoleic 90/4), dehydrated castor (conjugated fatty acid/ricinoleic 80/10), safflower (linoleic/oleic 59/37), tung (elaeostearic/oleic 79/11), coconut (saturated/monounsaturated fatty acid 91/6), as well as other nontraditional seeds oils;

ii. Polyhydric alcohols (polyols): glycerol, pentaerythritol, sorbitol, ethylene glycol, neopentyl glycol, trimethylol propane, and others; and

iii. Polybasic acids (or corresponding anhydride): phthalic, isophthalic, adipic, maleic, fumaric acids, and trimellitic anhydride [1].

Alkyd resins have good color retention, durability in exterior finishes, good weathering resistance, and moderate resistance to corrosive fumes but show poor resistance to chemical splash and spillage, especially in alkaline medium. The thermal stability of these resins goes up to 105°C [3]. The properties of alkyd coatings are derived mainly from the properties of drying oils used in the manufacture of the resins. The extent and kind of unsaturation in drying oil fatty acids have a profound effect on the properties of finished alkyd. The drying time, hardness, color, and moisture resistivity of the resin depends on the degree of unsaturation of the oil used [1,4]. These unsaturation sites are responsible for the curing of alkyd resins through auto-oxidation process (Figure 2). The process creates the active free radicals leading to the formation of a three-dimensional cross-linked network. [1,7].

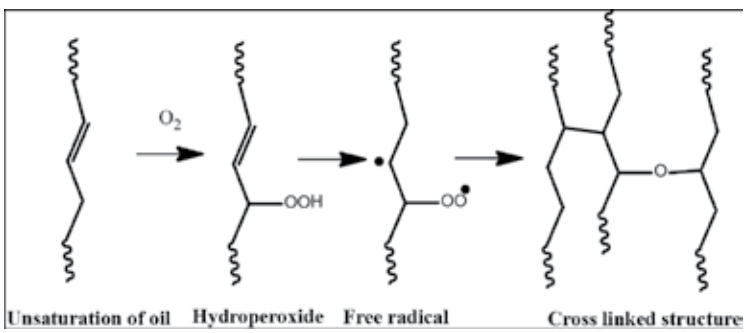

Figure 2. Autoxidation of alkyd.

The standard alkyds are usually soybean and linseed oil alkyds, which show moderate and faster drying rates, respectively. The former has good color retention, whereas the latter reduces the color retention requirement. Dehydrated castor and soybean oil-based alkyds are used for baked finishes. These alkyds in combination with urea formaldehyde and melamine formaldehyde resin exhibit shorter baking time and produce harder film. For light color and maximum color retention, nondrying oils, such as coconut, castor, and cottonseeds, may be used. The alkyd of this type does not dry because of the nonoxidizing character of the parent VSO. They must be blended with some cross-linkers and baked with amine resin, such as urea or melamine formaldehyde, at high temperature (**Figure 3**).

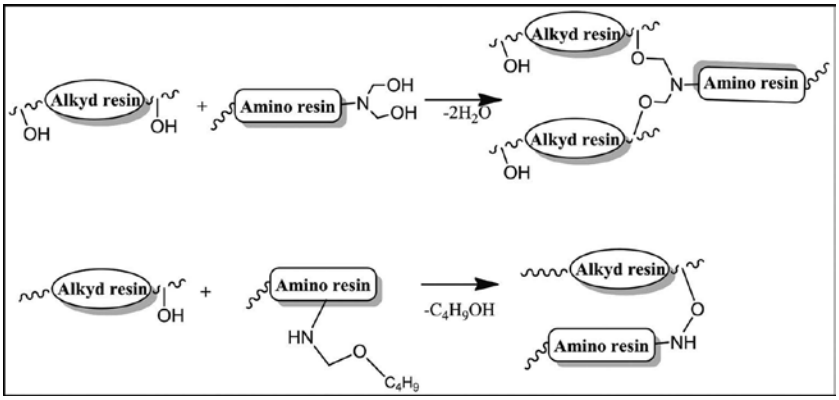

Figure 3. Curing reactions of alkyd resins with amino resins.

Nondrying VSO-based alkyds are also used as resinous plasticizers and other lacquer-type polymers. Tung and oiticica in combination with other VSO-based alkyds show faster drying and achieve earlier hardness. Safflower oil-based alkyd has excellent drying properties and color retention [1,8]. Besides these, some nontraditional VSO-based alkyds, such as nahar (*Mesua ferrea* Linn), kamala (*Mallotus phillipinensis*), mahua (*Madhuca longifolia*), barbados nut (*Jatropha curcas*), burra gokharu (*Tribulus terrestris*), undi (*Calophylum inophyllum*), karanja (*Pongamia glabra*), karinotta (*Samera indica*), nigerseed (*Guizotia abyssinica*), babul (*Acacia arabica*), and neem (*Azardirachta indica*), have been reported and used as coating materials [4,9–11]. Tobacco seed oil has been reportedly used in alkyd preparation for wrinkled finish paints [10]. The use of pentaerythritol as a polyhydric alcohol produces faster drying, greater hardness, better gloss, and better water resistance than alkyds based on glycerol of equal fatty acid content [12].

Modifications of alkyd resins are continuously carried out to achieve improved mechanical and chemical resistance properties and these systems find a wide scope of application as corrosion protective coatings. The modification with acrylic monomer, such as styrene, methyl methacrylate, vinyl toluene, and others, has been extensively done by researchers through unsaturation to improve the performance of resins up to the desired level [13]. Butylmethacrylate-co-maleic anhydride copolymer modified linseed and rubber seed oil alkyds through functional groups are used as co-curing resins with melamine formaldehyde resin to prepare baking-type coating compositions, whereas *Albizia benth* medium oil-based alkyd gives room temperature cured resin, with superior film properties [3,14,15]. The modification of alkyd with chlorinated rubber resulted in improved adhesion as well as improved acid, alkali, and water resistance. The chlorination of soybean and *A. benth* oil-based alkyd transforms into an air-drying, nonconvertible film former with improved mechanical properties [3,16,17]. Chain-stop alkyds from solvent fractionated *Argemone* and rubber seed oil are used for specialty alkyd [18]. Heated rubber seed oil-based films show excellent resistance to acid and salt solution. Its combination with cashew nut shell liquid formaldehyde resin has improved the drying ability and chemical resistance [19]. The phenol-modified alkyd resin improves gloss retention as well

http://dx.doi.org/10.5772/62448

as water and alkali resistance. Waterborne-baked and air-drying alkyds have also been developed from different VSO having properties similar to their solvent-borne counterparts and found application in paint and coatings [20,21]. In addition, alkyd resins can be modified with epoxies and polyurethanes or other thermoplastic resins to give coatings of improved performance. For example, urethane oils are prepared by reacting diglycerides with toluene diisocynate. The resulting oils are used in alkyd resin preparation or as additive for coatings. Besides these, other alkyds are also prepared, such as imide-modified alkyd, amide-modified alkyd, tetrachlorophthalic anhydride-based alkyd resin with fire-retardant properties, ketene and acetic anhydride modification with terminal hydroxyl groups of alkyd, zinc chromate containing alkyd resin, triphenyl phosphite containing alkyd resin with improved color and drying properties, oil-less alkyds, ultraviolet (UV) light hardenable pigmented alkyd resin laquer preparation, and maleic anhydride-cyclopentadiene adduct in alkyd preparations [22–24].

In recent years, due to concerns related to energy consumption and environmental contamination, regulations, and legislations directing us towards "sustainable development" and innovations, efforts are being focused towards the development of (i) "greener" environmentally benign materials (ii) with improved performance characteristics to meet the present-day demands. Environment-friendly technologies such as high solids, hyperbranched, waterborne, and UV curable, are being used to eliminate the use and/or generation of hazardous chemicals and emissions harmful to environment. For improvement in performance, the inclusion of nanosized fillers as nanoreinforcements is being accomplished. In this context, the world of alkyds has also witnessed greater modifications such as switching to high solids, hyperbranched, waterborne and UV curable alkyds (Figure 1)[22,23,25–29]. In our recent review articles, we have described alkyds and their modifications in terms of both in property enhancements and environment-friendly approaches, occurring in the last decade [22,23]. This manuscript provides a brief overview of environment-friendly recent advances that have taken place in the field of alkyds and also focuses on the properties and performance characteristics of high solids, hyperbranched, and waterborne alkyd nanocomposites along with the unexplored areas in the field and possible future research directions.

2. Environment-friendly recent advances in alkyds towards "greener" coatings

Considering the future predictions, energy concerns, associated hazards, and legislations, research progresses in the quest for improved and updated performance characteristics in every field. Alkyds have undergone several modifications recently in consideration of the aforementioned, such as the use of reactive diluents, resorting to solvent free approaches, and others. In alkyd-based coatings, towards the step to eliminate the use of organic solvents, which are often added to achieve the desired viscosity for application over the substrate, tung oil (TO)-based reactive diluents were added to soy alkyd formulations. TO-reactive diluents were modified with alkyoxylsilane, tetraallyl ether, and fluororinated side chain. These diluents participated in the film formation process and significantly reduced the viscosity of alkyds,

thereby serving as effective diluents. Alkoxysilane-modified diluents showed somewhat enhanced performance due to *in situ* polycondensation of silicon alkoxide within the organic polymer matrix, which provided an additional functionality for cross-linking [30]. To reduce the content of solvents and to achieve desirable viscosity, carboxymethyl cellulose nitrate ester/coconut alkyd blends were prepared, which resulted in hydrophilic transparent films [31,32].

In a recent "greener" approach, *Jatropha* oil (JO)-based alkyd was blended with citric acid cured JO-derived epoxy. The final product showed enhanced tensile strength, elongation at break, hardness, increment in gloss due to uniform and smooth surface morphology, good scratch hardness and adhesion conferred by highly cross-linked networks, flexibility of oil chains, and the presence of polar functionalities in the backbone, which also contributed to excellent resistance to solvents (water and ethanol), salt solution, and good acid and alkali resistance [33]. An interesting research includes the synthesis of alkyds from postconsumer polyethylene terephthalate (PET) bottles. Herein, waste PET was glycolyzed using glycerol, trimethylolethane, trimethylolpropane, and pentaerythritol, giving tetra- and hexafunctional glycolyzates. PET glycolyzates were then used as hydroxyl components in the synthesis of alkyd resins. The approach has multiple advantages: (i) value addition to a waste material (i.e., PET), (ii) reduction in the amount of waste PET in dumps and landfills, (iii) reduction in amount of phthalic anhydride, and (iv) improved performance of alkyd. The best performance was achieved by the inclusion of trimethylolethane and trimethylolpropane, as they had four sterically unhindered primary hydroxyl groups that produced alkyds with higher degree of branching, consequently higher molar mass, which led to improved mechanical, drying, and chemical resistance properties [34].

Laccases are enzymes first discovered in Japanese lacquer tree *Rhus vernicifera* by Yoshida in 1883, which are found in fungi, different bacteria, and plants. In an effort to completely replace the toxic heavy metals by nontoxic and environment-friendly catalysts, laccase-mediator systems have been considered as potential cross-linking and functionalizing agents for alkyds [35]. In the synthesis of alkyds, heterogeneous base catalysts are used such as hydroxides of calcium, potassium, sodium, lithium, oxides of calcium, zinc, and others. Recently, CuO nanocatalyst was introduced, which had dual effects: (i) it catalyzed the alcoholysis-polyesterification reaction, reducing the reaction time, and (ii) it conferred antimicrobial properties to the resin [36]. Thus, the addition of nanofillers leads to enhancement in several properties, often drastically, such as aesthetic appeal, UV resistance, corrosion resistance, scratch resistance, impact resistance, thermal stability, and others, thus reinforcing the matrix, without losing transparency and other properties. The enhancement in properties is a consequence of the much greater surface-to-volume ratio of the nanofiller. The incorporation of nanoparticles in the polymer matrix offers significant barrier properties for corrosion protection. It reduces blistering or delamination and also enhances the integrity and durability of coatings (the fine particles uniformly dispersed in coatings can fill cavities and can cause crack bridging, crack deflection, and crack bowing) [37,38]. After having a brief idea of the recent advances in the field towards environment-friendly "greener" coatings, in the proceeding sections, we will discuss about some of the recent developments in alkyd-based environment-friendly (waterborne, high solids, hyperbranched) nanocomposite coatings.

http://dx.doi.org/10.5772/62448

3. Waterborne alkyd nanocomposite coatings

In these types of coatings, the alkyd matrix selected is waterborne and is further modified with nanoreinforcements depending on the property that needs improvement (Figure 4). Thus, the choice of nanofillers for modification depends on the property that is needed to be augmented or enhanced. The inclusion of nanoalumina improved the scratch, corrosion, UV, and abrasion resistance of coatings. The increased content of nanoalumina reduced the pinhole formation tendency and defended the coatings against humidity [37]. The corrosion protection Occurred by (a) nanoparticles occupying the vacant spaces in the coating matrix, (b) reducing porosity, (c) bridging and interconnecting the constituents of matrix, (d) increasing cross-linking, (e) providing longer diffusion paths to corrosive ions, and (f) improving barrier performance [39]. A similar enhancement in the performance of coatings was also observed when waterborne alkyd coatings were modified with nano-Fe_2O_3 by the described corrosion protection mechanism. Even at the lower loading of nano-Fe_2O_3 (0.05%, 0.1%, and 0.2%), the corrosion process was delayed, whereas, at 0.3% loading of nano-Fe_2O_3, adequate coating performance was achieved [40,41]. Nano-silica modification improved scratch resistance, abrasion resistance, adhesion properties, impact resistance, glass transition temperature, and thermal stability [42,43]. The introduction of ZnO nanoparticles improved film compactness and abrasion resistance and had a catalytic influence on curing reaction, thus facilitating the formation of hard and complex network. The stronger interactions between nanoparticles and alkyd matrix also conferred enhancement in mechanical properties. As nano-ZnO has UV blocking properties, the incorporation of nano-ZnO also improves the UV resistance of coatings [44–46].

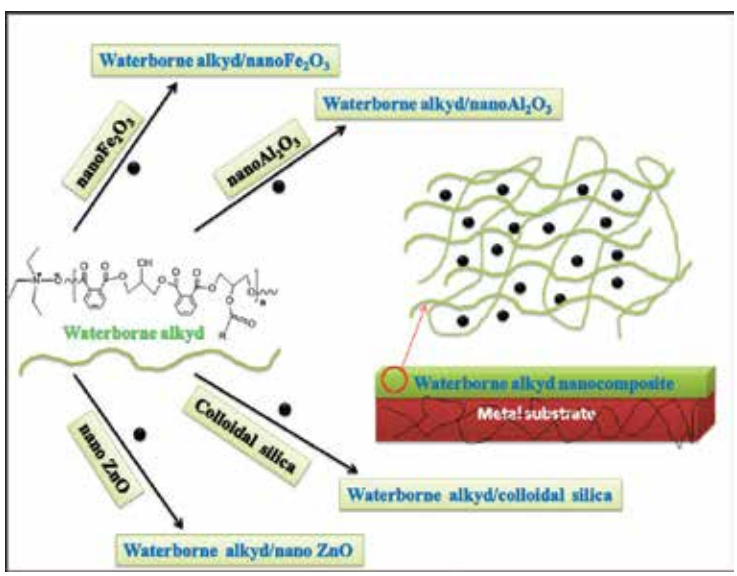

Figure 4 Waterborne alkyd nanocomposites.

Poly(methylmethacrylate-butylacrylate)/nanocalcium carbonate, prepared by emulsion polymerization, was blended with alkyd coating with 50 wt% water as solvent, in various ratios, with dual objectives: (i) using polymer nanocomposite as partial binder and (ii) As a filler to improve the properties. The coatings showed good gloss, mechanical and thermal properties; however, impact resistance was found to be lower. The highly crystalline calcium carbonate nanoparticles deteriorate the impact strength at locations in coatings where the aggregation of particles occurs, thus generating stress at these specific sites [47].

4. Hyperbranched alkyd nanocomposite coatings

The use of dendritic or hyperbranched polymers as binders in coatings is considered as one of the effective ways to reduce volatile organic compounds (VOCs; **Figure 5**).

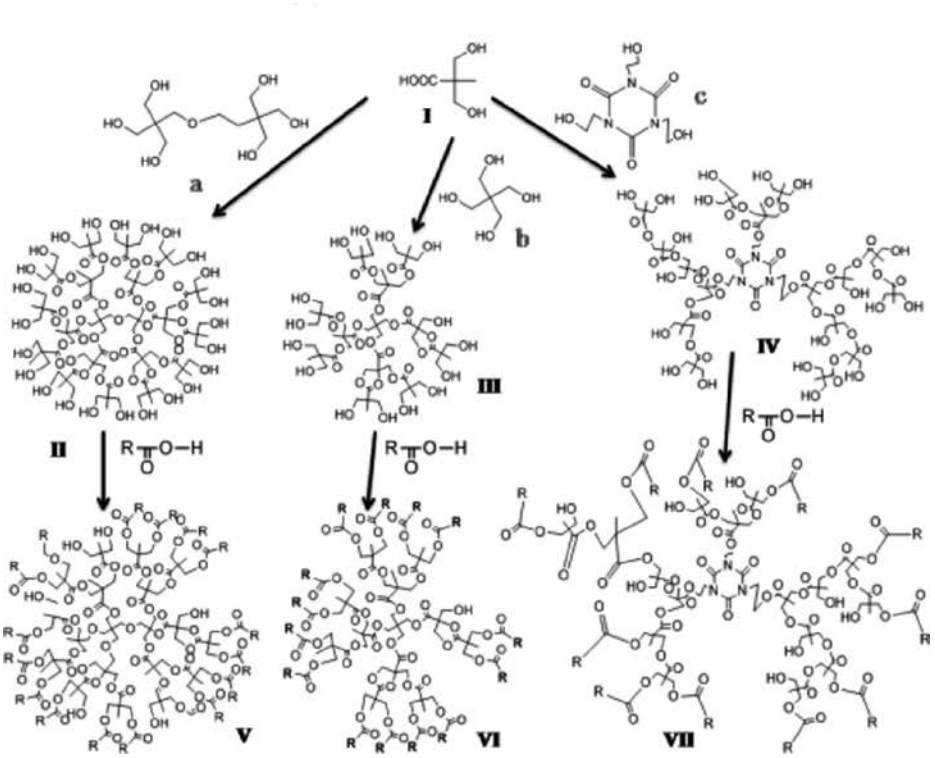

Figure 5 Hyperbranched alkyd, where I=dimethylolpropionic acid, II–IV=hyperbranched polyesters (HBPs), and **V–VII**=their respective hyperbranched alkyds; a–c are dipentaerythritol, pentaerythritol, and 1,3,5-tris(2-hydroxyethyl)cyanuric acid, respectively; and R=fatty acid chain (unsaturated or saturated).

These polymers have three-dimensional compact structures. They show low viscosity even at higher molecular weight. Thus, the development of hyperbranched nanocomposites has double advantages: (i) overcomes the use of VOCs and (ii) leads to property enhancement.

http://dx.doi.org/10.5772/62448

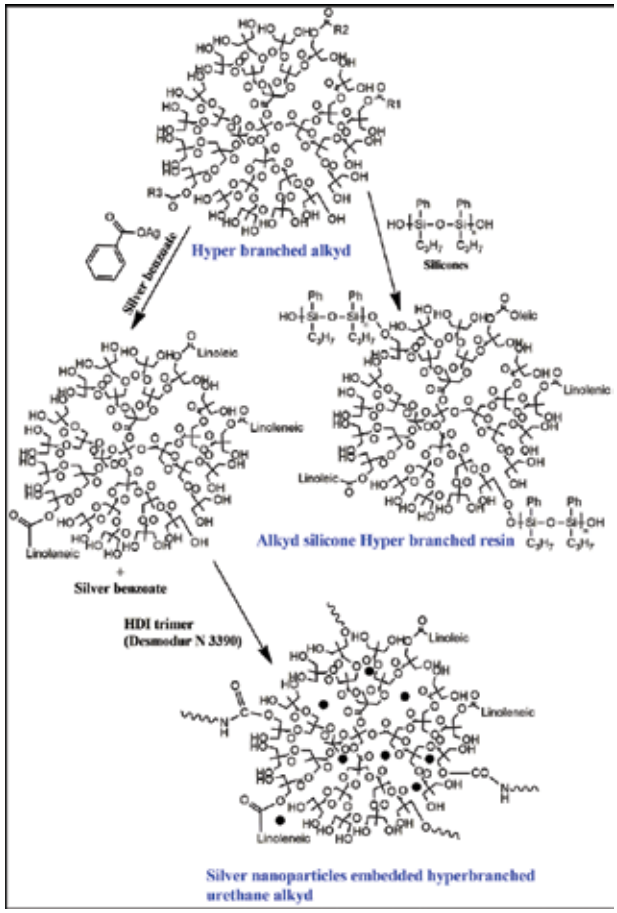

Figure 6 Hyperbranched alkyd/silicone or silver nanocomposites.

In a recent research, nanosilver was embedded in hyperbranched urethane alkyd by an *in situ* approach that prevented agglomeration of nanoparticles (**Figure 6**). The nanocomposites showed good antibacterial activity against *Serratia marcescens*, as studied by using agar overlay and disk diffusion methods, and the coatings were gloss retentive and nonleaching. The resin required much lesser solvent for coating formulation and showed improved mechanical properties [48].

An interesting research work was performed on carbon nanofiller modification of hyperbranched alkyd. Here, three geometrically different carbon nanofillers, carbon black (CAB), multiwall carbon nanotubes (MWCNT), and graphene (GR), were treated with a surfactant Nonidet P-40 (**Figure 7**). This led to the uniform dispersion of carbon fillers as facilitated by the interactions of π-electron clouds of carbon nanofillers with the delocalized π-electrons of the surfactant and H-bonding interactions between surfactant and hyperbranched alkyd backbone. The former interactions reduce the van der Waals forces present between carbon nanofillers, and the latter interactions improve the interfacial adhesion between the matrix and

nanofillers. Due to their stronger interactions with the alkyd backbone and the high aspect ratio and surface area, MWCNT and GR showed better dispersion in the matrix relative to CAB. Thus, modifications with MWCNT and GR provided relatively higher scratch resistance, adhesion, and tensile strength to alkyd coating as well as higher thermal stability. The water vapor transmission rate was found to be lower in nanocomposite alkyd, and least in GR alkyd (due to its plate-like structure), compared to the unmodified alkyd, as the nanofillers provided tortuous path to water and oxygen molecules hindering them to reach the substrate of the coating easily. However, compared to others, GR-alkyd showed the highest corrosion resistance performance due to good dispersion and adhesion of GR; moreover, its plate-like structure also proved advantageous in enhancing the corrosion resistance [49]. The modification with silicones reduces the drying times and improves the adhesion to the substrate, hardness, and gloss of coating (**Figure 6**) [50].

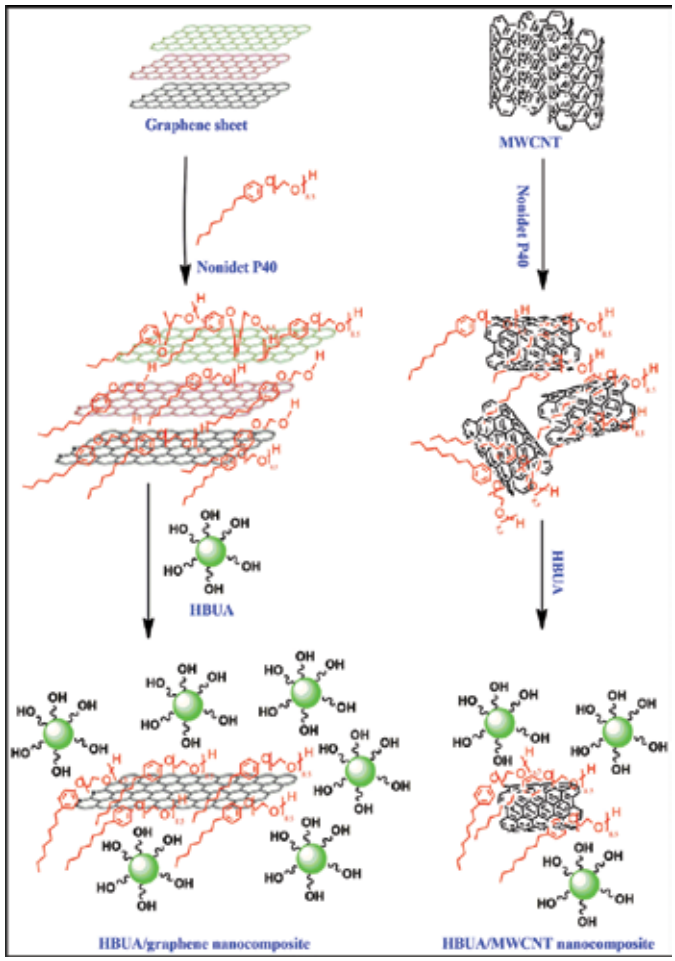

Figure 7 Hyperbranched alkyd urethane/GR or MWCNT nanocomposites.

http://dx.doi.org/10.5772/62448

5. Future suggestions and conclusion

Environment-friendly alkyd nanocomposites are an emerging field of research. They comprise a vast field for commercial coating applications. They find promising applications as corrosion-protective, antimicrobial, eco-friendly coatings. However, more efforts are required in the field to be established further as "greener" coatings in terms of performance, cost, and environment-friendly applications. A lot of modifications have been accomplished and much remains unexplored.

The synthesis of alkyds requires higher temperatures and longer reaction times. In view of this, alkyd synthesis can be performed via microwave-assisted methods that reduce reaction times and often temperatures. Another alternative is the synthesis by enzymatic approach. Hydroxylated oils (or polyols) can be used to prepare monoglycerides, which would introduce extra hydroxyl functionality in alkyd backbone increasing the adhesion of coatings produced due to polar hydroxyls. The alkyd with extra hydroxyls in its backbone will serve as alkyd polyol. Considering the present drives towards environment-friendly coatings, efforts should be laid on the development of low solvent or solvent-free alkyd nanocomposite coatings to reduce the use of harmful solvents during the synthesis, processing, formulation, and application of coatings. More emphasis should be laid on the development of waterborne, high solids, hyperbranched, and UV curable alkyd nanocomposites using different nanofillers. A completely water-soluble alkyd nanocomposite would be a significant achievement in the field. Greener isocyanates may be used as curing agents for alkyd polyurethane nanocomposites. The introduction of nanoparticles by *in situ* approach may reduce reaction steps and also the problems associated with the agglomeration of nanoparticles. Blending with cost-effective reinforcing components will also effectively reduce cost and improve performance characteristics. The greater utilization of nonedible and nonmedicinal oils in the preparation of alkyds must be encouraged to add value to underutilized oil as a bioresource. Efforts may also be focused on studying the biodegradation behavior of these materials to determine their eco-friendly disposal.

Acknowledgements

Dr. Fahmina Zafar is thankful to the University Grants Commission, India, for the Dr. D.S. Kothari postdoctoral fellowship, Ref. #F.4/2006(BSR)/13-986/2013(BSR), with Prof. Nahid Nishat.

Author details

Eram Sharmin[1*], Fahmina Zafar[2*], Nahid Nishat[2] and Sharif Ahmad[3]

*Address all correspondence to: eramsharmin@gmail.com

*Address all correspondence to: fahmzafar@gmail.com

1 Department of Pharmaceutical Chemistry, College of Pharmacy, Umm Al-Qura University, Makkah Al-Mukarramah, Saudi Arabia

2 Inorganic Materials Research Laboratory, Department of Chemistry, Jamia Millia Islamia (A Central University), New Delhi, India

3 Materials Research Laboratory, Department of Chemistry, Jamia Millia Islamia (A Central University), New Delhi, India

References

[1] Lanson H. Chemistry and technology of alkyd and saturated reactive polyester resins. ACS Symposium Series. Oxford University Press; 1985. pp. 1181–1204.

[2] El-Hai FA, Sabbah I, Naser A, Abdel-Rehim N. High performance alkyd resin compositions for coating. Int J Polym Mater 2004;53:871–878.

[3] Akintayo C, Adebowale K. Synthesis and characterization of acrylated *Albizia benth* medium oil alkyds. Prog Org Coat 2004;50:207–212.

[4] Tiwari S, Saxena M, Tiwari S. Preparation and characterization of penta alkyds based on mahua oil. J Sci Ind Res 2002;61:110–116.

[5] Chandra S, Pasari S. Synthesis of styrenated alkyds. J Sci Ind Res 1982;41:248–257.

[6] Igwe IO, Ogbobe O. Studies on the alcoholysis of some seed oils. J Appl Polym Sci 2000;78:1826–1832.

[7] van Gorkum R, Bouwman E, Reedijk J. Fast autoxidation of ethyl linoleate catalyzed by [$Mn(acac)_3$] and bipyridine: a possible drying catalyst for alkyd paints. Inorg Chem 2004;43:2456–2458.

[8] Thurmond C, Hempel A, Marling P. Safflower oil in alkyd resins and treated oils. J Am Oil Chem Soc 1951;28:354–356.

[9] Dutta N, Karak N, Dolui S. Synthesis and characterization of polyester resins based on Nahar seed oil. Prog Org Coat 2004;49:146–152.

[10] Tiwari S, Saxena M, Tiwari SK. Mahua-oil-based resins for the high-temperature curing of fly ash coatings. J Appl Polym Sci 2003;87:110–120.

[11] Boruah M, Gogoi P, Adhikari B, Dolui SK. Preparation and characterization of *Jatropha curcas* oil based alkyd resin suitable for surface coating. Prog Org Coat 2012;74:596–602.

[12] Rokicki G, Lukasik L, Florjańczyk Z, Żukowska G. Water-based air-drying alkyd polyester resins modified with glycerol allyl ether. J Macromol Sci Pt A Pure Appl Chem 1996;33:509–521.

[13] Duhon M. Vinyl toluene modified alkyd resins. Paintindia 2002;52:82–84.

[14] Raval D, Patel P, Mannari V, Sinha T. Acid-functional acrylic copolymer modified alkyds for applications in surface coatings. J Sci Ind Res 1996;55:806–810.

[15] Patel P, Raval D, Mannari V, Patel R. Acid functional acrylic copolymer modified alkyds for applications in surface coatings-II. J Sci Ind Res 1998;57:70–78.

[16] Bhandari S, Chandra S. Synthesis, characterization and evaluation of chlorinated soybean oil alkyds. Indian J Chem Technol 1994;1:45–45.

[17] Akintayo C, Adebowale K. Synthesis, characterization and evaluation of chlorinated *Albizia benth* medium oil alkyds. Prog Org Coat 2004;50:138–143.

[18] Dighe A, Toliwal S, Kotpal R. Chain stop alkyds from solvent fractionated *Argemone* and rubber seed oils. J Sci Ind Res 2000;59:808–813.

[19] Aigbodion A, Pillai C, Bakare I, Yahaya L. Synthesis, characterization and evaluation of heated rubber seed oil and rubber seed-oil modified alkyd resins as binders in surface coatings. Indian J Chem Technol 2001;8:378–384.

[20] Wang C, Jones FN. Stability and film properties of tung oil modified soybean alkyd emulsion. J Appl Polym Sci 2000;78:1698–1706.

[21] Majumdar S, Kumar D, Nirvan Y. Acrylate grafted dehydrated castor oil alkyd—A binder for exterior paints. J Coat Technol 1998;70:27–33.

[22] Alam M, Akram D, Sharmin E, Zafar F, Ahmad S. Vegetable oil based eco-friendly coating materials: A review article. Arab J Chem 2014;7:469–479.

[23] Sharmin E, Zafar F, Akram D, Alam M, Ahmad S. Recent advances in vegetable oils based environment friendly coatings: A review. Ind Crops Prod 2015;76:215–229.

[24] Wright HJ, Puis RND. Imide-modified alkyd resins. Ind Eng Chem 1946;38:1303–1308.

[25] Dhoke SK, Sinha TM, Dutta P, Khanna A. Formulation and performance study of low molecular weight, alkyd-based waterborne anticorrosive coating on mild steel. Prog Org Coat 2008;62:183–192.

[26] Pirvu C, Demetrescu I, Drob P, Vasilescu E, Vasilescu C, Mindroiu M, et al. Electrochemical stability and surface analysis of a new alkyd paint with low content of volatile organic compounds. Prog Org Coat 2010;68:274–282.

[27] Ang DTC, Khong YK, Gan SN. Novel approach to enhance film properties of environmentally friendly UV-curable alkyd coating using epoxidised natural rubber. Prog Org Coat 2013;76:705–711.

[28] Ang DTC, Gan SN. Novel approach to convert non-self drying palm stearin alkyds into environmental friendly UV curable resins. Prog Org Coat 2012;73:409–414.

[29] Soucek M. Synthesis of UV-curable tung oil and UV-curable tong oil based alkyds. 2012.

[30] Wutticharoenwong K, Dziczkowski J, Soucek MD. Tung based reactive diluents for alkyd systems: Film properties. Prog Org Coat 2012;73:283–290.

[31] Duan H, Shao Z, Zhao M, Zhou Z. Preparation and properties of environmental-friendly coatings based on carboxymethyl cellulose nitrate ester and modified alkyd. Carbohydr Polym 2016;137:92–99.

[32] Aulin C, Ström Gr. Multilayered alkyd resin/nanocellulose coatings for use in renewable packaging solutions with a high level of moisture resistance. Ind Eng Chem Res 2013;52:2582–2589.

[33] Gogoi P, Boruah M, Sharma S, Dolui SK. Blends of epoxidized alkyd resins based on *Jatropha* oil and the epoxidized oil cured with aqueous citric acid solution: A green technology approach. ACS Sustain Chem Eng 2015;3:261–268.

[34] SpasojevićP, PanićV, DžunuzovićJ, MarinkovićA, Woortman A, Loos K, et al. High performance alkyd resins synthesized from postconsumer PET bottles. RSC Adv 2015;5:62273–62283.

[35] Greimel KJ, Perz V, Koren K, Feola R, Temel A, Sohar C, et al. Banning toxic heavy-metal catalysts from paints: enzymatic cross-linking of alkyd resins. Green Chem 2013;15:381–388.

[36] Ong HR, Khan MMR, Ramli R, Rahman MW, Yunus RM. Tailoring base catalyzed synthesis of palm oil based alkyd resin through CuO nanoparticles. RSC Adv 2015;5:95894–95902.

[37] Dhoke SK, Sinha TJM, Khanna A. Effect of nano-Al_2O_3 particles on the corrosion behavior of alkyd based waterborne coatings. J Coat Technol Res 2009;6:353–368.

[38] Deyab M. Effect of carbon nano-tubes on the corrosion resistance of alkyd coating immersed in sodium chloride solution. Prog Org Coat 2015;85:146–150.

[39] Dhoke SK, Khanna A. Electrochemical impedance spectroscopy (EIS) study of nano-alumina modified alkyd based waterborne coatings. Prog Org Coat 2012;74(1):92-99.

[40] Dhoke SK, Khanna A. Effect of nano-Fe_2O_3 particles on the corrosion behavior of alkyd based waterborne coatings. Corros Sci 2009;51:6–20.

[41] Dhoke SK, Khanna A. Electrochemical behavior of nano-iron oxide modified alkyd based waterborne coatings. Mater Chem Phys 2009;117:550–556.

[42] Nikolic M, Barsberg S, Larsen FH, Löf D, Mortensen K, Sanadi AR. Mechanical characteristics of alkyd binder reinforced by surface modified colloidal nano silica. Prog Org Coat 2016;90:147–153.

[43] KurtİI, Acar I, GüçlüG. Preparation and characterization of water reducible alkyd resin/colloidal silica nanocomposite coatings. Prog Org Coat 2014;77:949–956.

[44] Dhoke SK, Bhandari R, Khanna A. Effect of nano-ZnO addition on the silicone-modified alkyd-based waterborne coatings on its mechanical and heat-resistance properties. Prog Org Coat 2009;64:39–46.

[45] Dhoke SK, Khanna A. Study on electrochemical behavior of nano-ZnO modified alkyd-based waterborne coatings. J Appl Polym Sci 2009;113:2232–2237.

[46] Dhoke SK, Khanna A, Sinha TJM. Effect of nano-ZnO particles on the corrosion behavior of alkyd-based waterborne coatings. Prog Org Coat 2009;64:371–382.

[47] Gumfekar S, Kunte K, Ramjee L, Kate K, Sonawane S. Synthesis of $CaCO_3$-P (MMA-BA) nanocomposite and its application in water based alkyd emulsion coating. Prog Org Coat 2011;72:632–637.

[48] Naik RB, Ratna D. Synthesis of silver nanoparticles embedded novel hyperbranched urethane alkyd-based nanocomposite for high solid antimicrobial coating application. J Coat Technol Res 2015;12:1073–1083.

[49] Naik RB, Jagtap S, Ratna D. Effect of carbon nanofillers on anticorrosive and physico-mechanical properties of hyperbranched urethane alkyd coatings. Prog Org Coat 2015;87:28–35.

[50] Murillo EA, Lopez BL, Brostow W. Synthesis and characterization of novel alkyd–silicone hyperbranched nanoresins with high solid contents. Prog Org Coat 2011;72:292–298.

Chapter 9

Preparation of Cu_2ZnSnS/Se_4 Thin Films from Oxide Precursors and its Prospect for Other Cu_2MSnS_4 Thin Films

Guilin Chen, Shuiyuan Chen and Zhigao Huang

Additional information is available at the end of the chapter

http://dx.doi.org/10.5772/63049

Abstract

In this chapter, the preparation of $Cu_2ZnSnSe_4$ (CZTSe) and Cu_2ZnSnS_4 (CZTS) thin films from oxide precursors was described. Such an oxides-based route is a low cost, facile way for the kesteries thin films. The rationality of applying oxides method into CZTSe and CZTS thin films was also clarified, including the reactive thermodynamics and annealing process. Finally, this oxide-based approach is also expected for the preparation of the other Cu_2MSnS_4 (M= Co^{2+}, Fe^{2+}, Ni^{2+}, Mn^{2+}) thin films.

Keywords: Cu_2ZnSnS/Se_4 thin films, oxides, annealing, oxide nanoparticles, Cu_2MSnS_4

1. Introduction

As the exponential growth of the conventional energy consumption, environmental pollution and greenhouse effect, human beings need to find and exploit renewable, clean energy e.g. solar energy. Solar cell is one of the effective routes to utilize solar energy. Such a green technology produces less effect on the environment and human health. The wide-scale use of clean, renewable solar energy requires a reduction in the manufacturing costs of solar panels. Thin film solar cells (TFSCs) can convert sunlight into electricity with much less material than conventional crystalline silicon solar cells, resulting in a potential for lower material cost. There are three main thin film photovoltaic (PV) technologies in the PV market, such as CdTe, $CuIn_xGa_{1-x}Se_2$ (CIGS), and Si thin film. However, Si TFSC shows low efficiency and instability from the Staebler–Wronski effect. As for CdTe and CIGS TFSC, they have been considered as the most promising material for TFSC due to respectable conversion efficiency and

their outdoor stability [1].But the above two compounds contain toxic or expensive materials such as Cd and In (Ga). These factors reduce the production capacity of the existing CdTe and CIGS technologies. Recently, Cu_2ZnSnS_4 (CZTS), Cu2ZnSnSe4 (CZTSe) and their solid solutions $Cu_2ZnSn(S_xSe_{1-x})_4$ (CZTSSe) have attracted significant attention owing to their interesting photoelectric properties [2, 3]. They have a tunable optical band gap ranging from 1.0 to 1.5 eV, a high absorption coefficient of 10^4 cm^{-1} and a suitable charge carrier concentrations ($5 \times 10^{15} \sim 6 \times 10^{16}$ cm^{-3}) [4-6]. All the constituents of CZTS-based thin films are rich on earth. The content of Zn and Sn are about 79 ppm and 2.2 ppm in the crust, which is about 1500 and 45 times the content of In respectively. As they consist of low-cost and readily available elements, they have high potential for mass production as solar absorber material [7, 8].Because of these optimal characteristics, 32.2% power conversion efficiency is expected for CZTS thin films solar cell, according to Shockley-Queisser theory [9]. Until now, the highest efficiency, which is up to 12.6%, has been obtained by adopting mixed sulfoselenide CZTSSe thin film as absorber layers, which was prepared from hydrazine solution [10].

There are many methods to prepare CZTS-based thin films. In this chapter, we will consider a low cost, facile, and green oxides-based route for absorber thin films in three parts. The first part, we will briefly review the deposition techniques of CZTS-based thin films. The second is a review on the oxides-based method for CZTS/CZTSe TFSC. The third part is the study of the possibility of applying such an oxide precursors method to prepare the other Cu_2MSnS_4 ($M = Co^{2+}$, Fe^{2+}, Ni^{2+}, Mn^{2+}) thin films. Meanwhile, the prospect for forming new type Cu_2MSnS_4 (i.e. M= Ba, Ca, Mg) will also be carried out.

2. Deposition techniques of CZTS thin films

To prepare absorber films for solar cell, such as CdTe and CIGS, many methods were developed. These different processes generally include evaporation, sputtering, electroplating, solution processing, and nanoparticles [11]. Due to the similar crystal structure and properties of CIGS thin films, most of the above techniques have been developed for the TFSCs-based CZTS absorber layers. The techniques for the deposition of CZTS thin films may be classified into two categories: vacuum (evaporation, sputtering) and non-vacuum based approaches (electroplating, solution processing, and nanoparticles) [12]. The development of the non-vacuum process for CZTS thin films can greatly reduce the production cost because they abandoned using expensive vacuum equipment.

2.1. Evaporation

Evaporation techniques are the most straightforward choice for preparing thin films due to the easy control of evaporation process by adjusting pressure and temperature. Meanwhile, this method has been successfully used to evaporate other absorber materials, and also provides better opportunity for fabrication of high quality thin film devices. Evaporation deposition routes can produce high uniform thin films, which also have a good reproducibility. Various evaporation technologies such as electron beam (EB), co-evaporation, fast evaporation, and thermal evaporation have been employed for the deposition of CZTS thin films [13-

15]. Recently, IBM has successfully fabricated CZTS TFSC by using the thermal evaporation method, which shows a high efficiency of 8.4% [16]. They adopted two step routes to deposit CZTS thin films. Firstly, the CZTS thin films were grown by thermal evaporation with elements Cu, Zn, Sn, and S. Secondly, the CZTS thin films were then annealed at 570°C for 5 min in air atmosphere. So far, this is the highest conversion efficiency reported for pure CZTS thin film based solar cells by using vacuum-based technique.

2.2. Sputtering

Sputtering is a conventional way for thin films 'growth in industry which have been successfully introduced in CIGS thin films. Typically, researchers used two steps to prepare high quality CZTS thin films [17]. The metallic precursors (Cu, Zn, and Sn) were firstly deposited in a stacking sequence, for example Cu–Zn–Sn/Cu–Zn–Sn–Cu or Cu–ZnS–SnS. The obtained metallic precursor was sequentially annealed under S vapor or H_2S atmosphere. The smooth CZTS thin films with high crystallinity can be achieve through the sputtering and post sulfurization method. A CZTS based TFSC with 6.7% efficiency had been fabricated by Katagiri et al using magnetron sputtered CZTS thin films, which showed Voc of 610 mV and Jsc of 17.9 $mA{\cdot}cm^{-2}$ with a filling factor of 0.62 [18].

2.3. Electroplating

Electroplating appears to be a promising technique for the low-cost, non-toxic solution preparation of semiconductors and was previously used in CdTe and CIGS TFSC. Similar to sputtering method, the common process of preparing CZTS thin films is known as two steps method: single step electrodeposition of precursors, followed by annealing at high temperature [19-21]. Shafaat Ahmed et al [22] have presented a high-performance CZTS TFSC by using the electrodeposition of metal stacks and the annealing of a CuZnSn precursor in a sulfur atmosphere. In their work, a champion electroplated CZTS solar cell achieves a power conversion efficiency of 7.3%, which is a record efficiency for electrodeposited CZTS TFSC [22].

2.4. Solution processing

Solution based coating technique is a very simple and low-cost route for the preparation of many thin films. This technique contains two steps: (I) preparation of precursor solution; (II) coating the precursor solution onto substrate to obtain desired thin films by using various wet coating methods (e.g. spin coating, drop casting, and doctor blade). The true solution mix chemical species in molecular level can enhance the homogeneity of chemical compositions. So a highly homogeneous CZTS thin film can be obtained by this method. Such solution precursors can broadly be sub-categorized as being: (1) metal salt based precursors; (2) organometallic precursors; (3) hydrazine-based precursors and related approaches. Comparing with other two methods, the hydrazine-related solution contains all required elements, but not extra elements (e.g. C, O, Cl) are included. After coating the solution on substrate, the precursor thin films were heated. During this process, hydrazine decomposes cleanly into N_2 and H_2 or NH_3 and H_2, facilitating good film morphology. By using this hydrazine-based approach, IBM have achieved a great energy conversion efficiency of CZTS TFSC (9.2%) [23].

2.5. Nanoparticles-based process

Nanoparticles-based processes use solid particles dispersed in a solvent to form an ink or slurry which can be coated onto a substrate. This offers an extremely materials-efficient method of depositing a thin-film precursor layer. Such a process is one of the successful non-vacuum approaches to formatting CIGS thin films, with variations employing particles composed of CIGS, oxides, metal, and binary selenide particulates as precursor. For example, CIGS TFSC showed an efficiency of 13.6% by using oxide nanoparticles-based process [24]. Nanosolar also reported 14% efficient cells by using mixed selenide nanoparticles and a single-stage annealing treatment [25]. Due to the similar structure and properties of CIGS thin films, the application of similar methods for CZTS thin films was widely studied. Most of the research focuses on the quaternary CZTS or binary-based process. Guo et al have fabricated CZTSSe TFSC with 9.6% efficiency from binary/ternary sulfide nanoparticles [26]. Those nanoparticles were synthesized by hot injection technique, which includes the injection of a cold solution of precursors into a hot surfactant solution (oleylamine) with the protection of inert gas. Such a complex process will increase production costs and be difficult to scale up, which needs to be solved before the commercialization of the CZTS solar cells [27]. Meanwhile, the nanoparticles capped with stabilizing molecules will be decomposed into carbon impurity, which will prohibit crystal growth in the CZTS film during thermal treatment [28].

On the other hand, coat oxide nanoparticles ink onto a substrate offers an extremely promising method for depositing a CIGS thin film precursor layer and such an approach led to CIGS solar cells with efficiencies of over 13.6% [24]. However, such a successful route in CIGS TFSC is rarely reported to be adopted in CZTS TFSC. The following sections will emphatically consider the deposition of oxides nanoparticles precursor layers for high quality CZTS and related materials CMTS (M = Co^{2+}, Fe^{2+}, Ni^{2+}, Mn^{2+}).

3. Oxides nanoparticles-based routes for CZTS/Se thin films

The reason for adopting oxide precursors for CZTS thin films can be claimed as following: (I) Preparation of oxide precursors is appealing because the published literature is full of information about synthesized method. (II) The stable oxides precursor is in favor of controlling the component of the final thin films during the sintering because oxides are stable against phase segregation during sintering. (III) Metal oxides are similar to metals in exhibiting a volume change during reactive conversion to a sulfide, due to S atom is larger than O atom. So the oxides-based method can lead to densification of the films.

Although there are so many advantages, oxide nanoparticles process is rarely reported. Washio et al fabricated 6% efficiency CZTS solar cell using oxide precursors by CVD [29]. However, as we know, CVD deposition process is complicated. Tang et al had reported a facile, low-cost route to fabricate CZTS thin films by sulfurization of the Cu–Zn–Sn composite oxides thin films [30]. This mixed oxide powder is prepared by the chemical co-precipitation of all metallic ions from solution. They have studied the effects of sulfurization temperature on the properties of the CZTS thin films. The resulted CZTS thin films show porous morphology and

http://dx.doi.org/10.5772/63049

an optical band gap about 1.35 eV. Such a CZTS thin films was applied in solar cells and showed a conversion efficiency of 1.22%. However, the chemical precipitation and sequential dry process may result in agglomeration of particles [31]. Meanwhile, the incorporation of organic binder in the ink also deteriorates the CZTS thin film during sulfurization treatment.

In our previous work, we tried to prepare $Cu_2ZnSnSe_4$ (CZTSe) thin films by the selenization of the oxide precursors [32]. This is exploration of applying the oxides-based approach into CZTSe thin films. To alleviate the hard agglomeration during the synthesis of oxide nanoparticles, a novel solvent-free (also called low temperature solid phase reaction) method was introduced to prepare oxides nanoparticles, as seen in **Figure 1**.

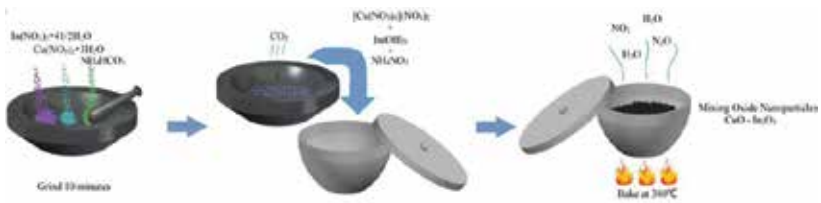

Figure 1. Illustrative diagram of oxide nanoparticles synthesis processes.

In a typical synthesis, the required amount of mixed nitrates and excess ammonium bicarbonate were mixed and reacted. The resulted mixture was then baked to obtain mixed oxide nanoparticles. During this heating process, those additional components were discharged as gases, leaving behind pure oxide nanoparticles. If the solvent free synthesis was properly extended, it would be also possible for the low cost and large-scale preparation of other mixed oxides nanoparticles for practical application. The XRD and SEM indicated that pure CZTSe thin films with micron-sized grains were obtained by selenization of the oxide precursors in our work, as shown in **Figure 2**. However, the films also were rough and porous.

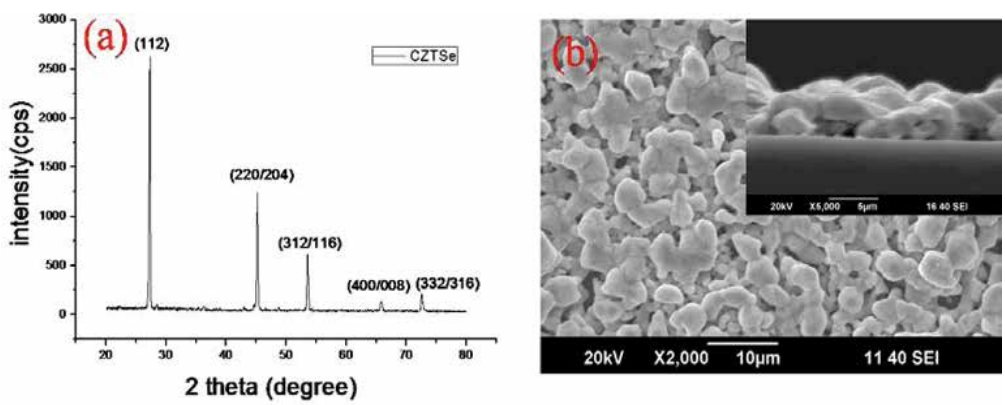

Figure 2. XRD patterns and morphology/cross-sections of CZTSe thin films.

It is well known that it is difficult to coat a uniform and dense precursor from nanoparticles, which is due to the irregular stacking of the nanoparticles. The rough and porous morphology of the precursor thin films will lead to corrosion of the back contact by excessive interaction with the sintering atmosphere. Therefore, before the heat treatment was carried out, the precursor must be densified. During the preparation of ceramic targets, the compression treatment was usually applied to obtain a compact green body [33]. Such an efficient method was introduced to compress the porous precursor thin films in the previous work, as shown in the **Figure 3**.

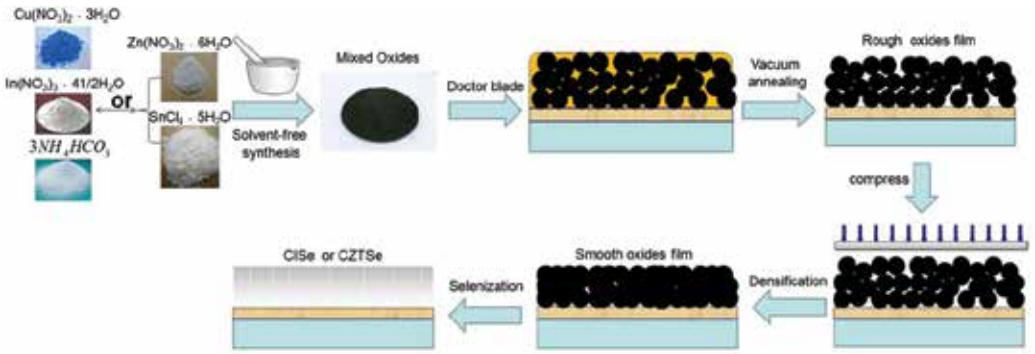

Figure 3. Schematic diagram of oxide-based CZTSe thin film fabrication processes [34].

Regardless of which coating technique, for example printing and spraying techniques as well as doctor blade and spin coating are used, to ensure that the technique is able to form porosity free thin films still exist with some difficulties. However, the density of precursor thin films is essentially improved after pressing. The introduction of compression in packing nanoparticles obviously has a beneficial effect on densification, which helps to achieve a sintered thin film with high quality. It is due to that, that the compact density significantly affects the phase transition during the selenization. The nucleation and growth of CZTSe or CZTS phase are considered to be facilitated by the mass transfer around the particle contacts.

To convert the oxides precursor into CZTSe or CZTS thin films, selenization or sulfurization was carried out respectively. Se or S sources were used to replace toxic H_2S and H_2Se gas. During the annealing process, oxides were translated into binary sulfide or selenide. Finally, the intermediate binary would react with each other under high temperature. According to references, such a conversion can generally be expressed as the following two routes:

$$2CuS + ZnS + SnS \xrightarrow{Annealing} Cu_2ZnSnS_4 \quad (1)$$

$$2CuS + SnS \xrightarrow{Annealing} Cu_2SnS_3 \quad (2)$$

http://dx.doi.org/10.5772/63049

$$Cu_2SnS_3 + ZnS \xrightarrow{Annealing} Cu_2ZnSnS_4 \quad (3)$$

For the first reaction path, the CZTS phase was directly obtained though reacting with each other. The moment product Cu_2SnS_3 was formed, it will react with ZnS. As shown in the **Figure 4**, all the XRD data confirmed the formation of CZTSe or CZTS by annealing the oxide precursors. Through comparing the pressured CZTSe and unpressed CZTSe thin films, it was found that the compression can effectively improve the crystallite of the CZTSe thin films. The study of the effect of annealing temperature on the CZTS thin films revealed the process of CZTS crystal growth. It was found that the order of stability of oxides was: SnO_2> ZnO > CuO. The moderate stability of SnO_2 can reduce the loss of Sn through evaporation of SnS [35].

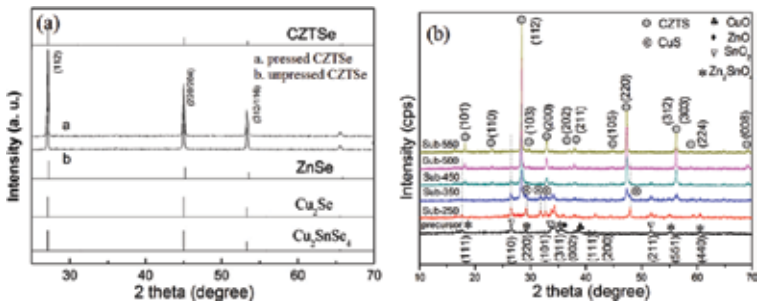

Figure 4. XRD patterns of oxide nanoparticles-based CZTSe (pressed and unpressed CZTSe) and CZTS under different sulfurization temperature) thin films [36, 37].

XRD is generally considered as the main tool to analyze the structure of such compounds, but it is difficult to identify most of the minors phases and the possible secondary phase with similar crystal structure, for example, $Cu_2SnS(e)_3$, CuS(e), ZnS(e), or $SnS(e)_2$. Raman scattering is a useful complimentary technique to detect the presence of secondary phases. Raman results (**Figure 5**) again distinguished the formation of pure CZTSe or CZTS thin films from oxide precursors.

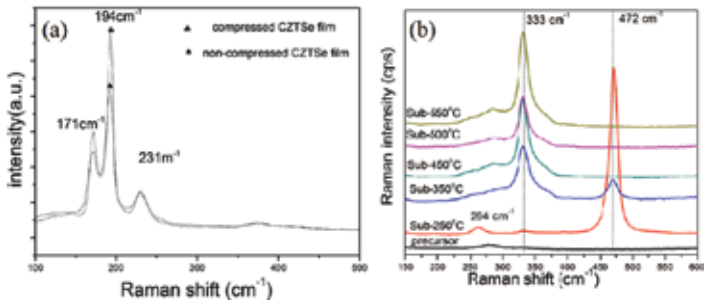

Figure 5. Raman patterns of oxide nanoparticles-based CZTSe (pressed and unpressed CZTSe) and CZTS (under different sulfurization temperature) thin films [36, 37].

The oxides-based CZTSe thin films showed a smooth film with very large grain. Many grains indeed extended across the entire thickness of the film from the cross-sectional SEM (**Figure 6(a)**). However, the pure sulfur CZTS thin films presented small grain size indicating poor crystalline. As we know, the large amount of grain boundary resulted from small grain size will deteriorate the performance of CZTS TFSC.

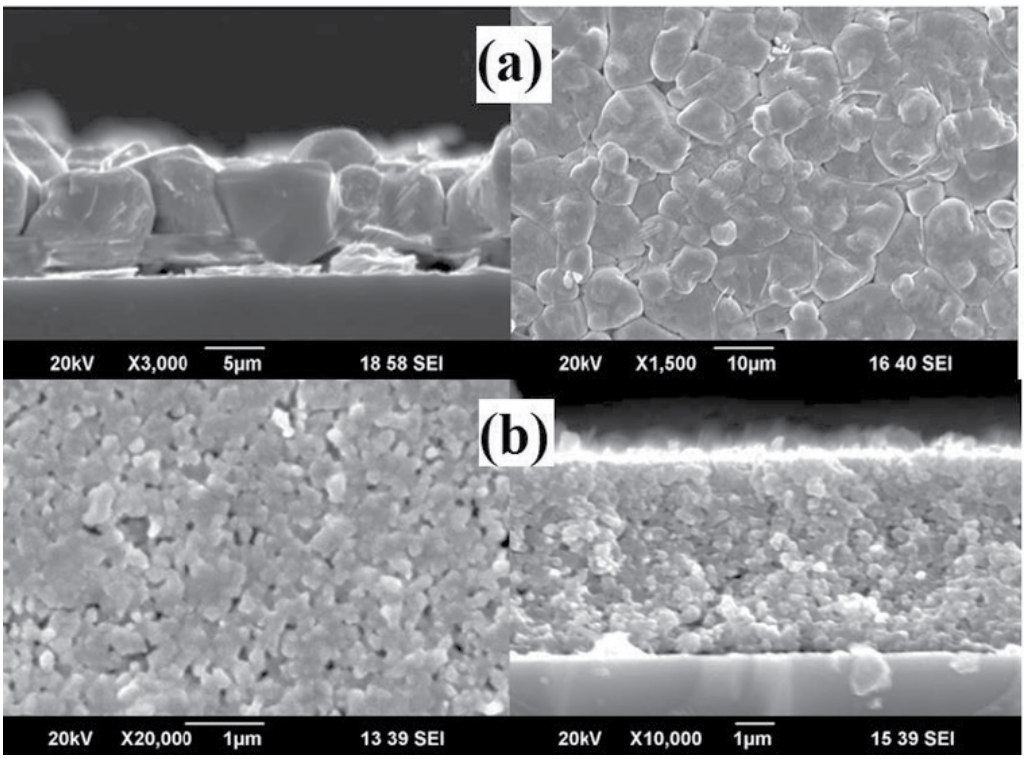

Figure 6. Morphology and cross-sections of oxide nanoparticles-based (a) CZTSe and (b) CZTS thin films [36, 37].

Grain growth is the key challenge for the preparation of pure sulfide CZTS thin films with large grain during annealing, due to the lack of suitable fluxing agent. The high thermal energy is expected to supply driving force for grain growth. As shown in the **Figure 7**, the crystal quality of CZTS thin films were improved significantly by using relatively high sulfurization temperature. The high quality CZTS thin films were comparable with the CZTS thin films prepared by the vacuum-based method. However, such high quality CZTS thin films did not produce CZTS TFSC with high conversion efficiency. From the J-V characteristics of CZTS TFSC (red curve of **Figure 8**), it can be seen that CZTS device prepared by sulfurizing oxide precursors at high temperature achieves a high Voc, but low Jsc. As the oxide precursors suffered from high temperature sulfurization, the sulfur gas with high activity and pressure will erode Mo back electrode. The thick MoS_2 layers with high resistance were formed during this high temperature sulfurization process, which sequentially reduce Jsc and FF.

http://dx.doi.org/10.5772/63049

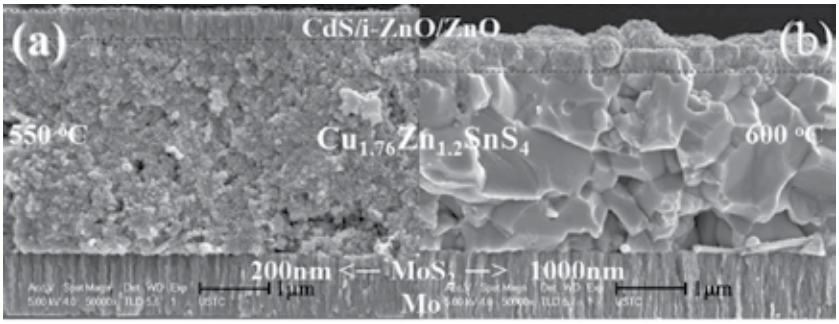

Figure 7. Cross-sectional SEM micrographs of photovoltaic devices using oxide nanoparticles-based CZTS thin films annealed under (a) 550°C and (b) 600°C [37].

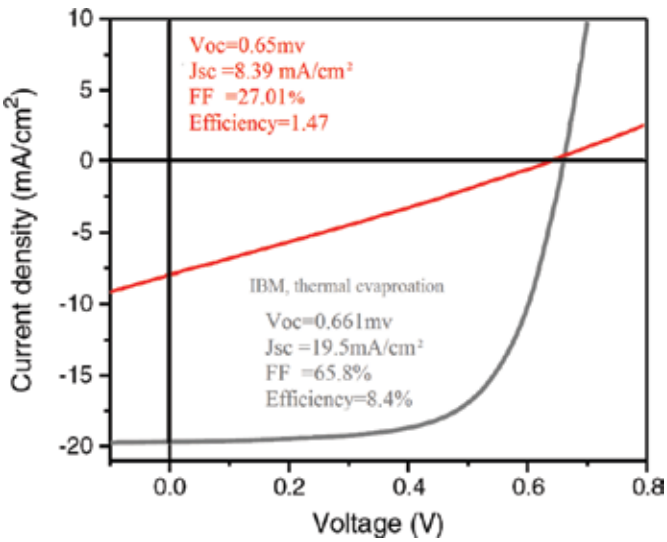

Figure 8. J-V characteristics of oxide-based CZTS TFSC and thermal evaporation based CZTS TFSC.

Such a similar phenomenon was also observed by Jin et al [38], they developed a novel combustion method for CZTS TFSC. The probable formation mechanism of oxide precursors drive CZTS thin films during the sulfurization process is analyzed. The preparation process is similar to our oxides-routes, excluding the synthesis of oxide nanoparticles. A relatively low efficiency of 1.6% was also obtained in their work, the resulted CZTS device present Voc of 505 mV, Jsc of 10.5 mA/cm^2 and FF of 30.3%. The thickness of MoS_2 layer was 1.4 μm in their work, which markedly deteriorate the performance of CZT TFSC.

In a word, the oxide nanoparticles-based method showed a great potential for preparation of CZTSe and CZTS thin films with high quality, which is expected to reduce the cost of production. However, a lot of efforts still need to be made to fabricate oxide nanoparticles-based CZTSe and CZTS thin films solar cell with high efficiency.

4. A general, low cost oxide nanoparticles routes for preparation of Cu_2MSnS_4 (M =Co^{2+}, Fe^{2+}, Ni^{2+}, Mn^{2+}) thin films

Besides CZTSe and CZTS, other earth abundant $Cu_2(X^{II})(Y^{IV})(S, Se)_4$ (X^{II} = Mn, Fe, Co, Ni, Cd, Hg; Y^{IV} = Si, Ge, Sn) chalcogenide semiconductor recently have caused widespread interest in the TFSCs because of their analogous structures to CZTSe and CZTS, suitable direct band gaps, and high absorption coefficients [39]. As Cd and Hg element are high toxic, the other quaternary Cu_2MSnS_4 (M = Co^{2+}, Fe^{2+}, Ni^{2+}, Mn^{2+}) compounds are supposed to be important potential solar cell materials. Recently, there are some reports on the synthesis of Cu_2CoSnS_4, Cu_2FeSnS_4, Cu_2NiSnS_4 and Cu_2MnSnS_4 compounds. Zhang et al [40] have reported the synthesis of monodisperse Cu_2CoSnS_4 nanocrystals with wurtzite phase by using a simple solution-based method. The wurtzite Cu_2CoSnS_4 nanocrystals can be obtained in a certain temperature range. The band gap of wurtzite Cu_2CoSnS_4 nanocrystals is determined to be 1.58 eV, which suggest the potential use of Cu_2CoSnS_4 as an active layer in low-cost thin-film solar cells. Murial et al [41] also presented a sol-gel solution routes for Cu_2CoSnS_4 thin films. The Cu_2CoSnS_4 thin films with larger grains have textured structures of stannite phase. Kamble et al [42] have synthesized Cu_2NiSnS_4 nanoparticles via hot injection. Phase transition of Cu_2NiSnS_4 was observed from wurtzite phase to cubic phase by changing the solvent. The obtained band gap (1.4 eV) and photo response behavior under illumination suggests Cu_2NiSnS_4 to be the potential absorber material for TFSCs. Cui et al [43] have reported the preparation of quaternary semiconductor Cu_2MSnS_4 (M = Co^{2+}, Fe^{2+}, Ni^{2+}, Mn^{2+}) nanocrystals through solvothermal method. The four types of nanocrystals exhibit significantly different morphology, but have similar band gaps in the range of 1.2-1.5 eV. Oze [44] have also reported the fabrication and characterization of earth-abundant quaternary semiconductor Cu_2MSnS_4 (M = Fe, Co, Ni, and Mn) nanofibers. Recently, Li et al [45] have reported the fabrication of Cu_2MSnS_4 (M= Zn, Cd, Mn) thin films from stacked layers by CBD-annealing route. Such a simple and low cost route is proposed for large-scale preparation of multi-elements TFSC.

As described above, the oxide nanoparticles process is one of the successful approaches to synthesize CIGS/CZTSe/CZTS. The electro negativity of Co, Fe, Ni, and Mn are about 1.88, 1.83, 1.91, and 1.55 respectively, which was also close to that of Zn (1.65). From the aspect of electro negativity, the Co, Fe, Ni, and Mn elements can be theoretically replaced by Zn element. Therefore, oxides based route is also regarded as an extremely promising method for the deposition of Cu_2MSnS_4 (M = Co^{2+}, Fe^{2+}, Ni^{2+}, Mn^{2+}) thin films. The oxide nanoparticles precursor can be synthesized by solvent free method. During the sequential sulfurization, the relative stable oxide can reduce the loss of elements. Therefore, the expanding of our earlier work that is called “low cost oxide ink for CIGS/CZTSe/CZTS thin films solar cell” is expected to prepare low cost, high quality Cu_2MSnS_4 (M = Co^{2+}, Fe^{2+}, Ni^{2+}, Mn^{2+}) thin films.

Except the above quaternary semiconductors Cu_2MSnS_4 (M = Zn^{2+}, Co^{2+}, Fe^{2+}, Ni^{2+}, Mn^{2+}), a class of I_2-II-IV-VI_4 can be designed. Through element-substitution, a series of quaternary semiconductors had been synthesized, for example, I_2-II-IV-VI_4 with I = Cu, Ag, II = Zn, Cd, IV = Si, Ge, Sn, Pb, and VI = S, Se, were designed as early as 1960s [46]. Recently, Wang et al [47] have evaluated the thermodynamic stability limit and chemical trend in kesterite-structured I_2-II-

IV-VI_4 semiconductors. Using the first-principles calculations, they found that I_2-II-IV-VI_4 with I = Cu, Ag, II = Zn, Cd, Hg, IV = Si, Ge, Sn, and VI = S, Se, Te are stable quaternary compounds, however those with II = Mg, Ca, Sr, Ba, IV =Ti, Zr, Hf, and VI = O are unstable on account of the phase separate into the competing binary and ternary compounds [47]. As shown in the **Table 1**, the calculated energy change of reaction of I_2-II-IV-VI_4 compound is exothermic ($\Delta E < 0$), implying that the phase separation of Cu_2IISnS_4 (II = Mg, Ca, Sr, Ba) will occur spontaneously. Therefore, I_2-II-IV-VI_4 with II = Zn, Cd, Hg, those with II = Mg, Ca, Sr, Ba are unstable from a thermodynamic perspective. It's worth noting that the above calculation is based on the equilibrium state, but the annealing process is always carried out under the high sulfur vapor pressure. The high sulfur vapor pressure may promote the reaction and avoids the phase separation of Cu_2IISnS_4. Therefore, we propose preparation of some new type Cu_2IISnS_4 (II = Mg, Ca, Sr, Ba) from oxide nanoparticles precursor in the future. The advantages of oxides-based routes will be integrated in those new compounds.

Compd.	Phase separation		Compd.	Phase separation	
	$Cu_2S+ZnS+SnS_2$	0.56		$Cu_2S+MgS+SnS_2$	0.47
Cu_2ZnSnS_4	2CuS+ZnS+SnS	0.40	Cu_2MgSnS_4	2CuS+MgS+SnS	0.31
	Cu_2SnS_3+ZnS	0.08		Cu_2SnS_3+MgS	-0.01
	$Cu_2+CdS+SnS_2$	0.51		$Cu_2S+CaS+SnS_2$	-0.23
Cu_2CdSnS_4	2CuS+CdS+SnS	0.35	Cu_2CaSnS_4	2CuS+CaS+SnS	-0.39
	Cu_2SnS_3+CdS	0.03		Cu_2SnS_3+CaS	-0.71
	$Cu_2S+HgS+SnS_2$	0.56		$Cu_2S+SrS+SnS_2$	-0.35
Cu_2HgSnS_4	2CuS+HgS+SnS	0.37	Cu_2SrSnS_4	2CuS+SrS+SnS	-0.51
	Cu_2SnS_3+HgS	0.08		Cu_2SnS_3+SrS	-0.83
				$Cu_2S+BaS+SnS_2$	-0.48
			Cu_2BaSnS_4	2CuS+BaS+SnS	-0.64
				Cu_2SnS_3+BaS	-0.97

Table 1. Calculated energy change ΔE (in eV/formula unit) of different phase-separation reactions of Cu_2-Π-SnS_4 (Π=Zn, Cd, Hg, and Mg, Ca, Sr, Ba) [47].

5. Remarks and conclusions

The rapid development of low-cost, abundant CZTSe/CZTS TFSC has aroused wide concern among the researchers. Out of the many possible technical solutions available for preparation of CZTSe/CZTS thin films, oxide nanoparticles based route is considered as one of low cost, facile, and green technologies. As the successful application of such an oxides-based route on CIGS thin films solar cells, it has also been successfully explored to fabricate CZTSe/CZTS thin films with high quality. This oxides-based route is appropriate deposition techniques in terms

of low production cost and high quality thin films. Also, the application perspectives of oxides nanoparticle-based for other Cu_2MSnS_4 ($M = Co^{2+}, Fe^{2+}, Ni^{2+}, Mn^{2+}$) thin films are also promising because of similar structure and element electro negativity, comparing CZTSe/CZTS thin films. What is more, the unstable Cu_2IISnS_4 (II = Mg, Ca, Sr, Ba) in thermodynamic perspective is expected to be synthesized under the high sulfur vapor pressure. In order to further develop the oxides-based CZTSe/CZTS or other Cu_2IISnS_4 compound, CIGS TFSC technology and related technologies can be transferred to the research of CZTSe/CZTS TFSC technology due to the great similarity between these two materials.

Acknowledgements

We acknowledge the financial support from National Natural Science Foundation of China (Grant No. 51502037), Natural Science Foundation of Fujian Province, China (Grant No. 2015J05096).

Author details

Guilin Chen*, Shuiyuan Chen and Zhigao Huang

*Address all correspondence to: glchen@fjnu.edu.cn

Fujian Provincial Key Laboratory of Quantum Manipulation and New Energy Materials, College of Physics and Energy, Fujian Normal University, Fuzhou, China

References

[1] M. Kemell, M. Ritala, M. Leskela, Crit. Rev. Solid State Mater. Sci. 30 (2005) 1–31.

[2] Z.Q. Li, J.H. Shi, Q.Q. Liu, Y.W. Chen, Z.Sun, Z.Yang, S.M. Huang, Nanotechnology 22 (2011) 265615.

[3] C. Wadia, A.P. Alivisatos, D.M. Kammen, Environ. Sci. Technol. 43 (2009) 2072–2077.

[4] H. Katagiri, N. Sasaguchi, S. Hando, S. Hoshino, J. Ohashi, T. Yokota, Sol. Energy Mater. Sol. Cells 49 (1997) 407–414.

[5] J.S. Seol, S.Y. Lee, J.C. Lee, H.D. Nam, K.H. Kim, Sol. Energy Mater. Sol. Cells 75 (2003) 155–162.

[6] N. Kamoun, H. Bouzouita, B. Rezig, Thin Solid Films 515 (2007) 5949–5952.

[7] T.M. Friedlmeier, H. Dittrich, H.W. Schock, The 11th Conference on Ternary and Multinary Compounds, ICTMC-11, Salford, 8–12 September 1997, pp. 345–348.

[8] H. Katagiri, N. Ishigaki, T. Ishida, K. Saito, Jpn. J. Appl. Phys. 40 (2001) 500.

[9] W. Shockley,H. J. Queisser, Jpn. J. Appl. Phys. 32 (1961) 510–519.

[10] W. Wang, M.T. Winkler, O. Gunawan, T. Gokmen, T.K. Todorov, Y. Zhu, D.B. Mitzi, Adv. Energy Mater. 4 (2014) 1301465.

[11] C.J. Hibberd, E. Chassaing, W.Liu, D.B. Mitzi, D. Lincot, A.N. Tiwari, Prog. Photovolt: Res. Appl. 18 (2010) 434–452.

[12] M.P. Suryawanshi, G.L. Agawane, S.M. Bhosale, S.W. Shin, P.S. Patil, J.H. Kim, A.V. Moholkar, Mater. Technol. 28 (2013) 98–109.

[13] H. Araki, A. Mikaduki, Y. Kubo, T. Sato, K. Jimbo, W.S. Maw, H. Katagiri, M. Yamazaki, K. Oishi, A. Takeuchi, Thin Solid Films 517 (2008) 1457–1460.

[14] T. Kobayashi, K. Jimbo, K. Tsuchida, S. Shinoda, T. Oyanagi, H. Katagiri, Jpn. J. Appl. Phys. 44 (2005) 783–787.

[15] B.A. Schubert, B. Marsen, S. Cinque, T. Unold, R. Klenk, S. Schorr, H.W. Schock, Prog. Photovolt: Res. Appl. 19 (2011) 93–96.

[16] B. Shin, O. Gunawan, Y. Zhu, N.A. Bojarczuk, S.J. Chey, S. Guha, Prog. Photovolt: Res. Appl. 21 (2013) 72–76.

[17] P.A. Fernandesa, P.M.P. Saloméa, A.F. da Cunha, Thin Solid Films 517 (2009) 2519–2523.

[18] H. Katagiri, K. Jimbo, S. Yamada, T. Kamimura, W.S. Maw, T. Fukano, T. Ito, T. Motohiro, Appl. Phys. Express. 1 (2008) 041201.

[19] S.M. Pawar, B.S. Pawar, A.V. Moholkar, D.S. Choi, J.H. Yun, J.H. Moon, S.S. Kolekar, J.H. Kim, Electrochim. Acta 55 (2010) 4057–4061.

[20] A. Ennaoui, M. Lux-Steiner, A. Weber, D. Abou-Ras, I. Kötschau, H.W. Schock, R. Schurr, A. Hölzing, S. Jost, R. Hock, T. Voؚ J. Schulze, A. Kirbs, Thin Solid Films 517 (2009) 2511–2514.

[21] R. Schurr, A. Hölzing, S. Jost, R. Hock, T. Voβ, J. Schulze, A. Kirbs, A. Ennaoui, M. Lux-Steiner, A. Weber, I. Kötschau, H.W. Schock, Thin Solid Films 517 (2009) 2465–2468.

[22] S. Ahmed, K.B. Reuter, O. Gunawan, L. Guo, L.T. Romankiw, H. Deligianni, Adv. Energy Mater. 2 (2012) 253–259.

[23] H. Hiroi, N. Sakai, T. Kato, H. Sugimoto, Proceedings of the 39th IEEE Photovoltaic Specialists Conference (PVSC). (2013) 0863–0866.

[24] V.K. Kapur, A. Bansal, P. Le, O.I. Asensio, Thin Solid Films 53 (2003) 431–432.

[25] D.J. Jvan, D. Jackrel, F. Jacob, C. Leidholm, A. Pudov, M. Robinson, Y. Roussillon, Conference Record of the Seventeenth International Photovoltaic Science and Engineering Conference 2007; Fukuoka, Japan.

[26] Q. Guo, Y. Cao, J.V. Caspar, W.E. Farneth, A.S. Ionkin, L.K. Johnson, M. Lu, I. Malajovich, D. Radu, K.R. Choudhury, H.D. Rosenfeld, W. Wu, PVSC 134(2012) 15644.

[27] K. Woo, Y. Kim, J. Moon, Energy Environ. Sci. 5(2012) 5340–5345.

[28] O. Zaberca, F. Oftinger, J.Y. Chane-Ching, L. Datas, A. Lafond, P. Puech, A. Balocchi, D. Lagarde, X. Marie, Nanotechnology 23 (2012) 185402–185413.

[29] T. Washio, T. Shinji, S. Tajima, T. Fukano,T. Motohiro, K. Jimbo, H. Katagiri, J. Mater. Chem. 22 (2012) 4021–4024.

[30] D. Tang, Q. Wang, F. Liu, L. Zhao, Z. Han, K. Sun, Y. Lai, J. Li, Y. Liu, Surf. Coat. Tech. 232 (2013) 53–59.

[31] G. Chen, G. Jiang, W. Liu, X. Chen, C. Zhu, Appl. Surf. Sci. 258 (2012) 3428–3432.

[32] G. Chen, L. Jin, W. Liu, G. Jiang, C. Zhu, Adv. Mater. Res. 418–420 (2012) 597–601.

[33] A. Moure, J. Tartaj, C. Moure,Synthesis, J. Eur. Ceram. Soc. 29 (2009) 2559–2565.

[34] G. Chen, B. Pan, L. Jin, G. Jiang, W. Liu, C. Zhu, J. Alloys Compd. 610 (2014) 20–26.

[35] X. Yin, H. Gong, Acta Materialia 60 (2012) 6732–6741.

[36] G. Chen, W. Liu, G. Jiang, B. Pan, C. Zhu, Solar Energy 92 (2013) 172–175.

[37] G. Chen, C. Yuan, J. Liu, Z. Huang, S. Chen, W. Liu, G. Jiang, C. Zhu, J. Power Sources 276 (2015) 145–152.

[38] X. Jin, J. Li, G. Chen, C. Xue, W. Liu, C. Zhu, Sol. Energy Mater. Sol. Cells 146 (2016) 16–24.

[39] Y. Cui, R. Deng, G. Wang, Da. Pan, J. Mater. Chem. 22 (2012) 23136–23140.

[40] X. Zhang, N. Bao, B. Lin, A. Gupta, Nanotechnology 24 (2013) 105706.

[41] B. Murali, M. Madhuri, S.B. Krupanidhi, Cryst. Growth. Des. 14 (2014) 3685–3691.

[42] A. Kamble, K. Mokurala, P. Bhargava, S. Mallick, PVSC 10 (2015) 7356378.

[43] Y. Cui, R.P. Deng, G. Wang, J. Mater. Chem. 22 (20123) 23136–23140.

[44] F. Ozel, J. Alloys Compd. 657 (2016) 157–162.

[45] J. Li, Y. Wang, G. Jiang, W. Liu, C. Zhu, Mater. Lett. 157 (2015) 27–29.

[46] B. R. Pamplin, Nature 188 (1960) 136.

[47] C. Wang, S. Chen, J.H. Yang, L. Lang, H.J. Xiang, X.G. Gong,A. Walsh, S.H. Wei, Chem. Mater. 26 (2014) 3411–3417.

Chapter 10

Friccohesity and Tentropy: New Models of Molecular Sciences

Man Singh

Additional information is available at the end of the chapter

http://dx.doi.org/10.5772/62240

Abstract

Understanding and developing new molecules in chemical sciences have been great thrust areas of research, not only to develop new synthetic methods or reaction mechanisms of new and greener experimental conditions but also to know what are the new molecule science and what are the new models which can track their new role in chemical processes and also their applications in allied interdisciplinary sciences. The SAR (structure-activity relationship) and STAR (structure-thermodynamics activity relationship) have been the most intimate theories in understanding and finding unique applications of the new molecules. Initially, simple molecules are the focus; however, proteins, hemoglobin, starch, and certain metallic complexes are also in the focus but as natural chemicals; but for past few decades, a lot of focus has been on synthesizing new complex molecules to make them suitable for varieties of applications such as solar, catalysts, biosensors, and others. Hence, it has been essential for focusing on structural sciences of the chemical substances. Dendrimers have been the invention of 1990s in the areas of biocomplexes, biomaterials which are hot thrust areas in molecular interaction engineering to focus on intramolecular potential for industrial applications. Thus, the molecule's internal structure signifies the various scientific components for playing or making their best use in materials sciences, semiconductor, spintronics, photonics, electronics, etc. Therefore, the molecule's interacting response with other molecules becomes cohesive or kinetic in nature or whether it induces structuredness or weakens the binding forces and allows more and more kinetic movement or the motion is noted or defined by friccohesity as it is expressed as frictional and cohesive forces. Thus, the friccohesity is a dual forces theory which deals with frictional and cohesive forces together and determined with Survismeter using Mansingh equation molecules [1–3].

Keywords: interaction engineering, friccohesity, intramolecular multiple forces theory, molecular dynamics, structure breaking and making, molecular motions

1. Introduction

Thereby, the friccohesity explains negative and positive deviations quantitatively, solvent structure breaking and making mechanism of the solute molecules based on the effective solvent binding in a most structured manner. If on adding solute the cohesive forces of the solvents undergo drastic decrease, i.e., the hydrogen bonds of the similar molecules are broken to the larger extent by the solute, then the cohesive force of the solvent is weakened. The weakening has been credited to an effective engagement of the solvent within 10 to 40 KJ mol^{-1}energy involvements. In this process, the solute molecules are able to dissolved in the bulk of the solvent, but when no solvent hydrogen bonding is broken then the solute is not dispersed or dissolved. For example, when oil is added in water, no cohesive forces of either is broken and no dispersion or dissolutions occurs. When cohesive forces are weakened or transformed into kinetic forces in binding or surrounding solute molecules, then the functionalization of cohesive forces into kinetic forces through frictional forces occurs. The solute molecules move in the bulk of the solvent despite structural resistance of the solvent molecules. Thereby, in this process the cohesive forces are mutually transformed into frictional forces, so the product of cohesive force and frictional forces is noted as friccohesity determined by pendant drop numbers where cohesive forces are demonstrated and the viscous flow times where the frictional forces are demonstrated. In these both measurements, the survismeter with similar dimension is used. It has been noticed that such situation is complicated in case of giant-like proteins, supramolecules such as calixarene, and smart molecules such as dendrimers where many local interacting sites exist; and rather than interaction with the outer surface of the molecule, they interact mutually within the molecules.

1.1. Quantitative magnitude of friccohesity

Such intramolecular interacting activities initiation induces numerous intramolecular motions having several isotropic phases or several self-assemblies of sites with definite order of their motions [3–5]. Thereby, the molecule is active and involve in intramolecular entropy similar to intramolecular hydrogen bonding, and such state of the activities within a single molecule are noted as tentropy. Thus, the multiple molecular factors or forces working inside the molecule are defined as intramolecular multiple forces theory (IMMFT). The IMMFT enables generation of several energy states which are expressed when FTIR is recorded, because the FTIR is direct data which track the integrated motions of intrinsic energy states subtle as an interacting site. In the processes of tentropy and IMMFT, the friccohesity plays a controlling role because each interacting site has its own cohesive force which could be oscillating on the infinitesimal mode but maintain the cohesivity along with oscillation with definite reversible forces or the frictional forces. Several forces like van der Waals, Lenard Jones potential, London dispersive forces, Columbic forces have been operational at an infinitesimal scale. Therefore, the book is aimed to deal with such sciences developing new theories and new examples with detailed explanation and insight of the intramolecular activities. Several peculiar sciences of intramolecular and intermolecular forces leading to have an overall effect could be incorporated in the book so that the book is

http://dx.doi.org/10.5772/62240

able to give a transparent, innovative, new and novel science of liquid mixtures to the readers. Currently, the significance of such sciences is enhanced because of the focus on individual molecules in interdisciplinary sciences. For example, why the expressions of the molecular forces in the form of meniscus are shown only on the air-liquid surfaces in case of the liquids, probably it indicates a state of the cohesive force in case of solvent or liquid mixtures. If an example of pure liquid solvent is considered, then the molecular force factors inside the liquid phase or the bulk phase are cancelled out as the similar molecules are in the bulk. There may also be a possibility that the interfacial forces are either cancelled out or optimized in bulk, but these forces are active at the surfaces only where there are interfaces of air and liquid. However, these expressions are the outcome of interfacial molecular arrangement of the molecular forces, and hence there seems to be a natural need to deal with or to study the molecular forces, taking their accurate account in bulk where the optimizing activities work and also at interfaces where partial optimization has taken place. Hence, the friccohesity has been considered along with tentropy and IMMFT authentic vibrant physicochemical parameters to depict a state of intramolecular as well as intermolecular forces.

1.2. Interdependence of friccohesity and tentropy

There are several examples where these parameters operate like vaporization though it is a surface phenomenon but very much affected by the internal arrangements of the atomic, electronic, electrostatic forces, responsible for resulting molecular force factors. Since the molecules in the bulk are under equally distributed energy function and equilibrium in terms of their binding force and no Brownian motion works, it becomes a kind of stationary waves till the parameters like temperature, pressure, additives are added. It could trigger forces like van der Waals, LDF (London dispersive forces based on redistribution of sigma bond electrons in alkyl chain), and Lennard Jones potential keep maintaining the equilibrium inside the bulk phase. Hence, it matters that how the molecules behave in the bulk due to their shared electron pair clouds, but on a surface such vacancy exists as the partial optimization occurs, and because of the interface structures the air phase cannot accommodate the vacant force factors at the interfaces. Since the force factors are nothing but the electron clouds that despite mixing or sharing do maintain their thin boundary or better to say that the electrons of one atom of molecules do not leave to another atom during the interaction except sharing electron clouds, but even certain pairs of the solvent molecules do not share their electrons also like oil and water on benzene and water so they form or constitute liquid-liquid interface or the soft boundaries or also the movable boundaries similar to the shape and size of the liquid state materials, contrary to the solid-state materials like ethylene (gas) and polyethylene (solid state). Also the solid iodine sublimates into gas form directly as of ammonium chloride. Thus, there is an urgent need to maintain the structural identity of the molecules, because later they have to perform functions like drugs, catalysts, hormones, enzymes, etc. Contrary to the surfaces phenomenon, the melting points, freezing points are deep processes taking place only in the bulk phase that starts from bottom whereas evaporation, surface tension, etc. occur on the surfaces where only the partial optimiza-

tion works, but in case of MP (melting point), azeotropic, hydrated complexes and FP (freezing points) initiate from the bottom of the containers.

Thus, it is seen that the highly polar molecules freeze at lower temperature but weakly polar at the higher temperature because of their kinetic energy as the weakly polar molecules do have weaker cohesive forces and keep colliding so to bring them to a solid form needs more and more cooling and so are solidified at very low temperature, such as nitrogen, which solidifies at less than −200°C. So, the N_2 gas has weaker cohesive forces and stronger frictional or kinetic forces. For example, the water having 91.97 mN/m surface tension gets evaporated at100°C, but ethanol with 22.6 mN/m gets evaporated at 78°C. The water has dipolar structures with van der waals forces, but the ethanol also has hydrophobic shorter alkyl chain that does not allow much or stronger IMF in the bulk and its outcome is noticed or extended to the surface with 22.7 and 78 data. For making bulk phase most active heating, mechanical stirring or chemical additives are used so that the unequal distribution of the internal potential could be generated. Why is it so? Because the new chemical additives, on heating or mechanical pressure, destabilize the equal distribution of the molecular force factors (MFF) where they become haphazardly distributed or unaligned. It is noted that anisotropy state of the MFF make bulk phase active similar to the activities at ALI (air-liquid interfaces).

2. Constitutional framework of friccohesity and tentropy

Thus, an interesting science exists between the activities of the bulk and air phases because of the different structures at the surfaces, thus it becomes a most interesting thermodynamics, kinetics of reorientation of MFF, because of creating different molecular structures of disordered motions in different directions so that the MFF becomes irregular in state.

2.1. Distribution of molecular forces

Such forces structurally affect the velocity gradient on viscous flow like $\partial u/\partial y$, where u is velocity cm/sec and y is distance (cm, nm) on y axis. Thus, it becomes similar to the phase as amorphous substances where each phase does have specific heat capacity and then show different expressions, and hence the linear and nonlinear viscous flows are generated in fluid dynamics and mechanics. The linear or laminar flow is easily explained because of an additive effective but a nonlinear flow predicts some structural transitions caused due to dissolution, association, aggregation, coalescence, or others. These changes alter the molecular behaviour during capillary flow with certain variability where a degree of variation is determined with the magnitude of the friccohesity data. Therefore, in case of plate theory it is assumed that the unit area of rigid solid wall applies opposing forces F on the laminar layer formed when the Newtonian liquid is permitted to flow. It becomes a best example of frictional forces because the molecules of the liquid contained in the unit area of the laminar layer want to go ahead but the opposing forces of the rigid wall counteract them. Ultimately, facing opposition of the opposing forces the molecules succeed in crossing over such hur-

http://dx.doi.org/10.5772/62240

dle because the frictional forces were weaker and could not stop flowing. However, it becomes most prominent when the liquid of high viscosity is permitted to flow, it is seen when the hard liquid flows down, for example, honey whose viscosity is about 2000 cP or mPa.s, which does not flow within the capillary of smaller id (inner diameter) because the F is stronger, and hence we need some space where less F is applied; otherwise, it becomes impossible to measure their viscosity.

In case of highly viscous liquids such as honey and glycerol, which have 1490 cP, they do not much involve in laminar flow because of their exceptionally stronger hydrogen bonding which do not allow molecules to flow so easily as of water and ethanol. For them, the velocity gradient is very high and hence they flow slowly because their molecules are not reoriented. Thus, it becomes a most pertinent question that how the molecules orient and reorient when they are in hydrogen bond networking or in contact of the plate assumed on the rigid wall of unit surface area noted by A. Interestingly, it also triggers liquid-solid interfaces; thus, the id, structure, dimension of survismeter matter a lot in case of causing kinetic energy correction which was not considered. Also, the cohesive forces in liquid mixtures respond during opposing forces, and hence these molecules face the plate area despite this interface they maintain the molecular dynamics and molecular mechanics. Therefore, it becomes a question of discussion which may lead to develop a new theory apart from friccohesity-like patterns of molecular motions, distance of hydrogen bonding, because HB distance matters a lot, which defines the manipulation of forces seen in extraction, separations, binding, evaporation, capping of nanoparticles, and functionalization of graphene as carbon nanotubes.

More interestingly, the torque and frictional forces become the most prominent for these situations. So such scenario could open a new facet of molecular interaction engineering leading to thermodynamics of structured liquids. Thus, the LLI have ventured with electronic, hydrophilic, hydrophobic, geometrical, electrostriction like cis and trans forms of H atoms. LET and LEM local equilibrium thermodynamics and local electronic motions, respectively, work on the infinitesimal mode to assist the friccohesity so that structural transitions are avoided. Till date, the viscosity theories existing could not take an account of the potential of plate liquid-solid interface (LSI) and so could not answer the treatment of actual behavior like how could these localized dynamics and mechanics (LDM) could affect the atomic motions, bond twisting, torsion, stretching, scissoring, rocking in planes and out of the planes. So, the friccohesity comes into existence because it takes into account the DM in terms of cohesive forces and also the frictional forces. So, anyone is in position to answer the complications of fluid dynamics of the giant molecules within prescribed experimental conditions and dimensions of the survismeter. Thus, the friccohesity is directly proportional to the stretching frequency of the molecules, and there is an urgent need to track all the surfaces of the molecules which undergo such changes.During such situations, the inner part of the molecules as per molecular dynamics, mechanics get freshly reoriented and the molecules with these activities maintain stronger rigidity and electronic stability [6–8]. They remain intact intramolecular; however, intermolecular forces undergo changes. Thus, the friccohesity is in relation with UV, visible light, FTIR, quantum chemistry.

2.2. Molecular bioengineering and molecular shock

In light of spectroscopic and thermodynamic scales of molecular identification, it seems valid that the friccohesity, tentropy, and IMMFT, the new concepts, become the most relevant and wanted tools to define overall interacting behavior of molecules. Since the molecule does have localized electrons cloud with stronger chemical bonds, which support the molecular motions with definite energy noted as follows.

$$E = \frac{1}{2}mv^2 \ \ or \ \ E = \frac{1}{2m}m^2v^2,\ p = mv \ \ or \ \ p^2 = m^2v^2 \ \text{ or } \ E = \frac{p^2}{2m}$$

Thus, if the molecules move from one point to another, they have energy or momentum as is listed in above equation. Such mass flux could have effect on the muscle or on other objects, which is noted as molecular shock; in practice it is noted when the hot water is used as heating agent to warm up the wanted object. Such molecular energy is obtained when the molecules on getting heat oscillate with definite kinetic or oscillatory or rotational or translational energies. Since a single molecule shows so many wave numbers in FTIR, these different stretching sites of molecules could have LET (local equilibrium thermodynamics), LEM (local equilibrium molecular dynamics), local energy distribution arrays (LEDA) with certain tentropy, and IMMFT scales of parameters of specific magnitudes. For example, the solubility of cholesterol attained through simple vegetables juices act as friccohesity destabilizing agents. Therefore the nature of juices or extracts of fenugreek, garlic, ginger, turmeric, butter guards etc. could have valuable physicochemical properties which may dissolve the cholesterol leading to have a useful bioengineering process. Several *in vitro* experiments are being conducted using survismeter which could explore and elucidate a role of friccohesity and tentropy as flux and force theory. Also magnetically, the rheological properties could be developed and hence the data could become the most effective to hammer out the cholesterol by physicomechanical methods. Therefore, the magnetic forces applied during viscous flow give an opportunity to the experimenter to identify a role of functional groups or the arrangements of coupling constants. Also, the multiple capillaries are effective to see whether there is some natural law of selection of reorientation of the motions, which may be useful in proteins. Molecular alignment of one solvent toward LLI (liquid-liquid interface) with respect to the immiscible solvent when brought together could also lead to develop molecular motions at LLI or in bulk of each solvent. Therefore, the molecular alignment of both the phases toward LLI could lead to:

Isotropic science at LLI or in individual phases

Alignment toward micelles

Sensing of double bond detection

Hydrogen bond and radii determination

http://dx.doi.org/10.5772/62240

Kinetic energy and surface inhibition activity

Nanoparticles like Au, ZnO, SiO_2, Ag, alkane thiol capping ability

Drug-binding ability of the dendrimers

Rationalized hydrodynamic volume that retrieves the viscosity B coefficient

Contribution of loan pair electrons of surfactants or the double bond of tweens which are determined with survismeter

Oscillating crystal for density in liquid mixtures is informatory

Thus, the friccohesity and tentropy study aligning the molecular orientation leading to form the favorable force patch noted as CF it could also be tracking that some of the molecules with higher KE (kinetic energy) could be out of the phase isotropy.

2.3. Interfaces of friccohesity of molecular solutions

1. How do molecular structures affect the overall interacting behavior with solvents polarity, functional groups, electronegativity, hydrophilicity and hydrophobicity?
2. How do van der waals forces, London dispersive forces, and Lennard Jone potential work interacting activities?
3. Structural input to the molecular interactions and reorientation of the molecules

Friccohesity of pure chemical compounds is a most important data, for example, the friccohesity of the pure water at specified temperature indicates purity and entropy level of the water. It is noted that the change in temperature induces a change in internal pressure because on raising the temperature the CF are weakened and the FF are strengthened as the molecular motions are intensified. Therefore, the molecular networking developed because HB gets weakened and motions are intensified. Thus, the friccohesity is applicable in case of pure substance. Thus, the friccohesity is directly proportional to the kinetic energy and the molecular motions. It is also applicable to the rule of the Kelvin, van der Waals, Lennard jones potentials. Actually, these scientists could not visualize the real picture of the molecular forces without going in deeper look of the molecular dynamics. The friccohesity is very much connected to the molecular dynamics because the CF and the FF are possible only when the molecular identity is maintained, otherwise the concept is not applicable. Thus, the friccohesity of catalyst could be possible because the catalyst allows the adsorbate molecules to adhere to the surface of the adsorbents. It is possibly when the adhesive forces are developed. Therefore, the types of the friccohesity are made. For example, if the cohesive forces are between the similar molecules, then it is symmetric friccohesity; but when it is applicable when solid and liquid develop cohesive forces like adsorbate and adsorbent where the adhesive forces work rather than the CF. Thus, in such cases the friccohesity is noted as asymmetric friccohesity.

In case of the Arrhenius equation, the following equation is used for determining activation energy when the reaction goes on.

$$k = Ae^{-\frac{E}{RT}} \qquad (\text{eqn.1})$$

Taking natural log, the eqn.1 becomes as follows.

$$\ln k = \ln A - \frac{E}{RT} \text{ or } 2.303 \log = 2.303 \log A - \frac{E}{RT} \text{ or } \log k = \frac{2.303}{2.303} \log A - \frac{E}{2.303R}.\frac{1}{T} \quad (\text{eqn.2})$$

Thus, the final equation is developed as given below.

$$\log k = \log A - \frac{E}{2.303\,RT} \quad (\text{eqn.3})$$

The eqn. 3 could also be applied for any physicochemical indicator.

$$\log \eta = \log A - \frac{E}{2.303\,RT} \quad (\text{eqn.3})$$

The k is reaction rate or rate constant attained when the forward and backward reactions gain equal thermodynamics equilibrium or the Gibbs energy = 0; the temperature remains constant; the molecular motions are optimized; and not any transition state is developed. Therefore, eqn. 3 depicts the non-transition state except equilibrated state. Also η is viscosity, thus the unit of k is the unit of A noted as frequency factor as the reaction rate depends on the frequency of collisions. Therefore, any other or similar condition could be fitted in place of k. It is noted that the viscosity, surface tension, friccohesity, and other parameters are depicting the interaction phase with constant state of the molecular phases or the state. It is noticed that the unlimited changes in the molecular motions in molecular processes in varieties of medium and experimental conditions do occur, which could be defined by several orders in terms of entropic sciences or friccohesity domains. Therefore, integrating the changes, the well-defined kinetics of molecular processes could be developed considering their tentropic domains with separate partition functions (w) is noted as in eqn. 4.

$$S = k \ln w \quad (\text{eqn.4})$$

http://dx.doi.org/10.5772/62240

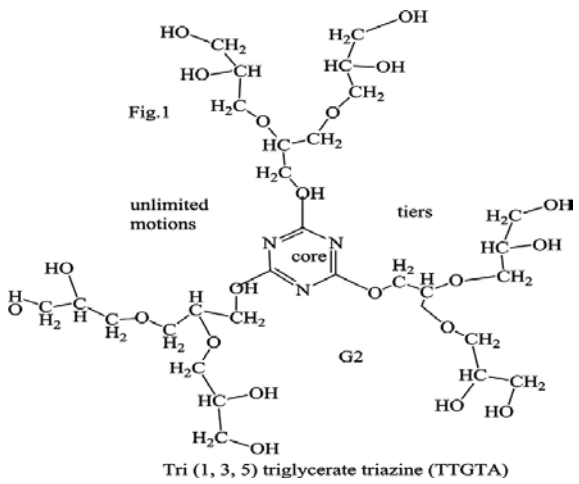

Figure 1. Innumerable isotropic orientations with rigorous molecular orientations in Tri(1,3,5) triglycerate triazine (TTGTA), a second-tier dendrimer.

Here, S is entropy, k is Boltzmann constant, w is partition functions; if any molecule has unlimited orders of the motions, S is higher where the tentropy is higher as per IMMFT model. Tri(1,3,5)triglycerate triazine (TTGTA) (**Figure 1**) is a second-tier dendrimer molecule which has different parts in different isotropic orientations with wider and rigorous molecular orientations, which affect the solvent molecules during flow [9–11]. Thus, the kinetic model of molecular activities could be extracted and developed in terms of physicochemical responses of the molecules with respect to the solvent and the experimental conditions.

For example, a first-order rate reaction could be fitted with k as rate constant and the unit of k is s^{-1} which is frequency per second of successful collisions for developing forward and backward reaction rates.

$$k = \frac{a}{(a-x)t}$$

When x = 0.5 or the 50% transformed from reactant to the product, so putting x = 0.5 from initially a = 1, solving 1= 0.5 = 0.5.

$$k = \frac{0.5}{(1.0-0.5)t} \text{ or } k = \frac{1}{t} \text{ or } k = s^{-1}$$

Thus the unit of k is s^{-1} noted as frequency factor; thus, if k is replaced by the viscosity, then its unit is Pa.s or kg $m^{-1}s^{-1}$. Thus, the mass transfer which does not react but interacts and gains a specific order of the molecular motions and orientations may be resulting as a laminar flow or the non-Newtonian flow. Therefore, the comparison of k and viscosity could be the most

interesting combination. Thus, considering the overall molecular stretching and oscillatory patterns, the net vector forces in case of ionic liquids, giant molecules in the area of supramolecular chemistry could be the most deciding in understanding the overall activities of the molecular species.

2.4. Determination of friccohesity

New creative ideas in respective areas of research and teaching work well provided a focus is on creating something new superseding the existing sciences in that specific area; it has to be absorbed in creative brains. Since time immemorial, the varieties of new creations have been the new state of arts and in succeeding steps have been the new path of development where

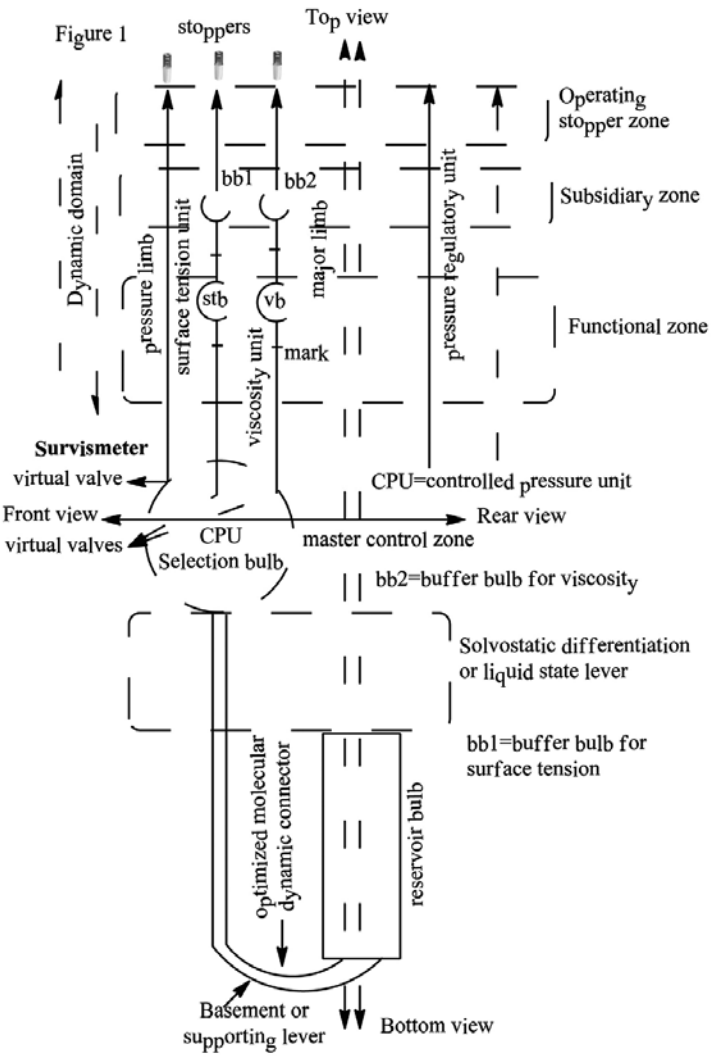

http://dx.doi.org/10.5772/62240

no new idea, bigger or smaller, loses its identity as the scale is based on the need and also creating new needs or applications. Thereby, right from late thirteenth to late fifteenth centuries, there was a huge hunger of idea developing and modeling something new as alternative sciences, which further led to a new era of industrialization of fundamentals from sixteenth century onwards, may be James Watt's vapor run engine or Robert Boyle's equation for ideal gases. Thus, the creativity has been the prime object of research and teaching in all the time of civilization. The Ostwald viscometer, Ubbelohde viscometer for viscosity, or Traub's stalagmometer for surface tension studies have been the foundation stones in measuring valuable physicochemical properties of liquid mixtures. Contrary to their work for measuring the parameters individually, the new research methodology named as survismeter has been successful in measuring surface tension, viscosity, activation energy, interfacial tension, wetting coefficient, and friccohesity. Currently, this new state of art is patented and 7 commercialized by Borosil named as Borosil Mansingh Survismeter (BMS). Schematic 8 illustration of survismeter is noted in **Figure 2**. There are four views of the survismeter, the top where stoppers are fitted to monitor the pressures and facilitate the liquid sampling and flow inside the bulbs. Number two is the bottom view which supports the anchoring of survismeter on the basement to keep the survismeter vertically at right angle maintained by spirit level. Thirdly, the front and rear views where the front view assists in taking measurements of the viscous flow times and pendant drop numbers for calculation of the viscosity and surface tension, respectively. The survismeter also contains virtual valves opening in the CPU or selection bulb or wisdom bulb and operates on 1:1 channel. The virtual valves are monitored by the stoppers to be fitted on the top opening of the survismeter units. The sample is loaded through the major limb without any air trap, especially in case of the surfactants or the ionic liquids which could trap air bubbles and create hurdle in natural fluid flow.

The subsidiary zone explains equilibration of the liquids in buffer bulbs whereas the functional bulbs explain the main bulbs where the prescribed liquid sample is filled and allowed to flow through standard orifice within the marks noted on the capillaries.

The data of several physicochemical properties generated on authentic reproducibility, high resolution, and repeatability modes have been published in American Chemical Society, Royal Chemical Society including several journals of leading publishing companies. The survismeter is being used by numerous industries such as inks, soaps and detergents, resins, nanoemulsions, along with introduction of academic curricula of several educational and research institutions. Thus, the science and potential of survismeter is most effective for study of multiple physicochemical properties of liquid mixtures. Science invention and craze (SIAC) creates a lot of self-inspiration to do more and more in life; there is only the craze that fills up new energy to move forward for more work of new nature and new beginning.

2.5. Determination of Brownian motions

The nanoemulsions are different from the solutions because the hydrophobic part could not interact with water if used as solvent and hence move toward surface in haphazard motions as the solvent is unable to develop stronger IMF. The alkyl chain thus involves in uncontrolled

motions in 1, 2, and 3Ds and thus is measured comparing the friccohesity of solutions with the equation noted as follows.

$$\text{Brownian motion} = \frac{\sigma_{IS} - \sigma_{SS}}{\sigma_{IS}} \times 100$$

The σ_{IS} stands for friccohesity of ionic solutions, σ_{SS} stands for friccohesity of surfactant solutions. Here the solvents are common; in most cases, the water could be an excellent solvent for both the ionic and the surfactant solutions. Also the difference in friccohesity data of two solutions as noted in the following equation could visualize the state of the Brownian motions.

$$\text{Brownian motion} = \text{friccohesity of ionic liquid} - \text{friccohesity of surfactant}$$

2.6. Scavenging activity of the antioxidant of free radicals

The studies could be extended for these activities determined with survismeter using the following equation.

$$\text{Scavenging activity} = \frac{\sigma_m - \sigma_S}{\sigma_m} \times 100$$

The σ_m and σ_s represent friccohesities of medium sample respectively at the prescribed experimental conditions. Similarly, the scavenging activity could also be calculated using the following equations.

$$\text{Scavenging activity} = \frac{\eta_m - \eta_S}{\eta_m} \times 100$$

$$\text{Scavenging activity} = \frac{\gamma_m - \gamma_S}{\gamma_m} \times 100$$

The symbols η and γ depict viscosities and surface tensions, respectively.

2.7. Golden rules of survismeter science and applications

The factors making survismeter a green and clean science for wider acceptability and use are listed as follows.

1. Critical reasoning of hypothesis and mechanism already used in surface tension and viscosity theories and to look for undiscovered or untouched or hidden interfaces and possibilities of new hypothesis

http://dx.doi.org/10.5772/62240

2. Ludwig Boltzmann energy distribution theories of energy homogenization and capping of nanoparticles
3. Rudolf Clausius entropic factors for homogenization and Gibbs Helmholtz energy
4. Boon and newly established novel sciences in areas of solutions and emulsion chemistries
5. Functional asset of liquid-solid interfaces
6. Combination of uniform functional capillaries for continuum and noncontinuum liquid flows within a length aligning and reorienting the molecules.
7. Establishes an operator noted as friccohesity, between continuum and noncontinuum fluid flows
8. Wonders of bulbs noted as CPU (controlled pressure unit) or selection bulb
9. The 1:1 channel selection wisdom or rule of CPU
10. Geometrical isomerism and symmetry in shape (GIASH) of functional bulbs, made for surface tension and viscosity measurements, as most critical coordinates of the survismeter noted as most specified coordinates
11. Transforming CF into AD around uniform glass circular surface with uniform surface tension, roughness, surface forces for the purpose of PDN formation and detaching kinetics
12. Liquid accessibility and development of excellent uniform liquid distributions around an exposed area of extreme lowermost tip of the capillary.
13. Distributions around uniform surface energy and liquid so that the nature of CF into AD are functional in PDN formation and falling that lead to equal distribution of the forces in all directions for excellent result.
14. Drop formation and size depending on liquid density in all directions so that the stress and strain are not developed.
15. Study of stress and strain on the drop formation must be completely avoided because of a jacket of CPU and vertically at 90 degree angle.
16. Flow remains constant and remains like a current which makes backlash and back jerk to influence the quality of data, so that the extruded distance of capillary is optimized and monitored by pressure regulatory limb (PRL).
17. The withdrawal of the pressure regulatory story is withdrawn smoothly so that no air bubble or some additional mechanical energy is not created inside the liquid filled in reservoir bulb.
18. Pressure distribution inside CPU is excellently and naturally distributed during the fall of PDN assisted by PRL.
19. Distance between the terminus of an extruded capillary and lower orifice of CPU is optimized to avoid the creation of mechanical energy and air trapping.

20. Entrance of the viscous flow capillary is at 45 degree angle so that backlash and jerking are avoided during measurements.

21. Top coordination among physical parts, orifices, capillaries, angles, opening, and regularity actions is made for accurate, reproducible, and reliable data.

22. Vertical positions alignment effect on fluid flow.

23. Asset for study of viscoelastic fluids noted as MRF (magnetorheological fluids) external forces.

24. Novel science for study of aero emulsions or aerated solutions for determination of adsorbed air, for example, adsorption of O_2 and CO_2.

25. Vertically aligning uniform flat plate at the top of survismeter.

26. UV and IR sensing mode of reservoirs bulb and magnetic doses to functional bulbs.

27. Friccohesity model of rupturing of molecular membrane to determine membrane strength made out of holding hydrophobic interactions together like lipid membranes.

28. Asset for study of rupturing/distorting of lipid membranes made up of hydrocarbon-water that decrease surface tension from $\gamma_0/_w \sim 40$ mN/m by analogy to disappearance of surface pressure in a lipid monolayer under large expansion at an oil/water interface.

29. IMMFT and thermodynamics of biomembrane ruptures (1 to 25 mN/m) based on lipid composition and rupture strength is a dynamical property.

This is not the question of measuring many parameters together, but it is the essential need since no such research methodology exists that is why people could not think and work with individual measurement as in isolations; however, simultaneously measurements go multi-faceted like redox, kinetics where complementary part characterization is essential. Thus, the purpose of measuring viscosity is to find out solute-solvent interactions, and currently the entangling or the trapping of the solvent with solutes or other chemical species like drug in dendrimers. This is supplemented by the surface tension or better known as coalesce or the cohesive forces [12].

The difference in fluid flow velocity and pendant drop numbers on loading the molecules in capillary flow of the survismeter gives the idea of solute-solvent interactions, size, shape, enthalpy, entropy, tentropy, IMMFT, friccohesity. Therefore, the difference in velocity between adjacent layers of fluid is listed as a velocity gradient depicted in simple terms as v/x, v is velocity difference and x is distance between the adjacent layers. To keep one layer of fluid moving at a greater velocity, the adjacent layer and a force F are necessary. It induces a shearing stress F/A. The 'A' is surface area in contact with the layer moving ahead. Also, the enthalpy released in process could be noted as follows.

$$\Delta H_{LBL} = friccohesity_{solution} - friccohesity_{solvent}$$

LBL stands for layer by layer flow in a closest manner during the viscous flow.

http://dx.doi.org/10.5772/62240

3. Friccohesity golden theme in nanoemulsion

The friccohesity becomes indispensable data in case of IL (ionic liquids), LC (liquid crystal), TGL (triglycerides), and NEL (nanoemulsions) because these molecules develop dispersion of hydrophobic part in aqueous phase, but at the same time their hydrophilic part develops different activity with water. Briefly, hydrophilicity induces enthalpic activity whereas hydrophobicity induces entropic activities, but at a nanometer range. Thus, the hydrophobic part by attacking structured water with definite Brownian motion leads to induce frictional forces as its cohesive forces are weakened, then only it is able to disperse in structured water. Similarly, the hydrophilic part leads to develop binding forces on disrupting structured water with more weakening of hydrophilic-hydrophilic transforming toward hydrophilic-water linkages. In hydrophilic-water linkages, more weakening of CF takes place and this could also lead to act as a favorable factor for increasing frictional forces too. Thus, the frictional forces in the form of hydrophobic tail causing Brownian motions are favored and also in case of the hydrophilic-water head weakens surfactant self-binding to its binding with water. If higher is Brownian motion, the surfactant approaches the surface of the liquids mixtures and settles at the surface; when the surfactant reaches to surface and gets settled at the surface, then the surface energy is utilized in larger amount. Thus, weakening surface energy, which is formed out of unbalanced molecular forces (UBMF) of the solvent molecules, leads to develop molecular reorientation to optimize the forces as per their geometrical activities. This process or movement of larger surfactant molecules to surface is noted as surface excess concentration occupying per unit area of the surface. At surface, still two thermodynamics domain work, one hydrophilic and another hydrophobic where hydrophobic dominates and surface tension decreases with higher pendant drop numbers if measured with survismeter.

At the same time, in such a situation the frictional forces also become active and in fact increase if measured in terms of viscous flow time using survismeter. In general, it is seen that in case of nonelectrolytes the surface tension decreases, resulting in an increase in viscosity which proves that on surfaces excess concentration is higher and bulk concertation is lower. This theory is defined by friccohesity as both the forces are active in such liquid mixtures; however, conductance could be another data which plays an important role in defining the exact location and binding and mobility of the molecules with higher forces or the lower forces. It is also defined by Walden product, but there is a need to also incorporate the surface or the CF forces somewhere in the ambit of the Walden which is not an effect for emulsion, thus the new version could be presented as physicochemical molecular mimicry (PCMM). The equation is noted as follows.

$$\mathrm{PCMM} = \left[(\mathrm{pdn})(\mathrm{vft})(\mathrm{OD})(\mathrm{density})(\mathrm{conductance})\right]$$

The pdn depicts pendant drop numbers, vft viscous flow time, OD is optical density, density is self-explanatory, conductance, and these parameters integrated offer the physicochemical profile of the molecules in any working medium and working experimental conditions. The

N-4-methoxybenzylidene-4-butylaniline could generate effective friccohesity if dissolved in several solvents under variable temperatures.

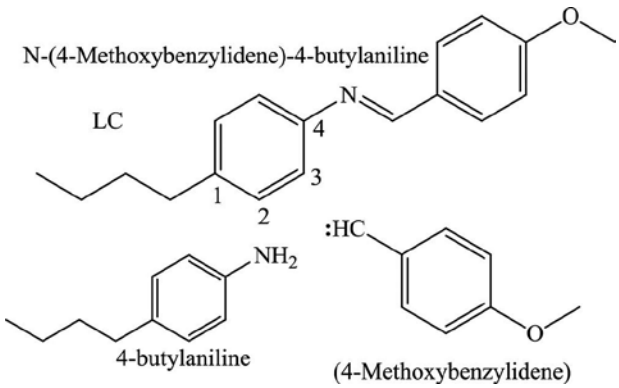

Also, the ionic liquids noted in the following could also develop very useful liquid mixtures, may be with metallic nanoparticles of the magnetic nanoparticles as an effective medium for light-sensitive process or the heat-sensitive processes. Both the ionic liquids 1,7-bis(3-methyl-imidzolium-1-yl)heptane and 1,8-bis(3-methylimidzolium-1-yl)octane could develop stronger solubilization of two immiscible solvents dissolving insoluble pollutant to recover them or to transform them into safer chemical forms, which may be used as medium, washing reagents, or coating materials. Their percentage solubilizing strength with respect to their hydrophobic chain could be estimated with their interfacial tensions with respect to air-liquid-interface (ALI) and liquid-liquid-interface (LLI). The ALI acts as standard data whereas another solvent, when used in forming LLI, is used as the test case or the sample. For example, air-water-interface is most widely used as standard if pure water is used in the experiment in a laboratory of pure air. The interfacial tension of ALI system is 71.97 mN/m (milli Newton per meter), but when CCl_4 is brought in contact with water, then the system is noted as LLI which has its own IFT.

$$\text{Mutual solubilization} = \frac{\gamma_{\text{ALI}} - \gamma_{LLI}}{\gamma_{ALI}} \times 100$$

The γ symbol indicates surface tension of the systems, thus γ_{ALI} indicates interfacial tension of the ALI, and γ_{LLI} the interfacial tension of the water-CCl_4 interface. Thus, γ_{ALI} is noted as standard and γ_{LLI} as the sample or the test sample [13]. Similarly, DPPH free radical scavenging activities by ascorbic acid or dendrimer in two immiscible solvent systems could be determined with the following equation.

$$\text{Scavenging activity} = \frac{\gamma_{\text{ALI}} - \gamma_{LLI}}{\gamma_{ALI}} \times 100$$

http://dx.doi.org/10.5772/62240

The LLI and also their impact on solubilization with series of alcohol, ketones, ester, organic acid, and mineral acids could be the most interesting experiments. Since interfacial tension is the most effective data for study of mutual solubilization of two immiscible liquids or any third component in the two.

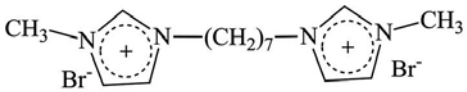

1,7-bis(3-methylimidazolium-1-yl)heptane bromide

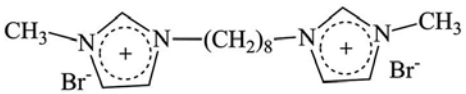

1,8-bis(3-methylimidazolium-1-yl)octane bromide

3.1. Friccohesity and tentropy for study of ionic liquid-based nanoemulsion

Quantitative study of friccohesity and tentropy of biomolecules like proteins, LDL (low density lipoproteins), in liquid media constituted of biocompatible ionic liquids at variable temperatures and pH could lead to develop new dimension of the liquid materials apart from ionic liquids, liquid crystal. Such liquid materials could be noted as isotopic or anisotropic liquid materials (IALM). Since the IALM are new study and no such concept is reported till date and no data on in vitro molecular arrangements are reported, and thus being potential population of the several substances in a most organized or nonorganized form could perform several tasks like medically essential outcome to prevent cardiovascular disease, fluid dynamics of the study, friccohesity engineering of the liquid mixtures, thermodynamical significance of the compositions of the LDL and IL, surfactants, TGL, homogenization of the liquid mixtures prepared out of various proteins, their effects on proteins conformations, their isotropy study, their spintronics, their micellization and aggregation. There are several surface area-based processes where the molecules do have entropic shock cum Brownian motions: Tyndale effect on molecules motions, Lechatelier and van der Waals' theories, Mansingh equations, UV and visible light effect, effects on free radical, tracking activities of the cancerous drugs, effect on drug solubilization, dendrimer effect on LDL emulsion, curcumin effect on emulsion, LC effect on nanoemulsion, DLS pattern aggregation, clustering, coalesces.

3.2. Biocompatible LDL nanoemulsions to dissolve fats in the body

The LDL particle effectively enables emulsification by surrounding fatty acids to push them to extracellular fluid. Each LDL particle contains a single apolipoprotein B-100 molecule (Apo B-100, having 4536 amino acid residues of 514 kDa), along with 80 to 100 ancillary proteins. The LDL has a polyunsaturated fatty acid hydrophobic core of linoleate and hundreds to thousands (≈1500) of esterified and unesterified cholesterol molecules.

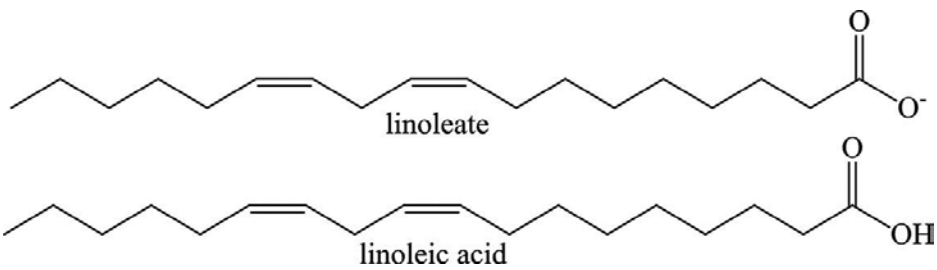

The core carries varying numbers of triglycerides and other fats surrounded by a shell of phospholipids and unesterified cholesterol, as well as a single copy of Apo B-100. The LDL particles are ≈ 22 nm diameter of ≈ 3 million daltons. Since LDL particles contain a variable and changing number of fatty acids, hence there is a distribution of LDL particle mass and size. Determining LDL structure has been a tough task because of its heterogeneous structure as a structure of LDL at human body temperature in native state, with a resolution of ≈ 16 Angstroms using cryo-electron microscopy, has been recently described.

3.2.1. Friccohesity of shifting of electron

Titration as an effective method utilizes reacting species as per a law of mass action which undergoes or materialized through structural activities [14]. For example, the structure of methyl orange from red to colourless depicted as canonical forms of reduction and oxidation. Of course, countless such species are generated but two out of them have been studied as delocalized structure noted in the following.

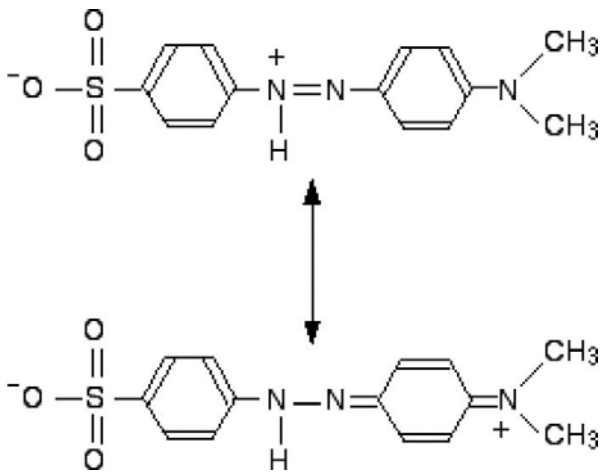

Thus, the titration at several time intervals could have different states of molecular dynamics and molecule expressions of forces with definite friccohesity and tentropy because several asymmetric structures exist. Such intramolecular dynamics or activities induced on several intramolecular motions develop countless arrays of motions or orders, which lead to develop

http://dx.doi.org/10.5772/62240

intramolecular entropy noted as tentropy. Therefore, the movements of electron in structure show that how the mutual structural changes occur as noted in the following.

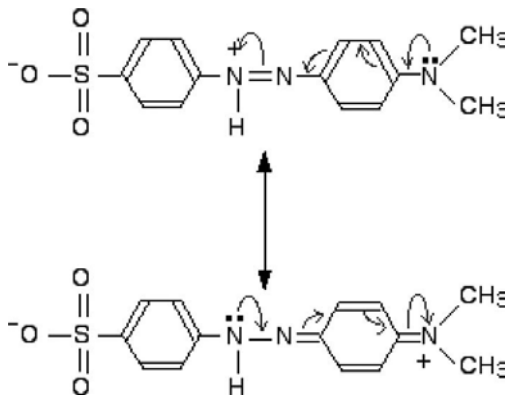

However, the electrons do not fully shift to either side, but remain in benzene case and an actual structure resonate somewhere in between these. It is most interesting to determine the friccohesity at each interval so that the intermolecular forces are determined with respect to a shift in the electrons within the structures. Therefore, the titration could be performed in the solution reservoir of the survismeter to estimate the possible changes, although the canonical structures may not have any effect on the geometrical changes like in bond lengths or bond angles. The lone pairs on N atoms induce delocalization and all the bonds around these N atoms remain in the same plane and the lone pair sticking up facilitating sideways overlap with orbitals on the subsequent next-door atoms. Hence, a kind of host canonical forms with double and single bonds along with positive charge located at various places around the rings and on the other N atom, and such structural orientations make these systems most active and suitable for the study of friccohesity of such liquid mixtures. It could be more interesting if the ionic liquids are also mixed with methyl orange for understanding of the multitude of canonical forms that induce delocalization. Therefore, the catalytic molecules may develop green upper critical solution temperatures using such systems with two immiscible solvents.

4. Future prospects

Thus, the friccohesity and tentropy, which deals with molecular or ionic forces in liquids mixtures, could effectively be applied or extracted and retrieved useful ideas about their behaviors.

New experimental research methodologies could be developed as follows.

1. Friccohesity, as new physicochemical property, assists formulation of molecular liquids.
2. Tentropy, new intramolecular potential for drug loading or adsorbing toxic metals.

Thrust areas of research studied in the proposed academic plan and project are as follows:

1. Molecular interaction engineering
2. Phase extraction based on chemical affinity and CF
3. Ionic liquids and their physicochemical properties
4. Enthalpic studies of salts based on Hofmeister series
5. Structure breaking and hydrodynamics molecules of
    a. Biomolecules in varied aprotic polar medium
    b. Salts on increasing size
    c. Re-engineering of solvents by salts
    d. Increase in friccohesity indicating structure breaking
    e. Dendrimers in increasing tiers
    f. Ionic liquids in increasing alkyl chain in imidazolium ring
    g. Flavonoids in increasing OH and double bonds
    h. Surfactants in increasing I+ effects
6. Nanochemical sciences of structured and non-structured miceller liquid mixtures
    a. Hydrophobicity and hydrophilicity of interacting molecules
    b. Brownian motions and hydrodynamic volumes
7. Adsorption and surface area of adsorbents
8. Heat capacity and mass transfer rate within rigid one-dimensional box
9. Enhanced intake of curcumin in nanoemulsion
10. Saving detergents during washing clothes kitchenwares
11. Pesticides in fields
12. Sprayants in houses
13. Hydrology and percolation of water
14. GPC and molecular weights of the materials
15. Aligning molecules isotopically on capillary flow and generating electric response
16. Viscous flow with ionic liquids for electric generator replacing concentration cells
17. Viscous flow of salts aqueous solutions for electricity generation

Author details

Man Singh*

Address all correspondence to: mansingh50@hotmail.com

School of Chemical Sciences, Central University of Gujarat, Gandhinagar

References

[1] Chandra A., Patidar V., Singh M., Kale RK., Physicochemical and friccohesity study of glycine, l-alanine and l-phenylalanine with aqueous methyltrioctylammonium and cetylpyridinium chloride from T = (293.15 to 308.15) K, Journal of Chemical Thermodynamics, 65, 18–28, 2013.

[2] Singh M., Combined device for measuring of osmotic pressure, conductance, surface tension, and viscosity, Russian Journal of Physical Chemistry A, 84(13), 2345–2350, 2010.

[3] Singh M., Survismeter—type I and II for surface tension, viscosity measurements of liquids for academic, and research and development studies. Journal of Biochemical Biophysical Methods, 67(2–3), 151–161, 2006.

[4] Singh M., Apparatus for measuring osmotic pressure, conductance, viscosity and surface tension of liquid solution, US 7987700 B2, 2 Aug 2011.

[5] Singh M., A simple instrument for measuring the surface tension and viscosity of liquids, Instruments and Experimental Techniques, 48(2), 270–271, 2005.

[6] Singh M., Effect of potassium halide salts on mutual solubility of water + aromatic hydrocarbons liquid–liquid interface studied with surface and interfacial tensions, Journal of Molecular Liquids, 200(Part B), 289–297, 2014.

[7] Singh M., Upper critical solution temperatures for immiscible solvent systems with halide salts, carboxylic acids, surfactants and polynuclear aromatic compounds and benzene derivatives, The Journal of Chemical Thermodynamics, 39(2), 240–246, 2007.

[8] Singh M., Pandey M., Yadav RK., Verma HS., Thermodynamic studies of molar volume, pair and triplet interactions at increasing side chain length of α-amino acids in aqueous potassium chloride solutions at different concentration and 310.15 K, Journal of Molecular Liquids, 135(1–3), 42–45, 2007.

[9] Kumar D., Chandra A., Singh M., Influence of urea on shifting hydrophilic to hydrophobic interactions of Pr(NO3)3, m(NO3)3, and Gd(NO3)3 with BSA in aqueous citric acid: a volumetric, viscometric, and surface tension study, J. Chem. Eng. Data, 59 (11), 3643-3651, 2014.

[10] Singh M., Kumar A., Hydrophobic interactions of methylureas in aqueous solutions 20 estimated with density, molal volume, viscosity and surface tension from 293.15 to 21 303.15 K, Journal of Solution Chemistry, 35(4), 567-582, 2006.

[11] Kitawat BS., Singh M., Kale RK., Robust cationic quaternary ammonium surfactant-catalyzed condensation reaction for (E)-3-aryl-1-(3-alkyl-2-pyrazinyl)-2-propenone synthesis in water at room temperature, ACS Sustainable Chemistry & Engineering, 1(8), 1040–1044, 2014.

[12] Singh M., Simultaneous study of interfacial tension, surface tension, and viscosity of few surfactant solutions with survismeter 40 (10), 1344–1349, 2008 .

[13] Kitawat BS., Singh M., Kale RK., Solvent free synthesis, characterization, anticancer, antibacterial, antifungal, antioxidant and SAR studies of novel (E)-3-aryl-1-(3-alkyl-2-pyrazinyl)-2-propenone, New Journal of Chemistry, 37, 2541–2550, 2013.

[14] Maktedar SS., Mehetre SS., Singh M., Kale RK., Ultrasound irradiation: a robust approach for direct functionalization of graphene oxide with thermal and antimicrobial aspects. Ultrasonic Sonochemistry, 21(4), 1407–1416, 2014.

Edited by Marcelo L. Larramendy and Sonia Soloneski

This book, Green Nanotechnology - Overview and Further Prospects, is intended to provide an overview and practical examples of the use of nanomaterials in the new scientific challenges of the green nanotechnology world. We aimed to compile information from a diversity of sources into a single volume to give some real examples, extending the concept that green nanotechnology is far from being a scientific conundrum, and instead a real answer to some of the actual problems the whole planet is dealing with.

ISBN 978-953-51-4199-0

Photo by dkidpix / AdobeStock

IntechOpen